

**Chemical Functionalization of Porous Carbon-based
Materials to Enable Novel Modes for Efficient
Electrochemical N₂ fixation**

Dissertation

zur Erlangung des akademischen Grades
Doktor der Naturwissenschaften (Dr. rer. nat.)
in der Wissenschaftsdisziplin „Kolloidchemie“

eingereicht an der
Mathematisch-Naturwissenschaftlichen Fakultät
der Universität Potsdam
von

Qing Qin

geboren am 09.10.1993 in Anhui, China

Potsdam-Golm, im September 2019

Published online at the
Institutional Repository of the University of Potsdam:
<https://doi.org/10.25932/publishup-44339>
<https://nbn-resolving.org/urn:nbn:de:kobv:517-opus4-443397>

Acknowledgement

Although words alone are not enough to give the appropriate gratitude to all people whom stood beside me and supported me during my PhD studies, I would like to express my most sincere acknowledgement to the efforts of these people.

Firstly, I want to express my deep acknowledgement to my great supervisor Dr. Martin Oschatz, the group leader in our carbon group and as well as a professor in replacement at Potsdam University. I really enjoyed the discussions with him about science, which nurtured my passion for carbon and encouraged me to embark on the path of academic area. I am sincerely thankful to his efforts, suggestions, and support towards my research topics and revision of my papers and thesis. If not for his motivation, dedication and energy, this study and many others not covered in this thesis would undoubtedly never achieve fruition. Beyond science, two important things that he taught me in the life are to be strong and patient. Thanks, Martin! I always feel privileged to be his PhD student.

Thanks to Prof. Dr. Yan Lu in Helmholtz-Center Berlin for Materials and Energy for being my second supervisor, discussing about my research topic, and reviewing this thesis.

Great thanks to the group members in my carbon group. Many thanks to Runyu, who is the first friend I made in MPI, and he helped me a lot not only in the life, but also in the experiment. Great thanks to Milena for helping me a lot when I first came to this unknown country, listening to my complains, sharing my happiness, and telling me more about German culture and rules. Great thanks to Ipek, a lovely girl who always looks happy, for the help and valuable friendship. Great thanks to Ralf for the

Raman and gas adsorption measurement. Many thanks to Konstantin, Feili, Sandy and Sol as well. It is really my great honor to meet and make friends with them. I love my carbon group!

I would like to show thanks to my good friend and collaborator of Dr. Yun Zhao from the Leibniz Institute for Catalysis, who helped me to do the DFT calculations and discuss the results with me. Also many thanks to Dr. Haijun Jiao, as he provided many useful suggestions for paper polishing and improvements of DFT calculations. Besides, I want to thank Max Schmallegger in Graz University of Technology for the EPR measurements and discussion of the results.

Great thanks to Jianrui, who can always share my happiness or sadness. Because of you, my life becomes more colorful and is thus full of fun. Many thanks to Qian, my good friend and my sister in MPI. She is also an excellent hair dresser. Thanks for the warm accompany and haircut.

I am very grateful to Ines and Ursula for the lab organization, which provides a clean and convenient environment for the research work. Great thanks to Tobias for measuring TEM, patiently discussing my projects, and teaching me a lot of knowledge about TEM. Many thanks to Antje for the TGA and elemental analysis, Johannes for XPS measurements, Heike and Rona for the SEM and TEM measurements, Elinor and Ursula for the electrospinning.

Thanks to Sasha, Clemens and Ryan for giving me the access to the facilities in their labs. Many thanks to my friends and very nice colleagues (Nieves, Jose, Marius, Lana, Paolo, Jin, Barius, Zhihong, etc.) in MPI, especially the meal pals (Guigang, Kai, Shaowen, Ang, Shuangyan, etc.) to Potsdam University every day, who have contributed to make my life here a great and memorable experience.

I would like to thank my idol, Bibi Zhou, who is a famous singer in China. I have loved her for 14 years since 2005. Daily life is always so trivial, but her figure fills up every stage of my youth. What is an idol and what does an idol mean? Everyone may have his or her own answer. For me, Bibi is my life mentor and source of positive energy. Her good personalities and attitudes towards life and dream have a deep influence on me. She is like the brightest star in my world to guide me to search for the light and hope. Every time I felt sad, lonely or stressed, her music and smile made me feel much better. The long distance between Germany and China, as well as the high workload made it impossible to attend most of her fans meeting activities and concerts. But on 11th November in 2018, she came to Germany. That had to be the most valuable gift and surprise for me. So life is wonderful, right? Thank you, Bibi, for warming my whole life.

Special thanks to my beloved and dear parents for their encouragement, accompany, patience and love. Although they cannot speak English and have no idea about my research, they try their best to support and encourage me to do what I want, and make me never feel alone. Many thanks to my grandparents, aunts, uncles, cousins and so on for all their love and help. The support of my good friends in China (Zhu, Meimei, Id, Xiaojing, Liting, Yu, Lu, Ling, Wuyong, Lei, Bei, Shuqi, etc.) also makes my life funnier, meaningful, and easier to keep on moving forward. Deep thanks to Liuliu for the always warm accompany and sharing of all my emotions.

I thank my committee members and reviewers for their valuable suggestions and time.

Deep thanks to the Max Planck Institute of Colloids and Interfaces and the Excellence Cluster “UniSysCat” for funding my research projects and travel expenses for the different conferences.

Great thanks to everyone I have met along the way. Thanks for all the love and injury in my life.

Finally, I would like to acknowledge my senior supervisor of Prof. Dr. Dr. h. c. Markus Antonietti, the director of the Colloid Chemistry Department of the Max Planck Institute of Colloids and Interfaces, for providing me the precious opportunity to pursue my doctorate here and acting as a role model for me not only in academics but also in life. I really enjoy the discussion with him, and his profound knowledge and patient guidance can always enlighten me. His good suggestions can also lead me to a more deep and systematic study of my research topics. With his encouragement, I finally make a plan for my future and I will try my best to achieve all my goals. I hope to be an excellent QQ, and to be one of his best PhD students.

Table of Contents

1. Motivation	9
2. Background and outline.....	13
2.1. An overview over carbon and carbon nanomaterials	13
2.2. An overview over porous amorphous carbon materials	14
2.2.1. Synthesis of porous carbon materials	15
2.2.2. Functionalization of porous carbon materials	18
2.3. Brief introduction of NH₃ synthesis	20
2.3.1. Haber-Bosch process	21
2.3.2. Biological process	23
2.3.3. Photochemical N₂ fixation	24
2.3.4. Electrochemical N₂ fixation.....	25
2.4. Main challenges for electrochemical N₂ fixation	29
2.4.1. Selectivity, activity and stability	29
2.4.2. Reaction mechanism	30
2.5. Outline	31
3. Enhanced electrocatalytic N₂ reduction via partial anion substitution in titanium oxide-carbon composites	33
3.1. Synthesis and characterization of M-Ts	35
3.2. Experimental studies of NRR active sites in M-Ts	47
3.3. Mechanism studies through DFT calculations (in collaboration with Dr. Yun Zhao and Dr Haijun Jiao).....	59
4. Single-site gold catalysts on hierarchical N-doped porous noble carbon for enhanced electrochemical reduction of nitrogen	65
4.1. Synthesis and characterization of AuSAs-NDPCs.....	66
4.2. Influence of Au single sites on the NRR performance	72

5. Electrochemical Fixation of Nitrogen and its Coupling with Biomass Valorization with a Strongly Adsorbing and Defect Optimized Boron-Carbon-Nitrogen Catalyst	83
5.1. Synthesis and characterization of BNC	84
5.2 Electrochemical tests of NRR.....	92
6. Conclusions and perspectives	102
7. Appendix.....	104
7.1. Abbreviations	104
7.2. Applied methods	106
7.2.1. Thermogravimetric analysis (TGA)	106
7.2.2. Electron paramagnetic resonance (EPR).....	106
7.2.3. Nuclear magnetic resonance (NMR) spectroscopy	107
7.2.4. X-ray Diffraction (XRD)	107
7.2.5. Infrared (IR) spectroscopy/Raman spectroscopy	108
7.2.6. Transitional electron microscopy (TEM) / Scanning electron microscopy (SEM)	109
7.2.7. X-ray photoelectron spectroscopy (XPS).....	110
7.2.8. High performance liquid chromatography (HPLC).....	111
7.2.9. N₂ physisorption	111
7.3. Experimental Section	114
7.3.1. Chemicals.....	114
7.3.2. Materials synthesis of enhanced electrocatalytic N₂ reduction via partial anion substitution in titanium oxide-carbon composites	116
7.3.3 Materials synthesis of single-site gold catalysts on hierarchical N-doped porous noble carbon for enhanced electrochemical reduction of nitrogen	116
7.3.4 Materials synthesis of electrochemical fixation of nitrogen and its coupling with biomass valorization with a strongly adsorbing and defect optimized boron-carbon-nitrogen Catalyst	117
7.3.5 Materials characterization	118
7.3.6 DFT calculations	119

7.3.7. Electrochemical tests	120
8. References	123
9. List of publications	144
9.1 Peer-reviewed journal publications	144
9.2 Conference contributions	145
9.2.1 Oral presentation as the presenting author	145
9.2.2 Poster presentation as the presenting author	145
10. Declaration	146

1. Motivation

Contemporary society is based on modern technology, and civilization level is largely related to energy utilization and availability.¹ Abundant energy in the earth can thus greatly accelerate the development of human civilization and improve the living quality, e.g., people today can drive the cars instead of the horses and keep warm in the cold winter by using heaters instead of fire. The improved living standards also result in soaring population growth. By 2050, the population is estimated to grow to 9.3 billion, and most of the humans will live in Asia and Africa, where the economy will rapidly grow leading to large consumption of energy.^{2, 3} According to the International Energy Agency (IEA), the exploding growth of global population and the ongoing industrialization in many developing countries will cause soaring demands for energy by comparing the years 2016 and 2040 (Figure 1.1).⁴ Daily consumed energy by humans can only be supplied if there are 3000 nuclear power plants like Palo Verde in Arizona, one of the world's largest nuclear power plants, generating electricity at full capacity every day. Therefore, there can be no doubt that energy availability will be one of the most serious problems in the 21st century.⁵⁻⁶

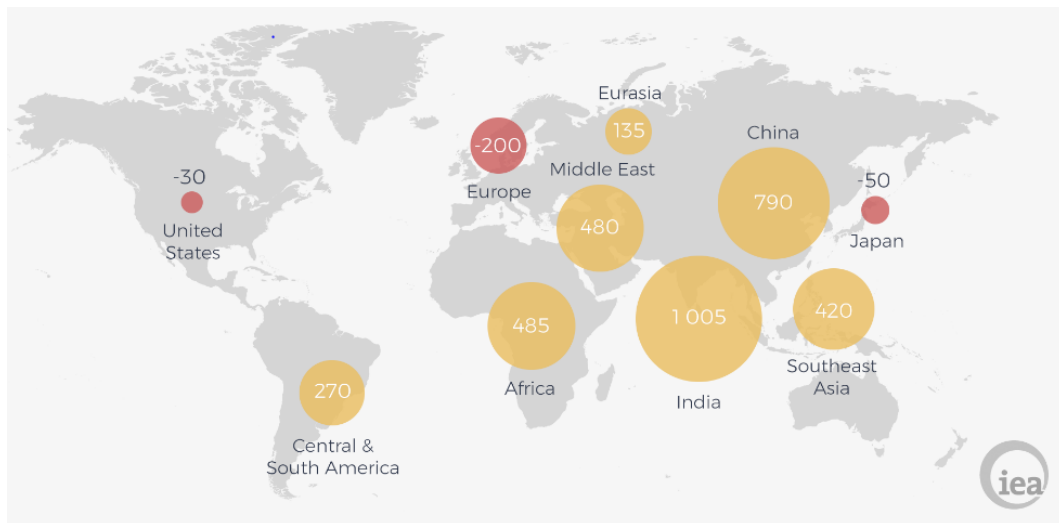


Figure 1.1. Change in primary energy demand for different areas in the world from 2016 to 2040 (Million Tonnes of Oil Equivalent).⁴

Turning to the energy supply side, fossil fuels remain dominant. The data from IEA shows that the world total primary energy supply (TPES) increased by around 2.5 times from 1971 to 2016 (Figure 1.2).⁷ Among different energy sources, non-sustainable energy sources of oil, coal, and natural gas remain dominant and are responsible for more than 80% of the energy production (Figure 1.2). Statistically, coal will become the only available fossil fuel by 2042 and all the fossil fuels will be used up by 2112, according to their current storage and consumption rate.⁸⁻

1. Motivation

⁹ Most importantly, the utilization of fossil fuels can result in a series of environmental issues (CO₂ emissions, acidic rain, dust, and many more) which is in fact the biggest challenge, will be beyond the energy crisis.

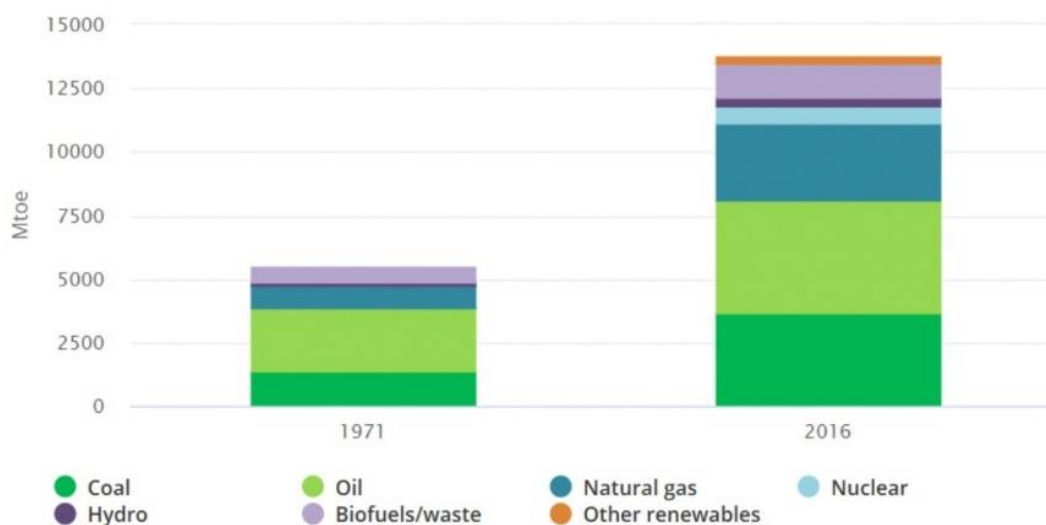


Figure 1.2. Total primary energy supply by different sources in the years 1971 and 2016.⁷

For those reasons, the world needs new energy supply chain and scientists should develop ways to utilize sustainable energy sources (solar energy, wind energy, hydropower, ocean energy, etc.) more efficiently to overcome the disadvantages of established fossil fuels. However, it is usually more difficult to directly use the sustainable energy sources with high efficiency in daily life. For example, oil combustion can be used to power cars. This is extremely hard with ocean energy. Considering that the mobility of the future is more electrified, which can make people's life more convenient,⁴ there will be a huge demand of electricity. Therefore, electricity production from sustainable energy sources with affordable cost is demonstrated as the more effective and promising route for the utilization of sustainable energy sources.

However, then the time discrepancy between the energy supply and usage provides a new challenge. For example, the electricity produced from solar energy is more powerful in the midday, but the demand for electricity is usually higher in the evening (Figure 1.3).¹⁰ Two main routes are possible to solve this problem, including either electricity storage or electricity conversion. Rechargeable batteries can store electricity through electrochemical processes.¹¹ Alternatively, electrochemical energy conversion should also be developed to obtain high-value energy-derived products by converting renewable electricity to chemical energy.¹² In this way, rational utilization of electricity can be achieved and some drawbacks of traditional synthetic strategies can be overcome.¹³ NH₃ is a desirable candidate due to its high energy density (1.32 kWh L⁻¹) and hydrogen content (17.8 wt. %), zero carbon content, as well as its critical role as

1. Motivation

agricultural fertilizer.¹⁴⁻¹⁵ NH_3 has been produced by the Haber-Bosch process for more than 100 years, but with large amount of natural gas consumption and CO_2 release.¹⁶⁻¹⁷ Recently, many scientists have thus studied NH_3 synthesis by the electrochemical N_2 reduction reaction (NRR). No hydrogen is needed for electrochemical NRR as protons come from water, and with this method, NH_3 can thus be produced everywhere where electricity can be generated. However, as for every technique, also here problems are to be solved, such as a low stability of catalysts and low efficiency of the overall energy conversion processes.

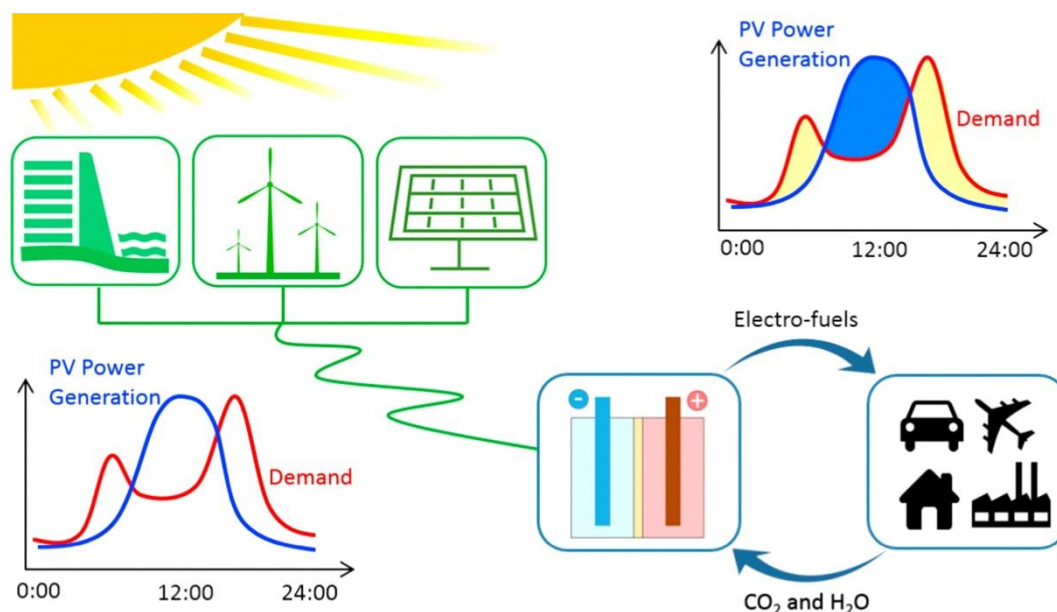


Figure 1.3. An overall schematic of electro-fuel enabled energy storage to migrate the mismatch between renewable energy generation (photovoltaic as an example) and energy demand.¹⁰

During those electrochemical energy conversion process, a series of electrochemical reactions takes place, such as the oxygen reduction reaction (ORR) and hydrogen oxidation reaction (HOR) in the hydrogen-oxygen fuel cell, oxygen evolution reaction (OER) and hydrogen evolution reaction (HER) in overall water splitting, CO_2 reduction reaction (CO_2RR) in CO_2 fuel cell and NRR in NH_3 synthesis.^{10, 18-20} Therefore, electrocatalysts obviously play an important role in those processes, which can influence the corresponding chemical reactions, such as lowering the reaction overpotentials and increasing the current densities. As in other fields of catalysis, there are three types of electrocatalysts, including heterogeneous, homogeneous and enzyme electrocatalysts.²¹ Considering the stability and recycling ability, heterogeneous electrocatalysts exhibit unique advantages, and in consequence, they attract more research attention. Porous carbon-based materials have been acknowledged as promising heterogeneous catalysts for electrochemical energy conversion, due to their abundant

1. Motivation

availability, high surface area, high defect density and porosity, desirable electric conductivity, and good stability. As the energy conversion efficiency for some reactions is still too low, especially for electrochemical NRR, the design of high-efficient porous carbon-based electrocatalysts is urgently needed. For the further targeted improvement, it is also crucial to understand the reaction mechanism.

This dissertation aims at developing novel porous carbon-based materials by adjusting and optimizing the composition and structure, as well as applying them to some crucial electrochemical reactions including electrochemical NRR and hydroxymethylfurfural (HMF) oxidation. The relationships between the structure and composition of carbon-based materials and their catalytic performance are elucidated. Reaction mechanisms are studied by density functional theory (DFT) calculations, which contribute to the future targeted design of optimized carbon-based electrocatalysts.

2. Background and outline

2.1. An overview over carbon and carbon nanomaterials

As the “king of the elements” with 15th most abundance in the Earth’s crust, carbon serves as essential building block for life.²² This is due to its unique characteristics and widespread important applications. Most importantly, carbon can versatilely bond with itself or other atoms with similar or very different electronegativities, allowing the formation of a majority of organic compounds and a smaller amount of inorganic compounds.²³⁻²⁴

Carbon materials are the main inorganic compounds, formed by only elementary carbon atoms bonding with each other in different ways. They exhibit versatile applications in many areas and revolutionized material science. The importance and potential of carbon materials have been demonstrated by some of the highest scientific awards, such as the Noble Prize in Chemistry for fullerenes in 1996, Kavli Prize in Nanoscience for carbon nanotubes in 2008, as well as the Noble Prize in Physics for graphene in 2010. In addition, the special honor is also endowed to carbon by the presence of the two peer-reviewed journals *Carbon* (Elsevier) and *C* (MDPI), which only publish carbon related papers.

Carbon is capable of forming different allotropes with versatile physical and chemical properties (Figure 2.1).²⁵ For example, graphite, a stacked hexagonal planar sheets with sp^2 hybridized carbon, is opaque and soft with good electrical conductivity, while diamond, a three-dimensional framework of cubic symmetry composed of sp^3 hybridized carbon, is transparent and has the highest hardness known. With the new age of nanomaterials, carbon nanofibers, carbon nanotubes, fullerenes, nanodiamonds, and graphene are emerging as promising carbon allotropes due to their extraordinary performance in various areas ranging from automobile to medicine, or from catalysis to energy storage and conversion. Fullerenes are cage-shaped molecules of different size, mostly composed of 6-ring or 5-ring units of carbon atoms, such as C_{60} . Graphene has been widely studied by scientists recently. It is a two-dimensional single layer of graphite with sp^2 hybridized carbon atoms, which shows good heat and electric conductivity, large and nonlinear diamagnetism, bipolar transistor effect, and high tensile strength. Besides, graphene can also be the start point for many other carbon nanomaterials, e.g., rolling up graphene layer(s) can form carbon nanotubes (CNTs), including single-walled CNTs and multi-walled CNTs. Porous amorphous carbon is another important sp^2 -rich carbon allotrope (a relative of graphene) with large internal surface area as well porosity, many defects, and disordered local structures.

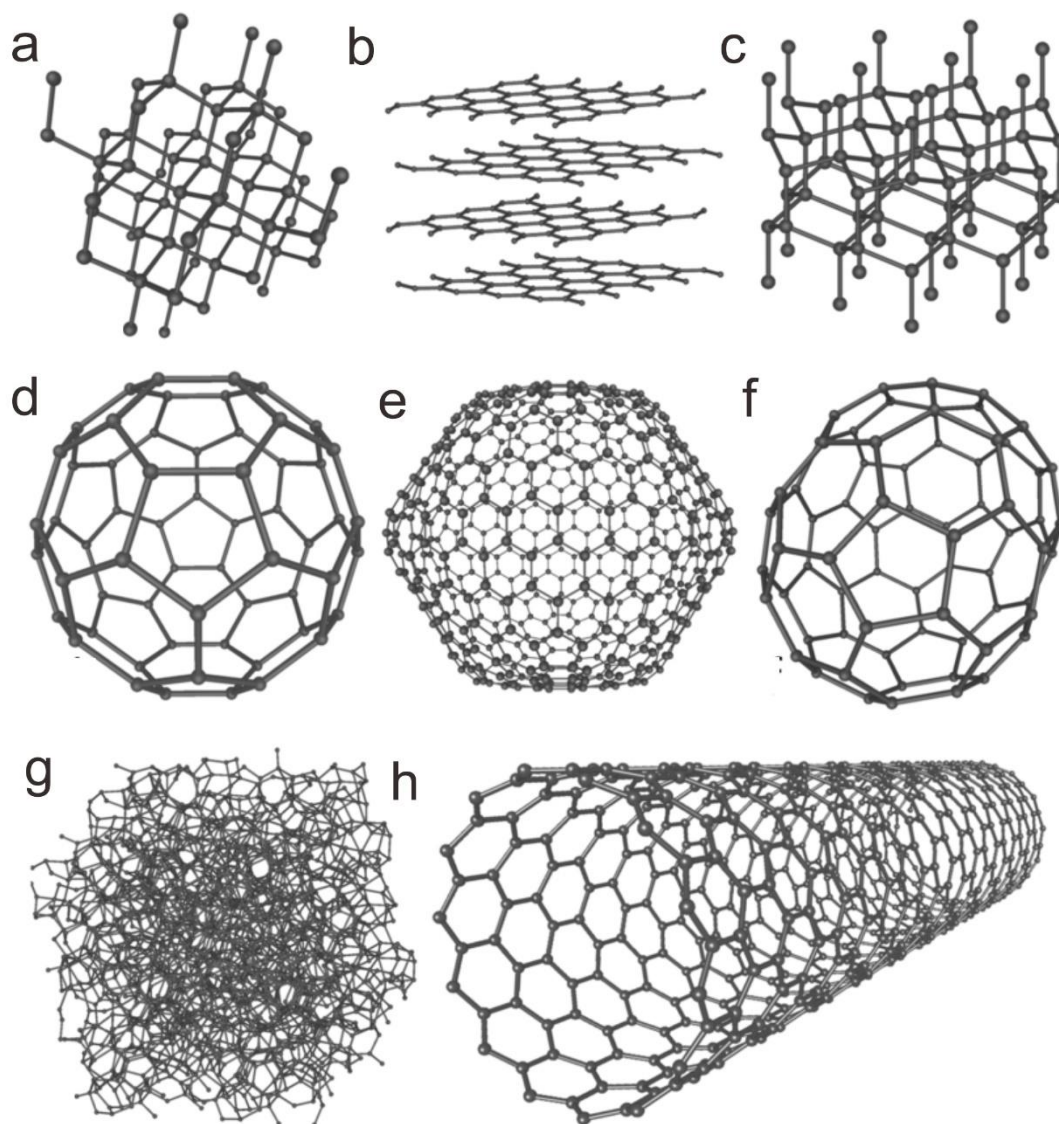


Figure 2.1. Structure of different carbon allotropes: (a) diamond, (b) graphite, (c) lonsdaleite, (d) C₆₀ buckminsterfullerene, (e) C₅₄₀, Fullerite (f) C₇₀, (g) amorphous carbon, and (h) single-walled carbon nanotube.²⁵

2.2. An overview over porous amorphous carbon materials

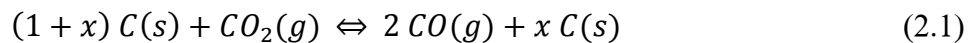
Among those carbon allotropes, porous amorphous carbon materials are a vital branch and receive a great deal of interests, due to their excellent stability, tunable porosity and surface chemistry, good electrical conductivity, structure diversity, and many other beneficial properties over other porous materials. Thus, they exhibit versatile applications in many areas, such as gas adsorption/separation, catalysis, pollutant treatment as well as electrochemical energy storage and conversion.²⁶⁻³⁰ According to the recommendation from International Union of Pure and Applied Chemistry (IUPAC), there are three types of porous carbon materials depending on their pore sizes, including micropores (< 2 nm), mesopores (2-50 nm), and macropores (>50 nm).³¹ Three parameters can be used to characterize their geometrical porosity,

2. Background and outline

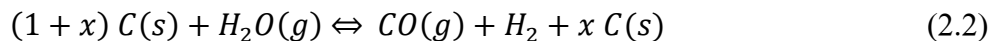
such as specific surface area (SSA), total (or micro) pore volume (TPV or MPV) and pore size distribution (PSD). The following part will introduce different methods for the synthesis of porous carbon materials. In addition, to improve their performance in catalytic applications, pristine porous carbocatalysts can be functionalized by doping heteroatoms and/or metal-based components to further tune their catalytic properties.

2.2.1. Synthesis of porous carbon materials

Activation method: The synthesis of so-called activated carbon materials can be divided into physical activation, chemical activation and a combination of both.³² Physical activation contains two simple steps of the initial carbonization and later activation. Raw materials with carbon content are firstly pyrolyzed into char with rudimentary porosity at high temperatures (> 500 °C) under the protection of inert gas, which can be further modified by physical activation agents, such as the most often used CO₂ and H₂O steam. Thus, carbon atoms in the carbon framework can be etched to generate desirable porosity. The CO₂ activation step is based on the well-known Boudouard equilibrium (Equation 2.1), named after Octave Leopold Boudouard. At high temperature, the equilibrium is shifted to the right and carbon atoms are removed from the framework due to carbon monoxide formation.



Similarly, H₂O steam activation is carried out according to Equation 2.2 with the formation of CO and H₂.



Chemical activation is carried out by the reaction between carbon precursors and chemical reagents.³² During the carbonization of the mixture, the highly concentrated chemical reagents are incorporated into the interior of carbon framework to inhibit their further contraction and etch carbon atoms thus giving rise to the development of porosity. Finally, as-obtained solids are washed to remove the remaining chemical reagents, followed by drying to obtain porous carbon.³³ The commonly employed chemical reagents are zinc chloride (ZnCl₂), phosphoric acid (H₃PO₄) and potassium hydroxide (KOH). For example, the possible KOH-activation mechanism is proposed by the following Equations 2.3-2.7:³⁴



2. Background and outline



The final formed free potassium metals can also penetrate into the lattice of carbon matrix and expand the lattice, followed by their removal to form porosity. Although large-scale synthesis of porous carbon materials can be achieved by the activation methods, the generated pores are often disordered and ill-defined, containing bottleneck or worm-like structures.

Templating methods: Templating methods are employed to achieve control over the pore structure by using different templates (structure-directing agents), including soft templates, hard templates and salt templates.³⁵⁻³⁶

The Soft-templating method is based on the self-assembly of carbon precursors on the surface of micelles or liquid crystals, mostly driven by van-der-Waals and Coulomb interaction forces (Figure 2.2).³⁷ Carbon precursors then undergo crosslinking and carbonization to obtain porous carbon materials. The most used templated molecules are surfactants and block co-polymers which are removed during cross-linking and/or carbonization.³⁸ However, the performance of such soft-templating carbon is usually obstructed by its lower SSAs ($< 1000 \text{ m}^2 \text{ g}^{-1}$)

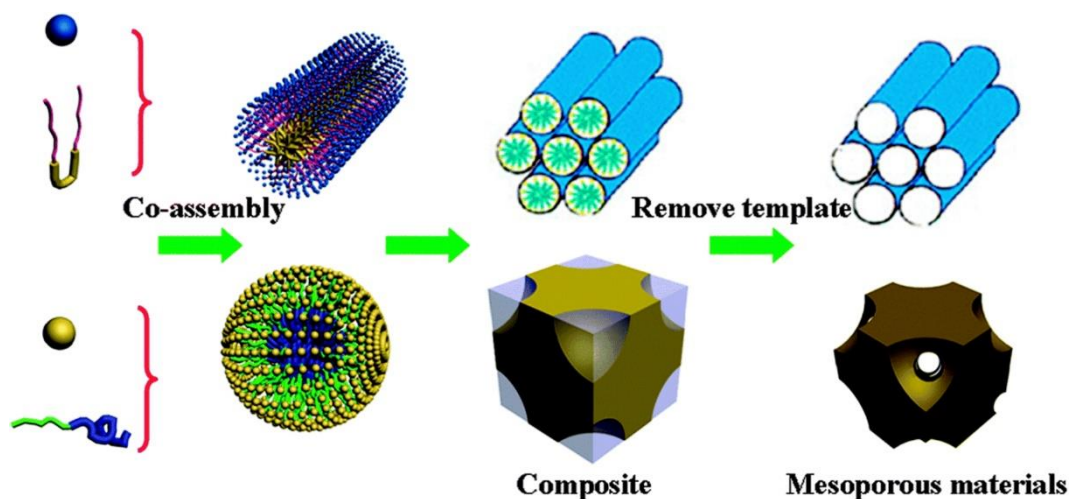


Figure 2.2. Soft-templating method based on the co-assembly of surfactant or block copolymer leading to mesoporous materials.³⁷

The Hard-templating method employs the space confinement of carbon precursors within porous solid templates (nanocasting molds). Generally, hard-templating includes four main synthetic steps (Figure 2.3).³⁹ Templates are firstly synthesized, followed by the infiltration of carbon precursors through wet impregnation, melt-infiltration, chemical vapor deposition, or combinations. The mixtures then undergo carbonization under high temperature to obtain

2. Background and outline

carbon-template composites. Finally, templates are removed, and the space occupied by the host templates turns into pores. Therefore, the size, structure and connectivity of generated pores can be adjusted by the structures of the applied templates. Widely used hard templates include porous silicas, zeolites and other nanostructured inorganic materials.⁴⁰⁻⁴² Another desirable templates are ZnO nanoparticles,⁴³ as they can react with carbon atoms by carbothermal reduction reaction (Equation 2.8) at high temperature. Zn and CO are removed, and micropores can be formed. Mesopores are generated by removing ZnO templates at high temperature or through acid washing. Although more controllable pore structure can be achieved by hard-templating method, high-cost and time-consuming process inhibit its large-scale application.

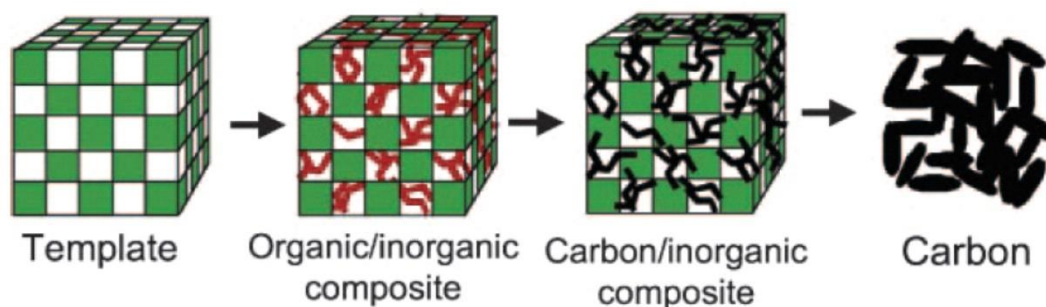
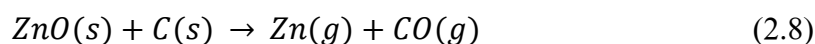


Figure 2.3. Hard-templating method for the preparation of porous carbon materials.³⁹

The Salt-templating method is based on the reaction of carbon precursors in a medium of molten salts (e.g., ionic liquids and eutectic salt mixtures).⁴⁴ Metal halides are the most commonly used molten salts for the synthesis of porous carbon materials due to their good stability, reusability, adequate solubility for carbon precursors, and adjustable melting point. For example, a mixture of LiCl/KCl has been used to facilitate the pyrolysis of glucose to generate porous carbon at high temperature.⁴⁵ Different components of metal halides can also play an important role in the modification of pores.⁴⁶

Direct carbonization method overcomes the complications of templating procedures, as it can be carried out by direct carbonization of porous carbon-containing materials as precursors, such as metal organic frameworks (MOFs).⁴⁷⁻⁴⁹ For example, Seung Jae Yang et al. used highly crystalline MOF nanoparticles (IRMOF-1) to synthesize porous carbon (Figure 2.4) with hierarchical pore structure and high pore volume up to $4 \text{ cm}^3 \text{ g}^{-1}$.⁴⁸ During the carbonization process, MOF nanoparticles act as sacrificial templates as well as secondary carbon precursors to form porous carbon frameworks. As an alternative to the above mentioned activation method and templating methods, MOF-derived porous carbons exhibit many advantages, including new

2. Background and outline

porous structures which can be hardly achieved by templating method, high SSA, and simple functionalization (by heteroatoms, metals, or metal oxides).⁵⁰ A disadvantage remains the often complicated synthesis and purification of the MOF precursors. Porous carbon with hierarchical pore structure can also be synthesized by direct carbonization of polymers. For example, intra- and inter- crosslinked polystyrene can be used as to synthesize porous carbon with tunable micropores, mesopores and macropores (Figure 2.5).⁵¹

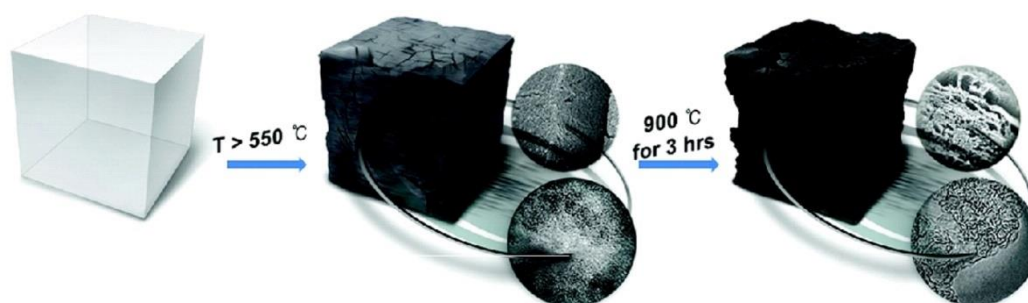


Figure 2.4. Synthesis of MOF-derived porous carbon materials with corresponding structural changes under heat treatment.⁴⁸

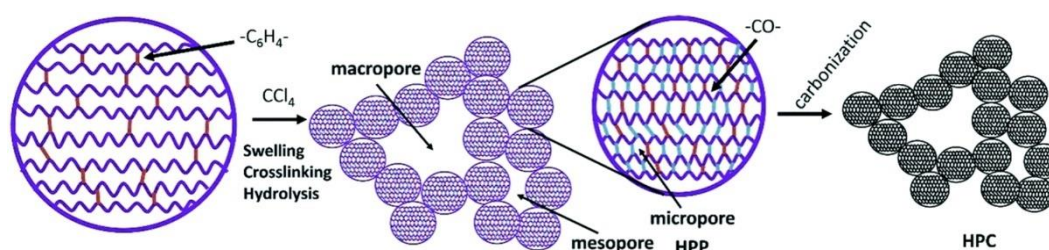


Figure 2.5. Mechanism for the formation of hierarchical porous carbon (HPC) by intra-/inter-sphere crosslinking of polystyrene chains in nanospheres via a template-free method.⁵¹

2.2.2. Functionalization of porous carbon materials

Pristine carbon materials usually suffer from limited performance in applications related to interphase phenomena, especially in energy storage and conversion. Therefore, they have to be functionalized by several methods to obtain porous carbon-based materials with improved performance due to tailored interaction with guest species. The main strategies include heteroatom-doping, metal-based material-doping, and the combination of both.

Functionalization by heteroatoms: Generally, heteroatom-doped porous carbon is synthesized by mixing carbon precursors with corresponding heteroatom-containing precursors, following by the procedures described in section 2.2.1. The major target of such a functionalization is to incorporate heteroatoms (e.g., B, N, O, F, S, and P) into the backbone of carbon materials, as

2. Background and outline

attaching organic groups (e.g., amine) on the surface cannot significantly change the original properties of carbon materials, while doping heteroatoms into pure carbon frameworks can alter their surface properties as well as electronic structure.⁵² For example, the work function of carbon materials is modulated by heteroatom-doping, as it can tune the position of the valence band and conduction band.⁵³ In addition, taking the most studied N-doped carbon as an example, nitrogen atom doping can introduce Brønsted basicity and thus form Frustrated Lewis pairs (FLPs) combined with electrophilic carbon atoms. Structurally, doped nitrogen can lower the valence band and increase the electron density at Fermi-level,⁵⁴ in other words, the electrochemical potentials can be modified, and doped carbon becomes more chemically stable (Figure 2.6). Such highly oxidation resistant carbon materials are called “noble carbon”, and possess excellent performance in numerous applications.⁵⁵⁻⁵⁶ By tuning the doping level of nitrogen atoms, different thermodynamically stable phases of doped carbon-based materials can be synthesized. For example, well-known C_3N_4 with high nitrogen content can be excellent photocatalysts, while N-doped carbons with lower nitrogen content are potential electrocatalyst.⁵⁷⁻⁵⁸ As another “neighbor” of carbon, boron is also an interesting candidate for the doping of porous carbon.⁵⁹ In addition, dual heteroatom co-doping can even modify the carbon framework through a more asymmetric structure and charge density distribution to provide active sites for catalytic applications. For instance, N and B co-doped carbon exhibits desirable performance in the oxygen reduction reaction (ORR).⁶⁰⁻⁶¹

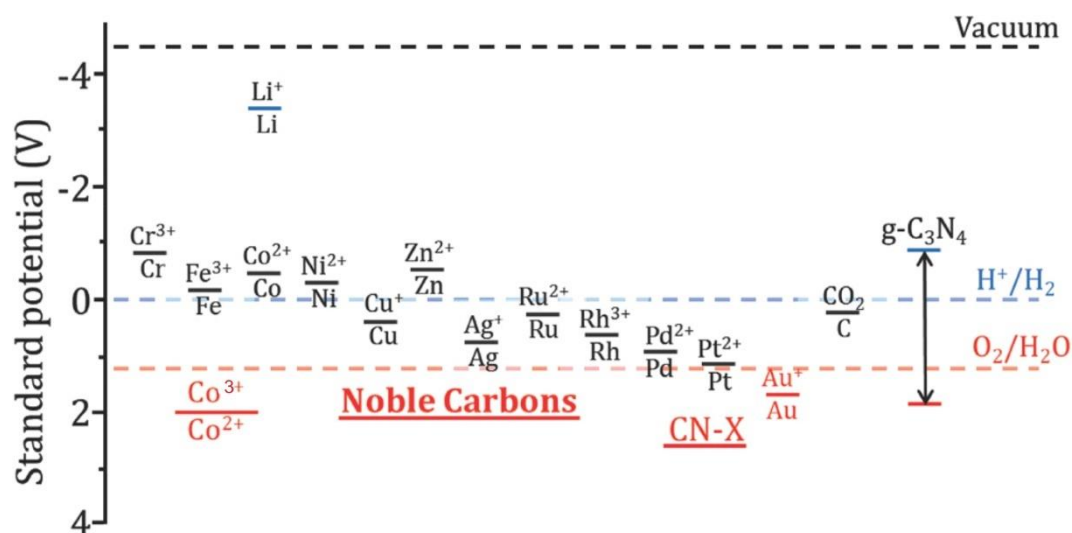


Figure 2.6. Electrochemical potentials or HOMO/LUMO levels (for semiconductors) for some known metals and materials. Note the CN-X is the improved carbon nitride; noble carbon marks just one position of a range of possibilities.^[55]

Functionalization by metal-based materials: Porous carbon can also be functionalized by introducing metal-based materials on the surface. The carbon structure with high SSA and

2. Background and outline

porosity can be used as a so-called “support”. Metal-functionalized carbon materials have shown versatile applications in many areas, such as energy, catalysis, industrial production of chemicals, and many others.⁶²⁻⁶⁴ Therefore, decorating porous carbon with metal-based materials can not only make the best use of both components from different aspects (e.g., improving the electronic interaction or mass transfer of reactants and reducing the cost by increasing the utilization of metal atoms), but also cover the individual shortages (e.g., undesirable stability of metal-based materials and lack of catalytic centers for pure carbon materials). In addition, some catalytically active sites, such as the Schottky contacts between the metal and carbon or the heterojunctions formed at the interface between the metal oxide and carbon, can also form after the functionalization. Confinement of metal nanoparticles into pores of porous carbon materials can also be used to slow down the growth and aggregation of metal or metal oxides nanoparticles.

Functionalization by combined heteroatoms and metal-based materials: Porous carbon can also be functionalized by both heteroatoms and metal-based materials. As mentioned above, heteroatom-doped carbon materials are more resistant against oxidation. After decorating with, e.g., metal nanoparticles, the opened band gap can result in a space charge layer between two components and improved electron transfer (Figure 2.7).⁵⁴ As an good example, metal single sites supported on the N-doped porous carbon, where metal ions as electrophile are stabilized by N atoms as nucleophile, have attracted increasing interests, due to their excellent performance in (electro or photo)chemical catalytic applications.⁶⁵⁻⁶⁷ Such combination of single ions and/or single atoms with heteroatoms can form FLPs, which usually show desirable activation ability toward small molecules (e.g., N_2 and CO_2).⁶⁸⁻⁷⁰

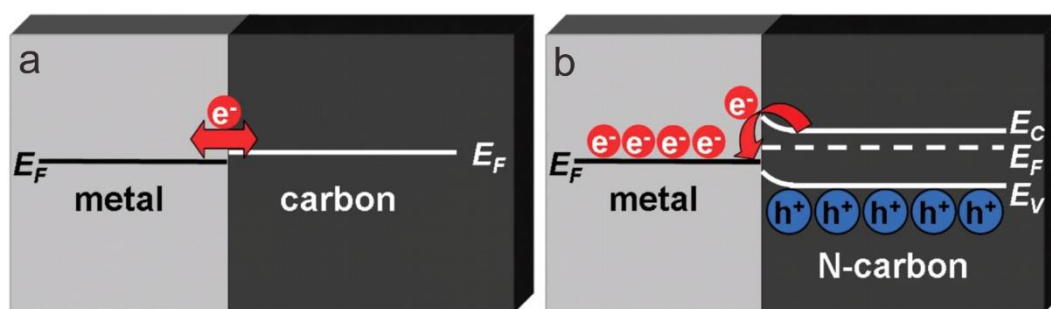


Figure 2.7. Typical (a) metal-carbon contact and (b) metal-N-carbon contact.⁵⁴

2.3. Brief introduction of NH_3 synthesis

The N_2 content in the atmosphere is more than 78%, but it is chemically inert and unusable, as living organisms cannot metabolize it from the gas form to synthesize basic building blocks of proteins, DNA or any other important compounds.⁷¹⁻⁷² Therefore, it is desirable to convert N_2 to other chemicals. This process is called N_2 fixation. NH_3 is the most established product of

2. Background and outline

artificial N₂ fixation. With annual worldwide production exceeding 160 million tons, NH₃ plays an extremely important role in agricultural fertilizers, fuels, as hydrogen carrier and in many other fields (Figure 2.8).⁷³⁻⁷⁶ The demand for NH₃ is continuously increasing with the exploding world population and improved living standard.^{16, 73, 77-78} It was estimated that about 27% of the world population is only enabled by the nitrogen fertilizer over the past century, and this value was even increased to 48% in 2008.¹⁶ NH₃-derived bioenergy and biofuel can also reduce the use of non-sustainable fossil fuels and contribute to a CO_x-free energy economy.¹⁶ Therefore, NH₃ synthesis from N₂ fixation has been intensively studied by scientists for a long time. There are four main types of N₂ reduction methods, including Haber-Bosch process, biological process, photochemical N₂ reduction and electrochemical N₂ reduction.

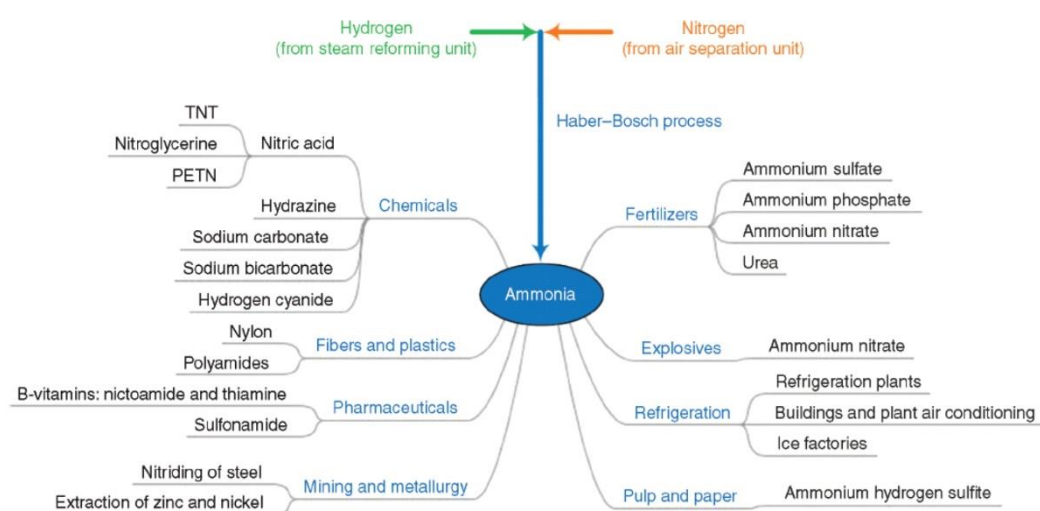
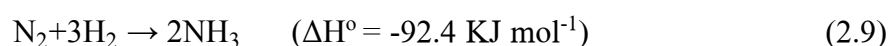


Figure 2.8. Range of applications of chemically fixed nitrogen in the form of ammonia.⁷⁹

2.3.1. Haber-Bosch process

The Haber-Bosch process is for sure one of the most important scientific contributions in the last century.⁸⁰ Since Fritz Haber firstly found that N₂ can react with H₂ in the presence of Fe-based catalysts at high temperature and pressure, Carl Bosch then further developed the process to the industrial scale, and both were rewarded for the Nobel Prize in 1931 (Equation 2.9).



Considering that this reaction is exothermic, low temperature is more favorable for the position of the chemical equilibrium and thus NH₃ yields, but it will also slow down the reaction rates and largely decrease the industrial efficiency, that is, the space-time yield of NH₃ production. According to the principle of Le Chatelier, increasing the reaction pressure can improve NH₃ yields, but safety reasons and engineering aspects limit the pressure value that can be applied. Typically, the reaction conditions are 400-600 °C and 100-200 bar.⁷⁹ The Haber-Bosch process

2. Background and outline

has been responsible for 80% of the NH_3 production for more than 100 years and the important role of this process for humans can also be indicated by the rapid growth of global population after the invention of Haber-Bosch process (Figure 2.9).⁸¹

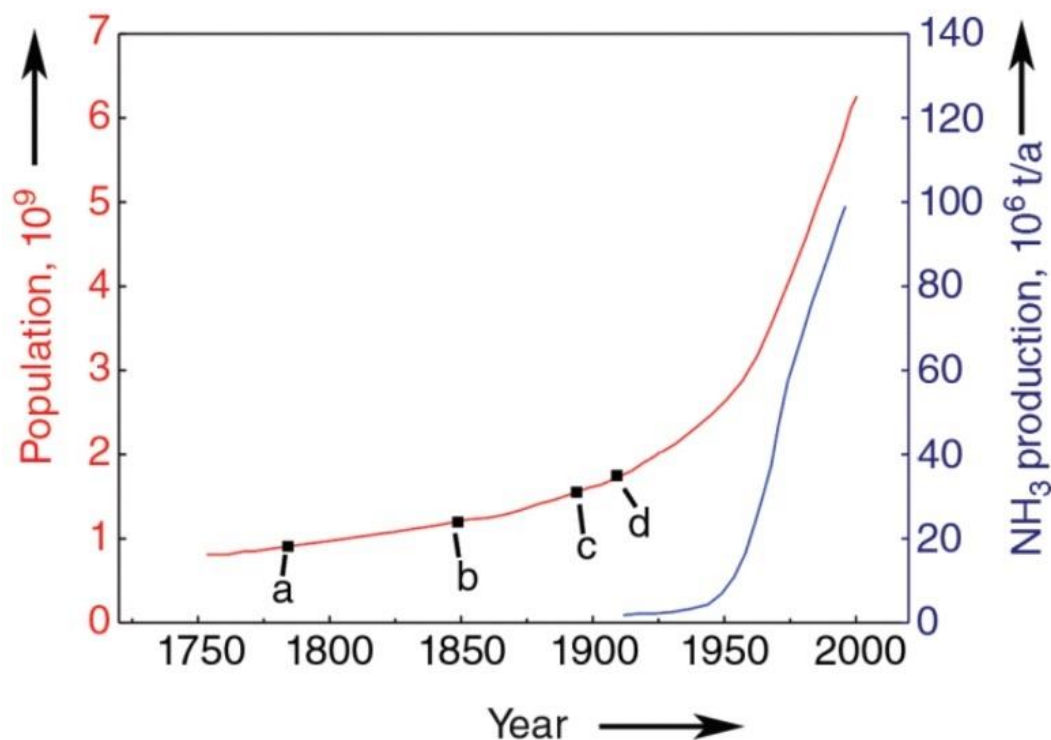


Figure 2.9. Global population increase and the nitrogen fertilizer consumption trends. (a) Nitrogen is discovered; (b) N is nutrient; (c) Biological fixation; (d) Haber-Bosch process.⁸¹

However, the construction of Haber-Bosch chemical plant requires a large amount of capital expenditure, because it is very complicated, has to provide extremely high temperature and pressure, and has to be optimized for ammonia production and for the recovery of the energy generated by the process.⁸² In detail, this process is composed of a series of steps with different reaction beds containing catalysts (Figure 2.10).⁸³ Firstly, a mixture of CH_4 and H_2O is reformed to produce H_2 which passes through the reactor along with N_2 gas. Besides, gas separator, heater, heater exchanger, and condenser are all needed for the whole process. Finally, a mixture of N_2 , H_2 and NH_3 is obtained, followed by the condensing step to separate NH_3 as the final product, while N_2 and H_2 can be recycled to the reactors. Although the Haber-Bosch process has to be carried out under harsh conditions with large amount of fossil fuels consumption (more than 1% of the industrial energy consumption) and CO_2 emission (1.5 t of CO_2 per 1 t of NH_3) and suffers from a relatively low NH_3 yield (conversion rate of 10%-15% from N_2 per cycle), it is necessary to use it for large-scale NH_3 production until another feasible

2. Background and outline

method is developed. Besides the search for alternatives, scientists keep studying this process to modify the reaction conditions and find more efficient catalysts.⁸⁴

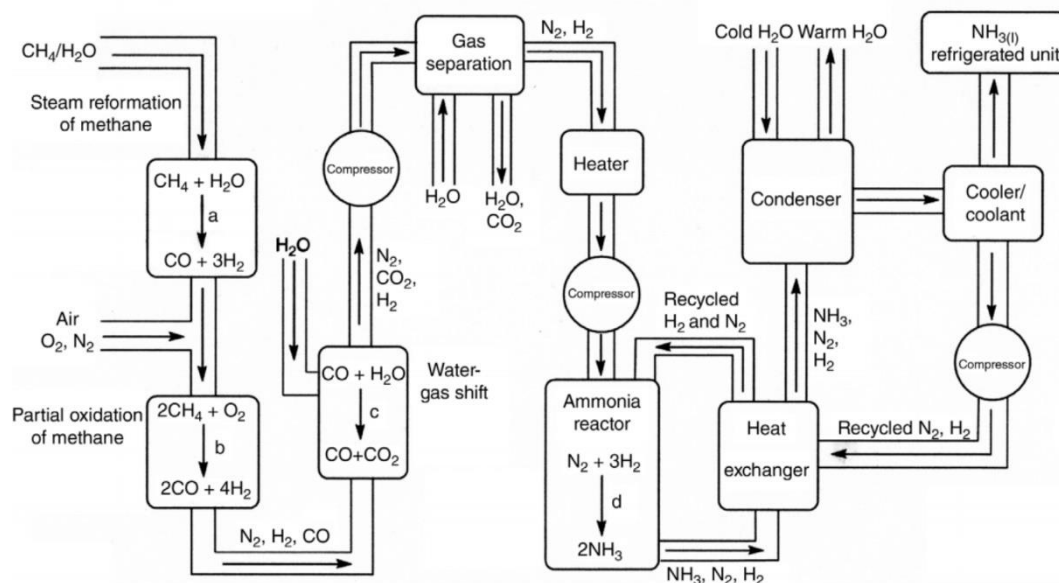


Figure 2.10. Energy-flow diagram of the Haber-Bosch process, initially producing H₂ to feed into a NH₃ production reactor. a) Catalyst, 700-1000°C, 3×10^5 - 2.5×10^5 Pa; b) Catalyst, 800-900°C; c) Catalyst, 500°C; d) Fe catalyst, 450°C, 3×10^7 Pa.⁸³

2.3.2. Biological process

NH₃ synthesis in the nature is achieved by biological N₂ fixation with the help of nitrogenases at the expense of ATP hydrolysis and a reductant. Given that more than 50% of fixed nitrogen input for humans is supplied by the biological N₂ fixation at ambient temperature and pressure, there is a high interest to systematically study the structure of nitrogenases and understand this N₂ fixation process.⁸⁵⁻⁸⁶ Jodin firstly proposed that microbes can achieve N₂ fixation in 1862,⁸⁷ and the first extraction of nitrogenase enzymes has been achieved in 1960s.⁸⁸⁻⁸⁹ After that, systematic research about nitrogenases has started. There are three main kinds of nitrogenases, including Mo nitrogenase, V nitrogenase and Fe nitrogenase.⁹⁰⁻⁹² Taking the most studied Mo nitrogenase as an example, the MoFe protein (dinitrogenase or component I) and the Fe protein (dinitrogenase reductase or component II) are the two main components.^{74, 93} During the reaction, Fe protein binds to MoFe protein, and electrons transfer from the hydrolysis of ATP molecules within Fe protein to the Fe-S cluster, then to the P cluster, and finally to the MoFe-cofactor to reduce the N₂ molecules to NH₃ (Figure 2.11).⁸⁵ However, this NH₃-synthesis process is not energy-efficient, as 16 ATP, corresponding to an energy expense of almost 5 eV, are consumed to reduce a N₂ molecule (Equation 2.10).⁸⁵



2. Background and outline

If nitrogenase is used *in vitro* for N_2 fixation, harsh conditions (e.g., low temperature, a strong reducing reagent and an organic solvent) are usually required, which is not suitable for the large-scale NH_3 synthesis.⁹⁴⁻⁹⁷ However, the deep understanding of nitrogenases structure (Fe-Mo-S cofactor) and their N_2 fixation mechanism gives a good instruction toward the development of NRR catalysts and artificial N_2 fixation techniques with higher efficiency.

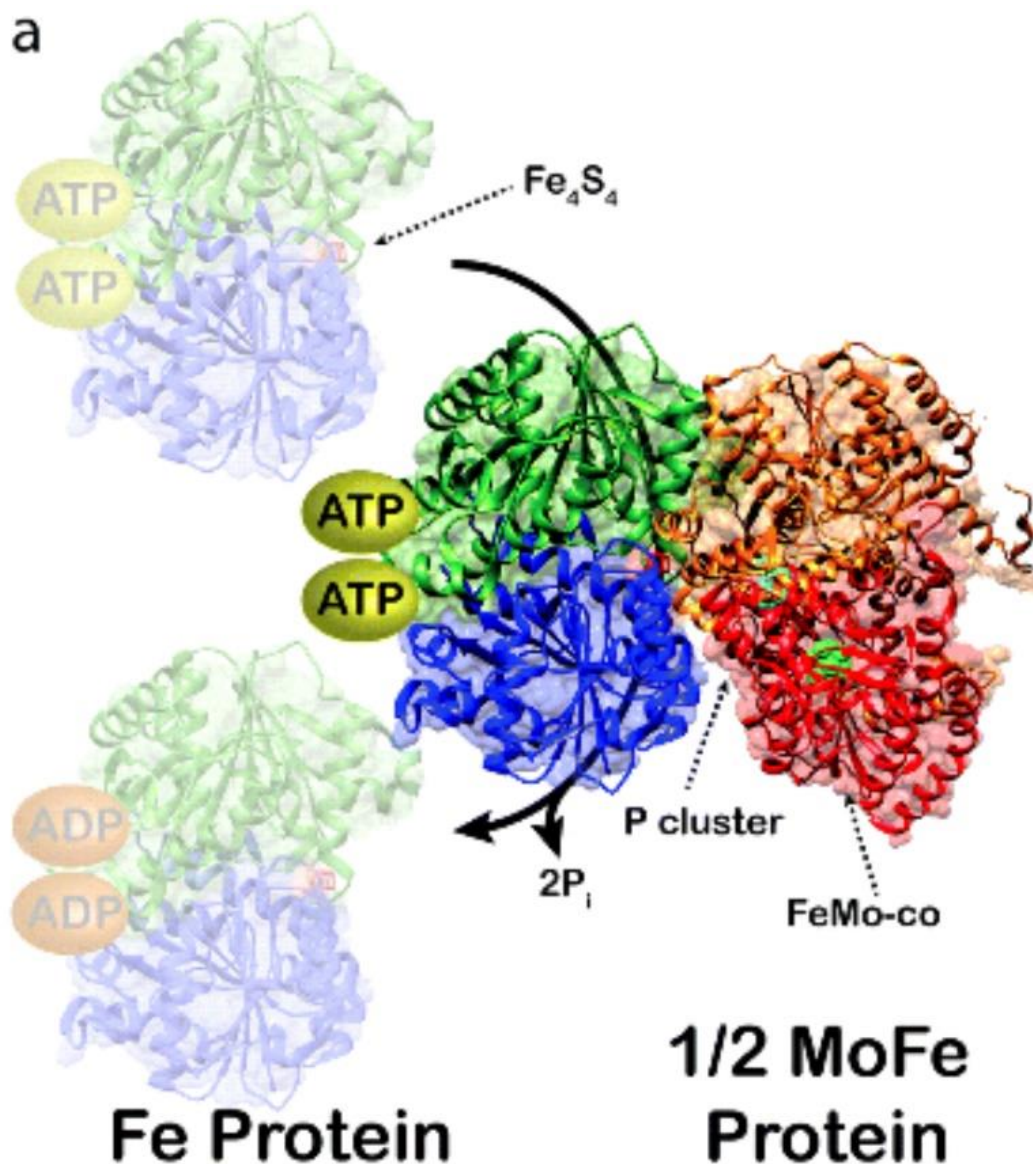


Figure 2.11. Crystal structure of nitrogenase (PDB: 4WZA) from *Azotobacter vinelandii* illustrating the transient association of the Fe protein to the MoFe protein.⁸⁵

2.3.3. Photochemical N_2 fixation

To overcome the disadvantages of the Haber-Bosch synthesis and the biological process, photochemical N_2 fixation at ambient conditions has attracted increasing attention, which uses light and water as energy source and reducing reagent, respectively.⁹⁸⁻¹⁰⁰ During the reaction,

2. Background and outline

light-induced valence band holes can oxidize H_2O to form protons, which can react with N_2 together with the conduction band electrons to synthesize NH_3 (Equation 2.11):¹⁰¹⁻¹⁰²



Efficient photocatalysts for N_2 fixation require high water oxidation ability and photostability. In addition, sacrificial electron donors are also needed, such as alcohols.¹⁰³⁻¹⁰⁵ Until now, different types of inorganic or organic semiconductors have been used in this reaction.¹⁰⁶⁻¹¹⁰ For example, as one of the most widely used photocatalysts, TiO_2 with high density of oxygen vacancies (OVs) are known to have good N_2 reduction ability. The presence of OVs can result in the formation of Ti^{3+} , with lower donor levels than the bottom of conduction band, which can effectively trap electrons and then reduce N_2 (Figure 2.12).¹¹⁰ Inspired by the biological N_2 fixation, Katherine A. Brown et al. combined a CdS photocatalyst with the MoFe protein. Under the excitation of light, electrons from CdS can be transferred to the MoFe protein and reduce N_2 .⁹⁴ However, the low photon utilization of photocatalysts and the recombination of electrons and holes make it difficult to obtain desirable efficiency for NH_3 synthesis.¹¹¹⁻¹¹³

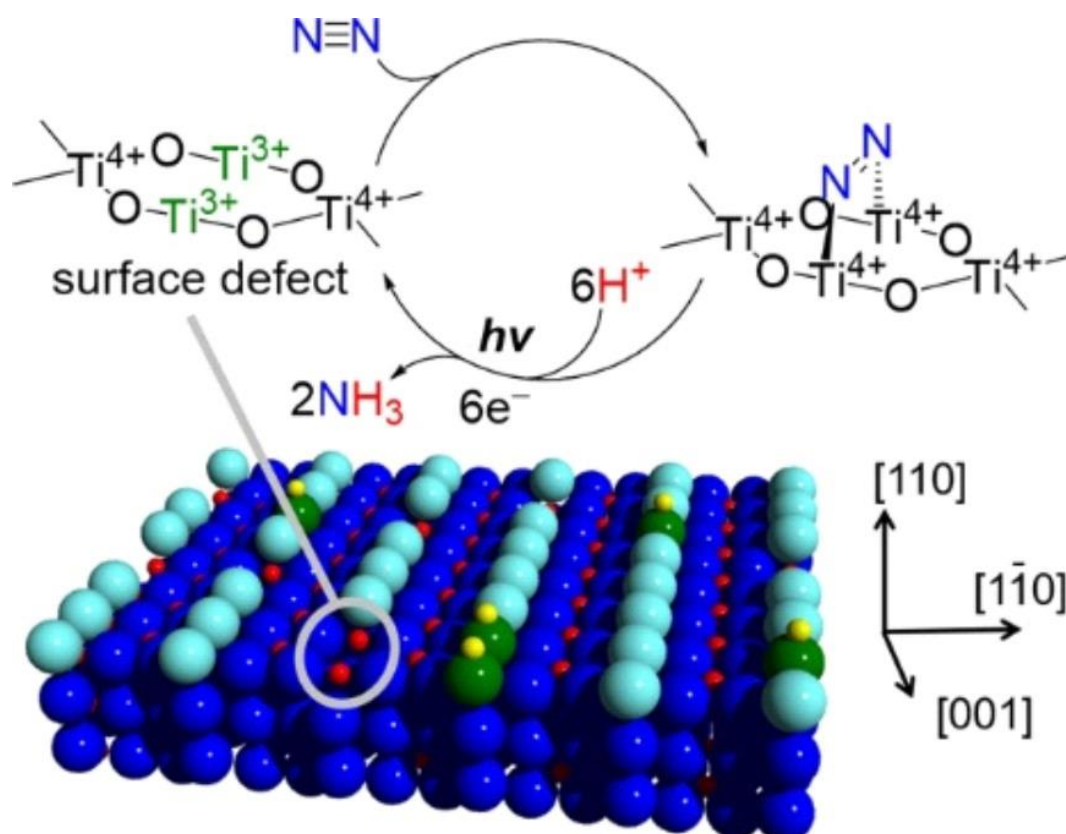


Figure 2.12. Proposed photocatalytic cycle for N_2 fixation on the Rutile TiO_2 (110) surface.¹¹⁰

2.3.4. Electrochemical N_2 fixation

Electrochemical N_2 reduction reaction (NRR) by using renewable electricity has also been widely studied because it is a CO_2 -emission free route. In addition, NRR can be performed

2. Background and outline

anywhere with suitable equipment supplied because it is geographically not linked to hydrogen production. This “decentral production” does eliminate the necessity to transport produced NH_3 over long distances and also simplifies production on demand. During the reaction, electrons flow from the anode to the cathode, and N_2 is reduced in the cathodic part, which mimicks the two-component configurations in nitrogenases. Date back to history, the first electrochemical NRR experiment was carried out by Humphrey Davy in 1807, which is much earlier than the development of the Haber-Bosch process.¹¹⁴ Then the reliable quantification of produced NH_3 was achieved by Fichter and Suter in 1922.¹¹⁵ Afterwards, electrochemical N_2 fixation under a wide range of temperatures (e.g., high-temperature route over 500 °C, intermediate-temperature route between 100-500 °C, and low-temperature route below 100 °C), by using different reaction cells (e.g., back-to-back cell, H-type cell and single chamber cell) and versatile electrocatalysts (e.g., metal, metal oxides and carbon-based materials) or electrolytes (e.g., aqueous solution, ionic liquid and molten salt) has been studied (Figure 2.13).^{20, 114-120} Especially, the research breakthrough by using transition metal-based catalysts resulted in wide interests for electrochemical NRR at the advent of 21st century. Based on those results, it is demonstrated that electrochemical N_2 reduction with H_2O at ambient conditions is the most promising alternative technique to the well-established Haber-Bosch process.

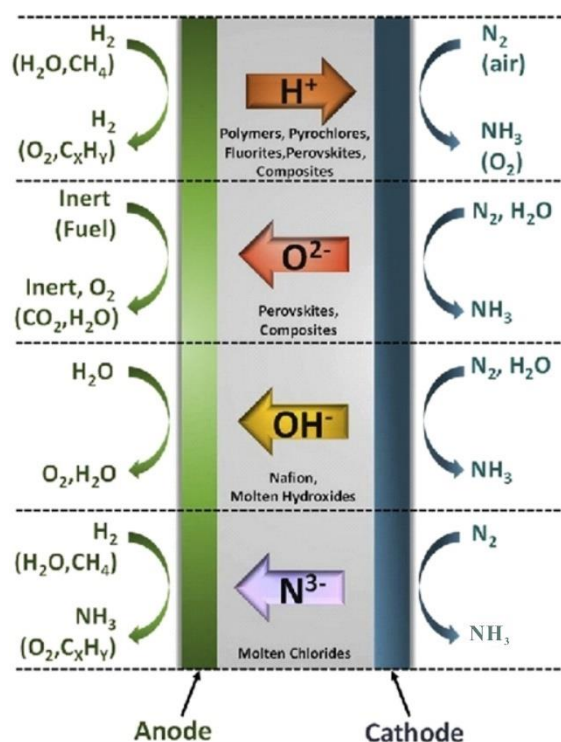


Figure 2.13. The four main strategies, electrodes, and electrolyte designs for the electrochemical synthesis of NH_3 from N_2 , H_2 , and H_2O , and a source of electricity, preferably renewable.¹¹⁸

2. Background and outline

Through much effort from experimental results and DFT calculations, the possible reaction process of electrochemical NRR is proposed, which includes three main steps: N_2 adsorption, N_2 activation and N_2 hydrogenation. Firstly, like many other heterogeneous catalytic reactions, N_2 molecules as the reactants, will adsorb on the catalyst surface to initiate the reaction. Therefore, catalysts, which can supply enough N_2 adsorption sites, are promising for enhanced NRR performance. A good example for that is the nanostructured catalysts with large SSA, such as the above mentioned porous carbons, which enable large amount of N_2 adsorption, can in principal improve NRR.¹²¹

Then, the adsorbed N_2 molecules should be activated in the activation step, which plays a key role in N_2 fixation, as N_2 molecules usually show inertness due to the high dissociation enthalpy of the N-N triple bond and high first bond cleavage energy. Considering their molecular orbitals (Figure 2.14),¹²²⁻¹²³ the first strategy for N_2 activation is to enhance the electron donation or back-donation effect between the catalyst and N_2 . For example, different types of vacancies or defects are found to be active for N_2 activation, such as oxygen vacancies, nitrogen vacancies and surface defects on metals, which can enhance the charge transfer between them and adsorbed N_2 .¹²⁴⁻¹²⁶ Lithium-mediated methods are another way for N_2 activation at ambient temperature and pressure because lithium can react directly with N_2 to form Li_3N , and NH_3 can be formed after hydrolysis of Li_3N .¹²⁷⁻¹²⁹ In addition, plasma can also be used to active N_2 by generating electrons with high energy.¹³⁰⁻¹³³

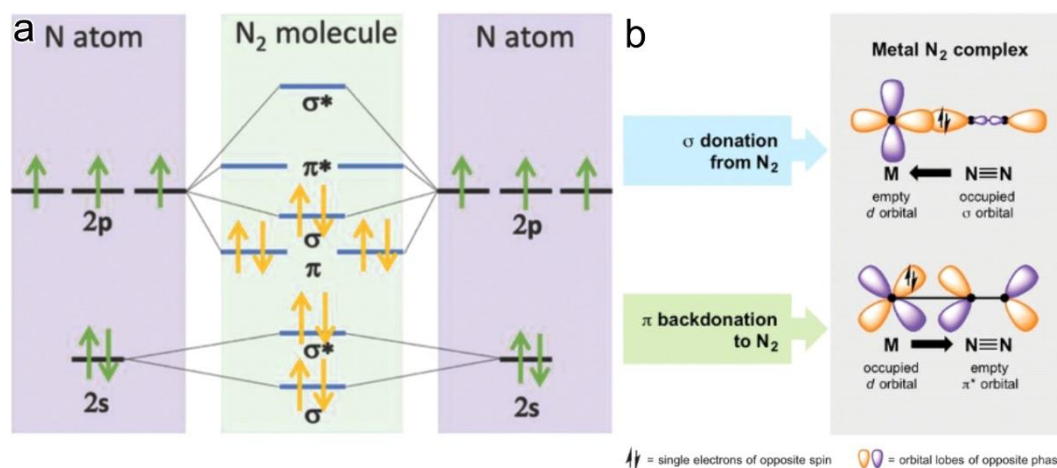


Figure 2.14. (a) Energy levels of N atomic orbitals and their hybridization of N_2 molecular orbitals.¹²³ (b) Simplified schematic of bonding end-on-bound transition metal N_2 complexes.¹²²

Finally, N_2 hydrogenation can be achieved with the help of protons from water. Taking heterogeneous electrocatalysts as an example, there are two types of reaction pathways for N_2 hydrogenation: associative and dissociative pathway (Figure 2.15), which can be distinguished

2. Background and outline

by the sequence of $\text{N}\equiv\text{N}$ bond breaking.^{20, 134} In detail, $\text{N}\equiv\text{N}$ bond firstly breaks before the hydrogenation of N_2 in the dissociative mechanism, while it is cleaved with the first release of NH_3 molecule in the associative mechanism. According to the hydrogenation sequences, the associative mechanism can be further divided into the distal pathway and the alternating pathway, according to the different hydrogenation processes. In the alternating pathway, two N atoms undergo hydrogenation at the same time, and NH_3 molecules are released one by one as the products. Notably, N_2H_4 could also be formed in this pathway. On the contrary, the N atom not directly bound to the catalyst surface firstly undergoes hydrogenation process and forms one NH_3 molecule with the break of $\text{N}\equiv\text{N}$ bond before the hydrogenation of the other N atom near the surface. For another dissociative mechanism, $\text{N}\equiv\text{N}$ bond is cleaved firstly to form two adsorbed N atoms on the catalyst surface, which then undergo hydrogenation process separately to produce two NH_3 molecules. Although the possible steps of N_2 hydrogenation can be simply summed up, the situation is often much more complicated in the practical process. Thus, the reaction could only occur at a more negative applied potential, because the high overpotential is required for overcoming the energy barriers during the hydrogenation pathways.

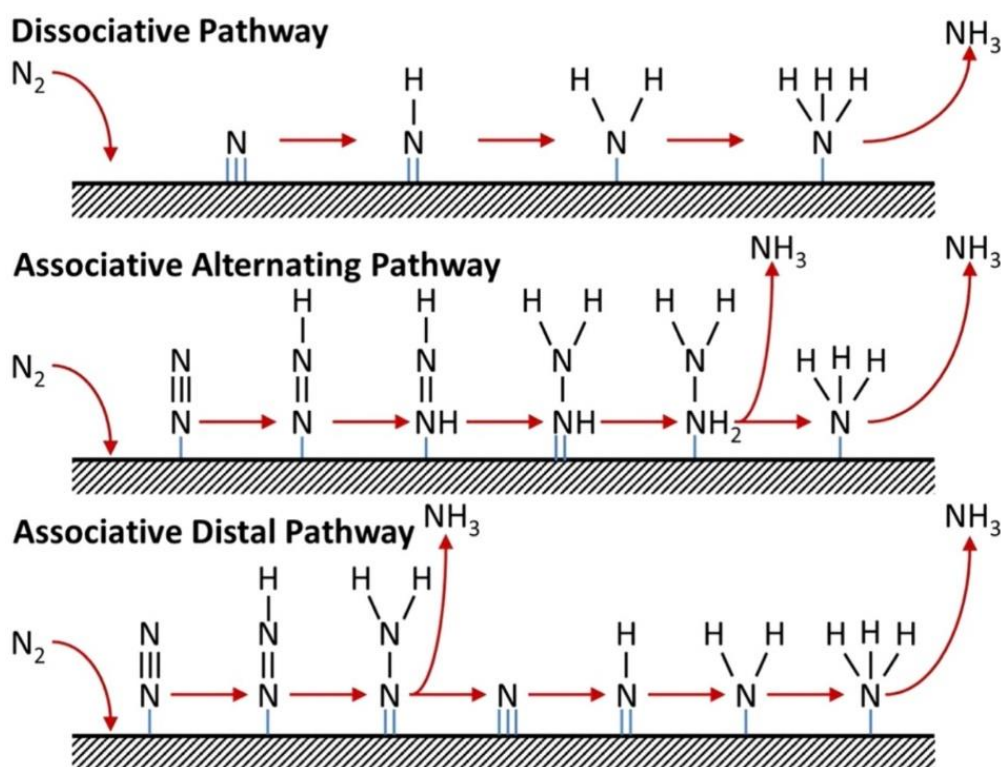


Figure 2.15. Possible reaction mechanisms for the NRR to form NH_3 .^[20]

Strikingly, some metal nitrides (VN , MoN , etc.) can undergo a different pathway, called Mars-van Krevelen (MvK) mechanism (Figure 2.16).¹³⁵⁻¹³⁷ In detail, it starts from the hydrogenation of an N atom on the catalyst surface and releases the first NH_3 molecule to form a nitrogen

2. Background and outline

vacancy, which can bind another nearby N_2 molecule to return the catalyst to its original state. This mechanism has been verified by using $^{15}N_2$ isotope labeling experiments and two products of $^{14}NH_3$ and $^{15}NH_3$ have been found.¹³⁸ Compared with associative and dissociative mechanisms, NH_3 formation via MvK mechanism requires relatively smaller overpotentials.¹³⁹

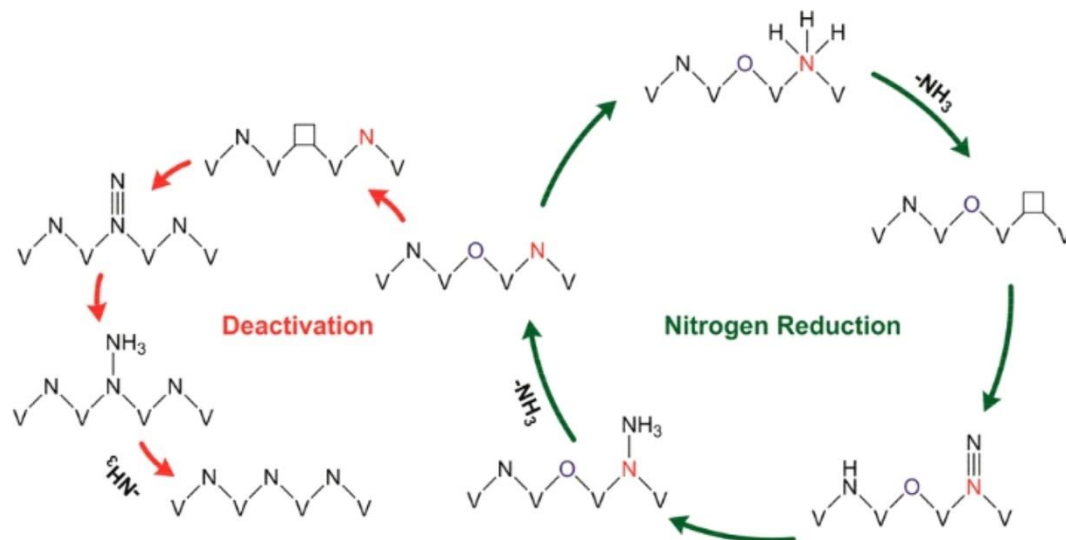


Figure 2.16. Proposed reaction pathway for nitrogen reduction on the surface of $VN_{0.7}O_{0.45}$ via a Mars-van Krevelen mechanism (right) and the catalyst deactivation mechanism (left). Reproduced with permission from reference.¹³⁸

2.4. Main challenges for electrochemical N_2 fixation

Despite the above advantages, there are still many challenges for the electrochemical N_2 fixation with H_2O and electricity at ambient conditions that have to be considered and need to be overcome.

2.4.1. Selectivity, activity and stability

The selectivity of NRR is often too low within aqueous electrolytes due to the strong competition from hydrogen evolution reaction (HER), as H_2O is used as hydrogenating agent. In acidic medium, NRR requires a multiple 6-electron transfer with a redox potential of 0.092 V versus reversible hydrogen electrode (RHE) (Equation 2.12):



As a comparison, there is only a 2-electron transfer for HER with a very similar redox potential of 0.0 V versus NHE (Equation 2.13):



Notably, those two reactions are both proton-coupled electron transfer (PCET) reactions and thus the 2-electron involved HER is more kinetically preferred,¹⁴⁰⁻¹⁴¹ which causes a low

2. Background and outline

Faradaic efficiency (FE) for electrochemical NRR. It can be overcome by using aprotic electrolytes, such as ionic liquid, and FE can thus be largely improved.¹⁴² Strong competition from HER can also cause the formation of N_2H_2 and N_2H_4 as byproducts which leads to a decrease of the NH_3 selectivity (Equations 2.14 and 2.15):¹⁴³



Besides, considering the extremely strong $N\equiv N$ bond with high dissociation enthalpy of 962 kJ mol^{-1} and high first bond cleavage energy of 410 kJ mol^{-1} , it is not surprising that N_2 molecules usually show inertness.¹⁴⁴ The first protonation of N_2 is also endothermic ($\Delta H^0 = -171 \text{ kJ mol}^{-1}$), which is the main rate-limiting step. This is the main reason why it remains difficult to obtain catalysts with high NRR activity. In addition, linear scale relations and Brønsted-Evans-Polanyi relations for different reaction intermediates adsorbed on the catalyst surface are responsible for the lower activity. For example, Joseph H. Montoya et al. used DFT calculations to study two key intermediates of $*N_2H$ and $*NH_2$ (* signifies a active site on the surface) on the surface of transitional metals with associative mechanism and found that NH_3 synthesis is severely limited by the linear scaling between the energetics of them.¹⁴⁵ In addition, considering the industrial applications, N_2 concentration has to be enhanced and some free-standing electrodes should also be used.

Stability is also an important criteria for accessing NRR performance. Good stability means that NH_3 production can be achieved over a long period of time. For example, NRR activity under the electrocatalysis of the above mentioned metal nitrides can decrease with the reaction time due to the deactivation of catalysts, as the formed active nitrogen vacancy in the MvK pathway is supplemented from another nitrogen atom in the bulk catalysts.¹³⁸

2.4.2. Reaction mechanism

Understanding the reaction mechanism can provide new perspectives for further targeted modification of the catalysts and reaction conditions to improve the NRR performance. Although the possible NRR mechanisms have been proposed, largely unexplored territories still exist. Some advanced equipment and techniques have been applied for investigating reaction intermediates (e.g., surface-enhanced infrared absorption spectroscopy, X-ray absorption spectroscopy and Raman), but it is still difficult to get a clear image about the reaction pathway for a given catalyst.¹⁴⁶ In addition, DFT calculations are also used to provide the most reasonable NRR mechanism.¹⁴⁷ However, multiple steps involved NRR process put critical

challenges on DFT calculations, especially for the determination of active sites. In addition, these DFT calculations do usually not take the presence of water and other critical aspects into consideration.

2.5. Outline

Based on above considerations, reaction kinetics, the interactions between the catalysts and intermediates and reaction stability all play important roles in determining NRR performance, which can be all tuned by the structures of the applied electrocatalysts. Thus, advanced electrocatalysts have to be developed, optimized and employed. Recently, intensive efforts have been devoted to the synthesis of NRR catalysts, e.g., metal, metal oxides, metal nitrides and non-metal-based materials. Among them, porous carbon-based materials tend to be quite promising and attract interests due to their low cost, good durability, high specific surface area to provide more active sites, versatile functionalization and controllable hierarchical porosity to adjust the optimum gas adsorption and mass transfer ability as well.^{55, 148-151} For example, Yanming Liu et al. firstly reported N-doped carbon in electrochemical NRR and elucidated that pyridinic and pyrrolic N species can promote N₂ reduction.¹²¹ However, in respect of reaction performance, the FE and NH₃ production rate under the catalysis of current materials are still undesirable, which largely hinders the large-scale implementation of NH₃ production. Moreover, the relations between the structure of porous carbon-based materials and NRR performance as well as the reaction mechanism still remain ambiguous. Therefore, the aim of the present dissertation is to rationally design carbon-based NRR electrocatalysts, and to reveal a deeper understanding of active sites and reaction mechanism.

Chapter 3 is reporting the rational design of C-doped TiO₂/C (C-Ti_xO_y/C) as porous carbon-based material derived from MIL-125(Ti) metal-organic framework. It can achieve a high FE of 17.8 %, which even surpasses most of the established noble metal-based catalysts. On the basis of the experimental results and theoretical calculations, the remarkable properties of the catalysts can be attributed to the doping of carbon atoms into oxygen vacancies (OVs) and the formation of Ti-C bonds in C-Ti_xO_y. This binding motive is found to be energetically more favorable for N₂ activation compared to the non-substituted OVs in TiO₂. This work elucidates that electrochemical N₂ reduction reaction (NRR) performance can be largely improved by creating catalytically active centers through rational substitution of anions into metal oxides.

In Chapter 4, Au single sites are stabilized on N-doped carbon to form metal and heteroatom co-doped porous carbon materials. This highly oxidizing (“noble”) carbons catalysts show excellent performance in N₂ electroreduction. At a potential of -0.2 V vs. reversible hydrogen

2. Background and outline

electrode (RHE), a stable NH_3 yield of $2.32 \mu\text{g h}^{-1} \text{cm}^{-2}$ is produced at an acceptable Faradaic efficiency of 12.3% at 20 °C (17.4% at 60 °C). Besides, there is no notable fluctuation of Faradaic efficiency and NH_3 yield in 6-cycle test which indicates good stability. The good performance can be attributed to the desirable N_2 activation ability through positively polarized Au single species and negatively polarized N or C atoms. This work opens up new insights to improve N_2 fixation performance by introducing active single sites into noble carbon catalysts for N_2 electroreduction.

Chapter 5 is reporting the synthesis of N and B co-heteroatom-doped porous carbons with large specific surface area (SSA) and abundant point defects. The constructed B-N motives combine abundant unpaired electrons and FLPs. They result in desirable performance for electrochemical N_2 reduction reaction (NRR) in absence of any metal co-catalyst. At a potential of -0.3 V vs. reversible hydrogen electrode (RHE), a maximum Faradaic efficiency of 15.2% with a stable NH_3 production rate of $21.3 \mu\text{g h}^{-1} \text{mg}^{-1}$ is obtained in NRR. Besides, electrooxidation of 5-hydroxymethylfurfural (HMF) has also been studied by using N and B co-heteroatom-doped porous carbons. 2,5-furandicarboxylic acid (FDCA) is firstly obtained by using non-metal-based electrocatalysts at a conversion of 71% and with yield of 57%. Gas adsorption experiments (N_2 at 273 and 298 K) elucidate the relationship between the structure and the ability of the catalysts to activate the substrate molecules. This work opens up new insights for the rational design of non-metal-based catalysts for potential electrocatalytic applications and the possible enhancement of their activity by the introduction of FLPs and point defects at grain boundaries.

3. Enhanced electrocatalytic N₂ reduction via partial anion substitution in titanium oxide-carbon composites

As mentioned in section 2.2.2, metal-based materials, such as transitional metal oxides (TMOs), modified porous carbon catalysts also attract significant interest due to their widely catalytic applications.¹⁵²⁻¹⁵⁴ TMOs usually exhibit many benefits, e.g., adjustable bonding structure and oxidation states, and thus TMO modified porous carbon materials can enhance their interactions and are promising to provide more active sites by synergistic effects.¹⁵⁵⁻¹⁵⁶ Although some MTOs have been proven to be efficient catalysts for electrochemical NRR,¹⁵⁷ the experimental study of MTO modified porous carbon materials in NRR and more detailed mechanistic understanding of their interactions are still needed for guiding the design of new-generation NRR electrocatalysts.

As the second most abundant transition metal in the earth's crust, Ti-based materials can be potential candidates due to their stronger binding towards N-adatoms than to H-adatoms leading to better N₂ reducing ability.¹⁵⁸ Thus, MXenes with a great number of exposed edge sites have been used as efficient NRR electrocatalyst.¹⁵⁷ In addition, TiO₂ has also been studied for their application in electrochemical NRR and oxygen vacancies (OVs) are demonstrated to be pivotal to N₂ activation.^{134, 159-160} However, achieving a higher FE of these Ti-based materials is still a big challenge, which means that the construction of more effective Ti-based active sites is highly required. My inspiration for a novel synthesis scheme for Ti-based NRR catalysts is coming from the versatile redox chemistry of oxygen-deficient titanium oxides. The wide distribution of possible electronic band structures as well as many possible anionic substitutions will provide abundant active sites for N₂ activation.¹⁶¹

Term of use: This chapter is adapted with permission from my own original work:

[1] Qin, Q., Zhao Y., Schmallegger M., Heil, T., Schmidt J., Walczak R., Gescheidt-Demner, G., Jiao, H-J., Oschatz, M. Enhanced electrocatalytic N₂ reduction via partial anion substitution in titanium oxide-carbon composites. *Angew. Chem. Int. Ed.* **2019**, *58*, 2-8. Published by John Wiley & Sons.

3. Enhanced electrocatalytic N₂ reduction via partial anion substitution in titanium oxide-carbon composites

Generally, based on the synthetic strategies described in section 2.2.1, MOF precursors are promising candidates to synthesize TMO modified porous carbon materials, due to their relatively simple carbonization procedure. MOF-derived composites have tunable porosity, high surface area, controllable functionalization, as well as good conductivity and thus provide great potential as electrocatalysts.¹⁶²⁻¹⁶³ To the best of my knowledge, Ti-MOF-derived materials have not been used in electrochemical NRR yet.

Ti₈O₈(OH)₄(BDC)₆ (MIL-125(Ti)) (BDC = benzene-1,4-dicarboxylate) (Figure 3.1) has been chosen as the MOF precursor and a novel NRR electrocatalyst based on a carbon-doped, oxygen deficient titanium oxide/carbon (C-Ti_xO_y/C) nanohybrid was prepared via a one-step thermal conversion with rich (O-)Ti-C bonds and OVs. Such partial anion substitution leads to excellent electrochemical NRR performance with highest FE of 17.8 % and a remarkable NH₃ production rate of 14.8 μg h⁻¹ mg⁻¹_{cat.}. The crucial role of carbon substitution in electrochemical NRR is proven for the first time by a combination of experimental and density functional theory (DFT) results and a new N₂ activation mode is thus provided.

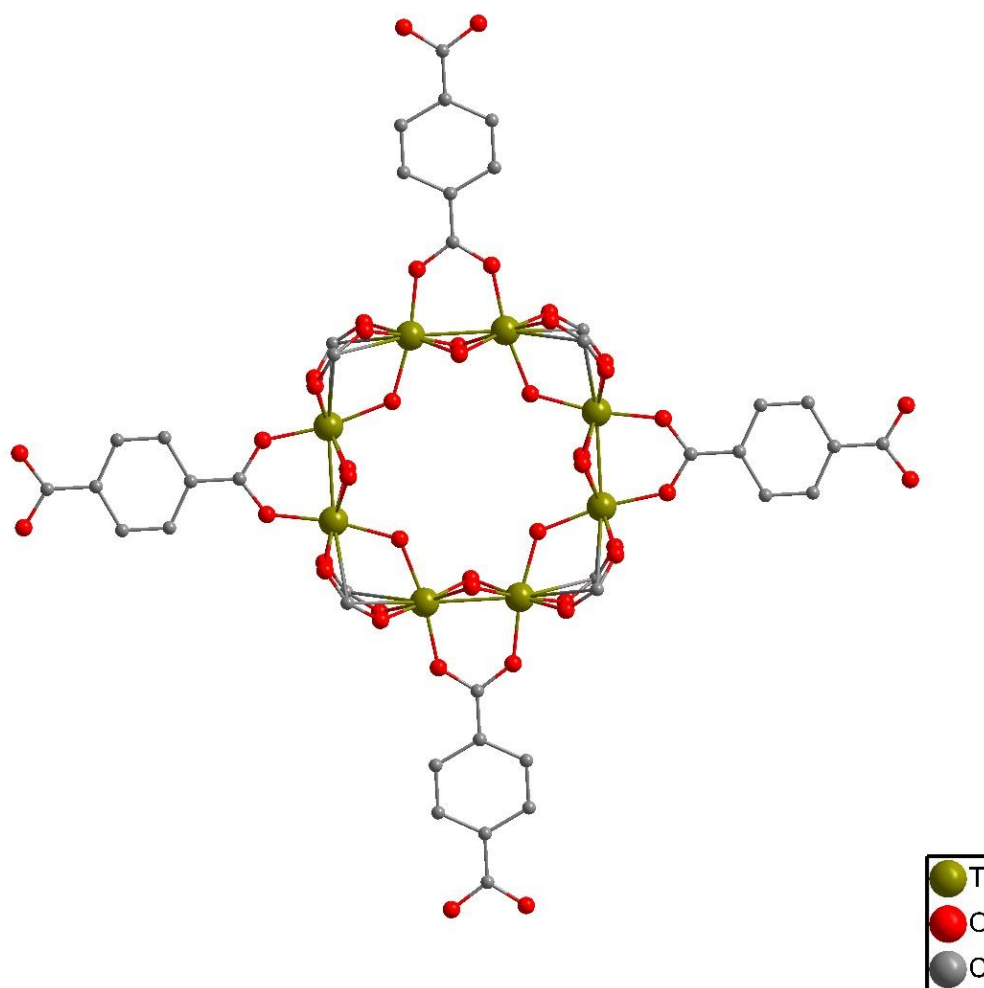


Figure 3.1. Structure of MIL-125.

3. Enhanced electrocatalytic N₂ reduction via partial anion substitution in titanium oxide-carbon composites

3.1. Synthesis and characterization of M-Ts

MIL-125(Ti) was synthesized according to the literature (see Appendix part for more details) (Figure 3.2).¹⁶⁴ C-Ti_xO_y/C hybrid nanostructures (denoted as M-Ts with T representing the pyrolysis temperature) were synthesized by annealing MIL-125(Ti) at 800, 900, 1000 and 1100 °C for 2 h under Ar atmosphere. Scanning electron microscopy (SEM) images (Figure 3.3a) and transmission electron microscopy (TEM) (Figure 3.3b-c) of as-obtained M-1000 reveal that the transformed MOF particles become much looser but retain the polyhedral geometry of the former MIL-125(Ti) crystals with an average size of 300 nm and contain some smaller nanoparticles with sizes between 3 and 20 nm.

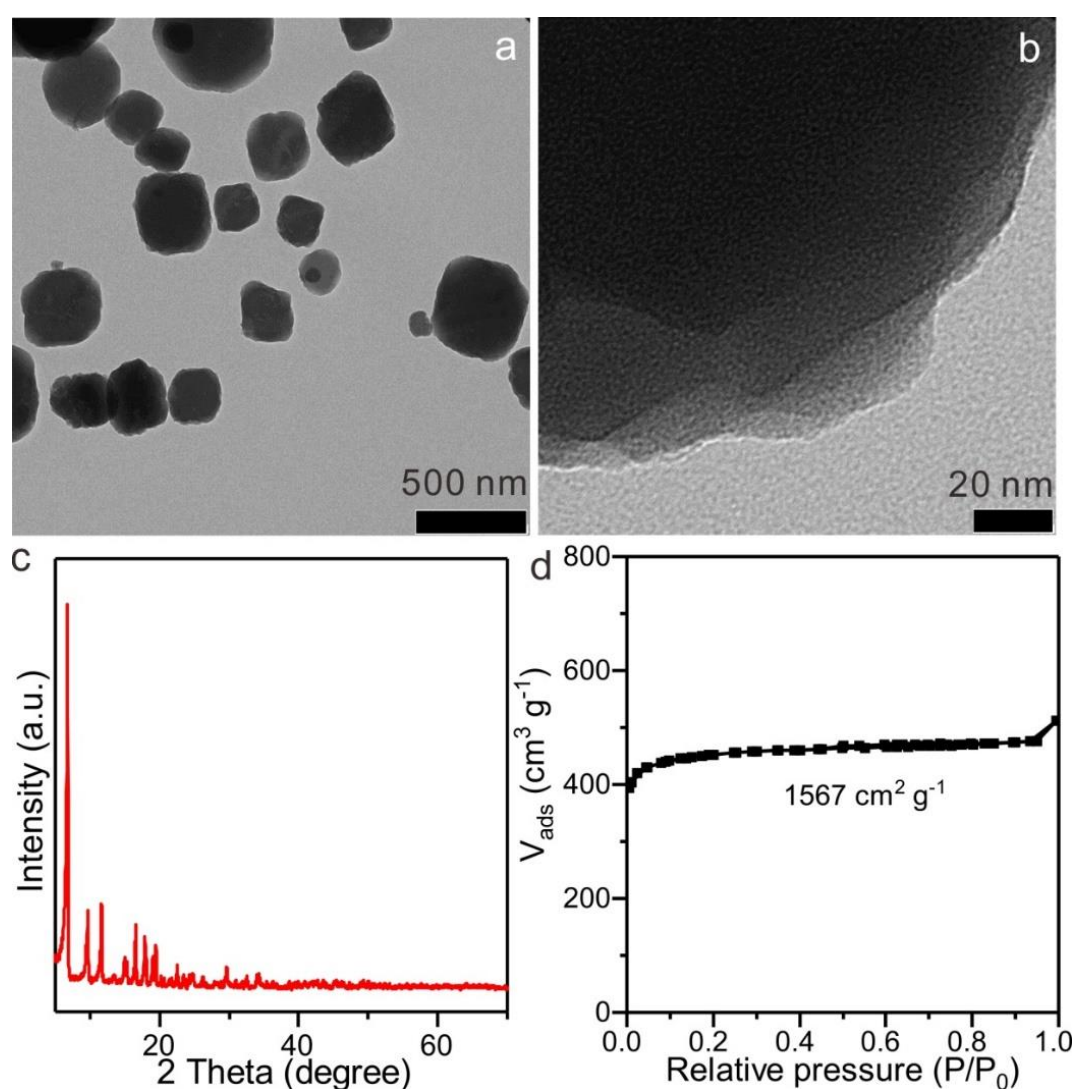


Figure 3.2. (a-b) Representative TEM images, (c) XRD pattern and (d) N₂ physisorption isotherms (measured at -196 °C) of MIL-125(Ti).

3. Enhanced electrocatalytic N₂ reduction via partial anion substitution in titanium oxide-carbon composites

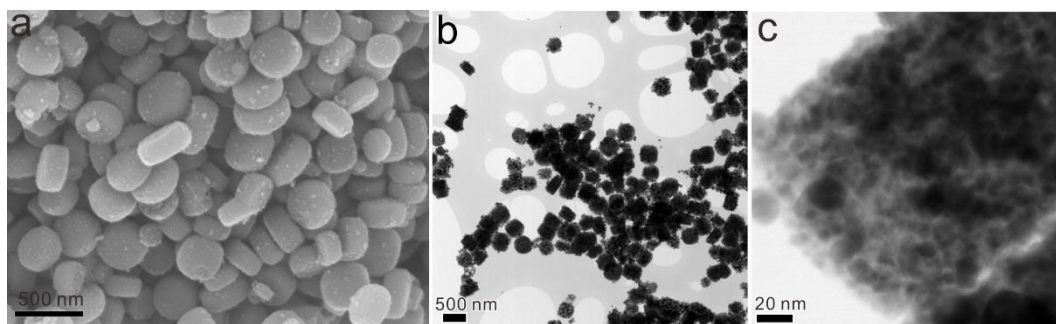


Figure 3.3. Representative (a) SEM and (b-c) TEM images of M-1000.

High-resolution TEM (HRTEM) images show that TiO₂ nanoparticles are well-dispersed in an amorphous environment with exposed (110) facets (Figure 3.4). TEM images of M-800, M-900 and M-1100 also exhibit a comparable structure (Figure 3.5).

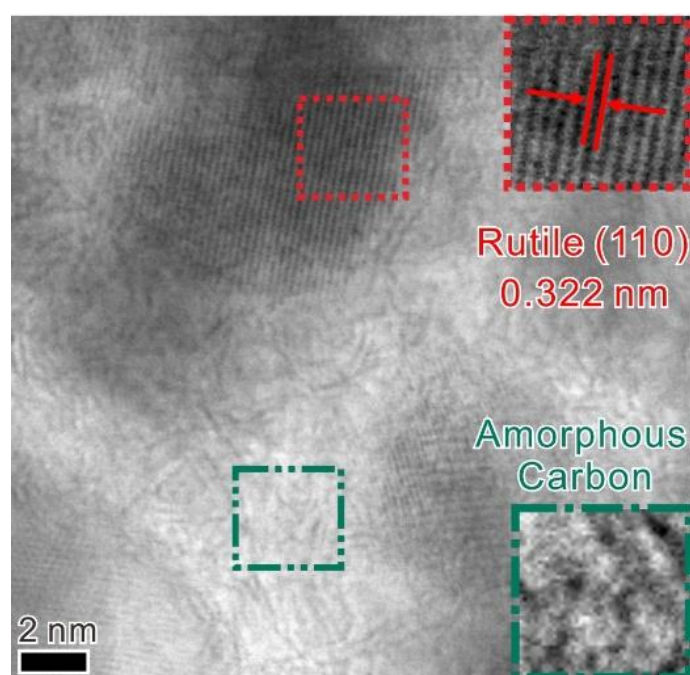


Figure 3.4. HRTEM image of M-1000. The insets are the corresponding HRTEM images of the marked square areas.

3. Enhanced electrocatalytic N₂ reduction via partial anion substitution in titanium oxide-carbon composites

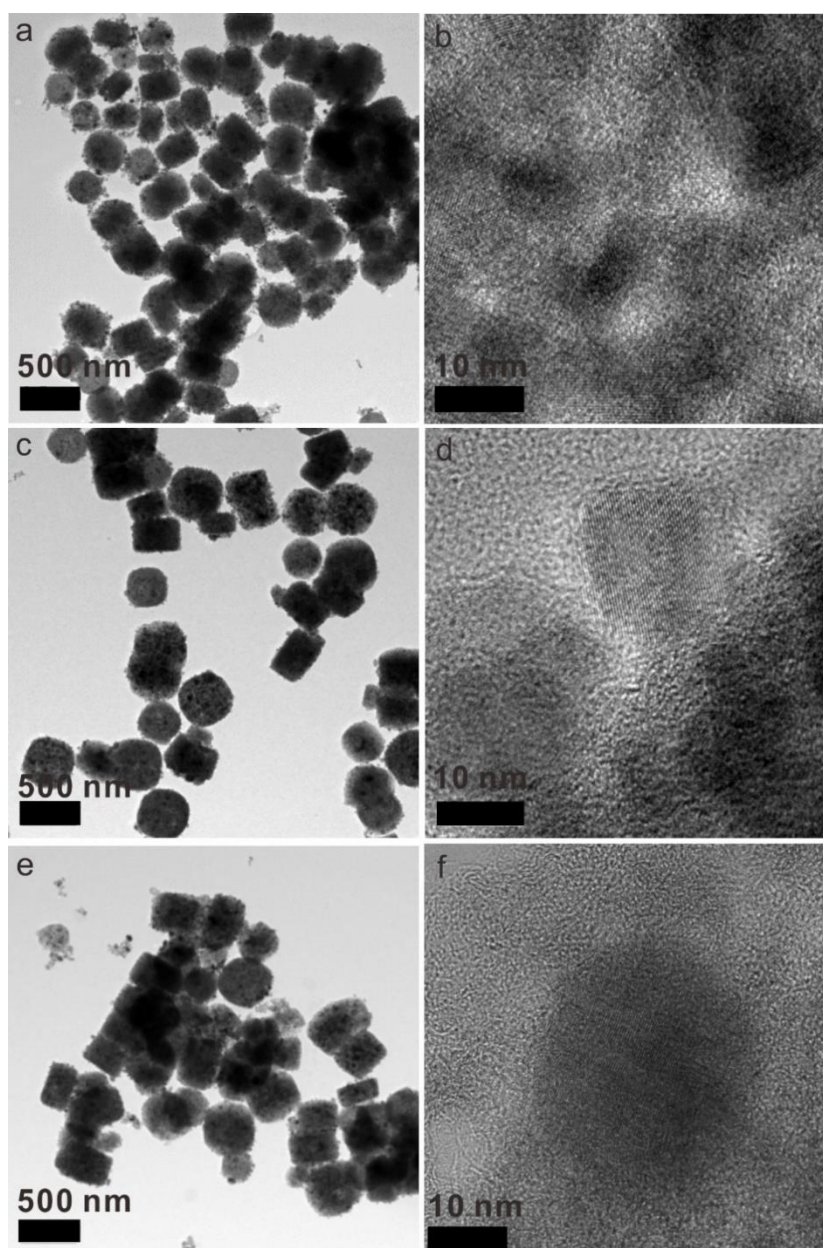


Figure 3.5. TEM images of M-800 (a-b), M-900 (c-d), and M-1100 (e-f).

The X-ray diffraction (XRD) patterns of as-obtained samples (Figure 3.6) indicate that M-800 are TiO₂-containing nanocomposites consisting of tetragonal Rutile (JCPDS No. 21-1276) and tetragonal Anatase (JCPDS No. 21-1272).¹⁶⁵ For M-900, the diffraction peaks of Anatase become much weaker, while only diffraction peaks of Rutile appear in M-1000 and M-1100. Notably, because of the carbothermal reduction of TiO₂, a small new diffraction peak at 43.5° appears in M-1000, which can be attributed to TiC.¹⁶⁶ With further increasing temperature, M-1100 shows more intense diffraction peaks of TiC, as its content increases at higher temperature due to the faster carbothermal reduction.

3. Enhanced electrocatalytic N₂ reduction via partial anion substitution in titanium oxide-carbon composites

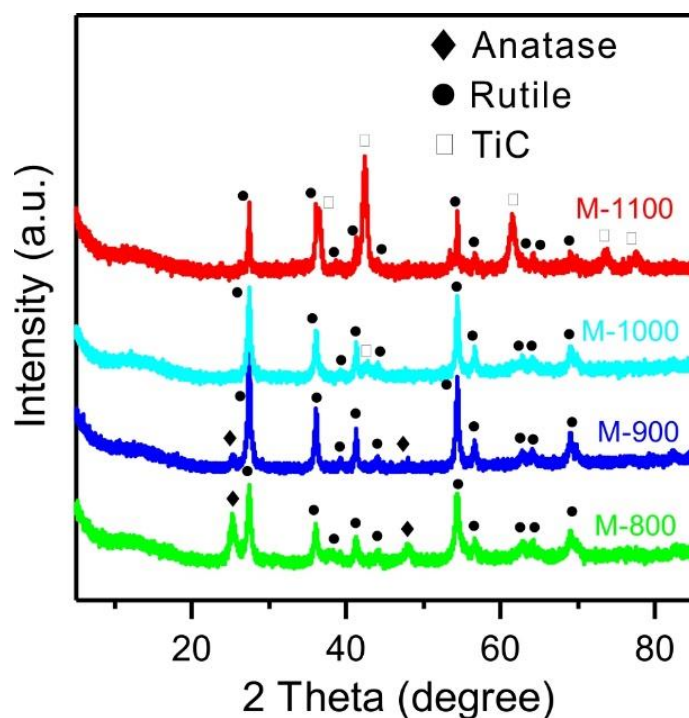


Figure 3.6. XRD patterns of M-Ts.

Raman spectra of the as-obtained materials (Figure 3.7) all exhibit three main bands centered at approximately 249, 413, and 601 cm^{-1} . By comparison of the Raman spectra of TiC, Anatase, and Rutile with M-1000 (Figure 3.8), it can also be concluded that Ti-C and Ti-O bonds may coexist in M-Ts due to the small Raman shift.¹⁶⁷ Besides, two small bands at ~ 1350 and 1590 cm^{-1} are assigned to disordered (D) and graphite (G)-like bands of free carbon.¹⁶⁸ It is worth to note that the latter bands almost disappear in M-1100, as more free carbon reacts with TiO_2 to form TiC at higher temperature.

3. Enhanced electrocatalytic N₂ reduction via partial anion substitution in titanium oxide-carbon composites

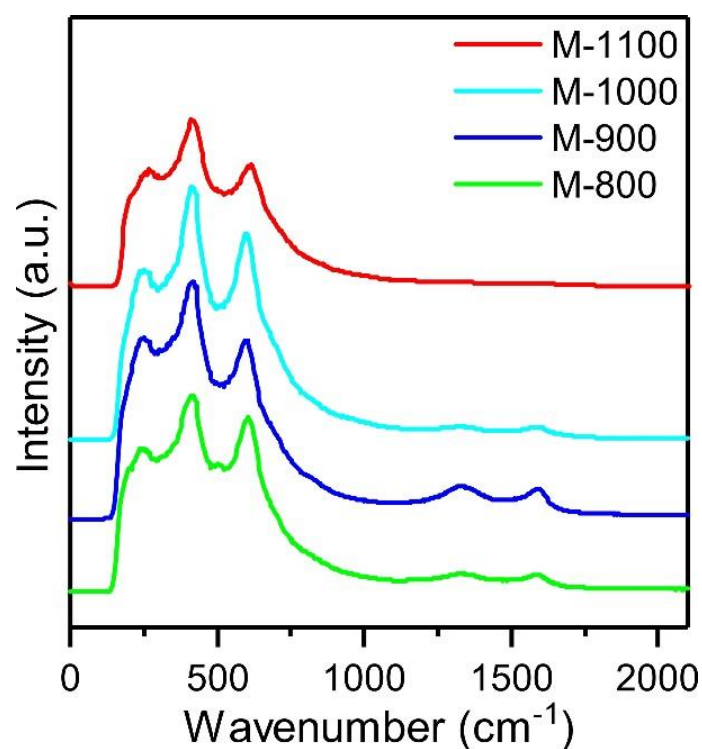


Figure 3.7. Raman spectra of M-800, M-900, M-1000 and M-1100.

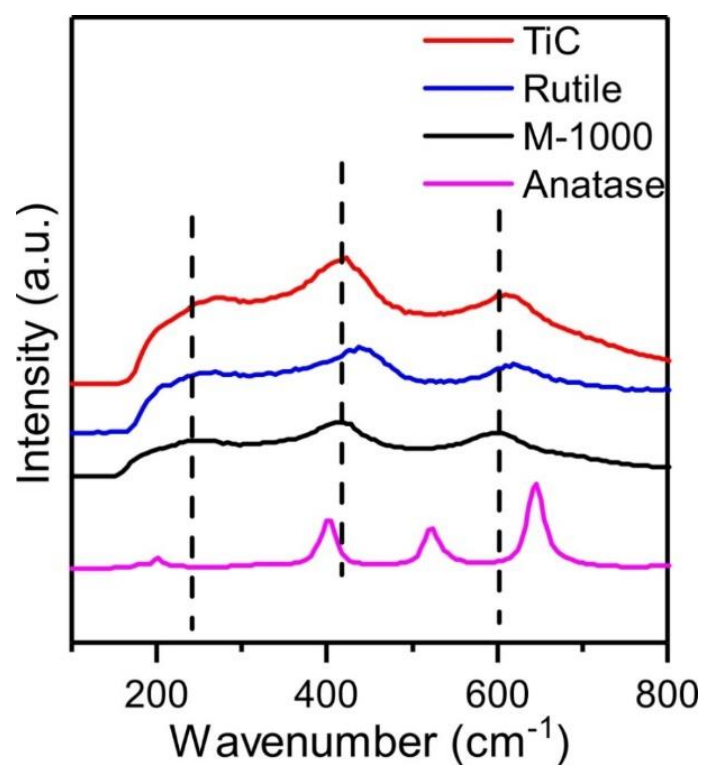


Figure 3.8. Raman spectra of TiC, Rutile, M-1000, and Anatase.

The formation process of M-Ts can also be followed by thermogravimetric analysis (TGA) (Figure 3.9). The first weight loss step is below 200 °C and could be attributed to the loss of adsorbed water and other volatile adsorbed compounds. The decomposition of organic ligands

3. Enhanced electrocatalytic N₂ reduction via partial anion substitution in titanium oxide-carbon composites

within the MOF to pristine carbon species appears between 200 and 500 °C. The minor weight loss between 800 and 1000 °C possibly results from carbothermal reduction of TiO₂, that is, carbon insertion into TiO₂ and carbon oxide formation due to oxygen substitution. Besides, TGA under air was carried out to investigate the structures of M-Ts (Figure 3.10). Notably, there is an obvious increase in mass within the temperature range between 164 and 316 °C for M-1000 and M-1100. This can be ascribed to the oxidation of Ti³⁺, carbon doped into TiO₂ as well as the carbon in TiC.¹⁶⁹ The higher increase in weight for M-1100 than for M-1000 indicates the higher carbide content in the former which is in line with the XRD results. In addition, the temperature of substitution of carbon shifts to higher values for M-1100 indicating the higher thermodynamic barrier for reoxidation in TiC than in C-Ti_xO_y. N₂ (-196 °C) physisorption curves (Figure 3.11) display that M-Ts still have a porous structure with high SSA. In contrast to MIL-125(Ti), the hysteresis loops indicate the presence of additional mesopores which are beneficial for the accessibility of catalytically active sites and transport of N₂ and ammonia within the catalysts during NRR. Whereas the sizes of the mesopores seem to remain in the same range with increasing pyrolysis temperature, the SSA and microporosities decrease significantly from M-1000 to M-1100 due to the increasing formation of TiC and the decreasing content of free carbon.

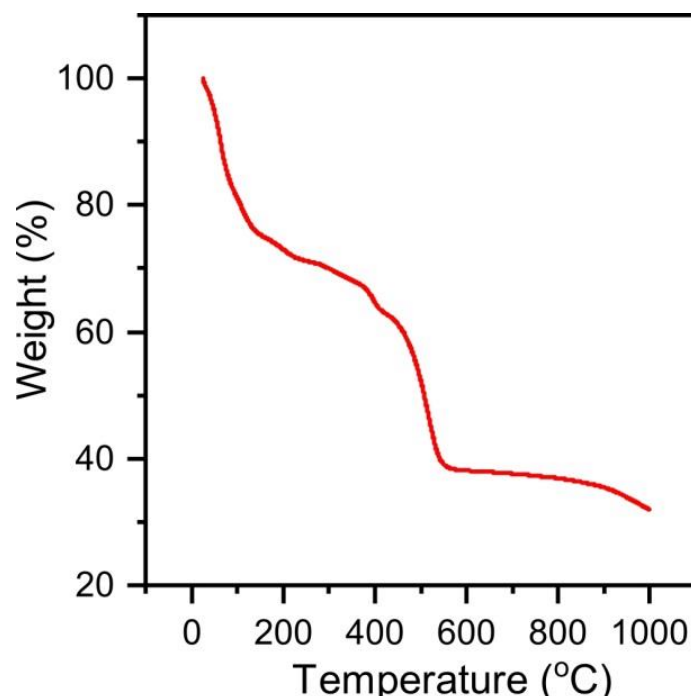


Figure 3.9. TGA analysis of MIL-125(Ti) under Ar atmosphere with a heating rate of 10 °C min⁻¹.

3. Enhanced electrocatalytic N₂ reduction via partial anion substitution in titanium oxide-carbon composites

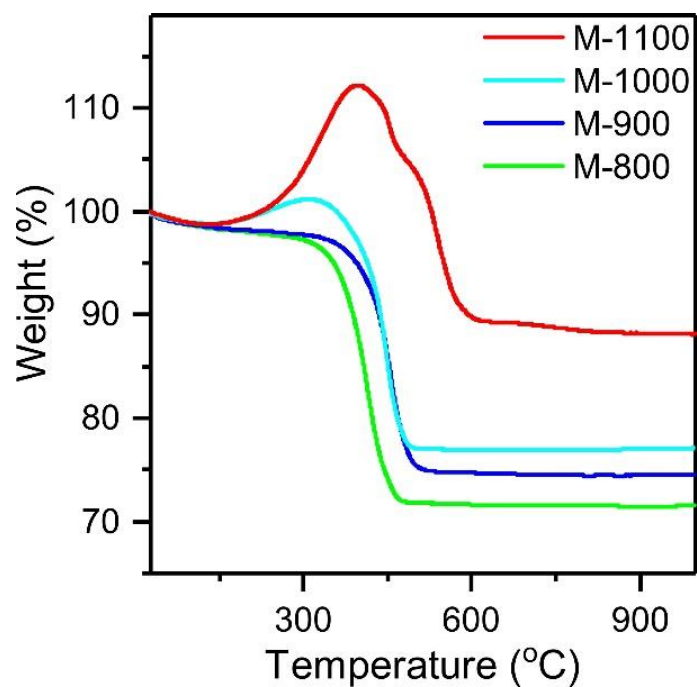


Figure 3.10. TGA analysis under synthetic air with a heating rate of 10 °C min⁻¹ of M-800, M-900, M-1000 and M-1100.

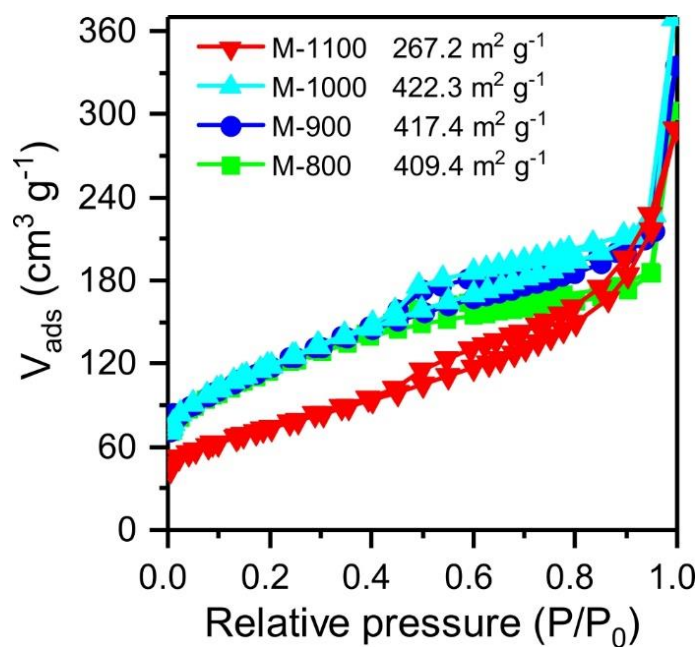


Figure 3.11. N₂ physisorption isotherms (measured at -196 °C) of M-800, M-900, M-1000 and M-1100.

3. Enhanced electrocatalytic N₂ reduction via partial anion substitution in titanium oxide-carbon composites

X-ray photoelectron spectroscopy (XPS) measurements were further performed to investigate the binding states of the elements present in the hybrid materials (Figure 3.12). The significant peak broadening of C 1s in M-1000 could be attributed to the presence of negatively polarized carbon atoms substituting oxygen in the anionic lattice of Rutile (Figure 3.13).¹⁷⁰ This broadening is not observed anymore in M-1100 but instead a new peak centered at 281.7 eV appears due to the existence of carbidic carbon in TiC with rather covalent character.¹⁷¹ High-resolution C 1s spectra of M-800, M-900 and M-1000 are mainly composed of four characteristic peaks (Figure 3.14), corresponding to the C-C, C-O, C=O, and O-Ti-C structures, respectively.¹⁷²⁻¹⁷³ Besides the above four peaks, a new characteristic peak assigned to Ti-C appears in M-1100.¹⁷¹

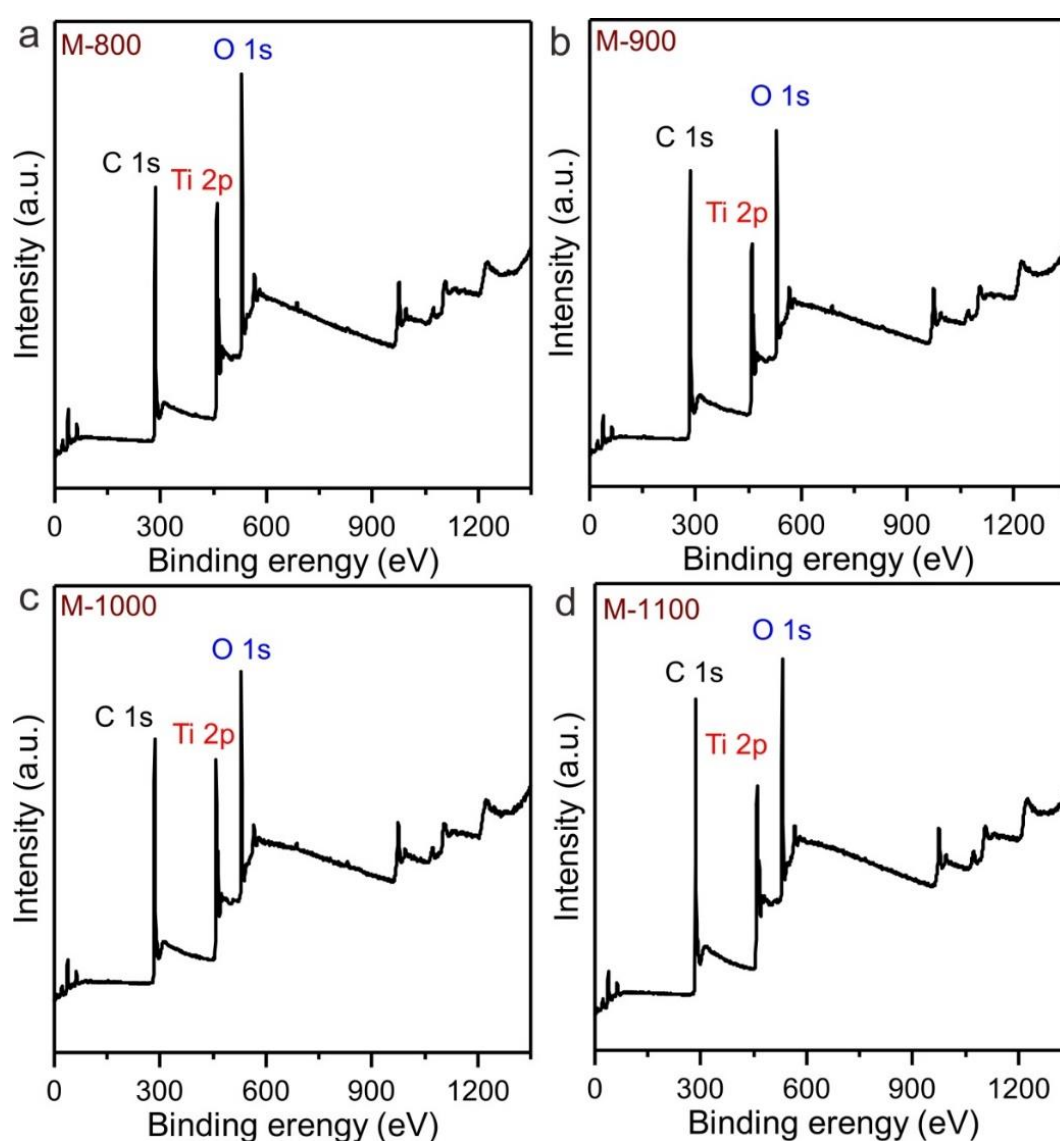


Figure 3.12. XPS survey spectra of (a) M-800, (b) M-900, (c) M-1000 and (d) M-1100.

3. Enhanced electrocatalytic N₂ reduction via partial anion substitution in titanium oxide-carbon composites

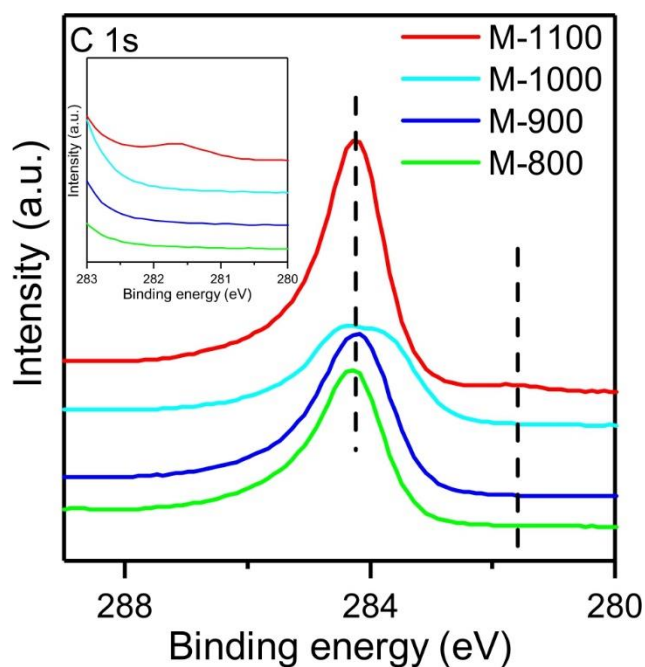


Figure 3.13. XPS spectra of C 1s for M-800, M-900, M-1000 and M-1100.

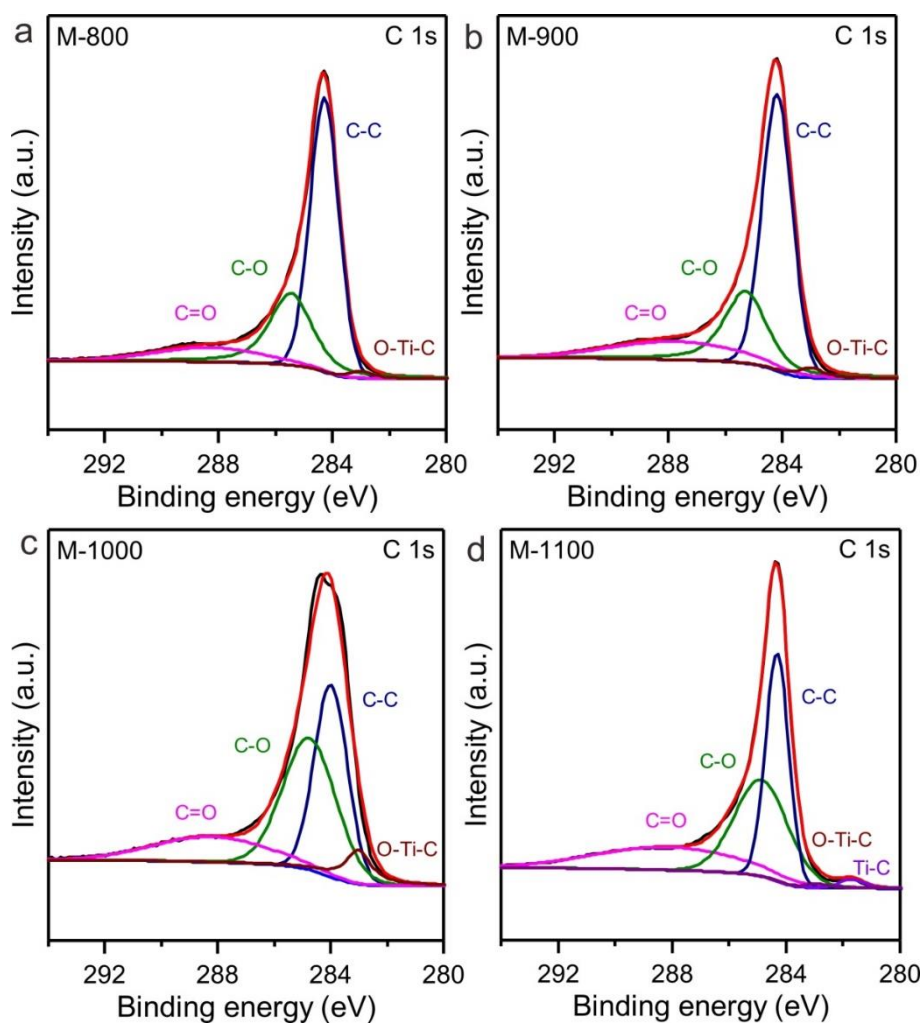


Figure 3.14. High resolution C 1s XPS spectra and corresponding fitting curves of (a) M-800, (b) M-900, (c) M-1000 and (d) M-1100.

3. Enhanced electrocatalytic N₂ reduction via partial anion substitution in titanium oxide-carbon composites

Similarly, XPS spectra of Ti 2p (Figure 3.15) also show a significant peak broadening for M-1000 due to an increasing portion of Ti atoms bonded to carbon instead of the more electronegative oxide anions. This indicates that the content of such “weakly anionic” carbon species is the highest in M-1000. Besides, M-1100 shows a new peak centered at 455.2 eV, which can again be attributed to the presence of oxygen-free TiC.¹⁷¹ The same peak broadening effect along with a minor binding energy shift is also seen in the XPS spectra of O 1s (Figure 3.16).

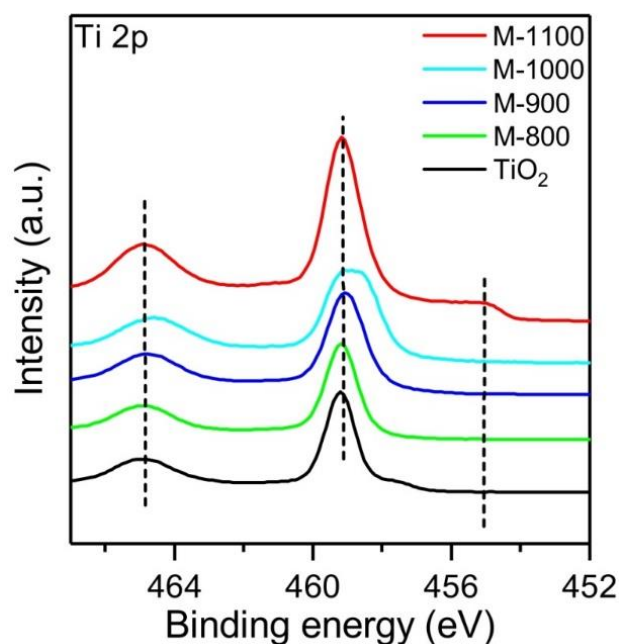


Figure 3.15. XPS spectra of Ti 2p for TiO₂, M-800, M-900, M-1000 and M-1100.

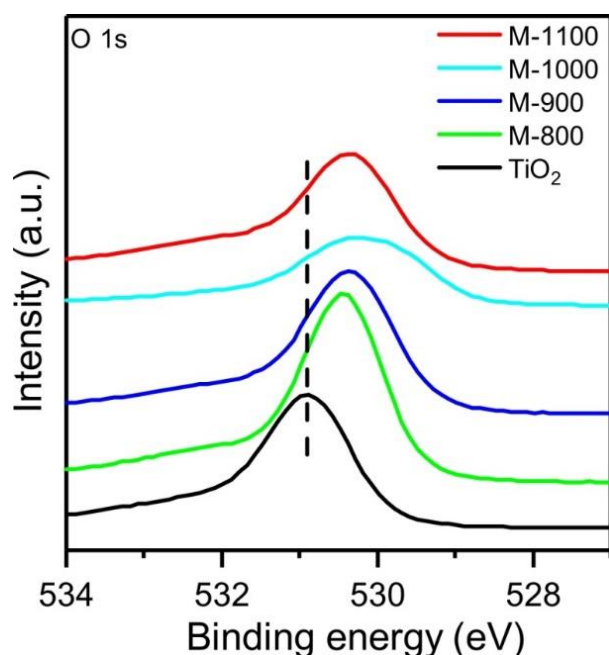


Figure 3.16. XPS spectra of O 1s for TiO₂, M-800, M-900, M-1000 and M-1100.

3. Enhanced electrocatalytic N₂ reduction via partial anion substitution in titanium oxide-carbon composites

Furthermore, the structure and reactivity of paramagnetic species were characterized at atomic level by electron paramagnetic resonance (EPR), which shows similar signals for M-800, M-900, M-1000 and M-1100 (g factors of 2.0038, 2.0040, 2.0043 and 2.0050, respectively) in EPR spectra (Figure 3.17). They are not resolved and essentially indicate an isotropic line shape, which is in line with Ti³⁺ centers being possibly present in C-Ti_xO_y.¹⁷⁴ The EPR intensity increases from M-800 to M-1100 revealing that treatment at higher temperature can induce higher concentration of OV's in the M-Ts.

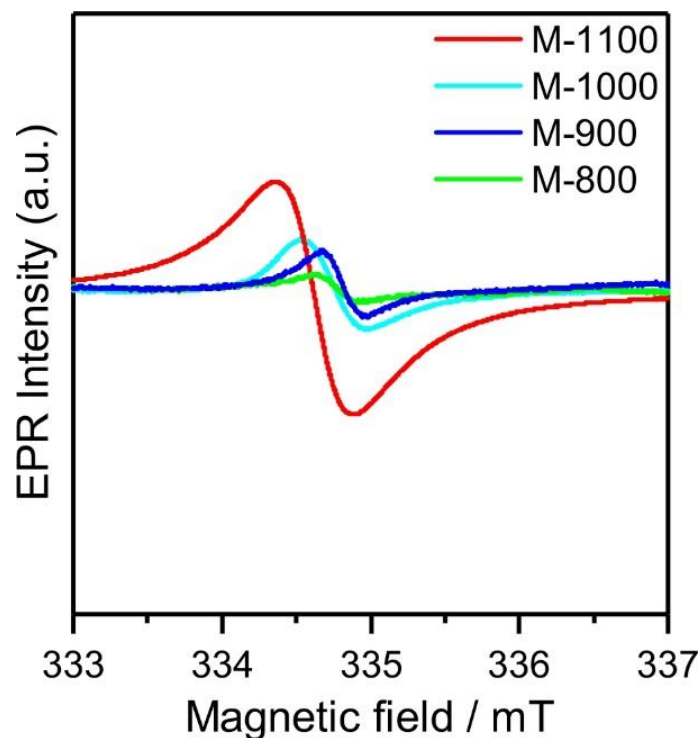


Figure 3.17. EPR spectra of Ti 2p for TiO₂, M-800, M-900, M-1000 and M-1100.

Based on the above analysis, the formation of the M-Ts nanocomposites could thus be understood as follows: Ti in MIL-125(Ti) reacts with the nearby oxygen and aggregates into stable TiO₂ nanoparticles. Meanwhile, the organic ligands also undergo pyrolysis under high temperature to obtain pristine porous carbon, which can substitute the oxygen in TiO₂ to form OV's. Formed OV's can be further occupied by other carbon atoms. At a temperature above 1000 °C, not only partial anion substitution takes place but then TiO₂ can be completely converted to TiC according to Equation 3.1:



Besides, as the amount of OV's increases with higher temperature, the amount of C-Ti_xO_y also increases from T-800 to M-1000. Although TiC starts forming at 1000 °C, the amount is quite low as XPS results show. When the temperature is increased to 1100 °C, the free carbon is fully

3. Enhanced electrocatalytic N₂ reduction via partial anion substitution in titanium oxide-carbon composites

consumed, thus transfer of carbon atoms to OV_s is inhibited even though more OV_s may form at such high temperature.

For comparison, the gas flow during pyrolysis was changed from Ar to N₂ and the corresponding samples with nearly similar pore structure (Figure 3.18a) are denoted as M-Ts-N₂. As shown in the XRD patterns, the diffraction peaks of TiN appear in M-900-N₂ and M-1000-N₂ (Figure 3.18b). Furthermore, elemental analysis (Table 3.1) also indicates a significant content of N in as-obtained M-Ts-N₂, and the amount of N increases with the increase of temperature. As there is no N present in the MOF precursor and M-Ts synthesized under argon atmosphere, the N₂ gas obviously participates in the calcination reaction of MOF precursor.

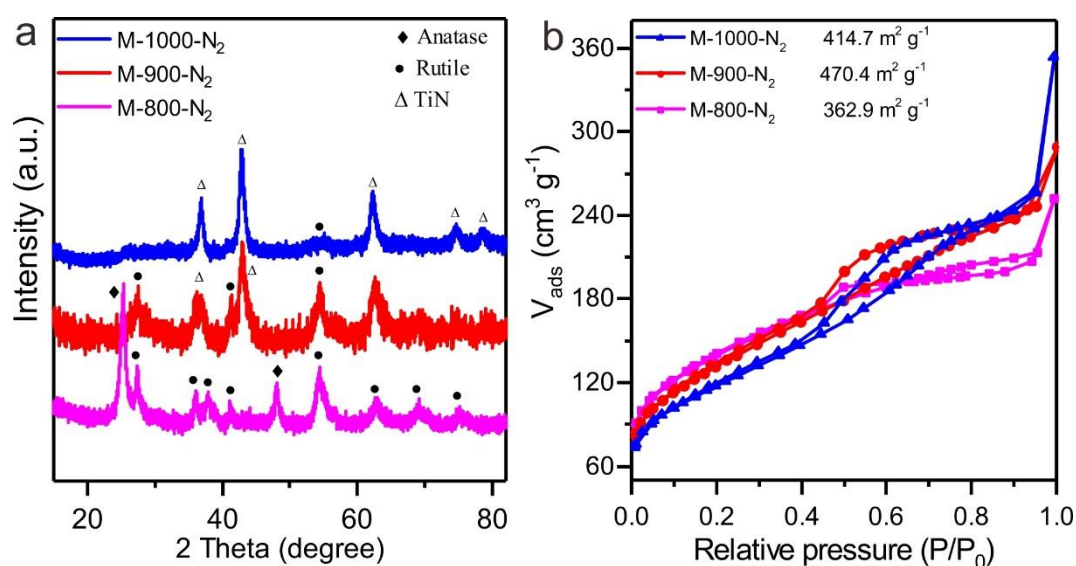


Figure 3.18. (a) XRD patterns and (b) N₂ physisorption isotherms (measured at -196 °C) of M-800-N₂, M-900-N₂ and M-1000-N₂.

Table 3.1. Elemental analysis of M-Ts and M-Ts-N₂.

Sample	C (at.%)	N (at.%)
M-800	26.44	0.48
M-900	25.26	0.61
M-1000	23.58	0.71
M-1100	20.13	0.77
M-800-N ₂	30.60	1.31
M-900-N ₂	25.91	4.84
M-1000-N ₂	20.71	7.78
TiC	19.84	0.15

3. Enhanced electrocatalytic N₂ reduction via partial anion substitution in titanium oxide-carbon composites

3.2. Experimental studies of NRR active sites in M-Ts

The idea to use this material for electrochemical NRR is motivated by this versatile chemistry of the anion-substituted titanium oxides and the possible high affinity of the M-Ts towards N₂. The catalytic performance in the electrochemical NRR was firstly tested for M-1000 by using a H-cell with three-electrode system. As shown in the linear sweep voltammetry (LSV) curves in Ar and N₂-saturated 0.1 M LiClO₄ aqueous solution, there is an obvious intense response in current densities under N₂ (Figure 3.19a). Chronoamperometry tests (Figure 3.19b) were also carried out to calculate NH₃ yields and corresponding FEs, based on NH₄⁺ calibration curves (Figure 3.20). The maximum FE of 17.8% with a remarkable production rate of 14.8 μg h⁻¹ mg⁻¹_{cat.} for NH₃ is achieved at -0.4 V vs. RHE (Figure 3.21).

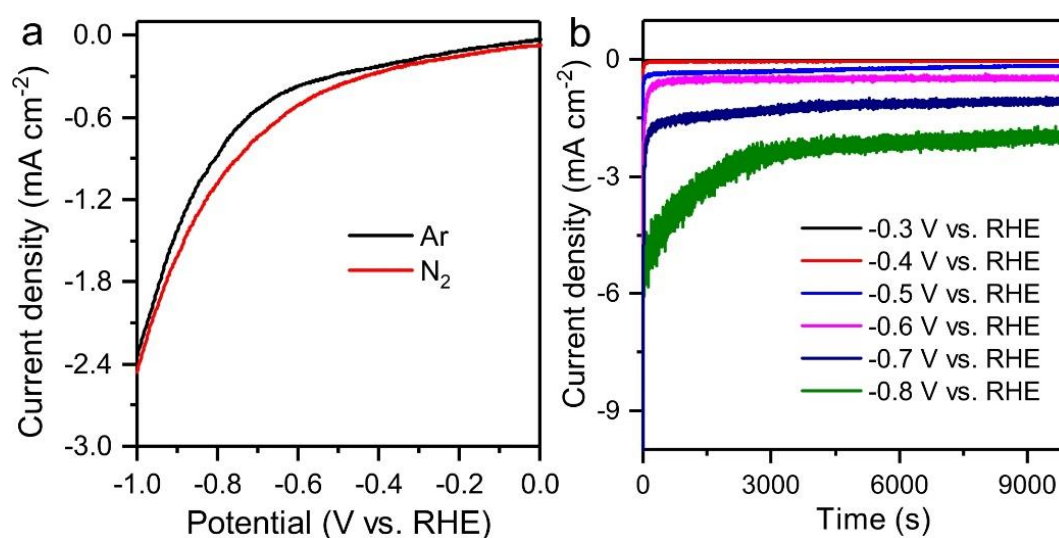


Figure 3.19. (a) LSV curves in N₂- and Ar-saturated aqueous solution of 0.1 M LiClO₄ under ambient conditions. (b) Chronoamperometry results of M-1000 at different potentials under N₂-saturated solution.

3. Enhanced electrocatalytic N₂ reduction via partial anion substitution in titanium oxide-carbon composites

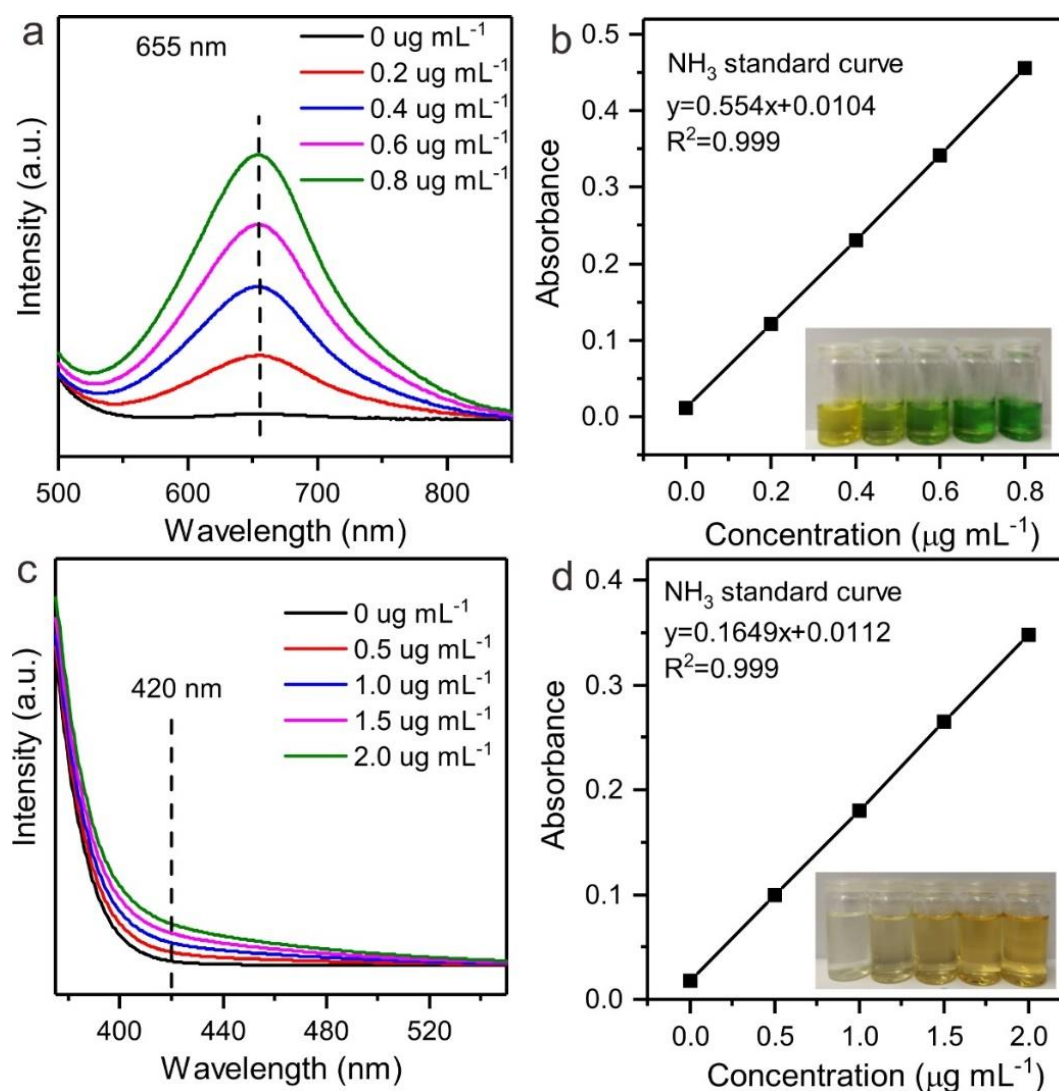


Figure 3.20. (a) UV-Vis spectroscopy curves of different ammonium chloride solutions with known concentration by using indophenol blue method, and the absorbance at 655 nm is referred to the concentration of NH₄⁺. (b) The corresponding linear calibration curve used for calculating the NH₃ production by indophenol blue method. (c) UV-Vis spectroscopy curves of different ammonium chloride solutions with known concentration by using Nessler's method, and the absorbance at 420 nm is referred to the concentration of NH₄⁺. (d) The corresponding linear calibration curve used for estimating NH₃ production by Nessler's method.

3. Enhanced electrocatalytic N₂ reduction via partial anion substitution in titanium oxide-carbon composites

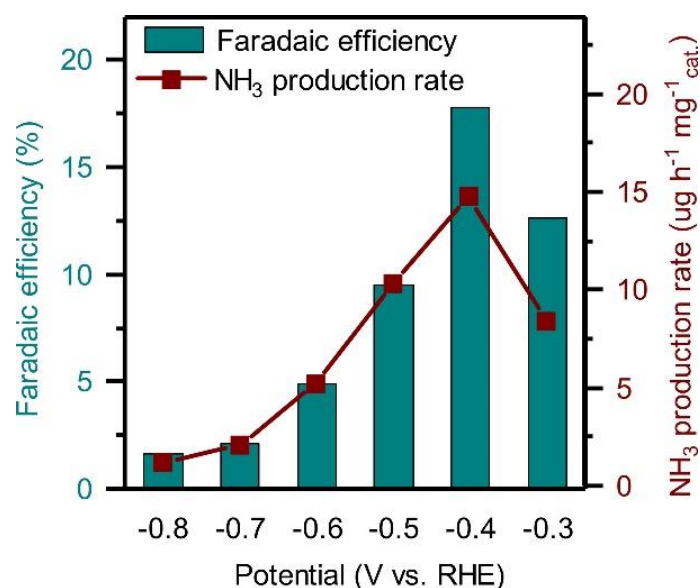


Figure 3.21. FE and NH₃ production rate of the M-1000 electrode at each given potential.

Besides, no N₂H₄ is detected as potential product as there is no obvious colour change before and after electrolysis when adding N₂H₄ colour reagent (Figure 3.22a). UV-Vis spectra also confirm that no N₂H₄ is produced independent of the applied potential (Figure 3.22b). At more negative potentials, FE and NH₃ production rate are both cast into shade due to the strong competition with HER, which is indicated by the largely increased FE and H₂ production rate (Figure 3.23).¹⁷⁵ As shown in the UV-Vis spectra (Figure 3.24a) and optical images (Figure 3.24b), NH₄⁺ cannot be detected under different control experiments. Meanwhile, there is no NH₃ produced in Ar-saturated electrolyte at all given potentials (Figure 3.25).

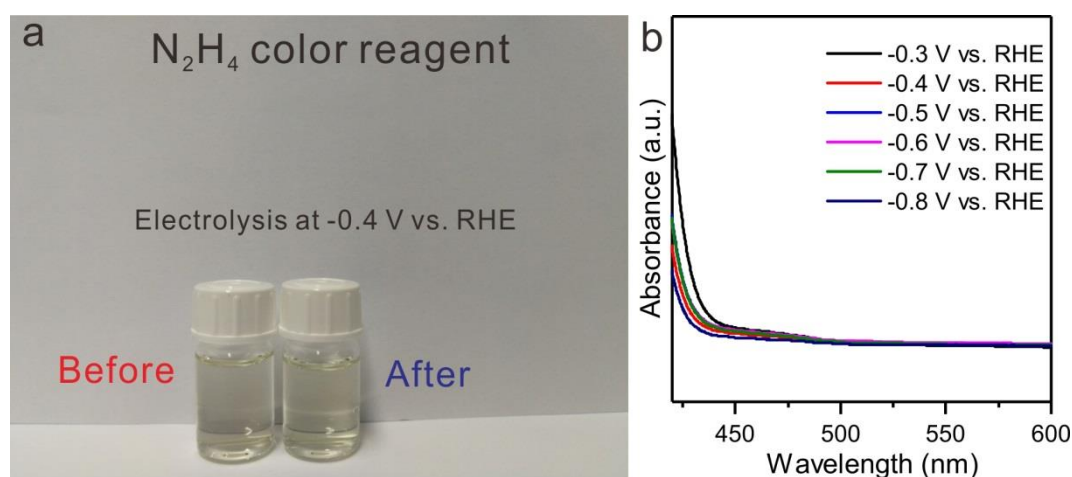


Figure 3.22. (a) Optical image of the N₂-saturated 0.1 M LiClO₄ electrolyte detected using N₂H₄ color reagent before and after NRR test for 10000 s on the M-1000 electrode at -0.4 V vs. RHE. (b) UV-Vis absorption spectra of the N₂-saturated 0.1 M LiClO₄ electrolyte with N₂H₄ color reagent after electrocatalytic test at different given potentials for 10000 s.

3. Enhanced electrocatalytic N₂ reduction via partial anion substitution in titanium oxide-carbon composites

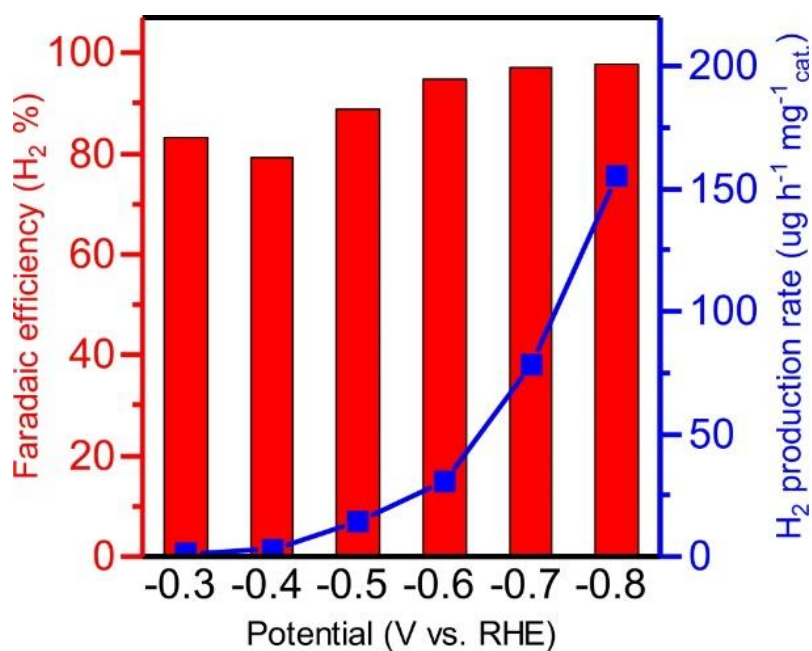


Figure 3.23. FE and rate of H₂ production of M-1000 at different applied potentials.

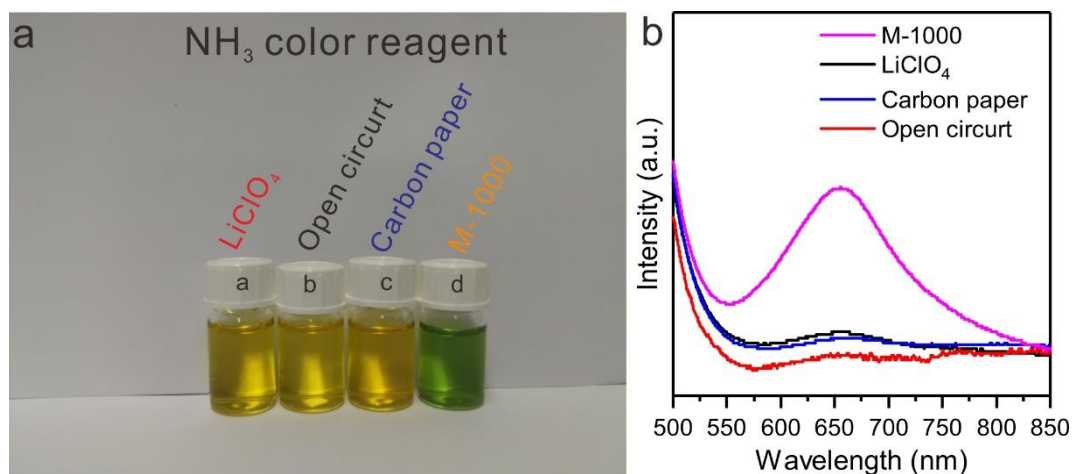


Figure 3.24. (a) Optical image and (b) UV-Vis spectra of the N₂-saturated 0.1 M LiClO₄ electrolyte detected using indophenol indicator under no treatment, open circuit, NRR test on pure carbon paper for 10000 s at -0.4 V vs. RHE and NRR test on the M-1000 electrode for 10000 s at -0.4 V vs. RHE.

3. Enhanced electrocatalytic N₂ reduction via partial anion substitution in titanium oxide-carbon composites

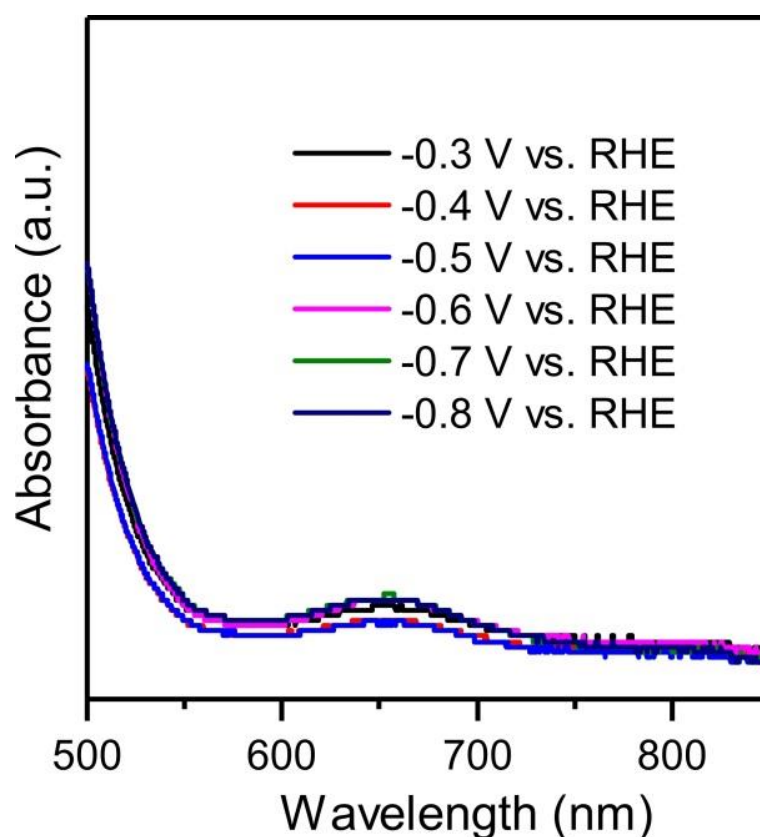


Figure 3.25. UV-Vis absorption spectra of the Ar-saturated 0.1 M LiClO₄ electrolyte with indophenol indicator after electrolysis on the M-1000 electrode at different potentials for 10000 s.

In addition, a ¹⁵N isotopic labelling experiment has been performed to verify the nitrogen source of the produced NH₃ (Figure 3.26). The ¹H nuclear magnetic resonance (¹H NMR) spectra of standard samples show a triplet coupling for ¹⁴NH₄⁺ and a double coupling for ¹⁵NH₄⁺. The use of ¹⁴N₂ and ¹⁵N₂ as the feeding gas yields ¹⁴NH₄⁺ and ¹⁵NH₄⁺, respectively. Based on these NMR results, it is verified that the detected NH₃ is exclusively produced from the reduction of the introduced N₂ and possible formation of NH₃ from possible traces of nitrogen present in M-1000 can be ruled out. In addition, based on the rigorous protocol for NH₃ synthesis,^[28] a control experiment has been performed by using ¹⁵N₂ and ¹⁴N₂ feeding gases separately and carrying out the chronoamperometry tests under the same conditions. The results show nearly the same FE and NH₃ production rate according to calibration curve of the ¹H NMR signal for standard ¹⁵NH₄⁺ solutions, which also excludes the possible presence of impurities from ¹⁵N₂ gas (Figure 3.27).

3. Enhanced electrocatalytic N₂ reduction via partial anion substitution in titanium oxide-carbon composites

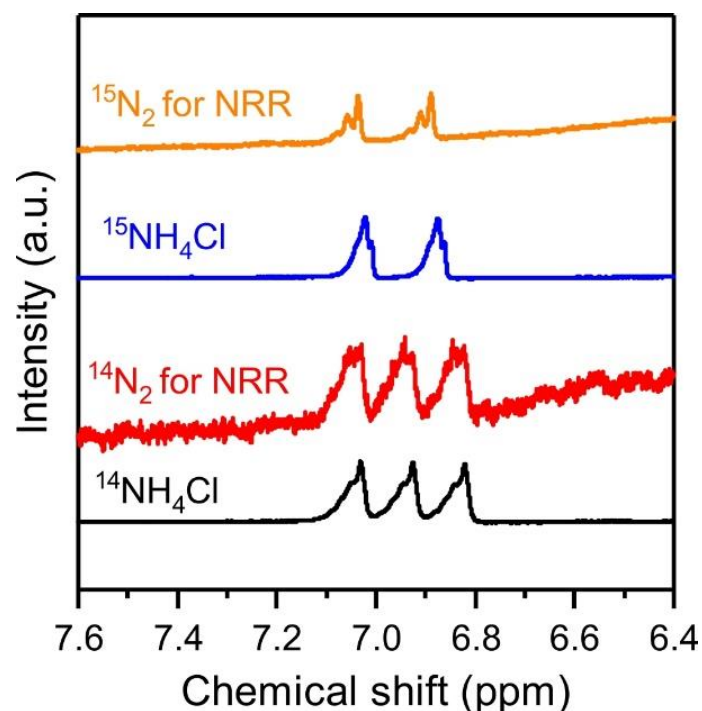


Figure 3.26. ¹H NMR spectra of standard ¹⁵NH₄⁺, ¹⁴NH₄⁺, and the sample by using ¹⁴N₂ and ¹⁵N₂ as the feeding gas yields, respectively.

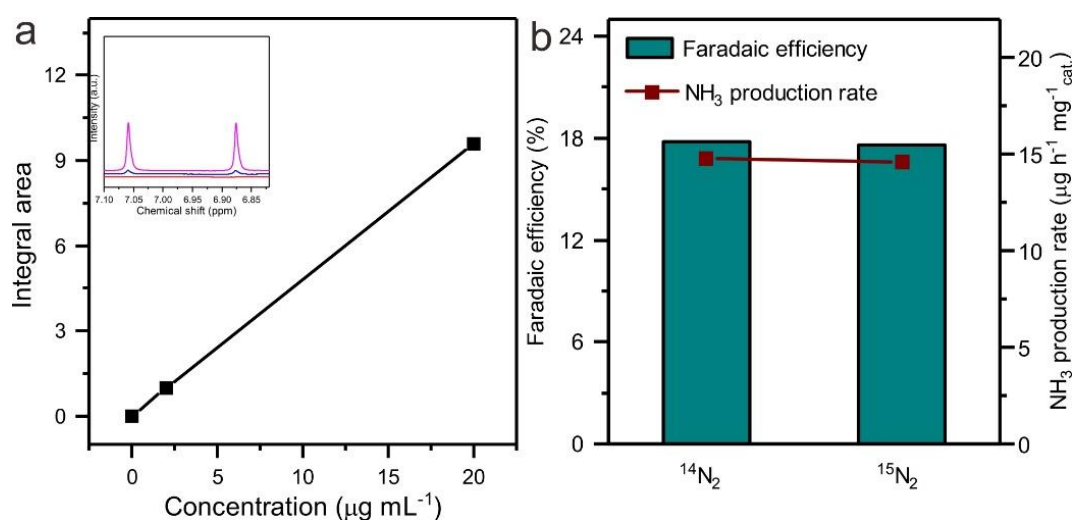


Figure 3.27. (a) ¹H NMR spectra of the standard solutions of ¹⁵NH₄⁺ ($y = 0.479x + 0.019$). (b) The comparison of FE and NH₃ production rate under -0.4 V vs. RHE by using ¹⁴N₂ and ¹⁵N₂ as the feeding gas, respectively.

In the recycling test (Figure 3.28a), no obvious fluctuation arises in the FE and NH₃ production rate (Figure 3.28b), demonstrating the good stability of M-1000 during the NRR, which is also confirmed by continuous production of NH₃ during the long-term chronoamperometry test (Figure 3.29). TEM images acquired after the test demonstrate the structural stability of the catalysts (Figure 3.30).

3. Enhanced electrocatalytic N₂ reduction via partial anion substitution in titanium oxide-carbon composites

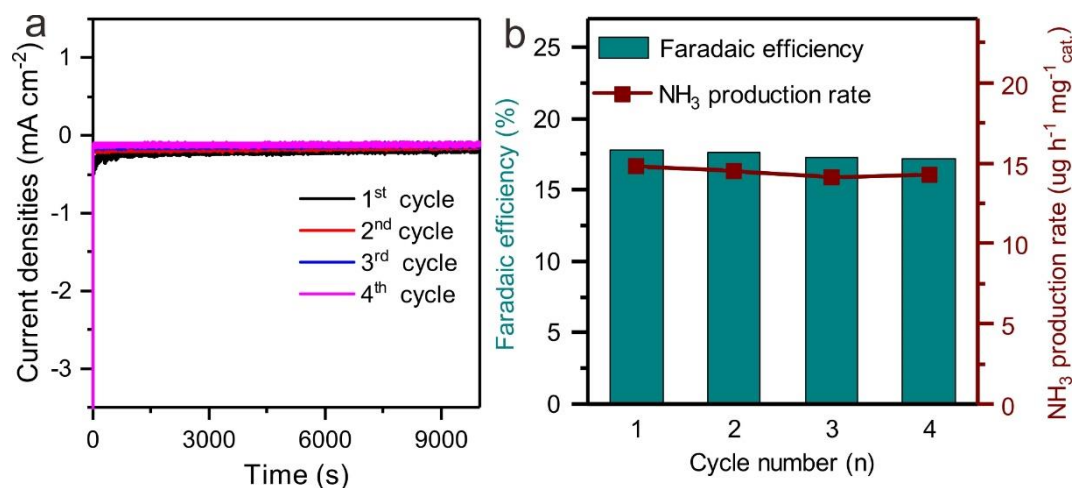


Figure 3.28. (a) Chronoamperometry test and (b) the corresponding FE and NH₃ production rate during the recycling test under the potential of -0.4 V vs. RHE.

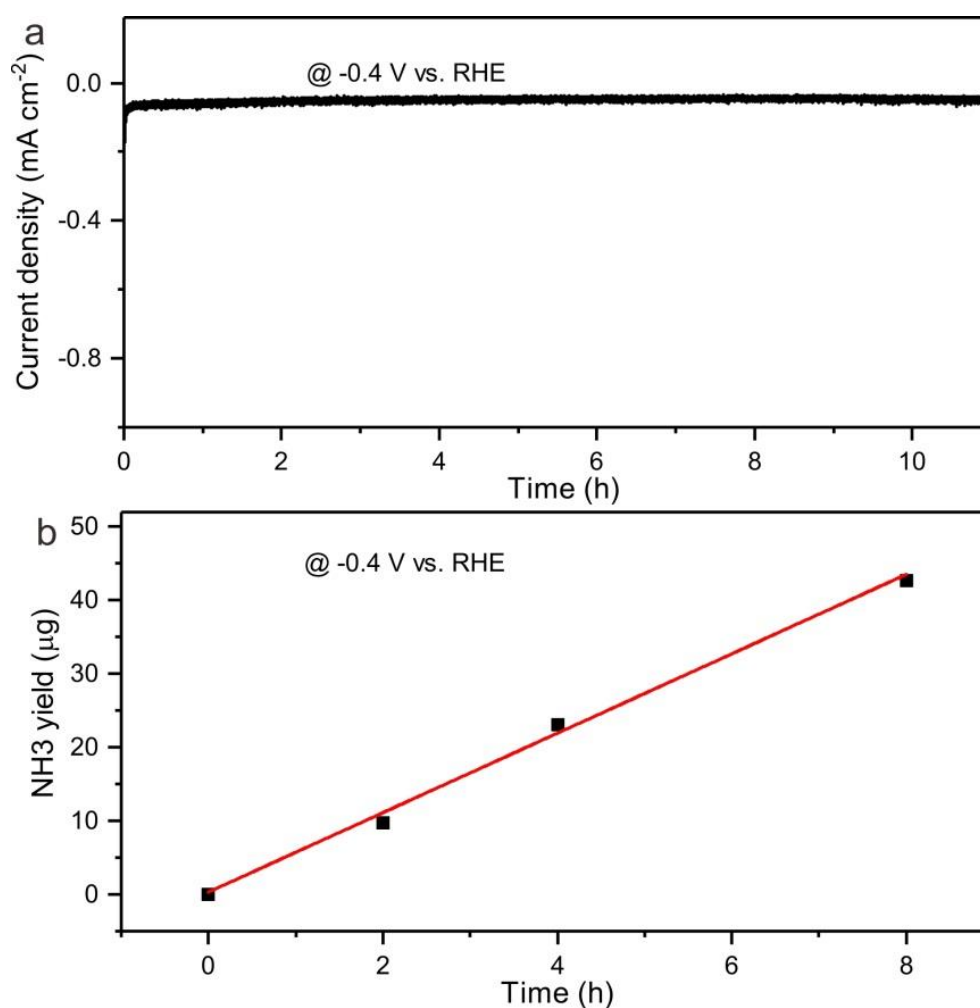


Figure 3.29. (a) Chronoamperometry test for M-1000 electrode at the potential of -0.4 V vs. RHE for over 10 h. (b) The curve of NH₃ production vs. reaction time on the M-1000 electrode at a potential of -0.4 V vs. RHE.

3. Enhanced electrocatalytic N₂ reduction via partial anion substitution in titanium oxide-carbon composites

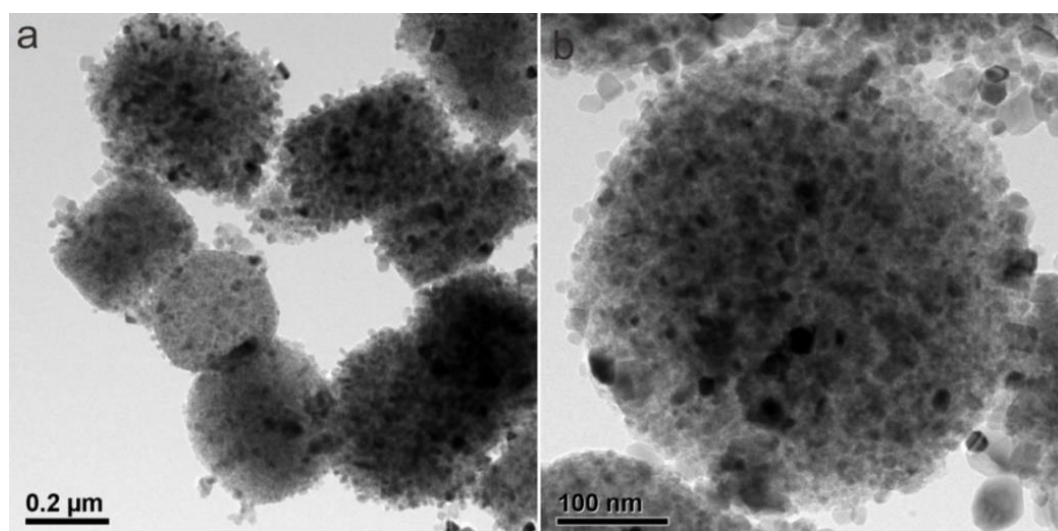


Figure 3.30. TEM images of the M-1000 catalyst after chronoamperometry test at the potential of -0.4 V vs. RHE for over 10 h.

To conclude on the influence of oxygen substitution by carbon in the anion lattice of TiO₂, the NRR performance of M-800 and M-900 is also tested. At the potential of -0.4 V vs. RHE, FE and NH₃ production rate of M-800 and M-900 lag far behind M-1000 (Figure 3.31) but with a stronger HER (Figure 3.32). For M-1100, both FE and NH₃ production rate go down again. Further considering the different content of doped carbon in M-Ts, it can be suspected that the formed (O-)Ti-C bonds in C-Ti_xO_y are the most favourable active sites for N₂ fixation. Based on previously published results, OVs in C-Ti_xO_y could also act active sites.^{134, 159-160} However, comparison of the NRR performance of M-Ts reveals that (O-)Ti-C bonds may play a more important role in NRR than non-substituted OVs and Ti-C bonds as present in crystalline titanium carbide. The amount of OVs and Ti-C bonds in M-1100 is much higher as compared to M-1000 but this material has inferior NRR performance. Besides, NRR performance was tested by using commercial TiO₂ catalysts without any carbon doping, which show bad NRR performance. The same result was also observed in commercial TiC catalysts. Although there are enough Ti-C bonds present, they are not as active as (O-)Ti-C bonds in C-doped Ti_xO_y, where C atoms replace OVs.

3. Enhanced electrocatalytic N₂ reduction via partial anion substitution in titanium oxide-carbon composites

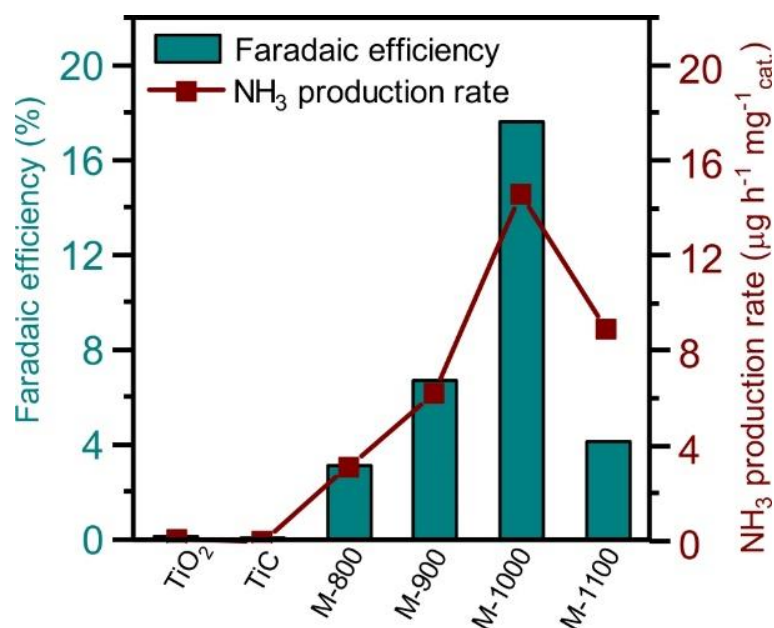


Figure 3.31. FE and NH₃ production rate of TiO₂, TiC, M-800, M-900, M-1000, and M-1100 catalysts.

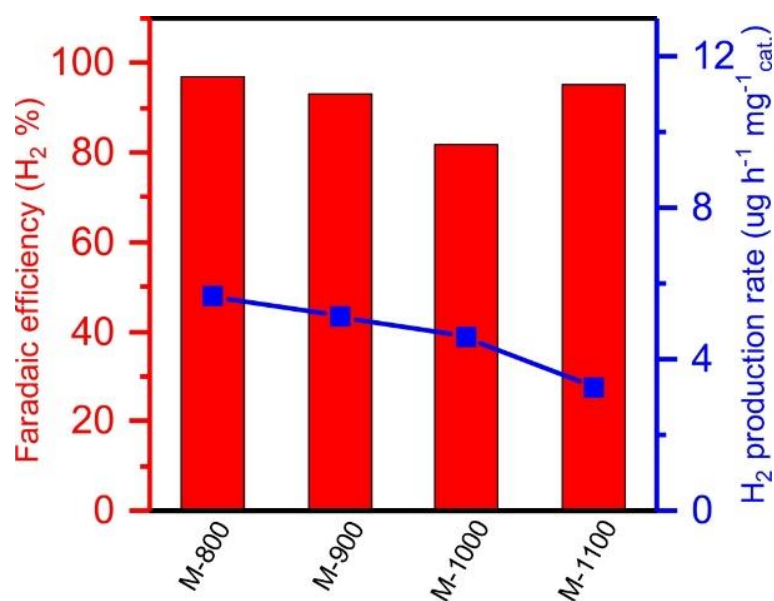


Figure 3.32. The FE and production rate of H₂ for M-Ts at -0.4 V vs. RHE.

The electrochemical active surface area (ECSA) of M-1000 in 0.1 M N₂-saturated LiClO₄ is larger than those of M-800, M-900 and M-1100. This clearly confirms that the more available active sites are present in M-1000 (Figure 3.33 and 3.34). It should be noticed that these measurements can only provide a relative comparison between the samples and can not give direct evidence about the chemistry of the active sites but relative comparison shows that the highest ECSA is present in M-1000 that has the highest density of (O-)Ti-C binding motives. Besides, a N₂ adsorption test under different temperatures (Figure 3.35a and b) was conducted

3. Enhanced electrocatalytic N₂ reduction via partial anion substitution in titanium oxide-carbon composites

to investigate the N₂ affinity of as-obtained M-Ts by calculating the heat of adsorption (Q_{st}) of N₂ (Figure 3.35c), which shows that M-1000 has the strongest N₂ affinity and thus better N₂ activation ability.

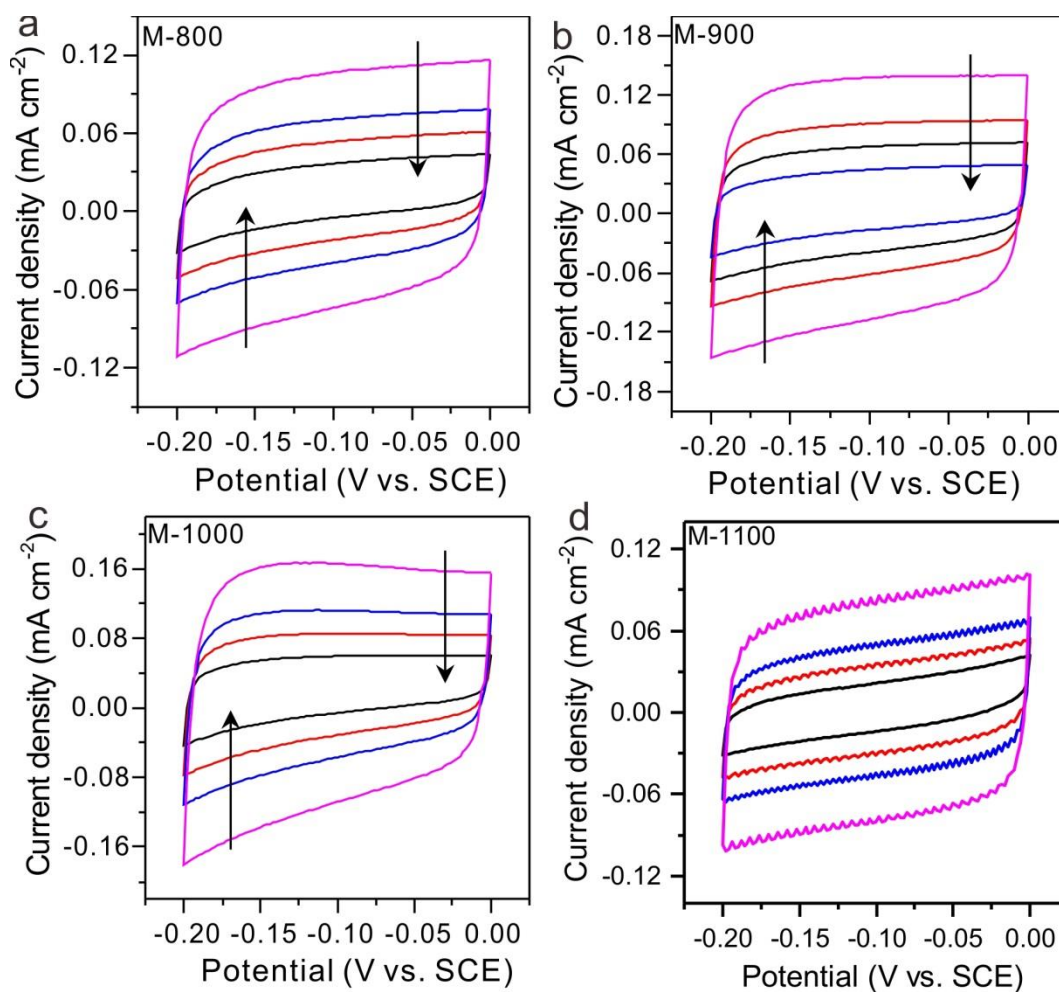


Figure 3.33. Cyclic voltammograms in the double layer region at scan rate of 60, 40, 30, 20 mV/s (along the arrow direction) of (a) M-800, (b) M-900, (c) M-1000, and (d) M-1100.

3. Enhanced electrocatalytic N₂ reduction via partial anion substitution in titanium oxide-carbon composites

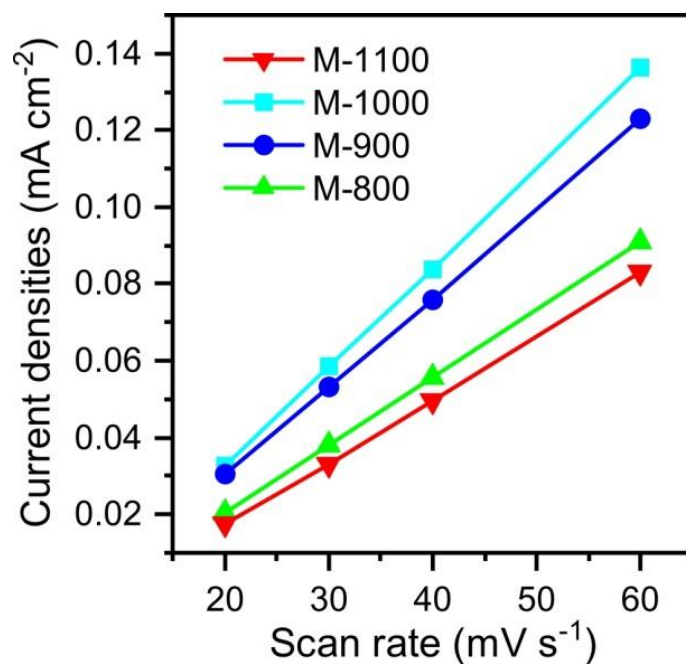


Figure 3.34. Current density as a function of scan rate for M-Ts catalysts.

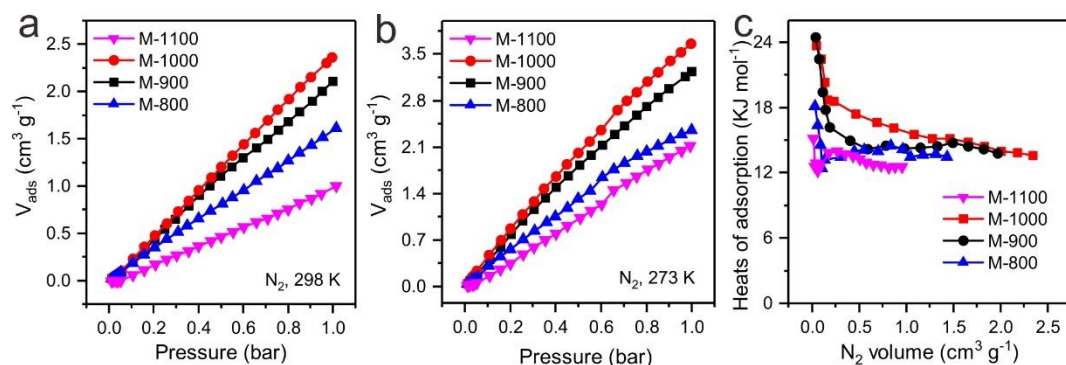


Figure 3.35. N₂ adsorption isotherms measured at (a) 298 K (room temperature) and (b) 273 K (ice-water bath) of M-800, M-900, M-1000 and M-1100. (c) Heat of N₂ adsorption for M-800, M-900, M-1000 and M-1100.

3. Enhanced electrocatalytic N₂ reduction via partial anion substitution in titanium oxide-carbon composites

In contrast to the M-Ts materials, the N species in M-Ts-N₂ are electrochemically unstable, as NH₃ can also be detected without N₂ as feeding gas after the chronoamperometry test (Figure 3.36).

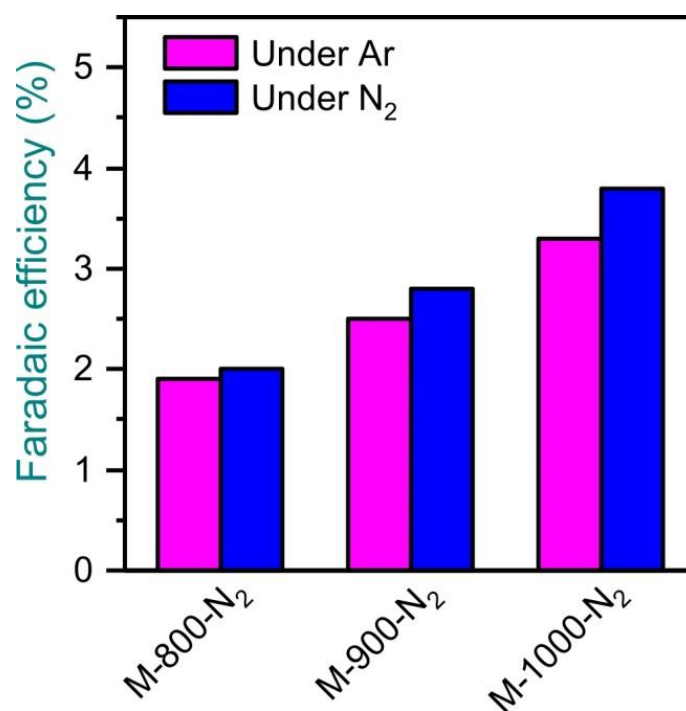


Figure 3.36. FE of M-800-N₂, M-900-N₂ and M-1000-N₂ catalysts under N₂ and Ar saturated electrolyte solution, respectively.

In order to further demonstrate that (O-)Ti-C bonds present in Ti_xO_y are the active sites in M-1000, commercial TiO₂ is mixed with the MOF linker Terephthalic acid (H₂BDC) and reduced under the same conditions as M-1000 (sample denoted as C-treated TiO₂). In this way, a comparable structure to M-1100 consisting of carbon-doped Rutile and TiC was fabricated with the small nanoparticles embedded into the carbon (Figure 3.37). The NRR performance of C-reduced TiO₂ is dramatically improved to the decent FE of 8% after carbon doping (Figure 3.38). This further indicates that C doping and (O-)Ti-C bond formation in TiO₂ are crucial for the N₂ activation. The apparently higher crystalline TiC content in C-treated TiO₂ and its lower SSA are likely responsible for the lower FE in comparison to M-1000. As a comparison, TiO₂ was also treated under the same conditions in absence of H₂BDC. The resulting material exhibited a much worse NRR performance (Figure 3.38). Therefore, the enhanced performance of C-treated TiO₂ in NRR also demonstrates that this anion substitution is applicable and universal for constructing efficient NRR electrocatalysts.

3. Enhanced electrocatalytic N₂ reduction via partial anion substitution in titanium oxide-carbon composites

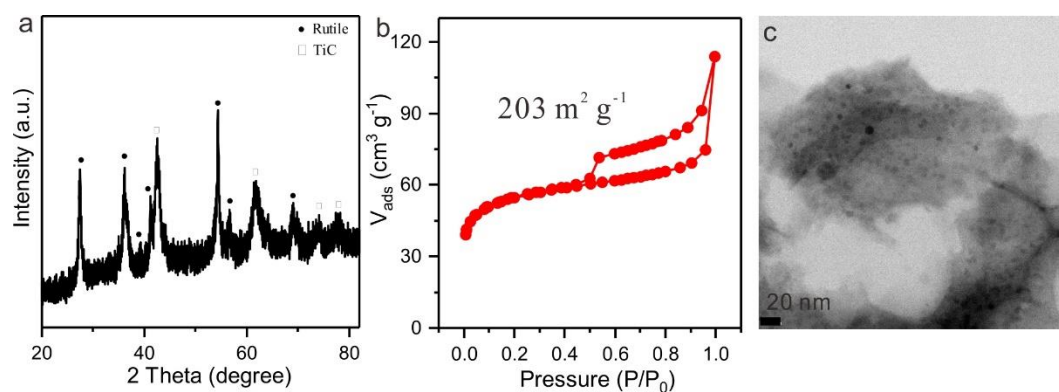


Figure 3.37. (a) XRD pattern, (b) N₂ physisorption isotherm (measured at -196 °C), and TEM image of C-treated TiO₂.

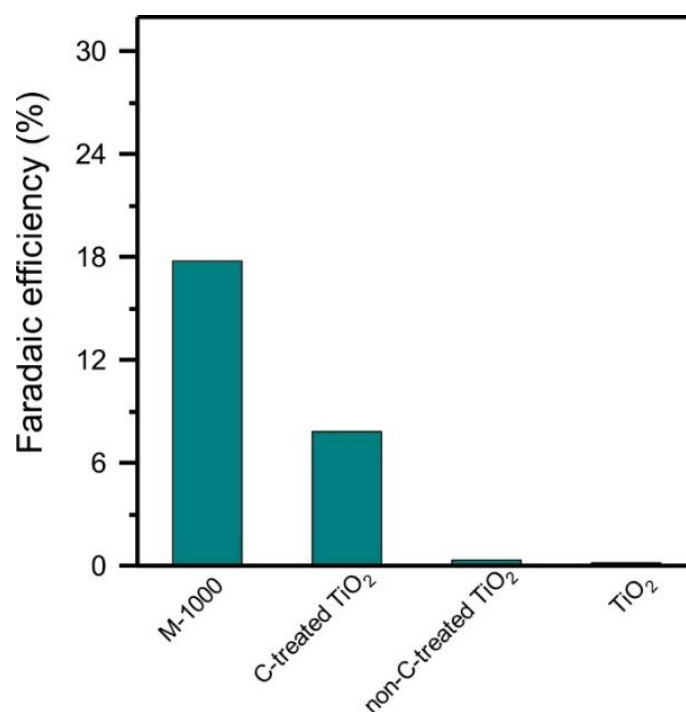


Figure 3.38. FE comparison of M-1000, C-treated TiO₂, non-C-treated TiO₂ and TiO₂.

3.3. Mechanism studies through DFT calculations (in collaboration with Dr. Yun Zhao and Dr Haijun Jiao)

To gain deep insights into the origin of the enhanced NRR performance of M-1000 catalyst and to highlight the role of carbon doping in NRR, density functional theory (DFT) calculations were carried out to investigate the mechanism of N₂ fixation on the C-doped TiO₂ (110) surface (C-Ti_xO_y) compared with non-doped OV_s enriched TiO₂ (OV_s-TiO₂). The computational methods and rationalized surface models (Figure 3.39 and Figure 3.40) as well as the optimized surface intermediates and their energies are given, respectively (Figure 3.41 and Figure 3.42).

3. Enhanced electrocatalytic N₂ reduction via partial anion substitution in titanium oxide-carbon composites

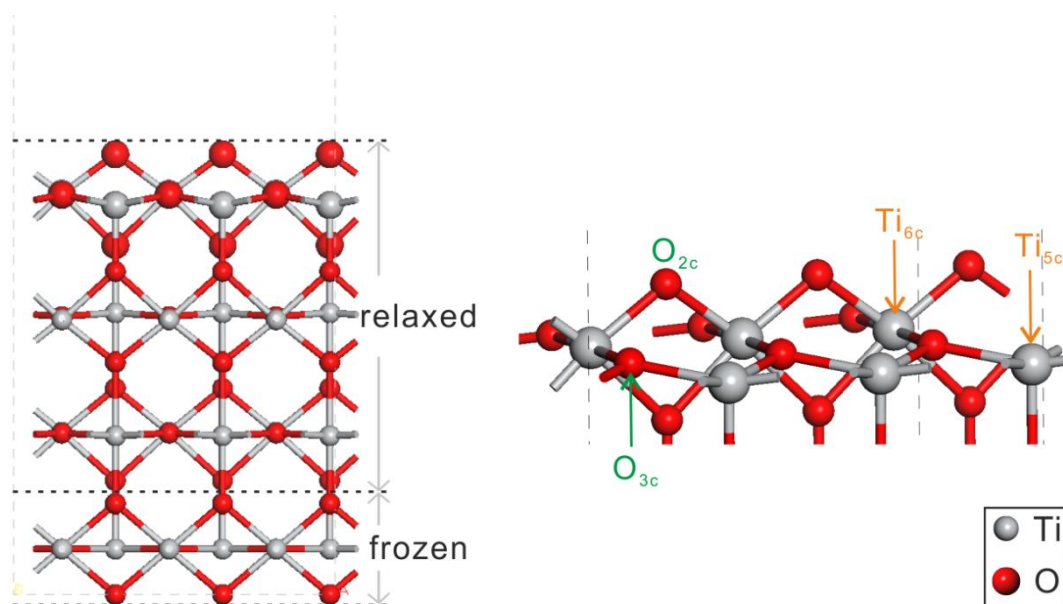


Figure 3.39. Side views of the Rutile TiO₂ (110) surface.

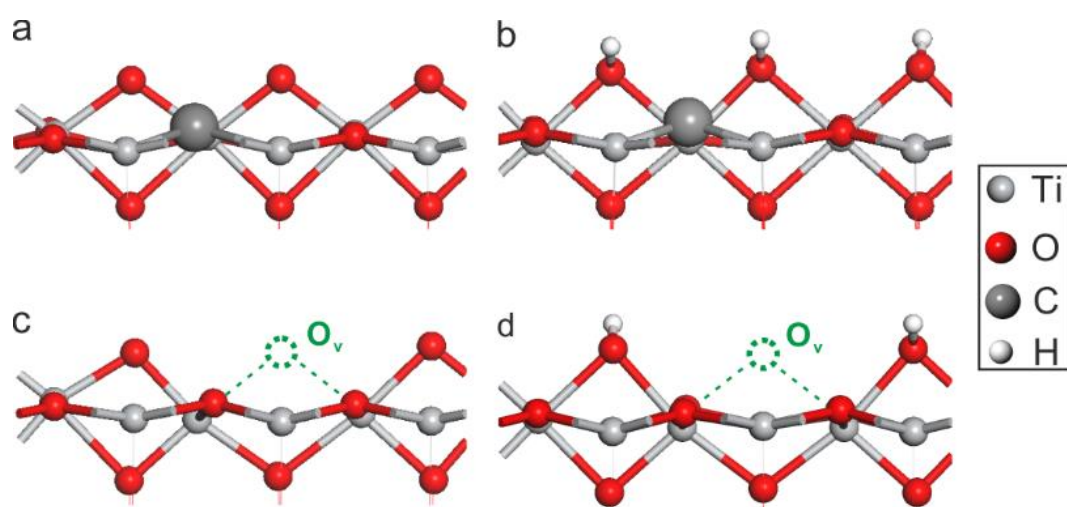


Figure 3.40. Side views of the optimized structures: (a) C doped O_{3c} of TiO₂ (110); (b) hydrogen saturated C-Ti_xO_y (110) (H at O_{2c}); (c) defect TiO₂ (110) with O_{2c} vacancy and (d) hydrogen saturated OVs-TiO₂ (110) (H at O_{2c}).

3. Enhanced electrocatalytic N₂ reduction via partial anion substitution in titanium oxide-carbon composites

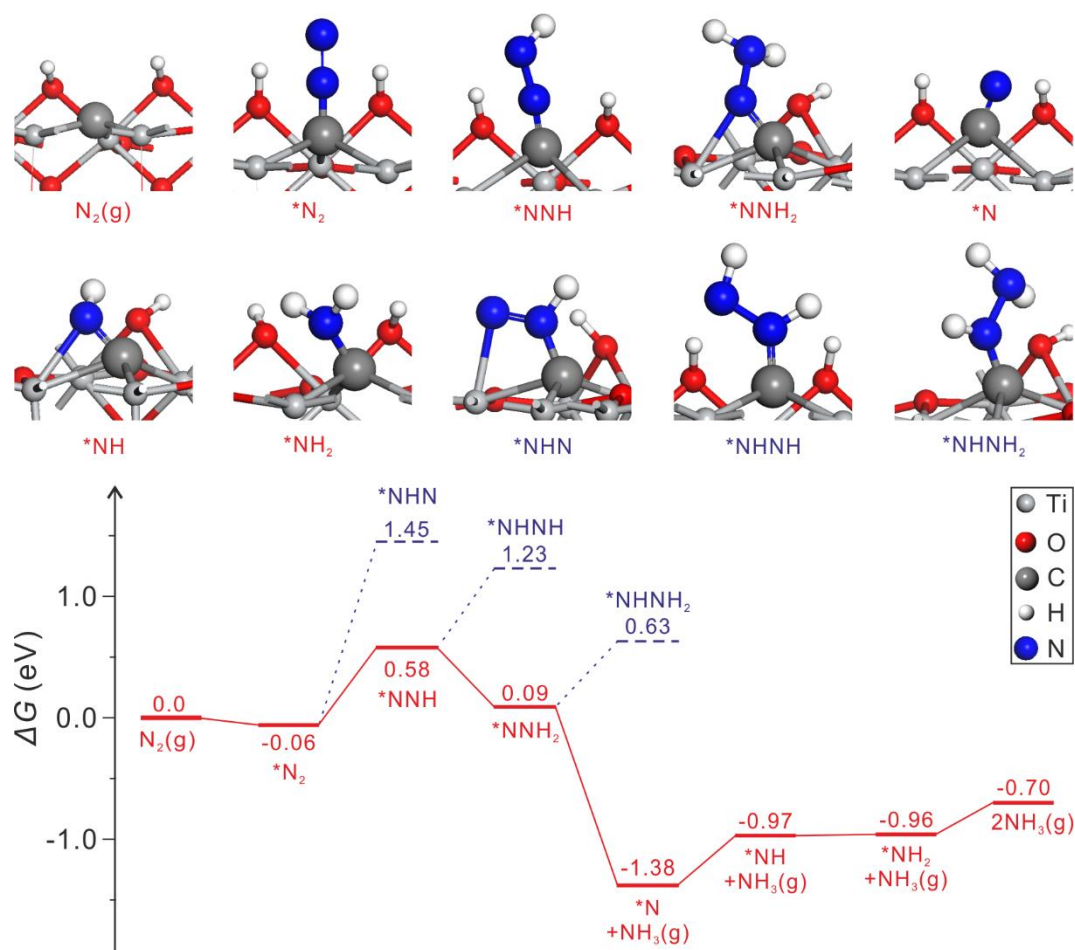


Figure 3.41. Free-energy diagram (298.15 K) for NRR on C-Ti_xO_y (110) surface and the optimized structures of different intermediates (red solid line for the more favored route and blue dotted line for the less favored route).

3. Enhanced electrocatalytic N₂ reduction via partial anion substitution in titanium oxide-carbon composites

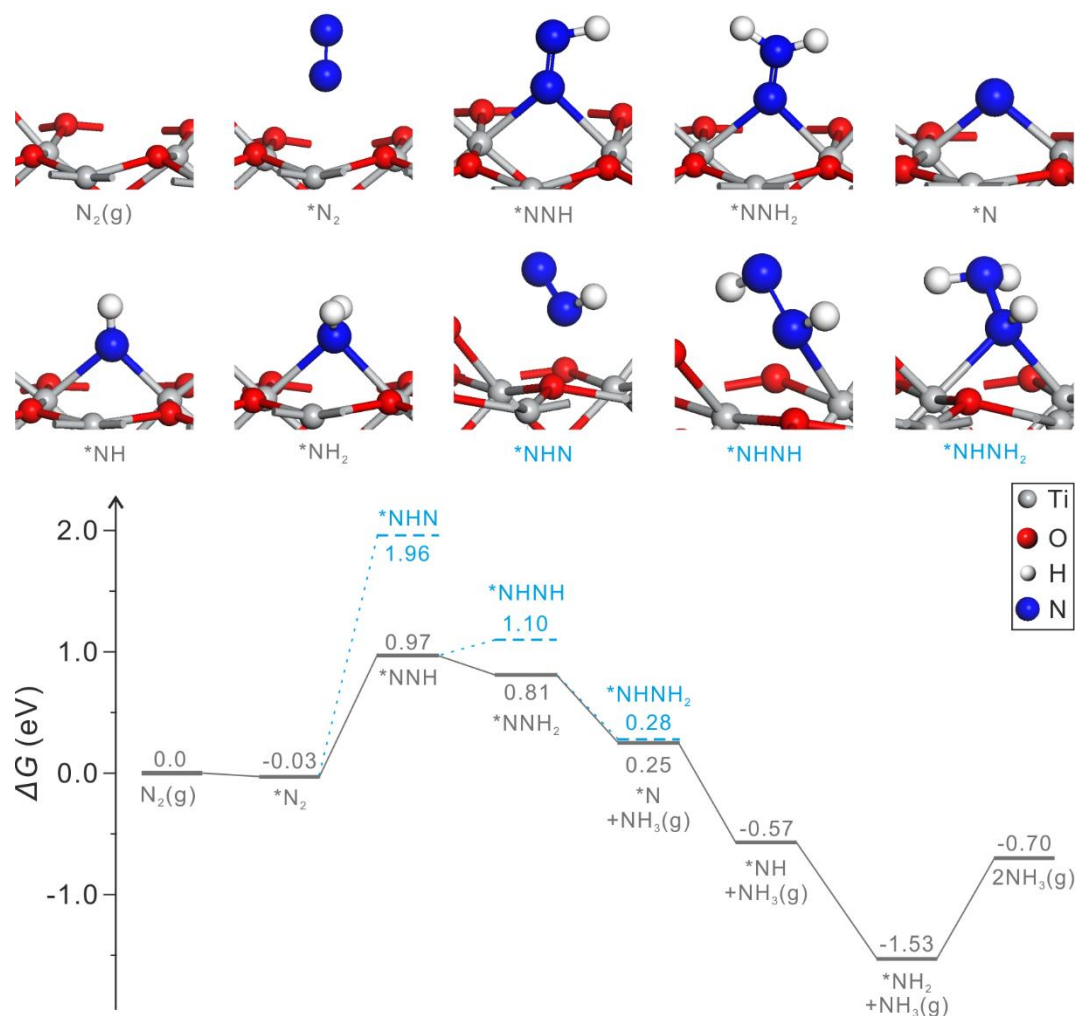


Figure 3.42. Free-energy diagram (298.15 K) for NRR on OV-TiO₂ (110) surface and the optimized structures of different intermediates (gray solid line for the more favored route and cyan dotted line for the less favored route).

According to the typical NRR distal pathway and the corresponding free energy diagram through the distal mechanisms of NRR on C-Ti_xO_y surface (Figure 3.43), N₂ is firstly adsorbed on the carbon site with an energy gain of -0.06 eV. It is also found that charge density difference between N₂ and C on the defect in C-Ti_xO_y is larger than that between N₂ and OVs in OV-TiO₂ (Figure 3.44). This clearly indicates that the doped carbon sites can more strongly activate N₂ and serve active sites for NRR. The key step of the first hydrogenation of C*N₂ to C*NNH is endergonic by 0.64 eV; and the N-N distance is elongated from 1.17 Å to 1.25 Å during this process. The subsequent formation of C*NNH₂ from C*NNH hydrogenation is exergonic by 0.49 eV. Similarly, this step is also accompanied by the elongation of the N-N distance from 1.25 Å to 1.36 Å. The next step, which involves the N-N dissociation as well the formation of surface N* and the first NH₃ gas molecule, is exergonic by 1.47 eV. The subsequent stepwise

3. Enhanced electrocatalytic N₂ reduction via partial anion substitution in titanium oxide-carbon composites

hydrogenation of surface C*N to surface C*NH and C*NH₂ as well the formation of the second NH₃ gas molecule is endergonic by 0.41, 0.01, and 0.26 eV, respectively.

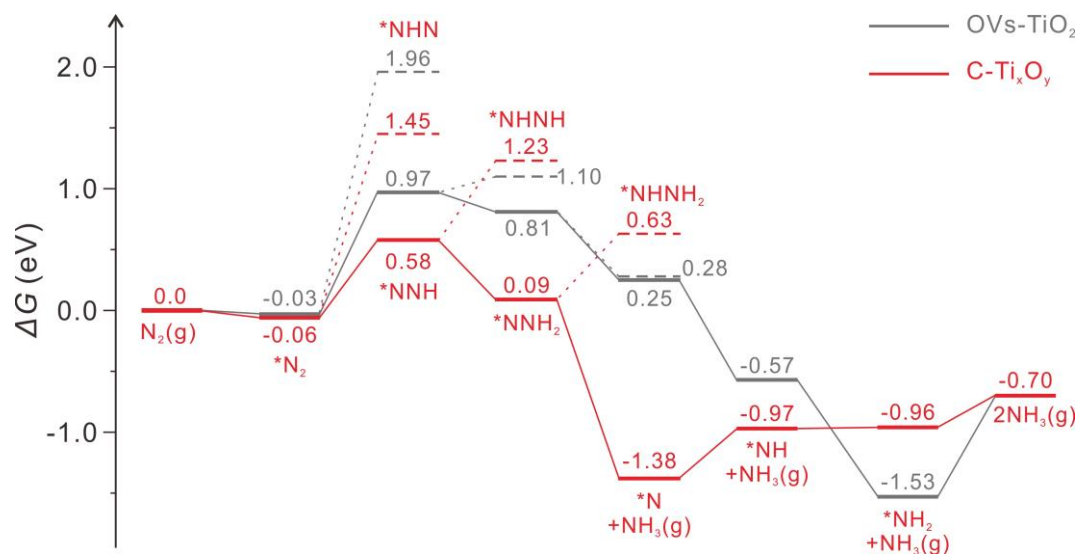


Figure 3.43. Free energy diagram (298.15 K) for NRR on C-Ti_xO_y (110) (red) and OV_s-TiO₂ (110) (gray) (solid line for the more favored route and dotted line for the less favored route on the corresponding surface).

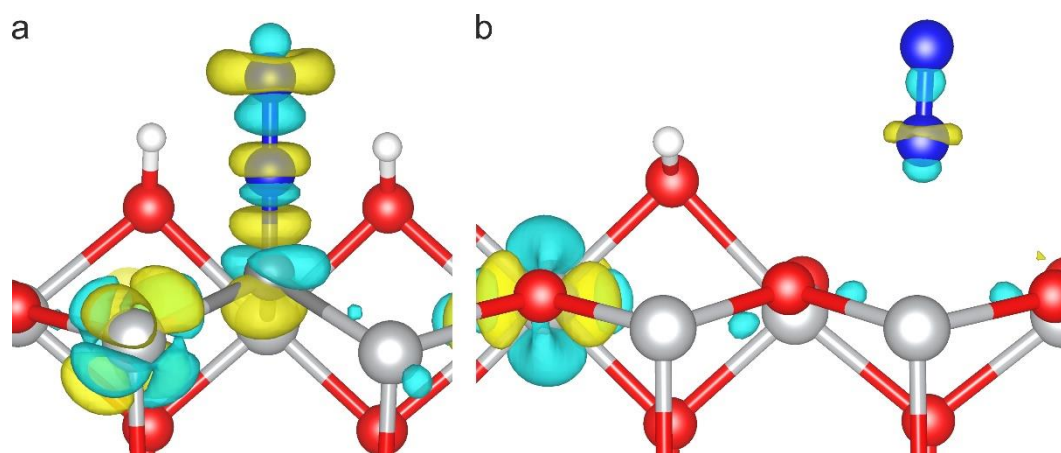


Figure 3.44. 3D isosurface of charge density difference of N₂ adsorption on (a) C-Ti_xO_y(110) and (b) OV_s-TiO₂, according to the equation $\Delta\rho = \rho(\text{N}_2/\text{surface}) - \rho(\text{surface}) - \rho(\text{N}_2)$, the isovalue is 0.01 |e|/Å³ (cyan stands for electron depletion and yellow for electron accumulation).

On the non-doped OV_s-TiO₂, a similar reaction path is found (Figure 3.42 and Figure 3.43). After the adsorption of N₂ on the surface (-0.03 eV), the formation of surface *NNH is endergonic by 1.00 eV, while the formation of surface *NNH₂ as well as *N and NH₃ gas molecule is exergonic by 0.16 and 0.56 eV, respectively. The subsequent hydrogenation of surface *N to surface *NH and *NH₂ is exergonic by 0.82 and 0.96 eV, respectively, while the formation of gas NH₃ molecule is endergonic by 0.83 eV.

3. Enhanced electrocatalytic N₂ reduction via partial anion substitution in titanium oxide-carbon composites

It is also worth to note that the *NHN, *NHNH and *NHNH₂ surface species have higher energy and are thus less stable than the corresponding *NNH, *NNH₂ and *N+NH₃ (g) intermediates (Figure 3.41), indicating that the formation of diazene (HN=NH) and hydrazine (H₂N-NH₂) is not favored thermodynamically which is in full agreement with the experimental observations.

Further comparison of the above reaction free energies on C-Ti_xO_y and OVs-TiO₂ demonstrates that the first step of N-H* formation is the potential-determining step in the electrochemical NRR; and most importantly C-Ti_xO_y is more active than OVs-TiO₂ (0.64 vs. 1.00 eV). Therefore, this advantageous low energy barrier on C-Ti_xO_y can significantly enhance the electrocatalytic activity for the NRR, which is in agreement with the experimental results.

In conclusion, a novel mode for activation of N₂ by the carbon-doped sites in the anion lattice of Rutile has been presented. An efficient NRR catalyst of C-Ti_xO_y/C nanocomposite has been developed via simple pyrolysis of MIL-125(Ti). The density of covalent Ti-C bonds originating from carbon atoms and OVs (which can both be active sites for NRR) can be regulated by the synthesis temperature. By comparing the NRR performance of M-Ts and by carrying out DFT calculations, it is found that the existence of (O-)Ti-C bonds in C-doped Ti_xO_y can largely improve the ability to activate and reduce N₂ as compared to unoccupied OVs in TiO₂. Given by the development of nanotechnology, the strategy of rationally dope heteroatoms into the anion lattice of transition metal oxides to create active centers may open many new opportunities beyond the use of noble metal-based catalysts for other reactions that require the activation of small molecules as well.

4. Single-site gold catalysts on hierarchical N-doped porous noble carbon for enhanced electrochemical reduction of nitrogen

Based on previous reports, Au is considered as one of the most effective catalysts for NRR due to its high affinity and ability to activate N₂ as well as its generally low tendency of hydrogen formation.¹⁷⁶⁻¹⁷⁹ Considering practical applications for low cost and as much as exposed active sites per unit mass of the catalysts, it is desirable to minimize the utilization of metal and create single active sites. Single site catalysts are also potential to further improve the NRR performance because of their theoretically perfect atom utilization for N₂ adsorption and activation.¹⁸⁰⁻¹⁸² However, such single sites require a suitable substrate on which they can be stabilized. N-doped porous carbons (NDPCs) are a particularly attractive substrate for the formation of single sites due to their high surface area, high porosity, and abundant N species which provide large possibilities to anchor and stabilize single sites.¹⁸³⁻¹⁸⁵ In contrast to heteroatom-free porous carbons, NDPCs stand out due to their “noble” character (i.e, they can oxidize material rather than being oxidized) and can thus stabilize single metal sites even at high loadings. On the other hand, such highly polarizable porous supports can improve the N₂ adsorption and mass transfer as well.¹⁸⁶ Especially in the presence of additional single metal Lewis acidic ions, electron-rich nitrogen and/or carbon atoms within noble carbons can act as Lewis basic sites, leading to FLPs and potentially strong activation of N₂ molecules by their strong electronic polarization.

To the best of my knowledge, the experimental investigation of single sites fixed at NDPCs supports in electrochemical NRR has not been reported yet. Here, a novel catalyst composed of Au single sites supported on N-doped carbons (denoted as AuSAs-NDPCs), which is characterized by a charming and stable NRR performance at comparably high NH₃ production rate is reported.

Term of use: This chapter is adapted with permission from my own original work:
[1] Qin, Q., Heil, T., Antonietti, M., Oschatz, M. Single - Site Gold Catalysts on Hierarchical N - Doped Porous Noble Carbon for Enhanced Electrochemical Reduction of Nitrogen. <i>Small Methods</i> 2018 , 2, 1800202. Published by John Wiley & Sons.
[2] Walczak, R.; Kurpil, B.; Savateev, A.; Heil, T.; Schmidt, J.; Qin, Q.; Antonietti, M.; Oschatz, M. <i>Angew. Chem. Int. Ed.</i> 2018 , 130, 10926. Published by John Wiley & Sons.

4. Single-site gold catalysts on hierarchical N-doped porous noble carbon for enhanced electrochemical reduction of nitrogen

4.1. Synthesis and characterization of AuSAs-NDPCs

NDPCs were first synthesized by a template-assisted method. In a typical synthesis, hexaazatriphenylene-hexacarbonitrile (HAT) was coated on SiO₂ nanospheres (Figure 4.1) by dispersing both in a mixture of acetonitrile and water. The light yellow solid was then collected by centrifugation after stirring at room temperature for 6 h. Condensation of HAT under N₂ flow at 900 °C and subsequent wet-chemical silica removal resulted in hollow, foam like catalytic frames with ultrathin N-doped carbon walls and good accessibility of all potential catalytic sites (Figure 4.2).

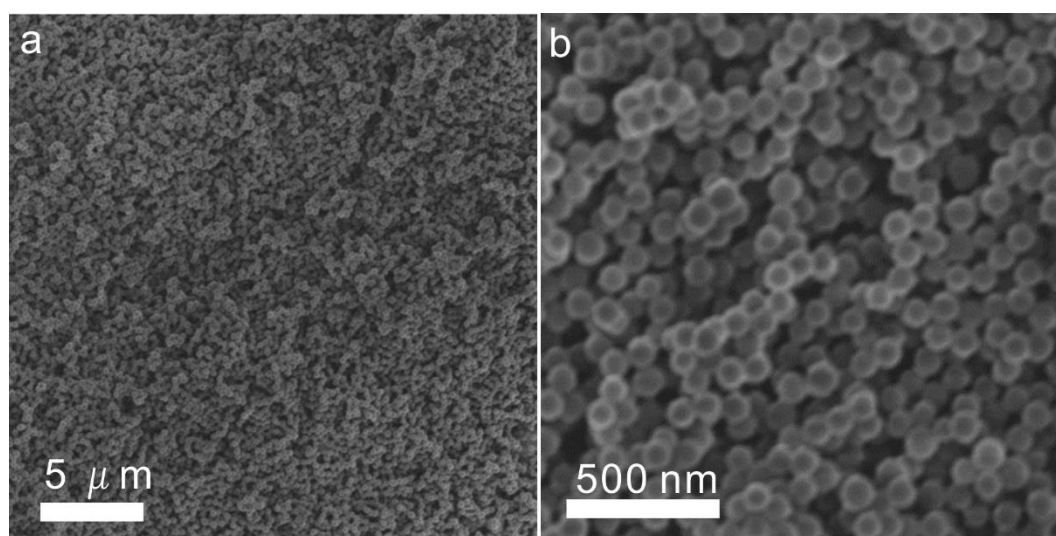


Figure 4.1. Representative SEM images of SiO₂ nanospheres.

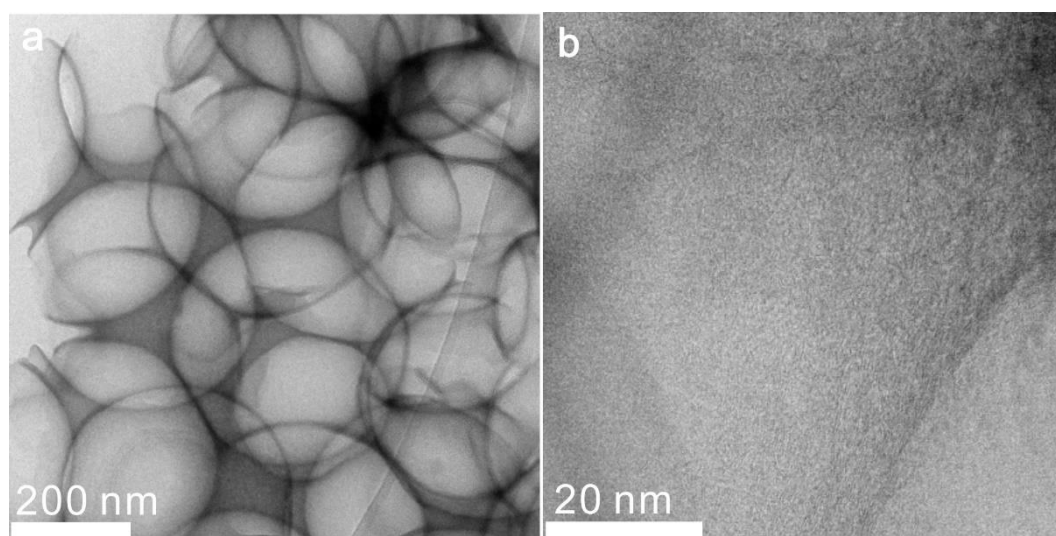


Figure 4.2. Representative TEM images of NDPCs.

4. Single-site gold catalysts on hierarchical N-doped porous noble carbon for enhanced electrochemical reduction of nitrogen

The homogeneous distribution of carbon and nitrogen is demonstrated by the energy-dispersive X-ray spectroscopy (EDX) mapping (Figure 4.3). A N content of 9.2 wt.% is determined by elemental analysis. X-ray diffraction (XRD) patterns (Figure 4.4a) exhibit only two broad carbon peaks at 26° (002) and 44° (101), which demonstrates the high purity and amorphous phase of the as-obtained HAT-carbon which is in agreement with a recent study.¹⁸⁷ N_2 physisorption experiments show a specific surface area (SSA) of around $979 \text{ m}^2 \text{ g}^{-1}$ (Figure 4.4b). The total pore volume is $0.66 \text{ cm}^3 \text{ g}^{-1}$. The shape of the isotherm with significant N_2 uptakes at low and high relative pressure clearly show the hierarchical character of the NDPCs including narrow micropores from tectonically controlled HAT condensation and larger pores from the silica template spheres. All the above mentioned of NDPCs provides innate advantages for the further coating of single sites and electrocatalysis.

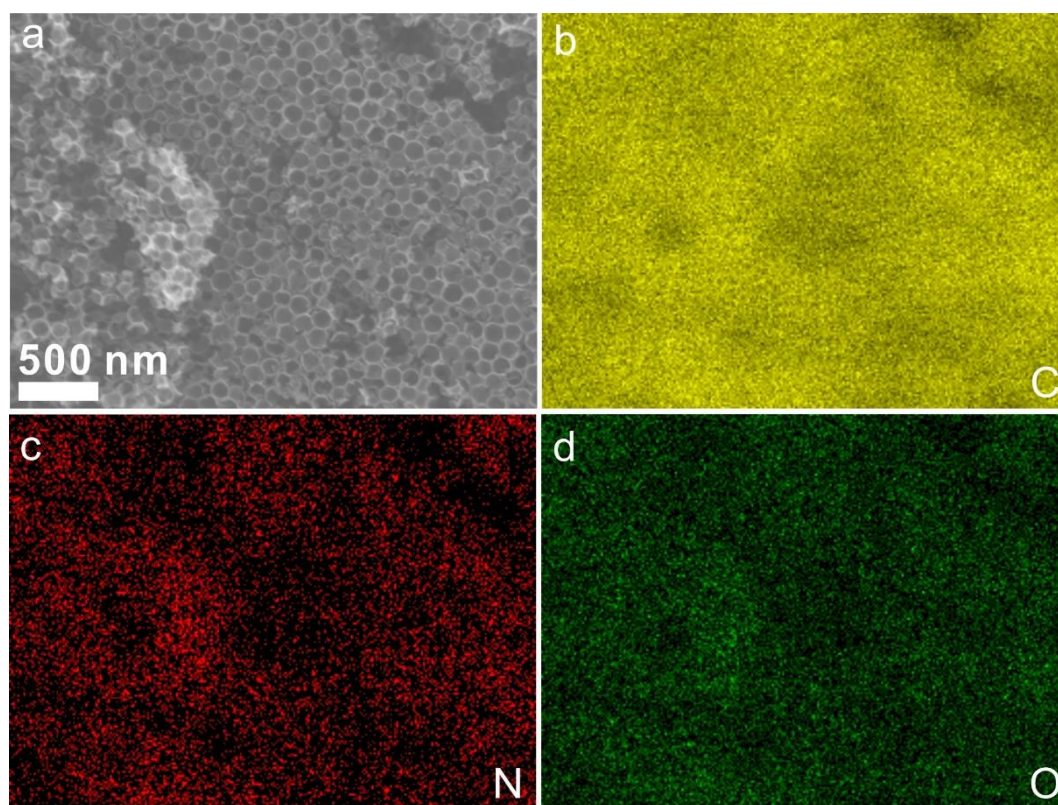


Figure 4.3. (a) SEM image and (b-d) EDX mapping images of NDPCs.

4. Single-site gold catalysts on hierarchical N-doped porous noble carbon for enhanced electrochemical reduction of nitrogen

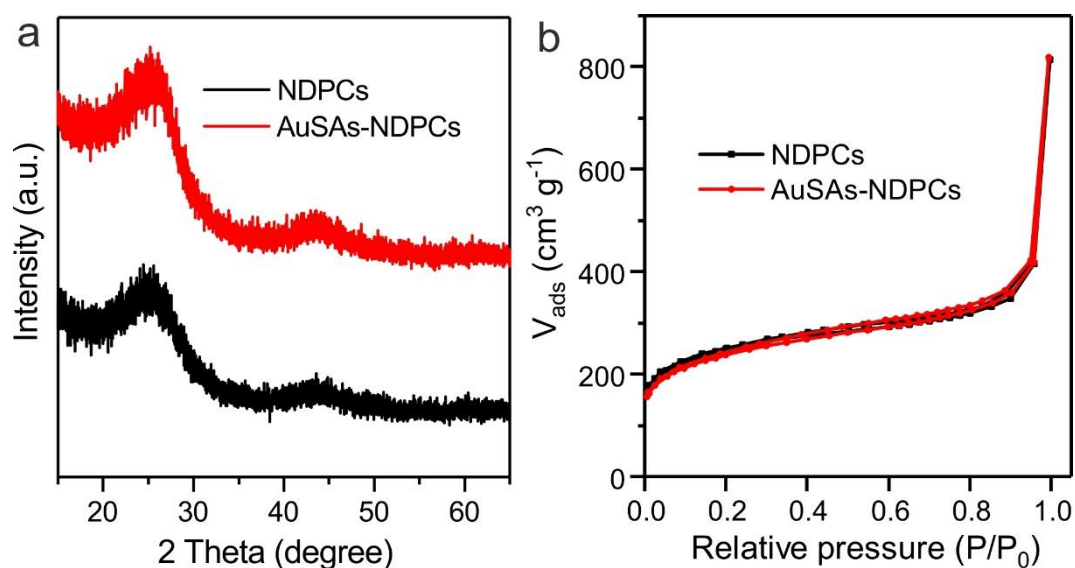


Figure 4.4. (a) XRD patterns and (b) N₂ physisorption isotherms (measured at -196 °C) of NDPCs and AuSAs-NDPCs.

AuSAs-NDPCs were synthesized by a simple impregnation method.¹⁸⁸ As-prepared NDPCs were mixed with a HAuCl₄ aqueous solution under continuous stirring for 7 h followed by subsequent annealing at 250 °C for 1 h under reductive Ar/H₂ (with 5 % of H₂ content) atmosphere. The morphology of AuSAs-NDPCs was characterized by high-angle annular dark-field scanning transmission electron microscopy (HAADF-STEM). As-obtained catalysts still show the open spherical porous structure of the initial NDPCs (Figure 4.5a), but no obvious Au nanoparticles or clusters can be observed (Figure 4.5b-c). Moreover, according to the high magnification STEM images (Figure 4.5d), isolated bright dots (Au single sites) are well-dispersed on the surface of NDPCs (Figure 4.6 for more details).

4. Single-site gold catalysts on hierarchical N-doped porous noble carbon for enhanced electrochemical reduction of nitrogen

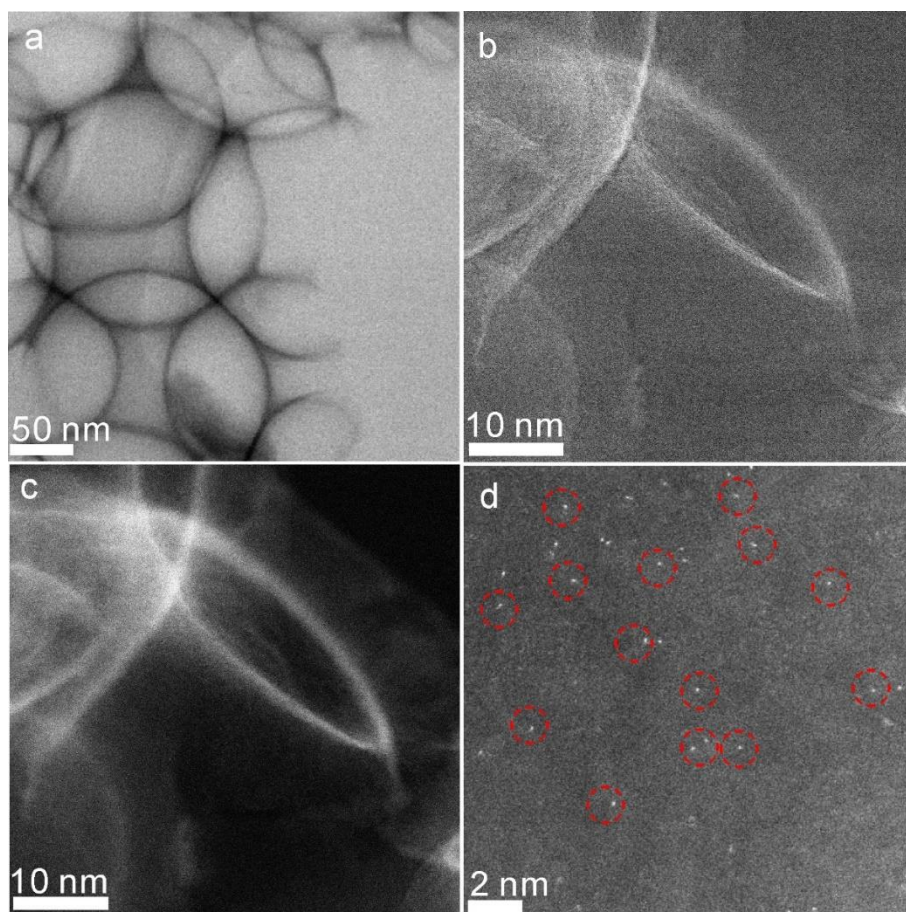


Figure 4.5. (a) Representative TEM image of AuSAs-NDPCs. (b) Aberration-corrected STEM image in bright field mode. (c) Aberration-corrected STEM image in dark field mode. (d) High magnification HAADF-STEM image, showing that only Au single species are present.

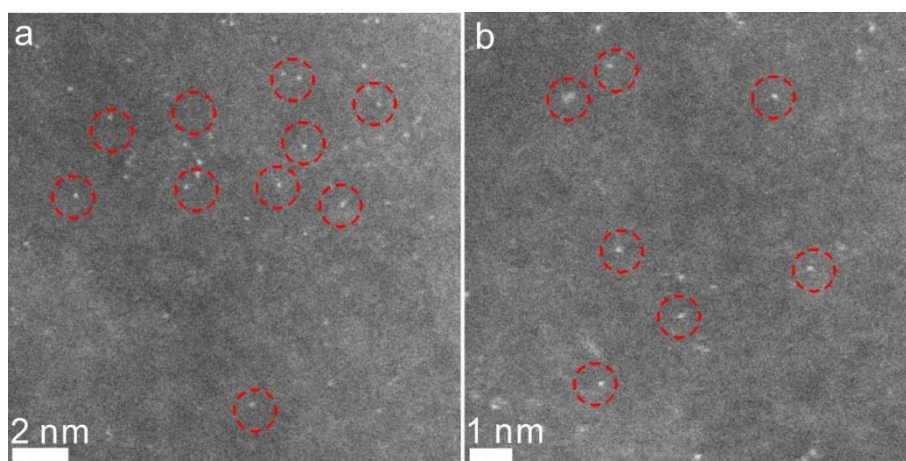


Figure 4.6. HAADF-STEM images of AuSAs-NDPCs catalysts in different areas. The high magnification images clearly reveal the presence of isolated single sites (indicated by the white dots).

4. Single-site gold catalysts on hierarchical N-doped porous noble carbon for enhanced electrochemical reduction of nitrogen

The actual mass percentage of Au in AuSAs-NDPCs is 0.205 wt.%, which has been detected by inductively coupled plasma-atomic emission spectrometry (Table 4.1). In addition, the absence of crystalline Au is confirmed by the XRD patterns (Figure 4.4a), while the SSA of the NDPCs remains almost unchanged after Au decorating (Figure 4.4b). When the Au mass loading was increased to 0.713 wt.% (Table 4.1), Au nanoparticles with the size of around 10-20 nm emerged (Figure 4.7a). Their presence can be further confirmed by the presence of a diffraction peak corresponding to metallic Au (111) after reduction (Figure 4.7b).

Table 4.1. Au loadings determined by ICP-AES.

	AuSAs-NDPCs	AuNPs-NDPCs	AuNPs-STCs
Actual (wt.%)	0.205	0.713	0.196

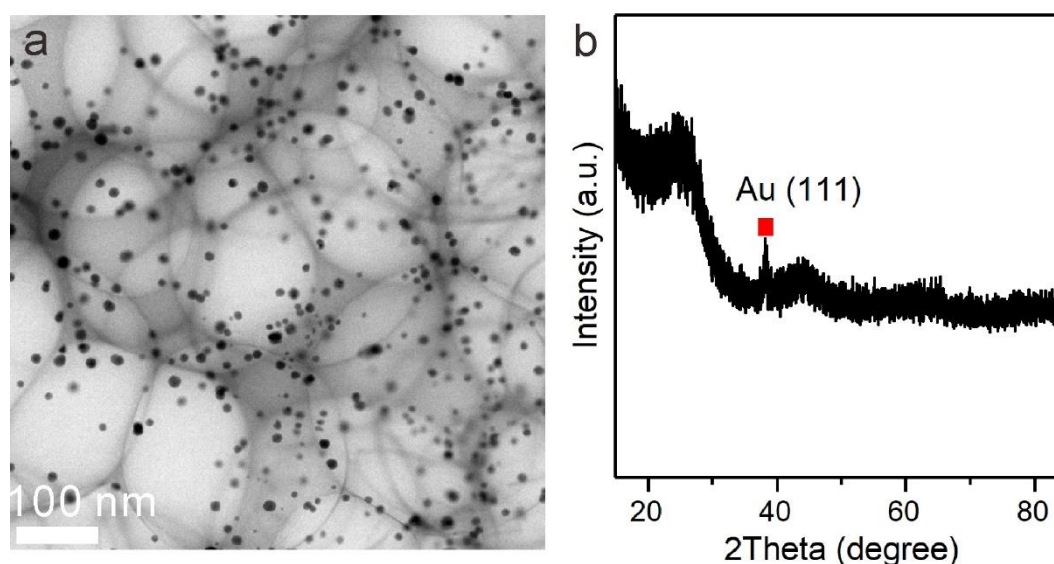


Figure 4.7. (a) Representative TEM images and (b) XRD pattern of AuNPs-NDPCs.

X-ray photoelectron spectroscopy (XPS) measurements of Au 4f in AuSAs-NDPCs (Figure 4.8) demonstrate the existence of Au species with a binding energy of electrons higher than in the metallic Au particles of AuNPs-NDPCs.¹⁸⁰ That means that noble NDPCs are stronger electron acceptors than Au atoms. i.e., they do indeed have a higher standard electrode potential than Au. It is imagined that the Au may not be fully ionized but that the electron density on these single sites is still lower than on an Au atom but higher than on an Au ion due to electron transfer from the Au “cation” to the support “anion”.

4. Single-site gold catalysts on hierarchical N-doped porous noble carbon for enhanced electrochemical reduction of nitrogen

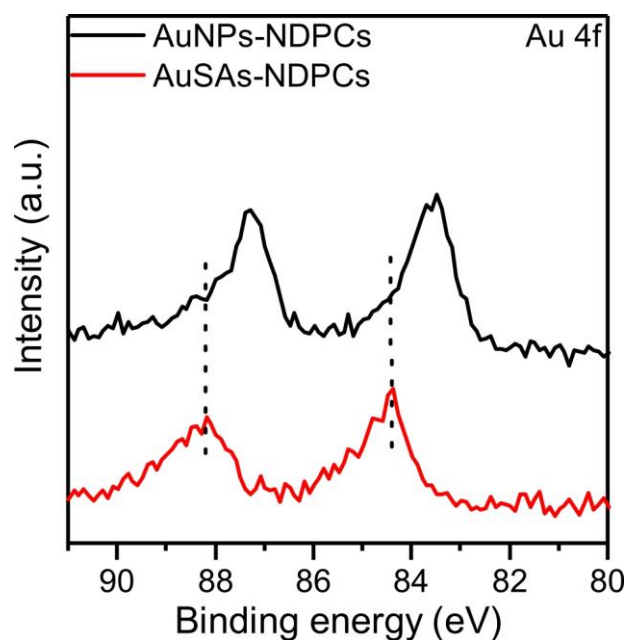


Figure 4.8. XPS spectra of Au 4f obtained from AuSAs-NDPCs and AuNPs-NDPCs.

Deconvolution of the C 1s line scans (Figure 4.9a) reveals the presence of graphitic C-C carbons at ~284 eV, sp^2 -hybridized carbons bounded to N atoms at ~286 eV, and oxidized carbon atoms at ~290 eV, with the binding energy all shift to slightly higher values in presence of single Au sites, as compared with NDPCs. Considering the low over-all Au content, this shift is remarkable. The same phenomenon is also observed in N 1s spectra (Figure 4.9b), which can be assigned to cyano- (~398 eV), pyrazine groups (~399 eV), quaternary N atoms (~400–401 eV) and oxidized N atoms (~402–403 eV).¹⁸⁹ Thus, the lower electron density of the C and N atoms in AuSAs-NDPCs indicate the strong electronic interaction of Au atoms with C and N atoms.¹⁹⁰

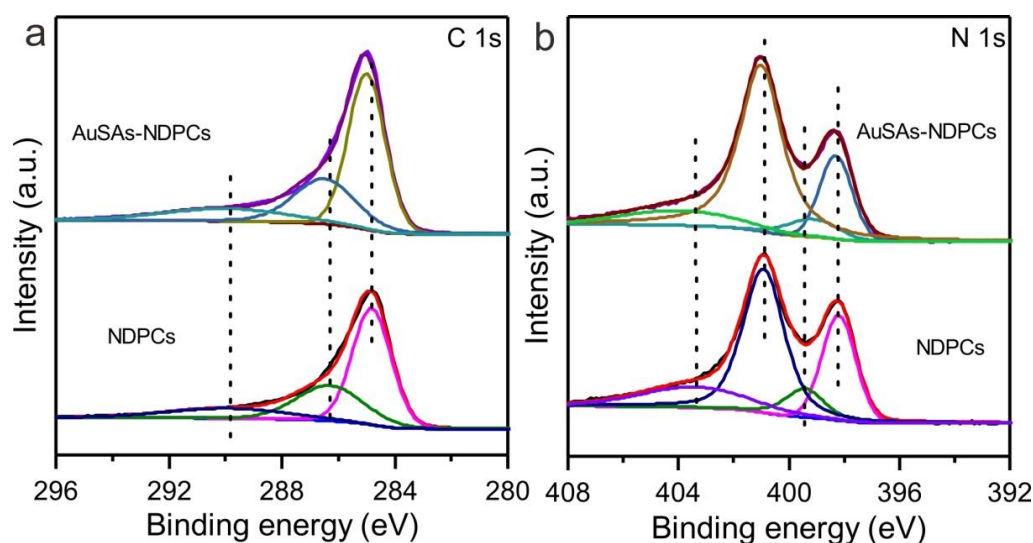


Figure 4.9. XPS spectra of (a) C 1s and (b) N 1s obtained from AuSAs-NDPCs and NDPCs.

4. Single-site gold catalysts on hierarchical N-doped porous noble carbon for enhanced electrochemical reduction of nitrogen

To further confirm the importance of heteroatom-sites, nitrogen-free salt-templated carbons (STCs) with SSA of $1130 \text{ m}^2 \text{ g}^{-1}$ (Figure 4.10a) were used as reference supports instead of N-doped carbons. Unlike in NDPCs, obvious XRD patterns of Au appeared (Figure 4.10b) at almost similar Au loading (the actual loading) as in AuSAs-NDPCs (Table 4.1), in line with TEM results (Figure 4.10c). Based on these results, the combination of large surface area and abundant accessible N species are crucial for the deposition and stabilization of Au single sites on the carbon supports.

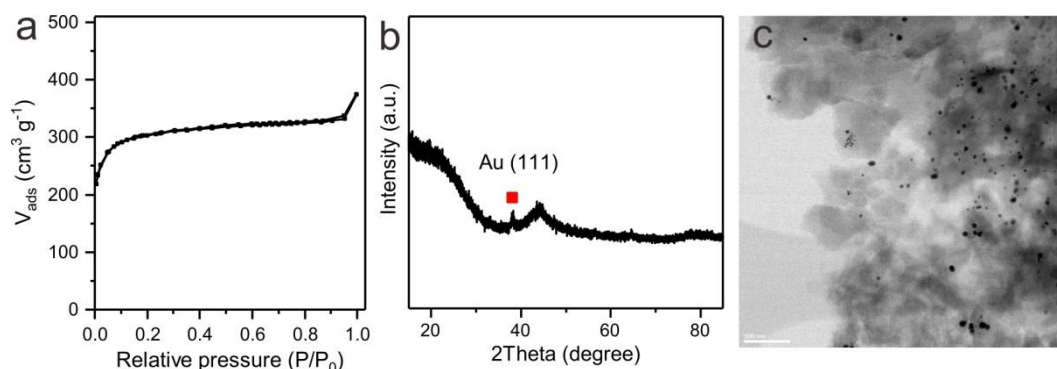


Figure 4.10. (a) N_2 physisorption isotherms (measured at -196°C) of STCs. (b) XRD pattern and (c) TEM images of AuNPs-STCs.

4.2. Influence of Au single sites on the NRR performance

In view of the unique structure of AuSAs-NDPC, its NRR performance has been investigated by using a two-compartment cell with three-electrode system. AuSAs-NDPCs catalysts were first coated on carbon paper as a working electrode. Linear sweep voltammetry (LSV) tests were performed in Ar and N_2 -saturated 0.1 M HCl aqueous solution ($\text{pH}=1$). The LSV curve in N_2 clearly differs from that in Ar (Figure 4.11), which means that there is a significant response of the AuSAs-NDPCs electrode to the presence of dissolved N_2 .

4. Single-site gold catalysts on hierarchical N-doped porous noble carbon for enhanced electrochemical reduction of nitrogen

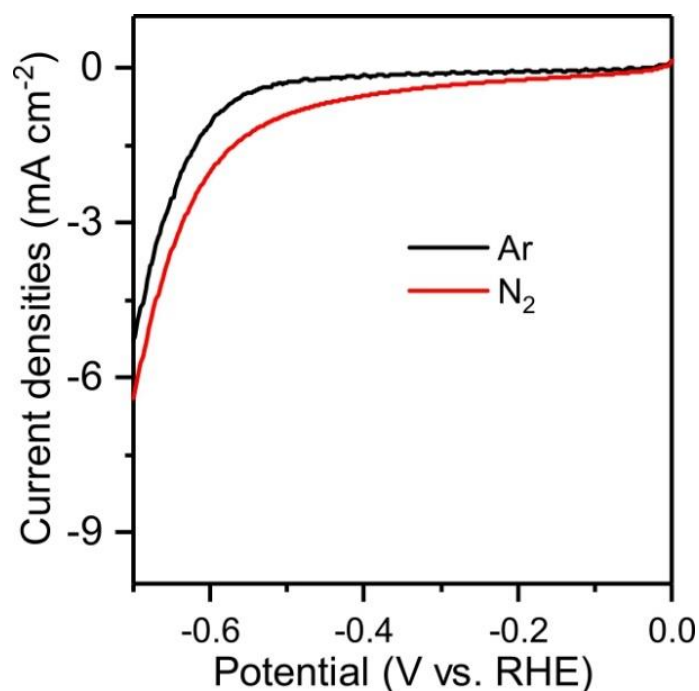


Figure 4.11. LSV curves of the AuSAs-NDPCs electrode in an N₂-saturated (black line) and Ar-saturated (red line) aqueous solution of 0.1 M HCl under ambient conditions.

Furthermore, controlled electrolyses (Figure 4.12a) were performed under different given potentials for 2 h to quantify the product concentration. NH₃ yields and corresponding Faradaic efficiencies have been calculated (Figure 4.12b) by UV-Vis spectroscopy after recording NH₄⁺ calibration curves (Figure 4.13). An ammonia production rate of 2.32 μg h⁻¹ cm⁻² with the maximum Faradaic efficiency of 12.3% for NH₃ was achieved at -0.2 V vs. RHE, as shown in the corresponding optical image by an obvious colour change before and after electrolysis (Figure 4.14). Regarding the very low local concentration of N₂ caused by its low solubility in water (which could even cause this reaction to be in a diffusion controlled mode), these Faradaic efficiencies and NH₃ yield are remarkable. With the increase of negative potential, Faradaic efficiency and NH₃ yield largely decreased due to the predominance of HER, which was also demonstrated by the sharply increasing current densities in LSV curves.¹⁹¹

4. Single-site gold catalysts on hierarchical N-doped porous noble carbon for enhanced electrochemical reduction of nitrogen

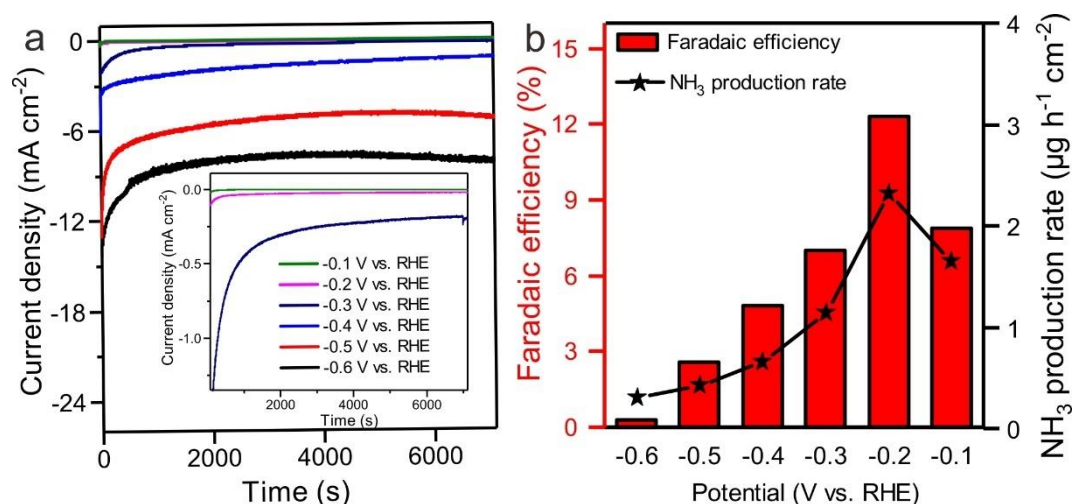


Figure 4.12. (a) Chronoamperometry results of the AuSAs-NDPCs electrode at different given potentials. (b) Faradaic efficiency (red) and production rate of NH₃ at the corresponding potentials.

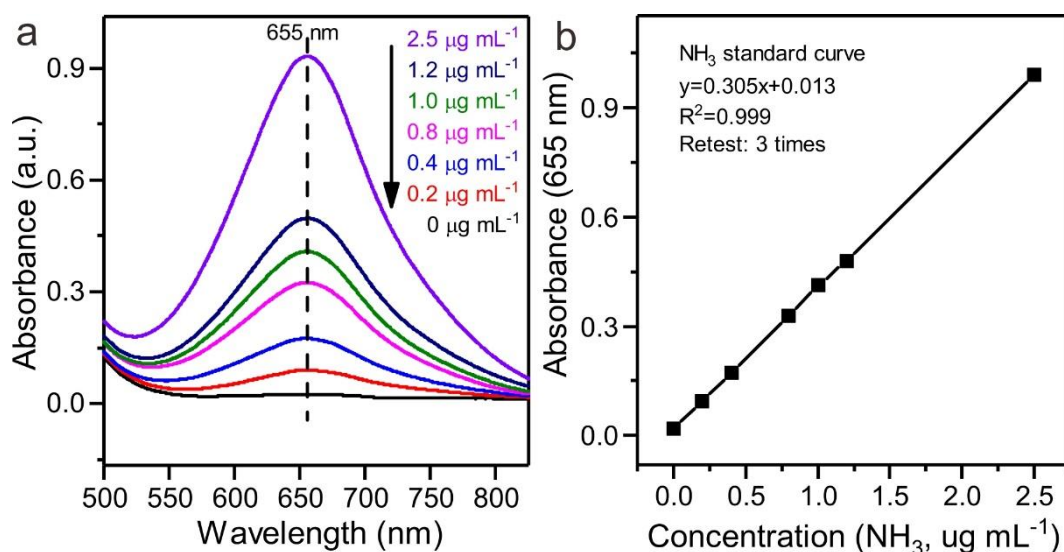


Figure 4.13. (a) UV-Vis spectroscopy curves of different ammonium chloride solutions with known concentration by using indophenol blue method, and the absorbance at 655 nm was referred to the concentration of NH₄⁺. (b) The corresponding calibration curve used for estimating as-obtained NH₃ by NH₄⁺ ion concentration, and the fitting curve exhibits good linear relation ($y = 0.305x + 0.013$, $R^2 = 0.999$) of three times independent calibration curves.

4. Single-site gold catalysts on hierarchical N-doped porous noble carbon for enhanced electrochemical reduction of nitrogen

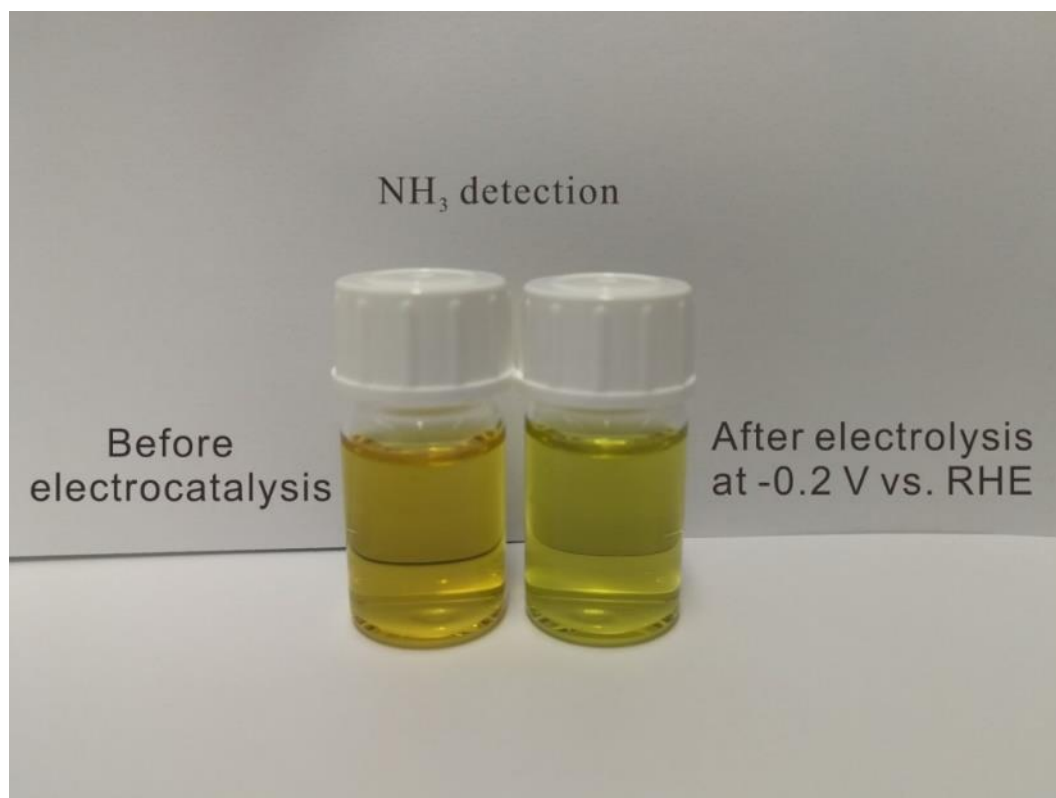


Figure 4.14. Optical image of the 0.1 M HCl electrolytes detected using indophenol indicator before and after a 2 h NRR test on the AuSAs-NDPCs electrode at -0.2 V vs. RHE.

Besides, there is no NH₃ produced from Ar-saturated electrolyte from -0.1 V to -0.6 V vs. RHE (Figure 4.15), indicating NH₃ formation solely from N₂ dissolved into the electrolyte and not from the nitrogen atoms bonded in the AuSAs-NDPCs electrode. NRR under different temperatures was also conducted at -0.2 V vs. RHE (Figure 4.16a). Faradaic efficiency and NH₃ yield both increase with increasing reaction temperature (Figure 4.16b) due to higher reaction rate according to the Arrhenius equation.¹⁹²

4. Single-site gold catalysts on hierarchical N-doped porous noble carbon for enhanced electrochemical reduction of nitrogen

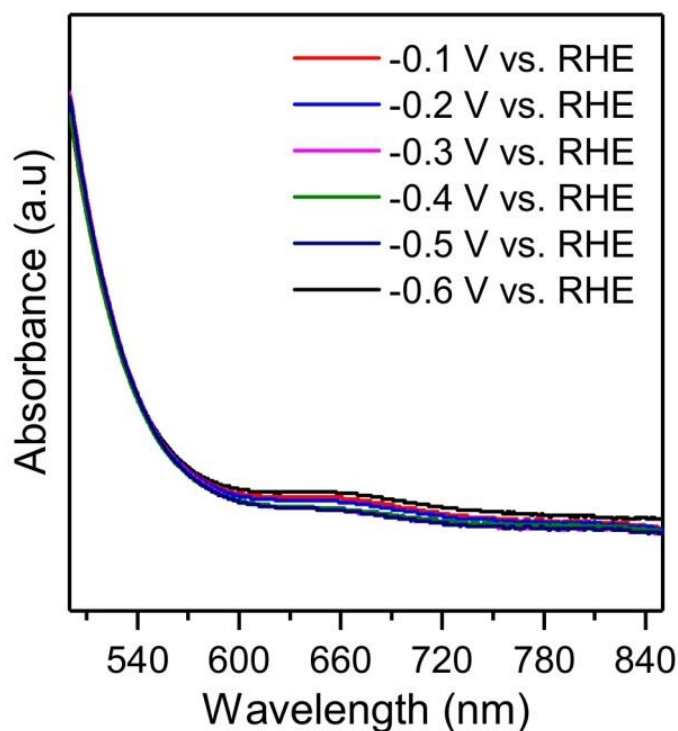


Figure 4.15. UV-Vis absorption spectra of the Ar-saturated 0.1 M HCl solution with indophenol indicator after electrolysis on the AuSAs-NDPCs electrode at different potentials for 2 h.

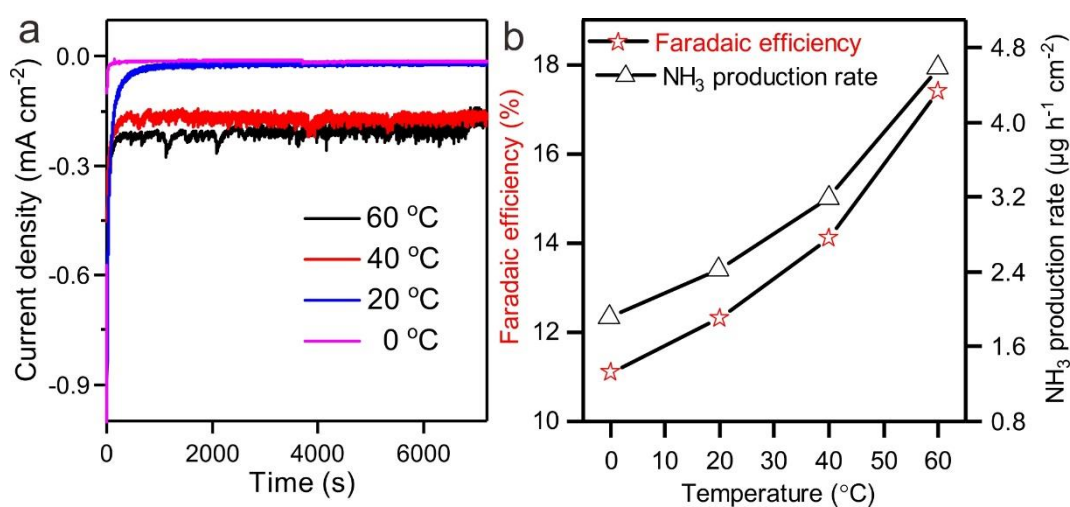


Figure 4.16. (a) Chronoamperometry results and (b) Faradaic efficiency and NH₃ yield plotted against temperature of the electrocatalytic test at -0.2 V vs. RHE of AuSAs-NDPCs catalysts in the temperature range from 0 °C to 60 °C.

4. Single-site gold catalysts on hierarchical N-doped porous noble carbon for enhanced electrochemical reduction of nitrogen

Besides the good activity, stability is also really important to value an electrocatalyst. After a recycling test for 6 times (Figure 4.17a), there is no obvious decrease of Faradaic efficiency and NH_3 yield for AuSAs-NDPCs (Figure 4.17b). Chronoamperometry test at -0.2 V vs. RHE for 50000 seconds and the LSV curve after it show no obvious decrease of the current densities (Figure 4.18), while TEM clearly shows that Au is still present as single species with no significant agglomeration after this test (Figure 4.19). NH_3 production over reaction time also demonstrates the good stability of as obtained AuSAs-NDPCs (Figure 4.20).

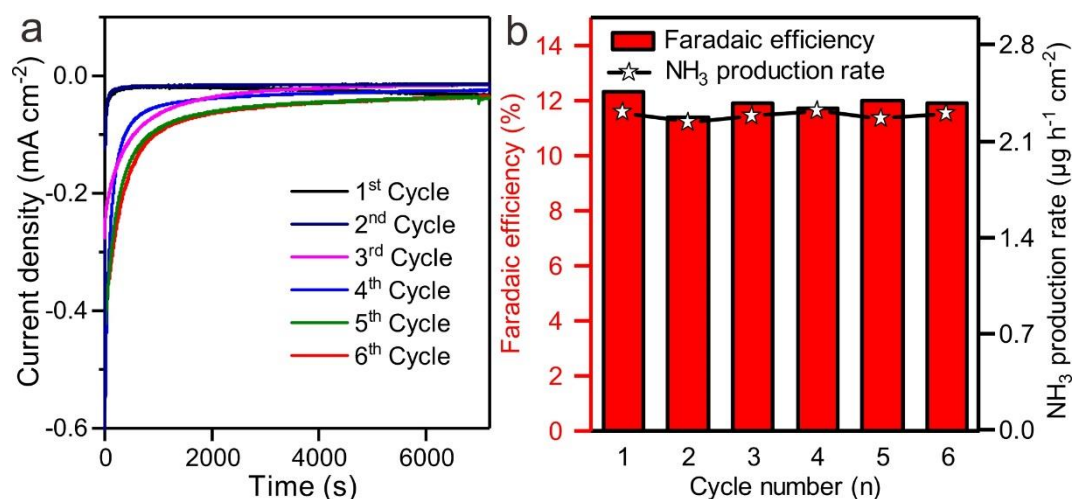


Figure 4.17. (a) Chronoamperometry results of AuSAs-NDPCs electrode for a stability test recorded at the potential of -0.2 V vs. RHE. (b) Faradaic efficiency and NH_3 production rate during the recycling test.

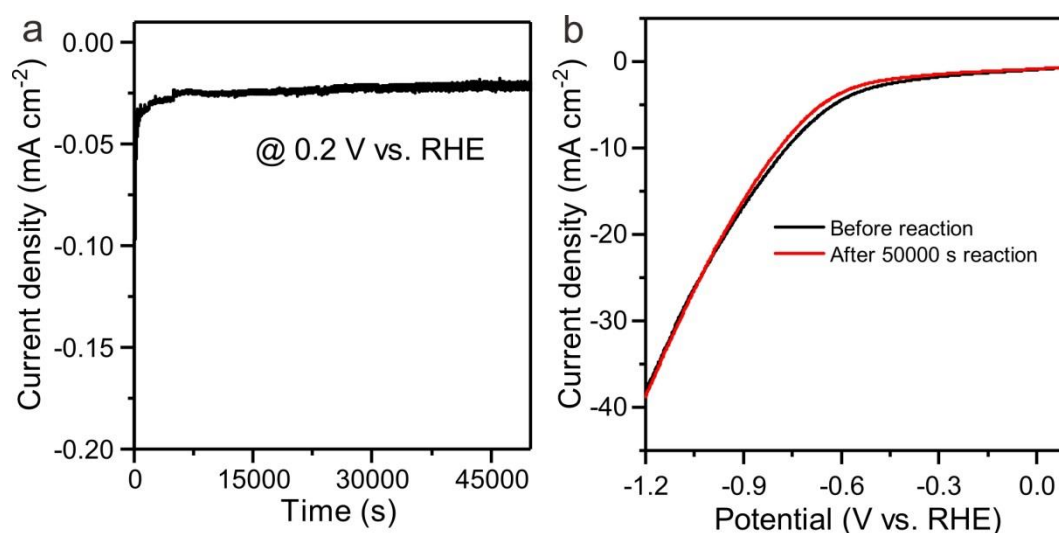


Figure 4.18. (a) Chronoamperometry test at the potential of -0.2 V vs. RHE for 50000 s and (b) LSV curves before and after chronoamperometry test using AuSAs-NDPCs catalysts.

4. Single-site gold catalysts on hierarchical N-doped porous noble carbon for enhanced electrochemical reduction of nitrogen

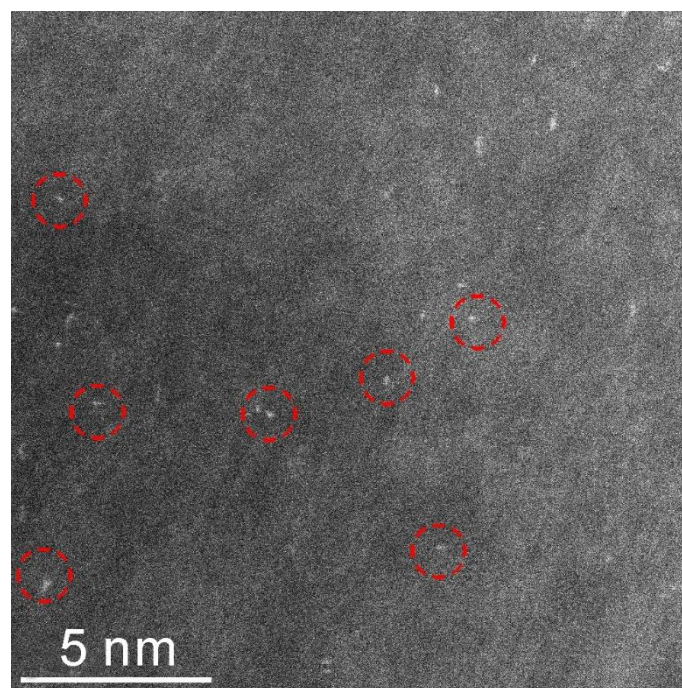


Figure 4.19. HADF-STEM images of AuSAs-NDPs catalysts after chronoamperometry test at the potential of -0.2 V vs. RHE for 50000 s.

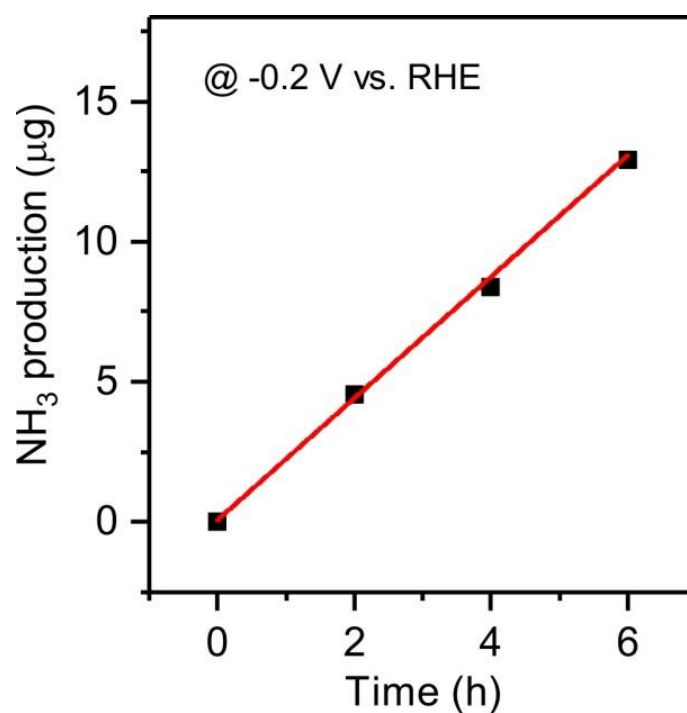


Figure 4.20. The curve of NH₃ production vs. reaction time on the AuSAs-NDPCs electrode at -0.2 V vs. RHE.

To better understand the specific advantages of Au single sites, the NRR test was also conducted for AuNPs-NDPCs and pure NDPCs. Compared with AuSAs-NDPCs, Faradaic efficiency of

4. Single-site gold catalysts on hierarchical N-doped porous noble carbon for enhanced electrochemical reduction of nitrogen

the AuNPs-NDPCs catalysts decreases to 5.7 % at -0.2 V vs. RHE (Figure 4.21). Likewise, as-prepared AuNPs-STC also shows a decreased Faradaic efficiency of 4.5% at the same potential (Figure 4.21). Metal-free NDPCs without Au could only reach the highest Faradaic efficiency of 2.1% at the potential of -0.6 V vs. RHE (Figure 4.22). Compared with AuSAs-NDPCs, the potential with the maximum FE of NDPCs shifts negatively, which might be attributed to the weaker N₂ activation ability with only N species. The corresponding UV-Vis adsorption spectra of catalytic products (Figure 4.23) further confirm the excellent performance of AuSAs-NDPCs.

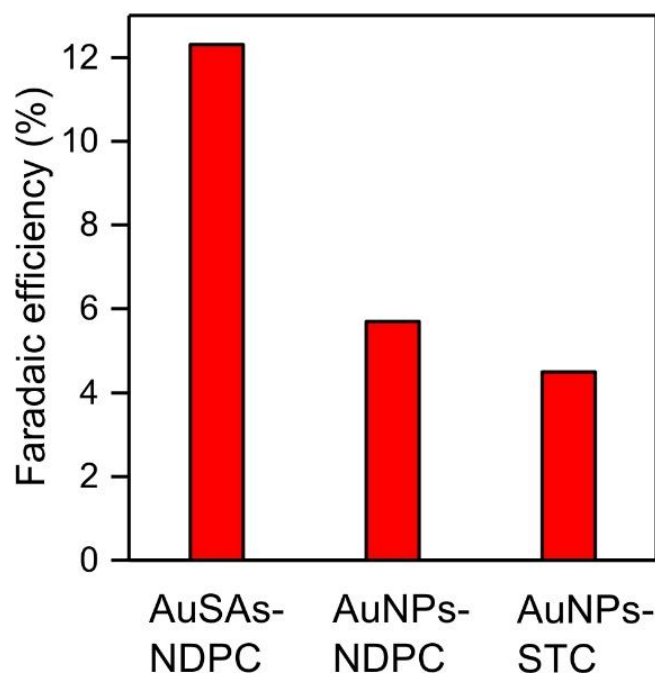


Figure 4.21. Faradaic efficiency of NH₃ with different catalysts at -0.2 V vs. RHE.

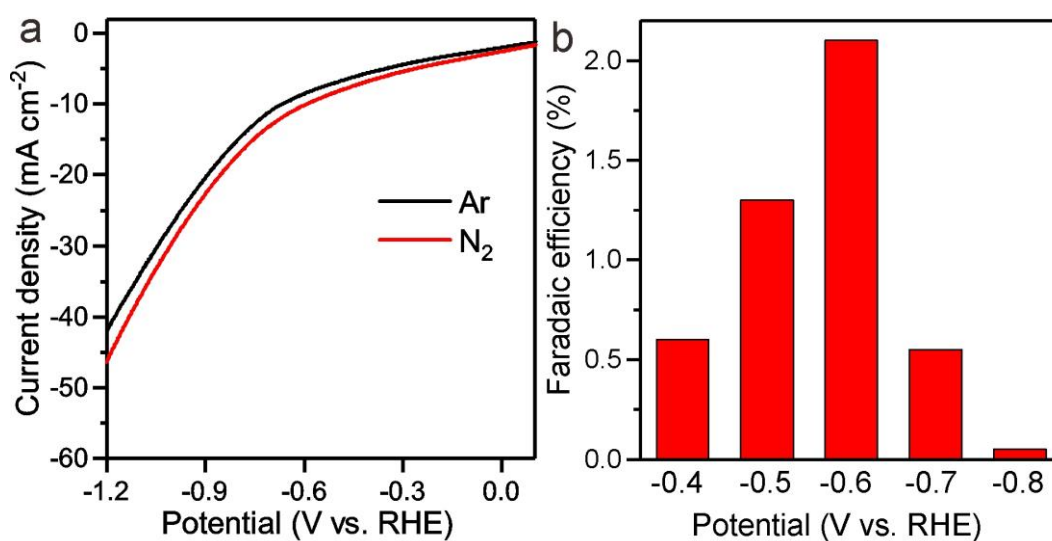


Figure 4.22. (a) LSV curves in 0.1 M HCl solution under Ar and N₂ of NDPCs. (b) Faradaic efficiencies for NH₃ at various applied potentials of NDPCs.

4. Single-site gold catalysts on hierarchical N-doped porous noble carbon for enhanced electrochemical reduction of nitrogen

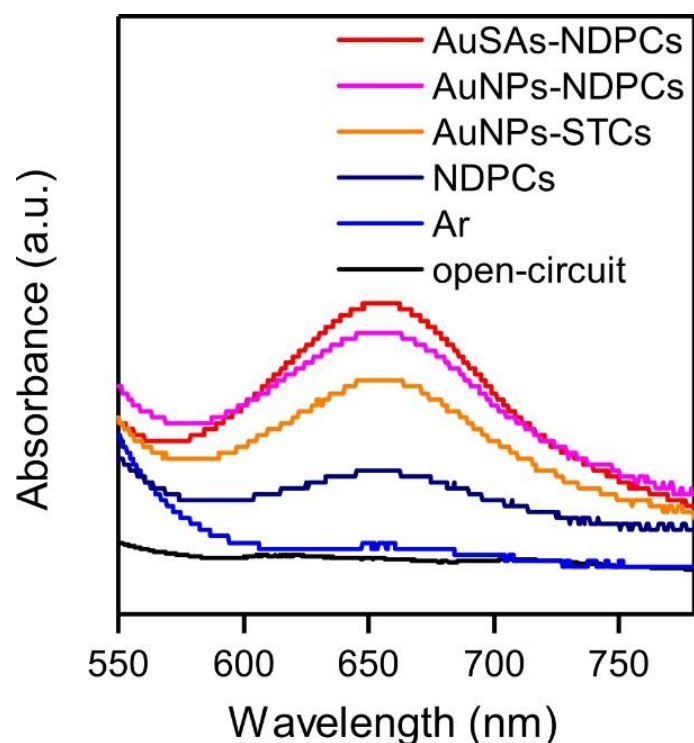


Figure 4.23. UV-Vis absorption spectra of the 0.1 M HCl solution with indophenol indicator after charging at -0.2 V vs. RHE for 2 h under various conditions.

In order to further verify that NH_3 was produced from NRR on AuSAs-NDPCs catalysts, pure carbon paper without any catalysts coating was tested in Ar and N_2 -saturated solution at -0.2 V vs. RHE (Figure 4.24a). No NH_4^+ could be detected based on the UV-Vis analysis (Figure 4.24b).

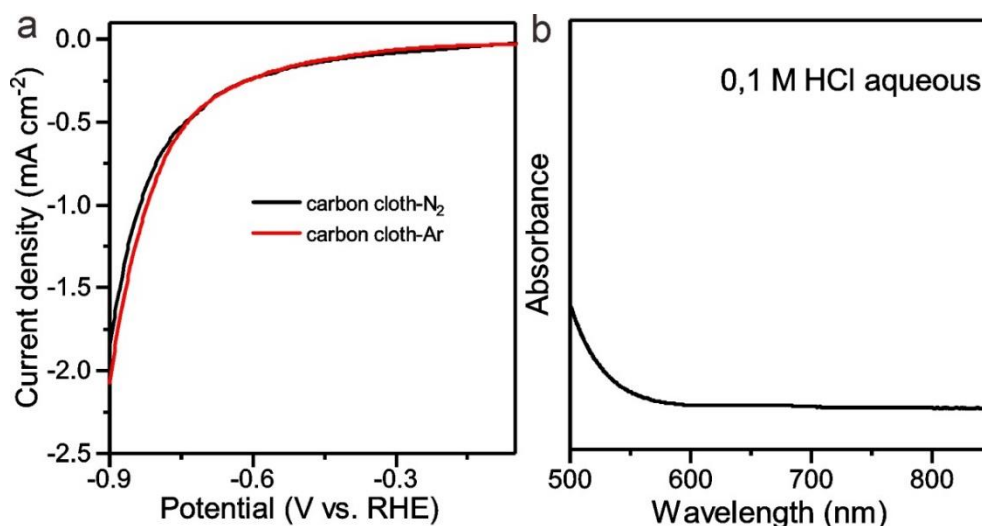


Figure 4.24. (a) LSV curves of carbon paper without catalysts in 0.1 M HCl solution under Ar and N_2 . (b) The corresponding UV-Vis spectrum of the N_2 -saturated solutions after the electrolysis at -0.2 V vs. RHE for 2 h.

4. Single-site gold catalysts on hierarchical N-doped porous noble carbon for enhanced electrochemical reduction of nitrogen

Based on the above analysis, it can be concluded that NDPCs and Au single sites both play crucial roles for the excellent NRR performance. NDPCs, as a highly open porous structure with high surface area, can create a favourable access to the active sites and mass transport during the electrochemical NRR. On the other hand, they also stabilize Au single sites due to the abundant N and C species with highly oxidizing character and strong polarization. It is worth to note that hydrazine (N_2H_4) as an intermediate product can be formed during electrochemical NRR.¹⁹³ However, there is no colour change before and after electrolysis at -0.2 V vs. RHE by adding N_2H_4 colour reagent (Figure 4.25). UV spectra confirm that no N_2H_4 is produced in this catalytic system under different potentials (Figure 4.26). Based on the above analysis, from a mechanistic point of view, N_2 may firstly absorb on the surface of the catalysts by interacting with (positively polarized) Au single species and (negatively polarized) N or C atoms. In other words, N_2 is bridged into an FLP-like structure motive in the catalyst. Then, activated N_2 undergoes hydrogenation independently by reacting with activated H in the solution to form N-H bonds.¹¹⁶ As the reaction proceeds, the $\text{N}\equiv\text{N}$ bond will be broken, and NH_3 is formed as the final product.

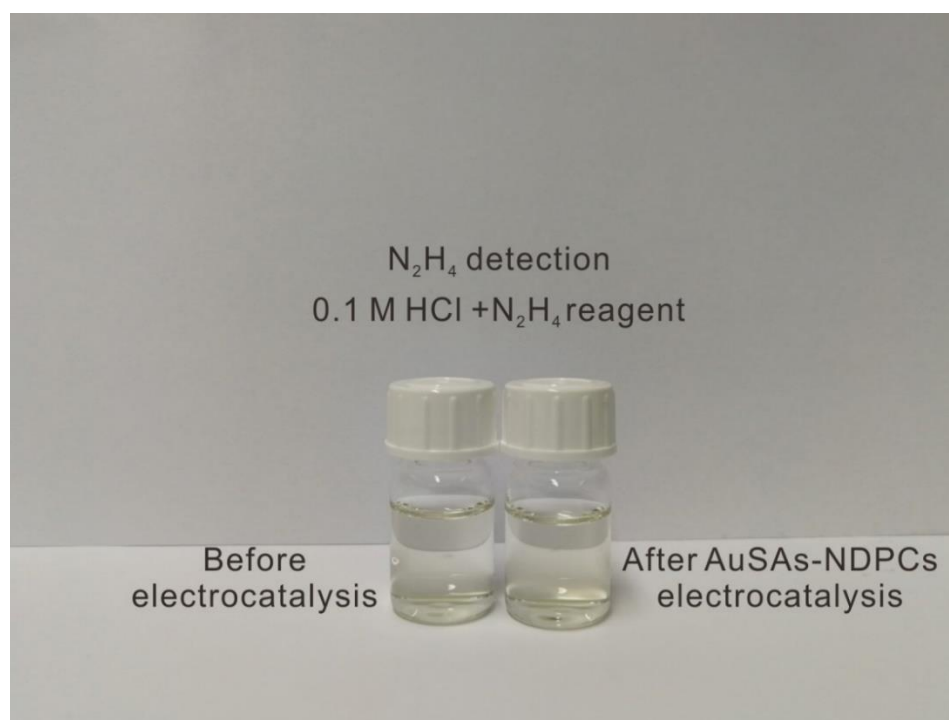


Figure 4.25. Optical image of the N_2 -saturated 0.1 M HCl electrolytes detected using N_2H_4 color reagent after a 2 h NRR test on the AuSAs-NDPCs electrode at -0.2 V vs. RHE.

4. Single-site gold catalysts on hierarchical N-doped porous noble carbon for enhanced electrochemical reduction of nitrogen

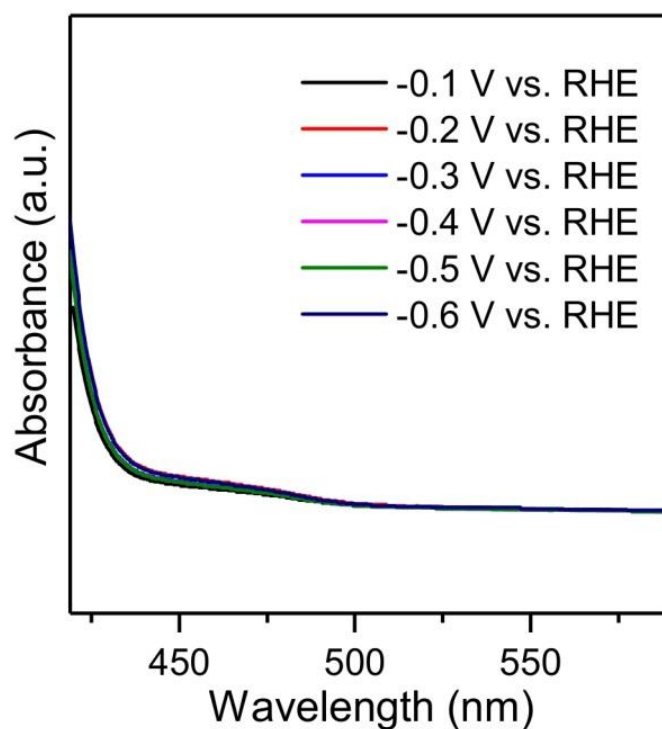


Figure 4.26. UV-Vis absorption spectra of the N_2 -saturated 0.1 M HCl solution with N_2H_4 color reagent after electrolysis on the AuSAs-NDPCs electrode at different potentials for 2 h.

In summary, a novel catalyst construction composed of Au single atoms decorated on the surface of NDPCs was reported. The introduction of Au single ions leads to active reaction sites, which are stabilized by N species in NDPCs. Thus, the interaction within as-prepared AuSAs-NDPCs catalysts enabled promising performance for electrochemical NRR. It is believed that this finding provides new opportunities for the design of single atom catalysts to achieve efficient N_2 fixation at ambient conditions.

5. Electrochemical Fixation of Nitrogen and its Coupling with Biomass Valorization with a Strongly Adsorbing and Defect Optimized Boron-Carbon-Nitrogen Catalyst

5. Electrochemical Fixation of Nitrogen and its Coupling with Biomass Valorization with a Strongly Adsorbing and Defect Optimized Boron-Carbon-Nitrogen Catalyst

To further reduce the utilization of metal-based materials, metal-free porous carbon materials are highly desirable, but they should always be functionalized to enhance the catalytic performance. As mentioned in section 2.2.2, heteroatom-doping of porous carbon causes inhomogeneous charge distribution and modifies the work function of the electrons in the catalysts. These effects can be used to tailor the redox potential of the catalysts and to modify the electron transfer mechanism to the substrate molecules.¹⁹⁴⁻¹⁹⁷ In consequence, many examples are known in which heteroatom-doped carbon materials show remarkable electrocatalytic performance, especially for the activation of small molecules in electrocatalytic reactions.^{182, 198-202} Constructing specific chemical binding motives and FLPs are two main routes for the activation of molecules such as N₂ or CO₂ due to strong polarization, which usually improves the corresponding electrocatalytic performance.^{68-70, 203} Another possible source of significant catalytic activity in graphene-based materials are point defects at grain boundaries. Such point defects can lead to the presence of a large number of unpaired electrons. This can even cause macroscopic ferromagnetism,²⁰⁴⁻²⁰⁶ and can be another source of catalytic activity.²⁰⁷ Doping graphene-based materials with B and N in fact significantly enhances the density of grain boundaries because of the preferred formation of nanoscale B-N domains/grains.²⁰⁸⁻²¹⁰ Although these principles are in general known and accepted, they have not yet been transferred to porous carbonaceous materials and their influence in NRR has not been investigated.

Especially, electrocatalysis is most rewarding when not only the reductive half-reaction, but also the coupled oxidative half-reaction creates a valuable product. Instead of coupling NRR with the oxygen evolution reaction (OER), selective oxidation of other substances such as biomass would be a more valuable reverse process in a full cell.²¹¹ However, these reactions

Term of use: This chapter is adapted with permission from my own original work:

[1] Qin, Q., Heil, T., Schmidt, J., Schmallegger M., Gescheidt-Demner, G., Antonietti, M., Oschatz, M. Electrochemical Fixation of Nitrogen and its Coupling with Biomass Valorization with a Strongly Adsorbing and Defect Optimized Boron-Carbon-Nitrogen Catalyst.

5. Electrochemical Fixation of Nitrogen and its Coupling with Biomass Valorization with a Strongly Adsorbing and Defect Optimized Boron-Carbon-Nitrogen Catalyst

are also far from simple and have high requirements on the catalysts as well. Biomass is a sustainable non-fossil-based carbon source and can serve as an alternative feedstock for the chemical industry.²¹²⁻²¹⁵ Among different biomass-derived platform molecules, 2,5-furandicarboxylic acid (FDCA) is particularly important as it is a widely applied starting monomer or intermediate for different polymeric materials and can potentially replace terephthalic acid.²¹⁶⁻²¹⁸ Currently, FDCA is mainly produced from the oxidation of 5-hydroxymethylfurfural (HMF) with O₂ under high pressure, while HMF can be derived from cellulosic biomass.²¹⁹⁻²²⁰ Electrocatalytic oxidation of HMF under ambient conditions is possible as well but requires the use of metal-based catalysts.²²¹

In this chapter, N and B co-doped porous carbon with abundant point defects and polar structure, in which positively charged B atoms acts as electron acceptors together with negatively charged N atoms as electron donors, will be introduced. The as-obtained BNC material will be applied for electrochemical NRR with a high FE of 15.2% and NH₃ production rate of 21.3 μg h⁻¹ mg⁻¹. Besides, this material is used as the first metal-free electrocatalyst for HMF oxidation with a FDCA yield of 57% at 71 % conversion with the reaction time of 6 h.

5.1. Synthesis and characterization of BNC

In a typical synthesis of B and N co-doped carbon, a mixture of melamine, L-cysteine and boric acid as precursors underwent pyrolysis at high temperature. In order to tune the amount and binding structure of the dopant atoms, different mass ratios of melamine to L-cysteine to boric acid were mixed, and as-obtained products were denoted as NC, BNC-1, and BNC-2 with the ratio of 2:1:0, 2:1:0.2, and 2:1:1, respectively. During the pyrolysis, the reactants were first pyrolyzed at 600 °C to form B-doped C₃N₄, which was further heated to 1000 °C to obtain BNC (Figure 5.1a).^{200, 222} Transmission electron microscopy (TEM) images of BNC-2 (Figure 5.1b-c) show a morphology of interconnected nanoribbons with uniform but defect-rich nanoporous structure. A comparable structure is observed for NC and BNC-1 (Figure 5.2). The individual ribbons of NC appear thinner but larger in the plane, which indicates that the co-doping of N and B can improve the interaction (stacking) between the single graphene-like layers and introduces more grain boundaries at the same time. Scanning electron microscopy (SEM) images (Figure 5.3) also show a rather dense appearance of the BCN samples when directly compared to the rather graphene-like NC material, in accordance with TEM results.

5. Electrochemical Fixation of Nitrogen and its Coupling with Biomass Valorization with a Strongly Adsorbing and Defect Optimized Boron-Carbon-Nitrogen Catalyst

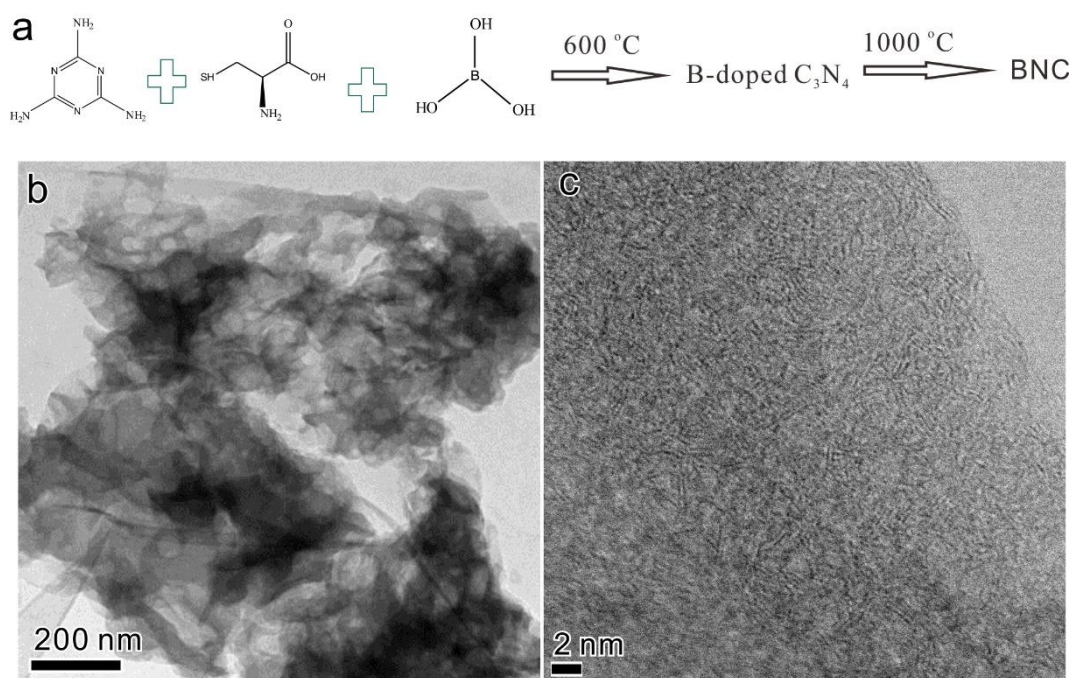


Figure 5.1. (a) Synthesis processes of N and B co-doped carbon. (b) Representative TEM image and (c) HRTEM image of BNC-2.

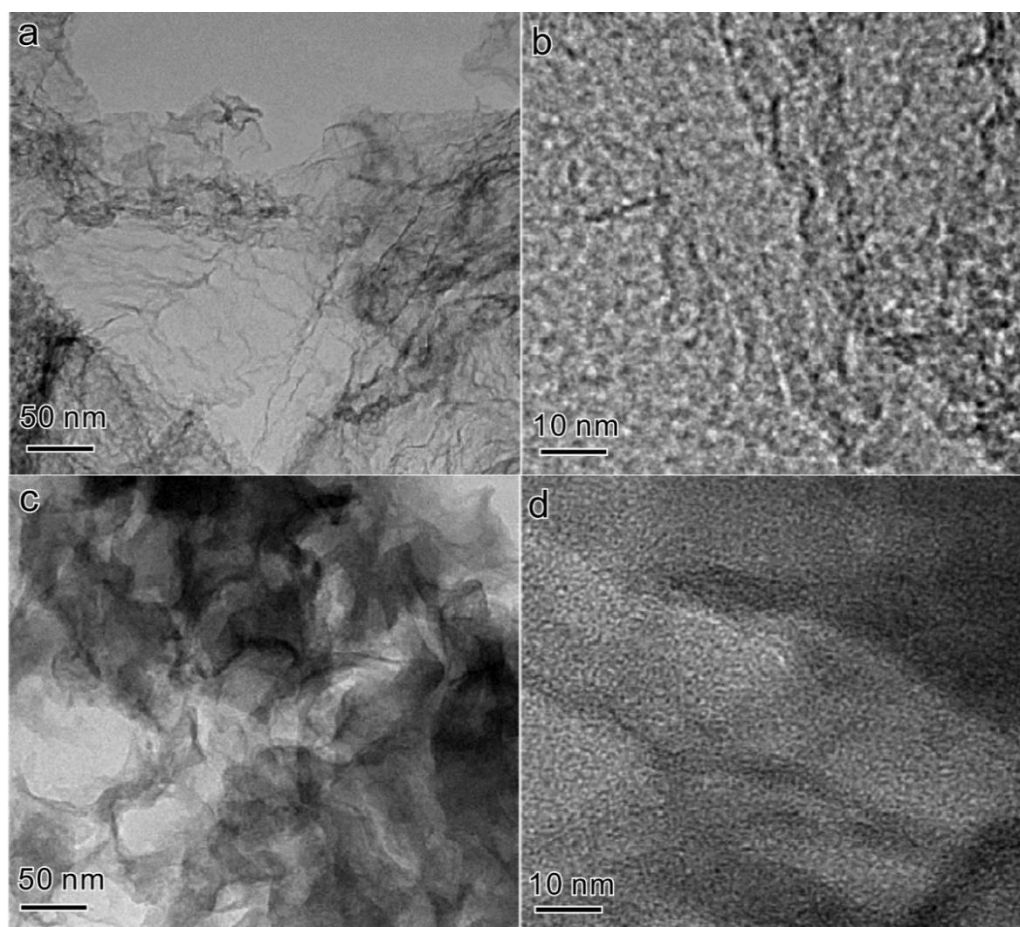


Figure 5.2. TEM images of NC (a-b) and BNC-1 (c-d).

5. Electrochemical Fixation of Nitrogen and its Coupling with Biomass Valorization with a Strongly Adsorbing and Defect Optimized Boron-Carbon-Nitrogen Catalyst

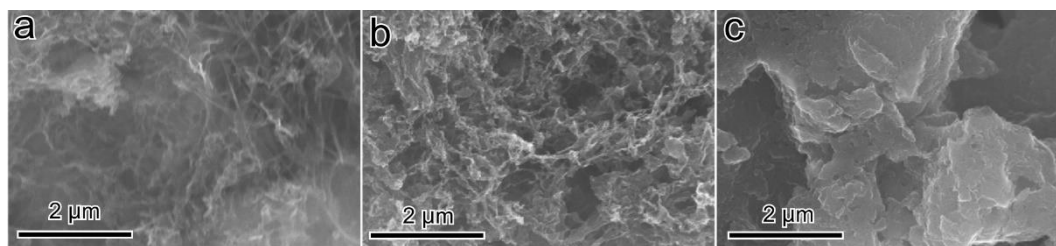


Figure 5.3. Representative SEM images of (a) NC, (b) BNC-1 and (c) BNC-2.

X-ray diffraction (XRD) patterns of BNC-2 show only broad peaks corresponding to (002) and (101) reflections at 26° and 44° , respectively, which are also present in NC and BNC-1 (Figure 5.4). This demonstrates the mainly amorphous structure that is typical for nanoporous carbon materials and the absence of crystalline BN in the as-obtained samples. The electron energy loss spectrum (EELS) (Figure 5.5) confirms the coexistence of B, C and N in the BCN-2, with the K-edges located at 191 eV, 284 eV and 401 eV, respectively.

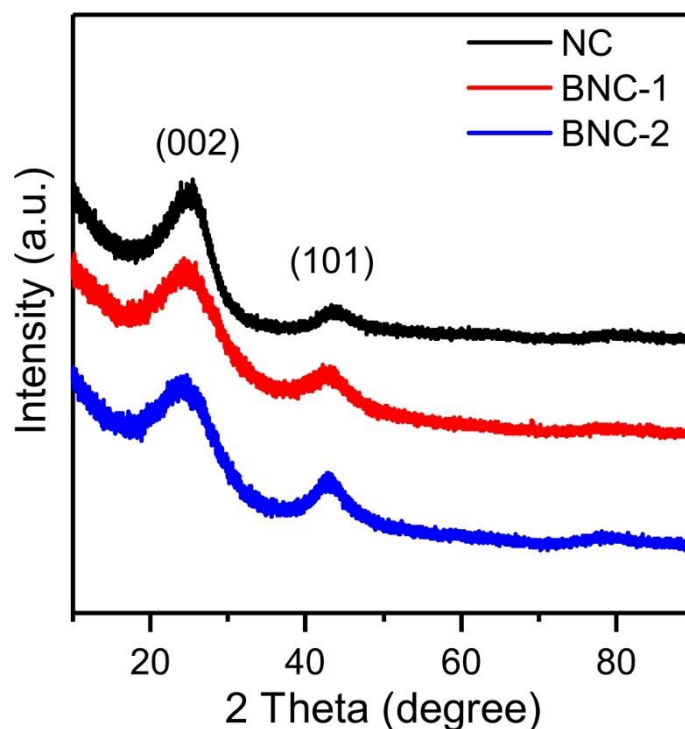


Figure 5.4. XRD patterns of NC, BNC-1 and BNC-2.

5. Electrochemical Fixation of Nitrogen and its Coupling with Biomass Valorization with a Strongly Adsorbing and Defect Optimized Boron-Carbon-Nitrogen Catalyst

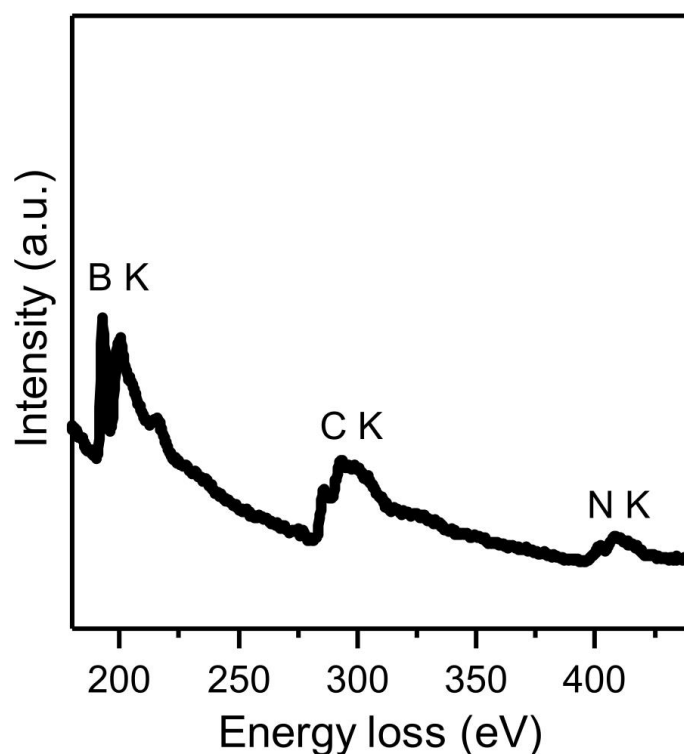


Figure 5.5. EELS spectrum of BNC-2.

X-ray photoelectron spectroscopy (Figure 5.6) was also conducted to investigate the chemical compositions of the samples. With increased addition of boric acid, the doping level of B and N increases (Table 5.1), i.e. B helps to keep N in the structures, presumably via B-N bonding.

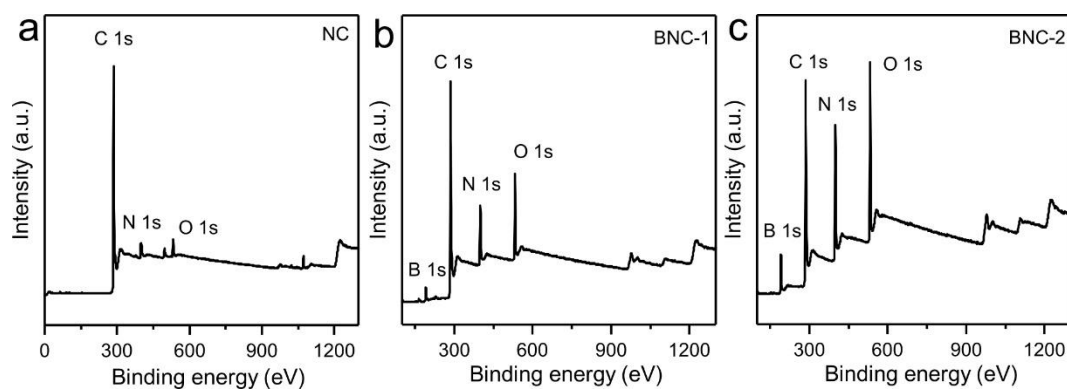


Figure 5.6. XPS survey spectra of (a) NC, (b) BNC-1 and (c) BNC-2.

5. Electrochemical Fixation of Nitrogen and its Coupling with Biomass Valorization with a Strongly Adsorbing and Defect Optimized Boron-Carbon-Nitrogen Catalyst

Table 5.1. Atomic compositions of NC, BNC-1 and BNC-2 determined from XPS measurements.

Sample	B (at.%)	C (at.%)	N (at.%)	O (at.%)
NC	0	89.8	6.6	3.6
BNC-1	6.89	68.63	13.52	10.96
BNC-2	19.5	48.41	19.65	12.44

XPS spectra of N 1s were then deconvoluted to elucidate the detailed binding motives (Figure 5.7). In BNC-1 and BNC-2, the four characteristic peaks centered at 398.1 eV, 398.5 eV, 399.7 eV and 400.8 eV can be ascribed to pyridinic N, N bonded to B atoms, pyrrolic N and quaternary N atoms, respectively. The content of electron-rich/Lewis basic N-atoms is apparently higher in BNC-2.²²³⁻²²⁴ N 1s spectra of B-free NC show the presence of pyridinic N, pyrrolic N, quaternary N and oxidized N atoms.¹⁸⁹ The high-resolution B 1s spectra show three obvious peaks corresponding to B-O, B-N and B-C species (Figure 5.8) in BNC-1 and BNC-2.²²⁵ The content of electron-deficient/Lewis acidic B-atoms is also apparently higher in BNC-2.

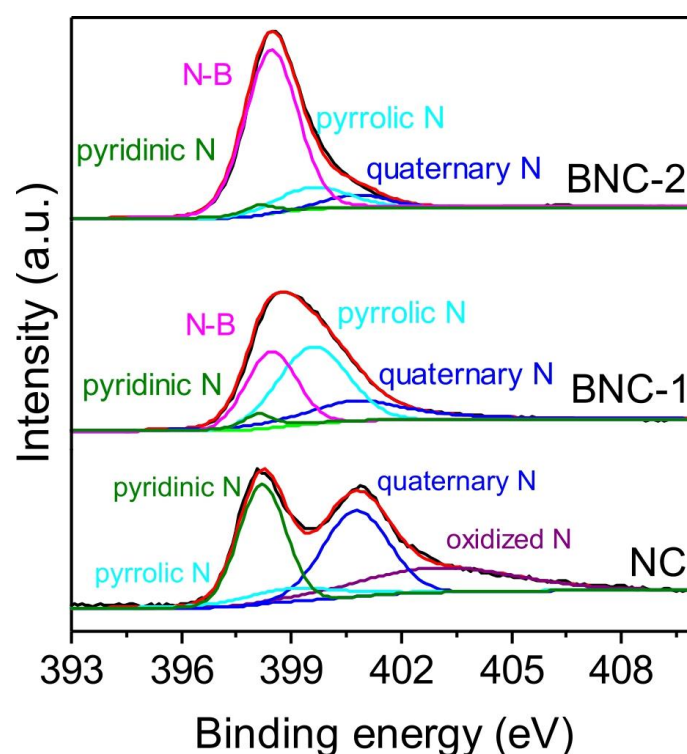


Figure 5.7. High resolution N 1s XPS spectra of NC, BNC-1 and BNC-2.

5. Electrochemical Fixation of Nitrogen and its Coupling with Biomass Valorization with a Strongly Adsorbing and Defect Optimized Boron-Carbon-Nitrogen Catalyst

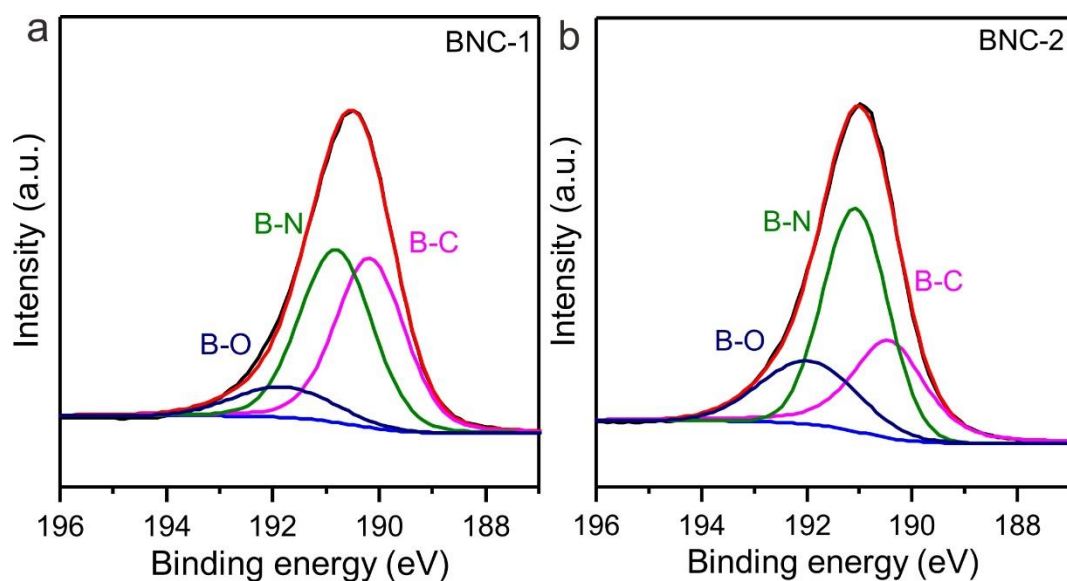


Figure 5.8. High resolution B 1s XPS spectra of (a) BNC-1 and (b) BNC-2.

The successful fabrication of B-N bonds in BNC-2 is also demonstrated by Fourier Transform Infrared spectra with obvious peaks located at 1380 cm^{-1} (Figure 5.9a), which can be attributed to out-of-plane stretching of B-N-B bonds.²²⁶ Raman spectra (Figure 5.9b) show two characteristic peaks at $\sim 1598\text{ cm}^{-1}$ and $\sim 1338\text{ cm}^{-1}$, which can be assigned to the so-called disordered (D) and graphite (G) bands of carbon, respectively. The low intensity of both bands indicates the very defective carbon structure in the materials because co-doping of N and B heteroatoms creates abundant point defects and possibly also vibrational dissymmetry in the sp^2 carbon structure.

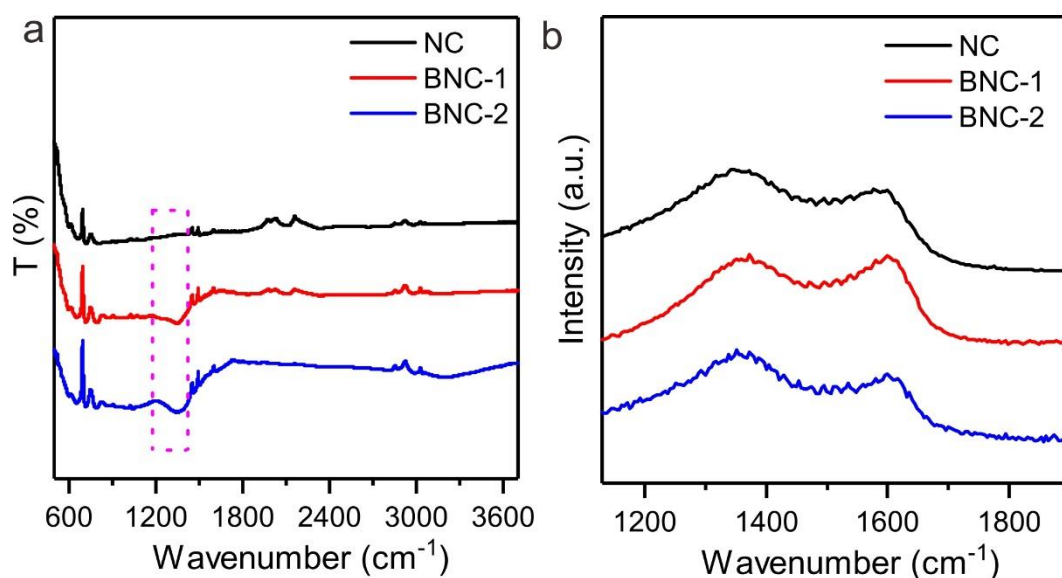


Figure 5.9. FT-IR spectra and Raman spectra of (a) BNC-1 and (b) BNC-2.

5. Electrochemical Fixation of Nitrogen and its Coupling with Biomass Valorization with a Strongly Adsorbing and Defect Optimized Boron-Carbon-Nitrogen Catalyst

Electron paramagnetic resonance (EPR) spectra show an obvious EPR signal for BNC with a g value of 2.006, and the signal intensity increases with the doping level of N and B, while there is almost no EPR signal for NC (Figure 5.10). This EPR signal can be attributed to the presence of plenty of unpaired electrons due to point defects at grain boundaries in BNC.²²⁷⁻²²⁹ In addition, FLPs can possibly be formed from non-saturated B and N atoms near these defects, providing the targeted-for unique advantages for the activation of small molecules in electrocatalysis. These properties are absent in NC and less pronounced in BNC-1, as also reflected in the lower intensity of the EPR signals.

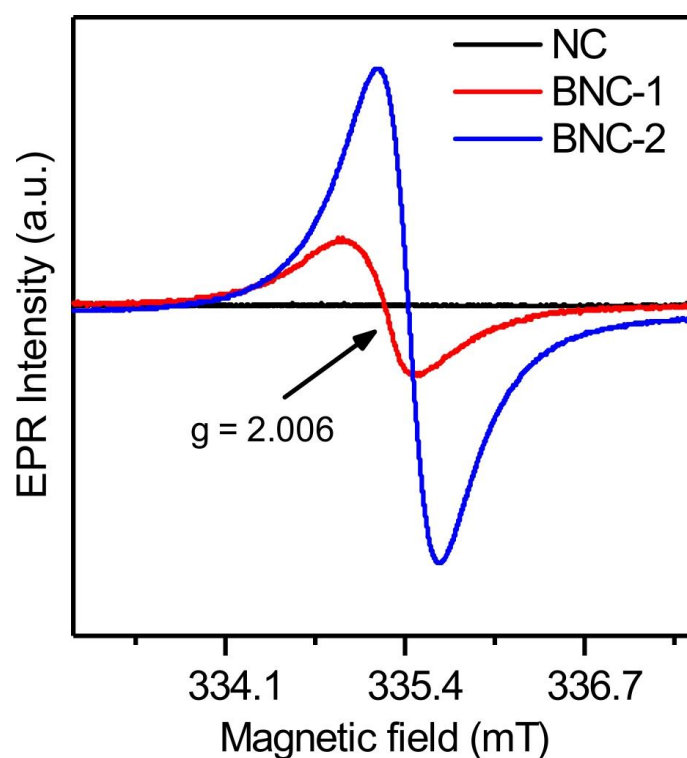


Figure 5.10. EPR spectra of NC, BNC-1 and BNC-2.

N_2 (-196 °C) physisorption experiments were carried out to analyze the textural properties of the BNC and NC materials (Figure 5.11). Compared with NC, doping of B and N in BNC-1 and BNC-2 results in significantly increased specific surface areas (SSAs) (Table 5.2). Note that most nanopores indeed rely on edge termination of the covalent BNC-sheets, i.e. these are the preferred locations of unpaired electrons and FLP motifs. The shapes of the isotherms at different relative pressures also represent specific hierarchical pore characters. The higher N_2 uptake at lower pressure indicates a high content of narrow micropores in BNC-2, especially when compared to BNC-1. In contrast, in NC there is only a small volume of micropores and mesopores but a higher macropore volume and external surface area. This is typical for sintered porous carbons which in general loose micropores due to covalent rearrangement and sintering

5. Electrochemical Fixation of Nitrogen and its Coupling with Biomass Valorization with a Strongly Adsorbing and Defect Optimized Boron-Carbon-Nitrogen Catalyst

at higher temperatures. BN-motifs obviously improve the stability of edge terminations against sintering. All that is confirmed by the pore size and pore volume distribution curves (Figure 5.12). Therefore, it can be concluded that co-doping of B and N can create a hierarchical nanoporous architecture, and the BN content has a significant effect on the pore structure and its stability, which provides innate advantages for the further catalytic applications.

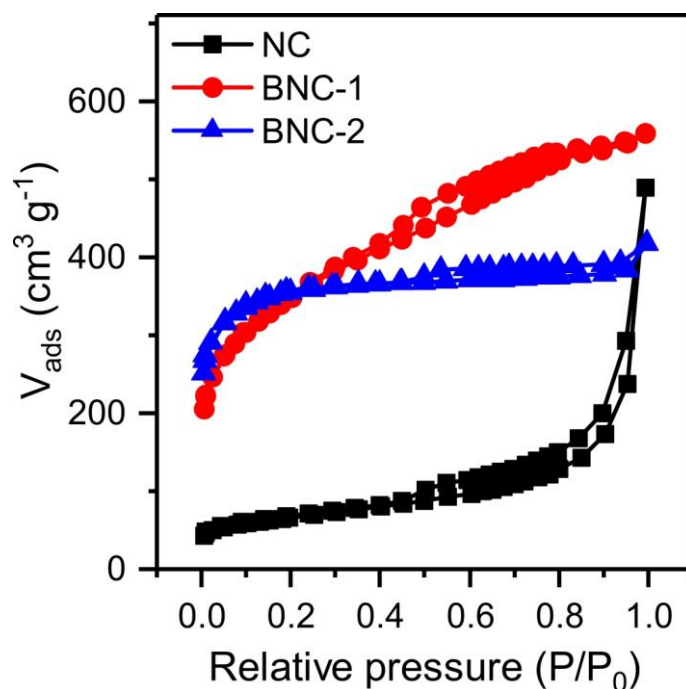


Figure 5.11. N₂ physisorption isotherms (at -196 °C) of NC, BNC-1 and BNC-2.

Table 5.2. BET specific surface area (SSA) and total pore volume (V_t) of NC, BNC-1 and BNC-2.

Sample	SSA (m ² g ⁻¹)	V_t (cm ³ g ⁻¹)
NC	233.6	0.42
BNC-1	1230.5	0.78
BNC-2	1356.9	0.55

5. Electrochemical Fixation of Nitrogen and its Coupling with Biomass Valorization with a Strongly Adsorbing and Defect Optimized Boron-Carbon-Nitrogen Catalyst

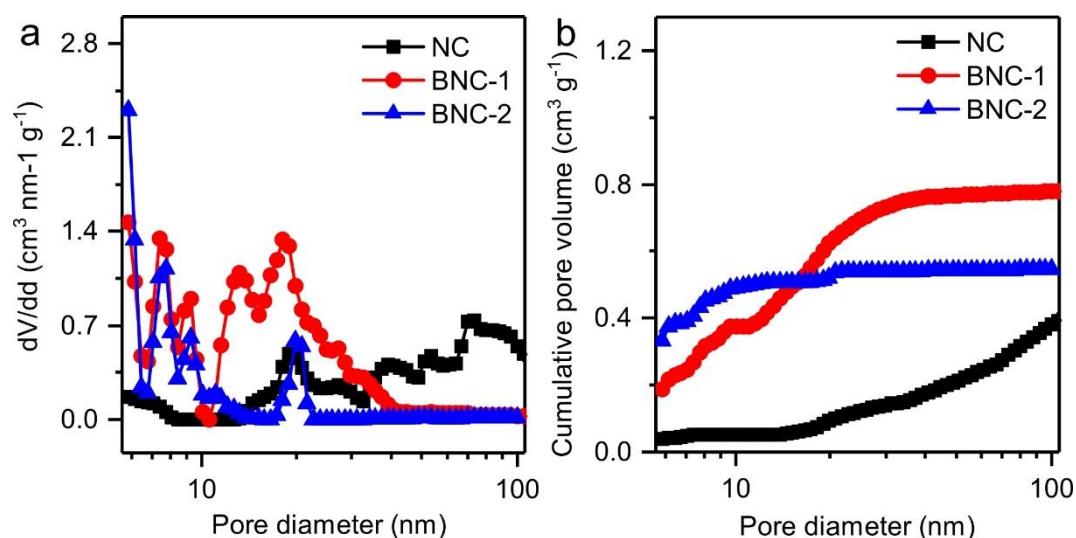


Figure 5.12. (a) Differential and (b) cumulative pore size distributions of NC, BNC-1 and BNC-2.

5.2 Electrocatalytic tests of NRR

In view of the unique structure of N and B co-doped carbon, including porosity and high heteroatom doping level as well as unpaired electrons and high oxidation potential, their electrocatalytic applications were studied. The electrochemical NRR performance of BNC-2 was firstly tested with a three-electrode system. The comparison of linear sweep voltammetry (LSV) curves under Ar- and N₂-saturated electrolyte solution indicates an obvious current response of the BNC-2 electrode towards N₂ (Figure 5.13a). Chronoamperometry tests were then conducted under different given potentials (Figure 5.13b), while the corresponding FE and NH₃ production rates were quantified from the NH₄⁺ calibration curve (Figure 5.14). A maximum FE of 15.2% with a comparably high NH₃ production rate of 21.3 μg h⁻¹ mg⁻¹ can be achieved at a potential of -0.3 V vs. RHE (Figure 5.15). At more negative given potentials, FE and NH₃ production rates both decrease mainly due to the fact that HER is becoming the dominant process.¹⁷⁵

5. Electrochemical Fixation of Nitrogen and its Coupling with Biomass Valorization with a Strongly Adsorbing and Defect Optimized Boron-Carbon-Nitrogen Catalyst

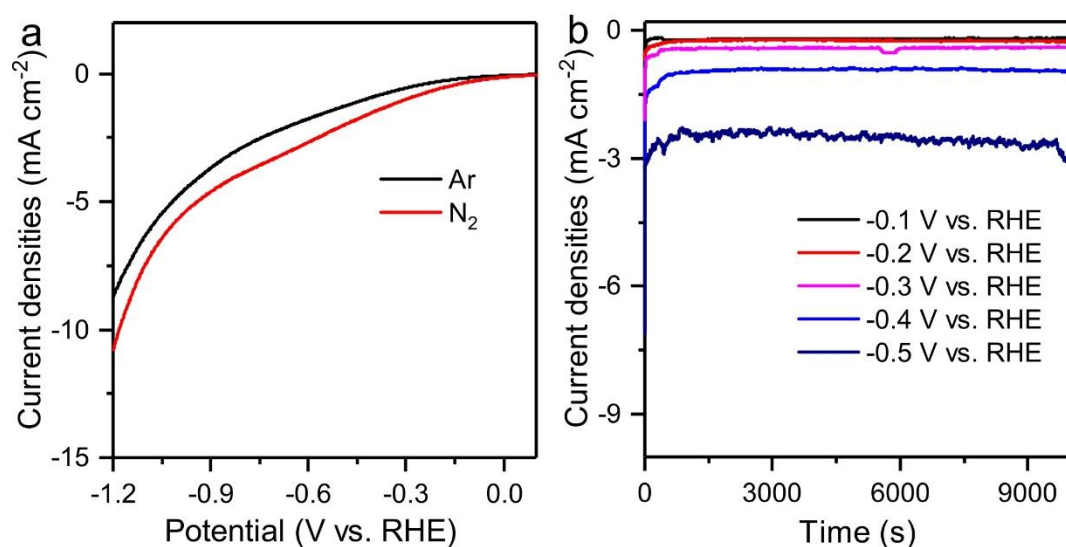


Figure 5.13. (a) LSV curves of BNC-2 under N₂- and Ar-saturated 0.1 M NaOH electrolyte solution. (b) Chronoamperometry results of BNC-2 electrode at different given potentials.

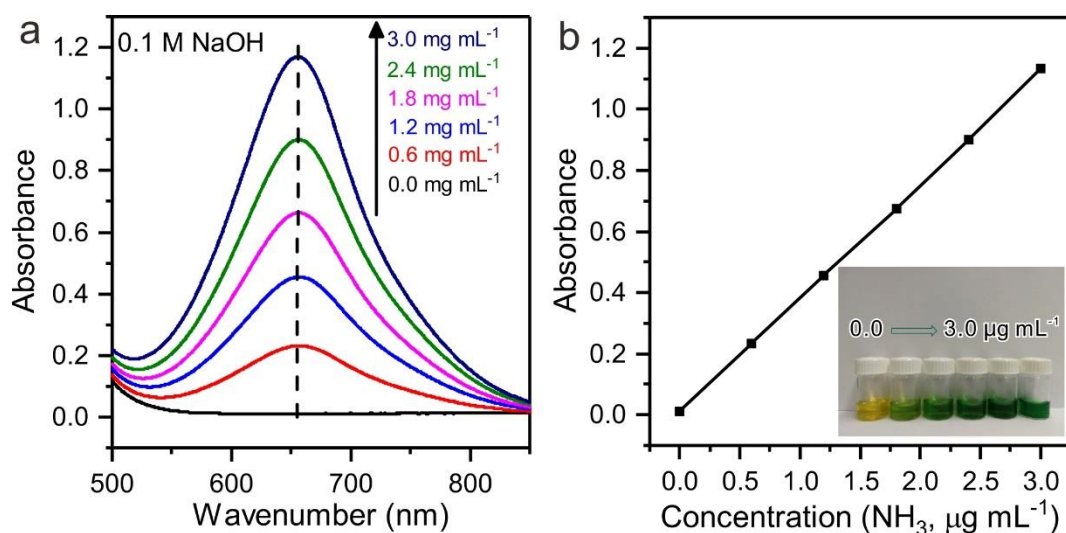


Figure 5.14. (a) UV-Vis spectroscopy curves of NH₄Cl solutions with different known concentration by using the indophenol blue method (the absorbance at 655 nm is referred to the concentration of NH₄⁺). (b) The corresponding linear calibration curve by indophenol blue method used to quantify the NH₃ yield (the inset is the optical image of NH₄Cl solutions with various concentrations).

5. Electrochemical Fixation of Nitrogen and its Coupling with Biomass Valorization with a Strongly Adsorbing and Defect Optimized Boron-Carbon-Nitrogen Catalyst

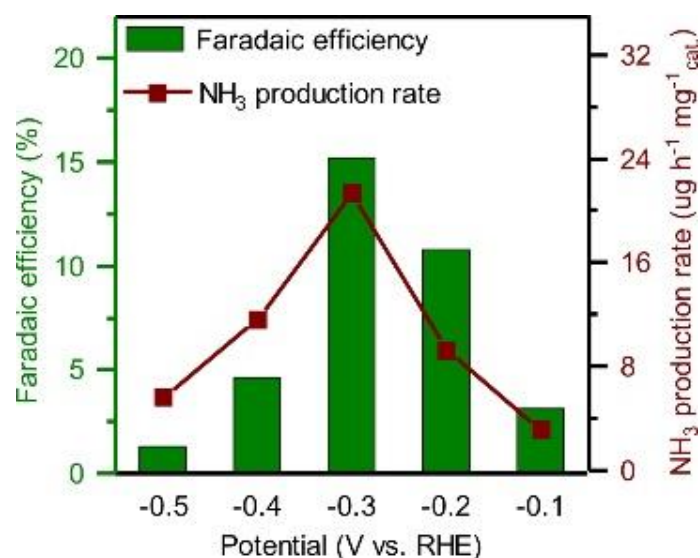


Figure 5.15. FE and NH₃ production rate of BNC-2 electrode at different given potentials.

Optical images and UV-Vis spectra show that the BNC-2 catalyst does selectively produce NH₃. The solutions have been tested for N₂H₄ as one possible by-product, and N₂H₄ cannot be detected, independent of the applied potentials (Figure 5.16). In addition to high activity, excellent stability is also required for a practical NRR catalyst. As shown in the recycling test (Figure 5.17a), FE and NH₃ production rates remain almost constant (Figure 5.17b) and the long-term chronoamperometry test also exhibits good current stability of BNC-2 (Figure 5.18).

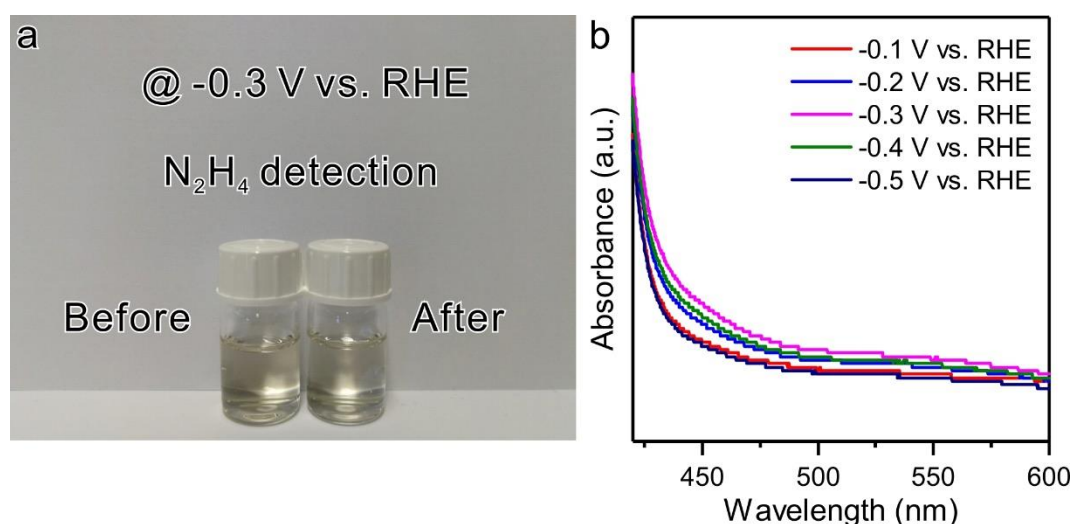


Figure 5.16. (a) Optical image of the N₂-saturated 0.1 M NaOH electrolyte detected by using N₂H₄ color reagent before and after NRR test on the BNC-2 electrode at -0.3 V vs. RHE. (b) UV-Vis absorption spectra of the N₂-saturated 0.1 M NaOH electrolyte with N₂H₄ color reagent after NRR test on the BNC-2 electrode at different given potentials.

5. Electrochemical Fixation of Nitrogen and its Coupling with Biomass Valorization with a Strongly Adsorbing and Defect Optimized Boron-Carbon-Nitrogen Catalyst

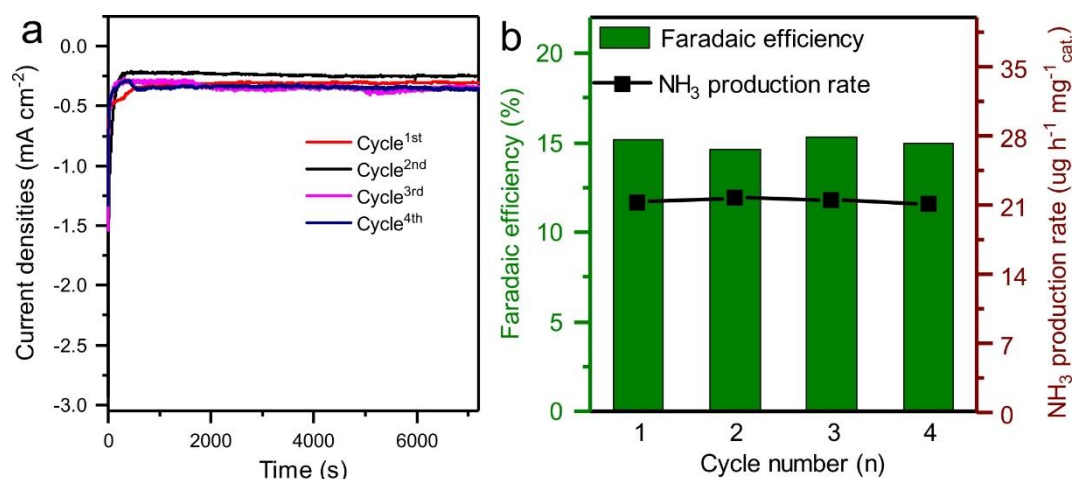


Figure 5.17. (a) Chronoamperometry results of BNC-2 electrode in a stability test recorded at the potential of -0.3 V vs. RHE. (b) FE and NH₃ production rate during this recycling test.

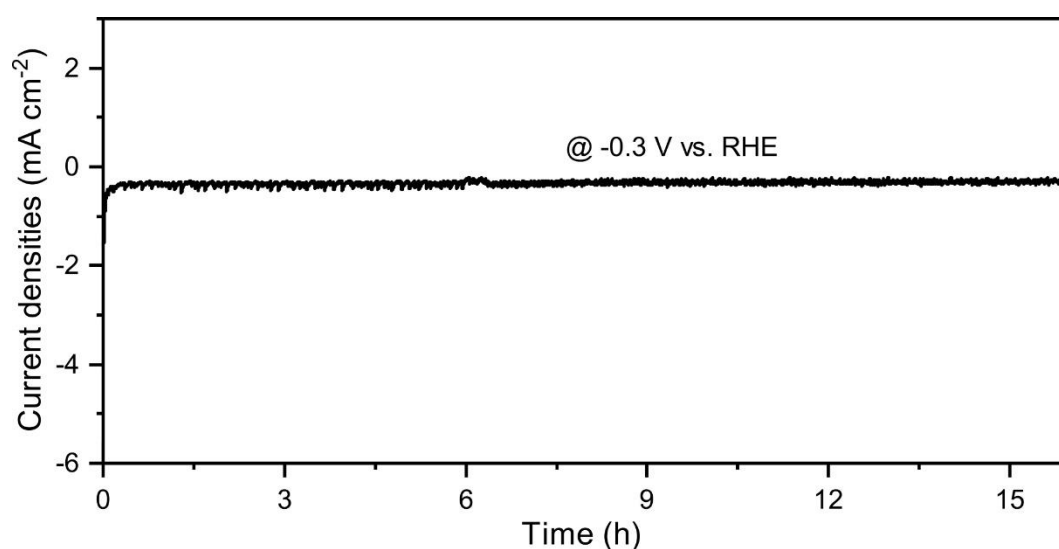


Figure 5.18. Chronoamperometry test of the BNC-2 electrode at a potential of -0.3 V vs. RHE for over 16 h.

In order to exclude NH₃ to come from other nitrogen sources, some control experiments were conducted by measuring the NH₄⁺ concentration within the pure electrolyte before the test, under open circuit potential, and by using pure carbon paper as the catalyst at the potential of -0.3 V vs. RHE. As shown in the UV spectra, there is no NH₄⁺ detected in those control experiments (Figure 5.19a) as well as under Ar-saturated electrolyte at different given potentials (Figure 5.19b). Therefore, it can be seen as proven that the NH₄⁺ in the electrolyte is generated via NRR catalysed by BNC-2 electrode. In order to highlight the influence of co-doping and

5. Electrochemical Fixation of Nitrogen and its Coupling with Biomass Valorization with a Strongly Adsorbing and Defect Optimized Boron-Carbon-Nitrogen Catalyst

porosity, NC and BNC-1 were also tested and compared with BNC-2 (Figure 5.20). Both materials exhibit a significantly lower FE and NH_3 production rate.

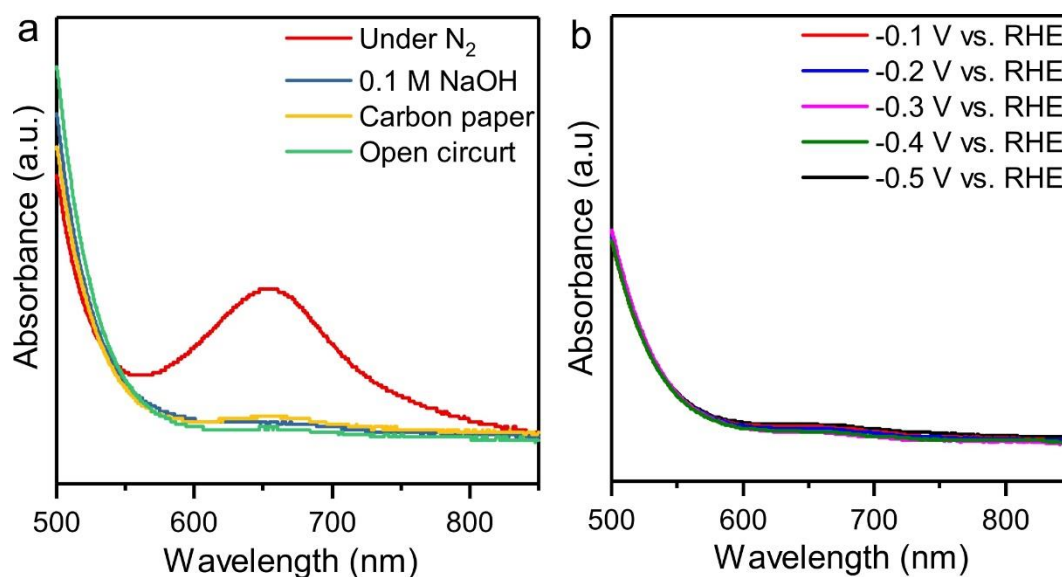


Figure 5.19. UV-Vis absorption spectra of (a) 0.1 M NaOH solution with indophenol indicator under various conditions and (b) Ar-saturated 0.1 M NaOH electrolyte with indophenol indicator after electrolysis on the BNC-2 electrode for 7200 s at different given potentials.

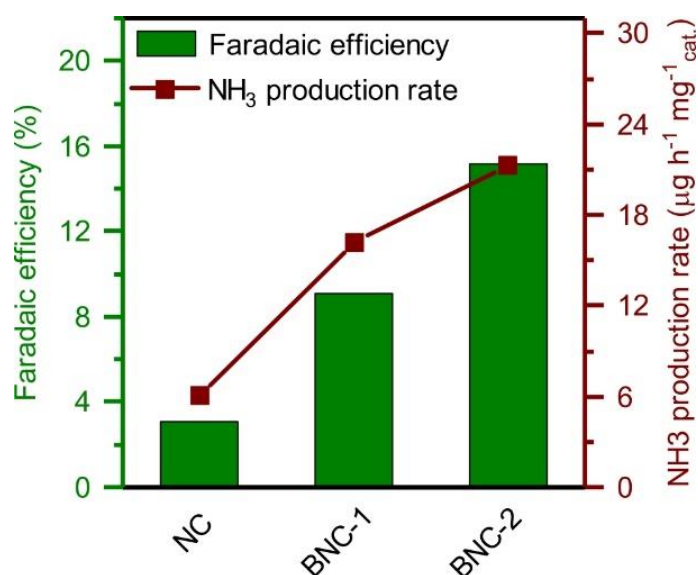


Figure 5.20. Comparison of FE and NH_3 production rate at a potential of -0.3 V vs. RHE for NC, BNC-1 and BNC-2.

Another requirement for the large-scale implementation of electrochemical NRR would be the coupling with a suitable value generating oxidation process on the opposite electrode in a symmetrical full cell. In addition to the electroreduction reaction, the ability of as-obtained

5. Electrochemical Fixation of Nitrogen and its Coupling with Biomass Valorization with a Strongly Adsorbing and Defect Optimized Boron-Carbon-Nitrogen Catalyst

samples to act as an oxidation catalyst was also tested. Compared with the electrooxidation of water producing oxygen, which is abundantly available from cryogenic distillation of air, selective oxidation of biomass by electricity is promising to synthesize high-value chemical compounds. Therefore, the electrooxidation of HMF was studied as a second application using BNC and NC materials as catalysts.

From the LSV curves of BNC-2 with and without the addition of 5 mM of HMF in 0.1 M NaOH (Figure 5.21a), it can be seen that current densities dramatically increase after adding HMF, indicating that the materials exhibit obvious catalytic activity for HMF oxidation. In absence of HMF, there is also an anodic current due to the water oxidation to O₂, which is the main competing reaction for HMF oxidation (in a comparable way as HER is for NRR).²³⁰⁻²³¹ Similarly, BNC-1 also shows obvious current response for HMF oxidation (Figure 5.21b). On the contrary, the current densities after adding HMF only slightly increase for NC, and at higher overpotentials (Figure 5.21c). In the absence of HMF, the current densities generated by the NC electrode are much higher when compared to the BNC electrode, which shows that NC is a more favorable catalyst for water oxidation/OER, while BCN is not.

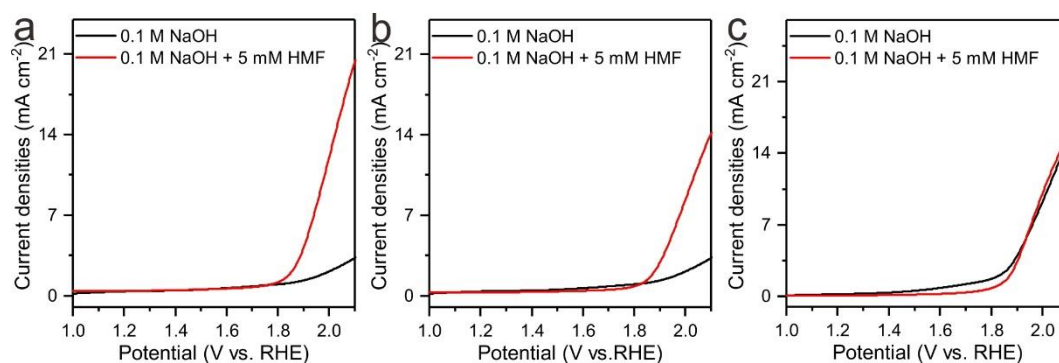
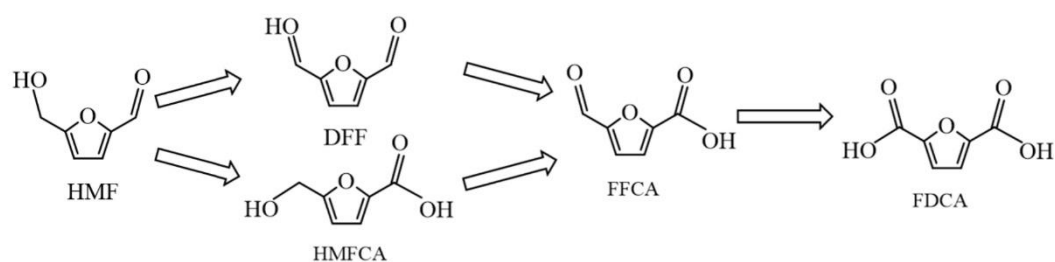


Figure 5.21. LSV curves in 0.1 M NaOH aqueous solution with and without the addition of 5 mM HMF with (a) BNC-2, (b) BNC-1 and (c) NC electrode.

There are several possible intermediates during the oxidation of HMF to FDCA (Scheme 5.1), such as 2,5-diformylfuran (DFF), 5-formyl-2-furancarboxylic acid (FFCA) and 5-hydroxymethyl-2-furancarboxylic acid (HMFCFA).²³² Therefore, chronoamperometry tests were further carried out to investigate the HMF conversion and FDCA selectivity over time. At a potential of 1.9 V vs. RHE and after 6 h, 71 % of HMF was successfully converted at the BNC-2 electrode, which by large surpasses the catalytic activity of NC and BNC-1 (Figure 5.22a). BNC-2 also provides a desirable FDCA yield of 57 % (Figure 5.22b).

5. Electrochemical Fixation of Nitrogen and its Coupling with Biomass Valorization with a Strongly Adsorbing and Defect Optimized Boron-Carbon-Nitrogen Catalyst



Scheme 5.1. Two possible pathways of HMF electrooxidation to FDCA.

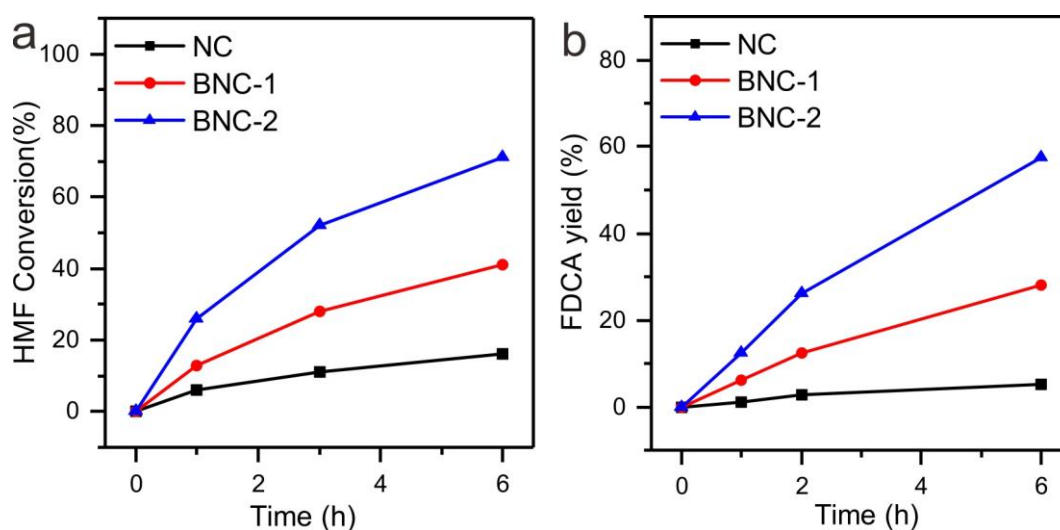


Figure 5.22. (a) HMF conversion and (b) FDCA yield over the 6 h chronoamperometry test of NC, BNC-1 and BNC-2 electrode, respectively.

Carbon paper without catalyst loading does not exhibit any activity for HMF oxidation (Figure 5.23). In addition, the stability test of BNC-2 for HMF oxidation (Figure 5.24) shows that the current densities firstly decrease due to the consumption of reactants and then recover immediately after re-addition of HMF. After 4 times, BNC-2 can still provide fast and sensitive response toward HMF addition, implying good stability and the absence of irreversible processes on the electrode.

5. Electrochemical Fixation of Nitrogen and its Coupling with Biomass Valorization with a Strongly Adsorbing and Defect Optimized Boron-Carbon-Nitrogen Catalyst

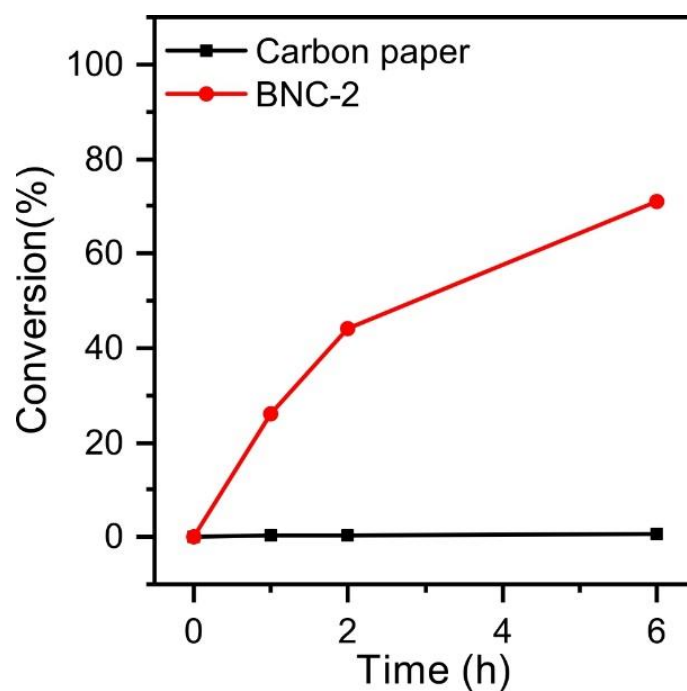


Figure 5.23. HMF conversion by using BNC-2 and pure carbon paper as electrocatalysts.

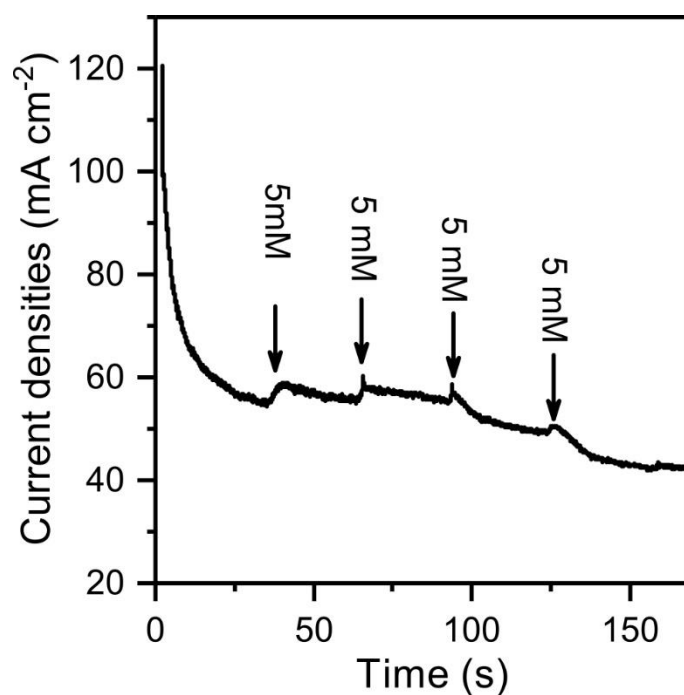


Figure 5.24. The current change over time of the chronoamperometry experiment at 1.9 V vs. RHE for BNC-2 electrode in 0.1 M NaOH containing 5 mM HMF and with the continuous addition of 5 mM HMF.

Based on the above analysis and comparisons, BNC-2 exhibits the best catalytic performances, both for nitrogen reduction as well as for biomass oxidation. Following the activity-structure relationships, the possible active sites for this catalysis must be discussed. Firstly, it has been

5. Electrochemical Fixation of Nitrogen and its Coupling with Biomass Valorization with a Strongly Adsorbing and Defect Optimized Boron-Carbon-Nitrogen Catalyst

recently reported that B-N bonds can act as the active sites for electrochemical NRR.²⁰³ As can be seen from XPS results, the excellent activity of BNC-2 indeed goes with a higher content of B-N bonds. Maybe more importantly, B and N atoms near defects could act as a FLP-like structure with positively polarized (electrophilic) B atoms and negatively polarized (nucleophilic) N atoms, and thus the reactants N_2 and HMF could be effectively activated by strong polarization on top of these structural motives.⁷ Furthermore, point defects at the grain boundaries between B-N and graphitic domains can lead to high catalytic activity because the unpaired electrons at such sites will provide binding sites for the substrate molecules and electron transfer activation. From a textural point of view, as a result of the higher nanoporosity, BNC-2 also exhibits higher electrochemical surface area (ECSA), according to capacitance measurements (Figure 5.25). This is of particular importance for the catalytic conversion of larger molecules such as HMF as they have to have access to the entire internal surface of the catalyst particles deposited on the electrodes.

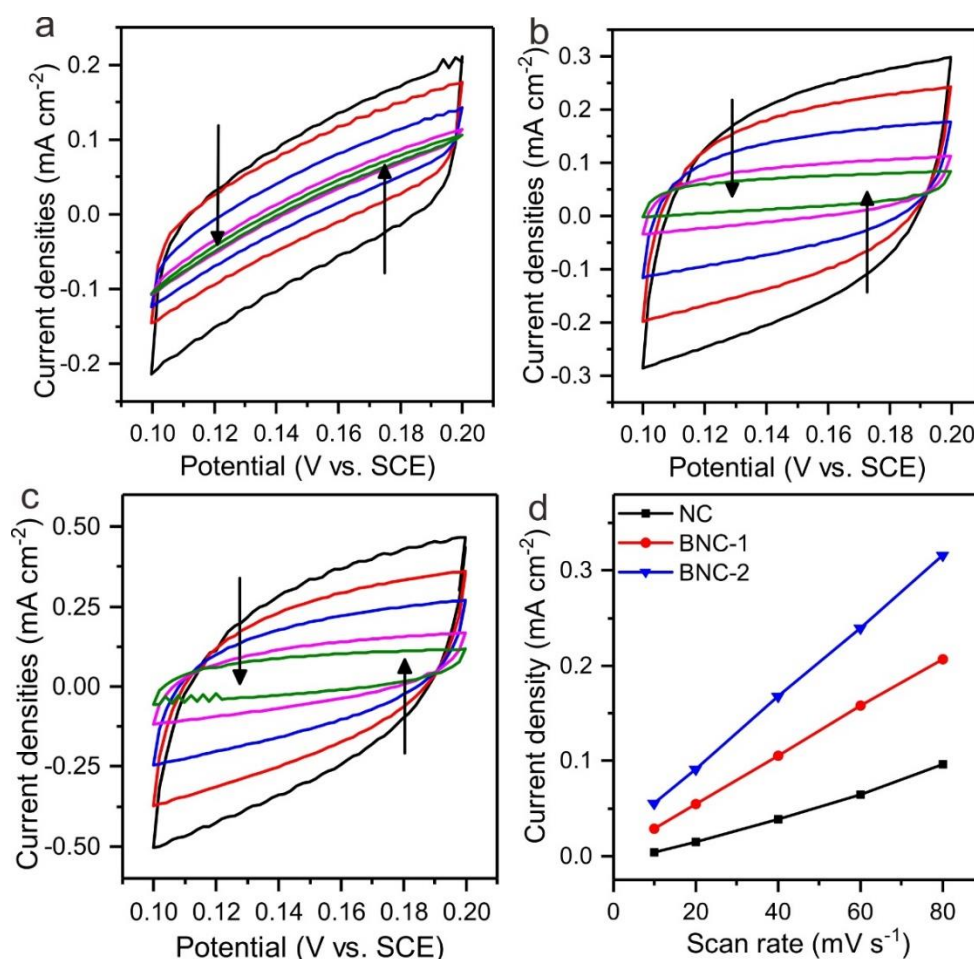


Figure 5.25. Cyclic voltammograms in the double layer region at scan rates of 80, 60, 40, 20, 10 mV/s (along the arrow direction) of (a) NC, (b) BNC-1 and (c) BNC-2. (d) Current density as a function of scan rate for NC, BNC-1 and BNC-2 electrode, respectively.

5. Electrochemical Fixation of Nitrogen and its Coupling with Biomass Valorization with a Strongly Adsorbing and Defect Optimized Boron-Carbon-Nitrogen Catalyst

As mentioned above, co-doping of N and B creates a porous structure with high SSA, which can be favourable for adsorption and activation of reactants as well as for electron/mass transfer. N₂ adsorption experiments at 298 K show that BNC-2 can indeed adsorb a higher volume of N₂ even at room temperature, compared with NC and BNC-1 (Figure 5.26a). N₂ adsorption at 273 K was also tested (Figure 5.26b) and exhibits the same trend. Based on those two datasets, the heat of adsorption (Q_{st}) for N₂ was estimated (Figure 5.26c). The Q_{st} values at low N₂ uptakes come with a rather high experimental error, and a comparison at higher volumes of adsorbed N₂ is more reliable. Indeed, the unusual high value of Q_{st} indicates strong affinity between BNC-2 and N₂ molecules. This quantifies the N₂ polarization beyond van der Waals binding and activation which is certainly one source of its higher NRR activity.

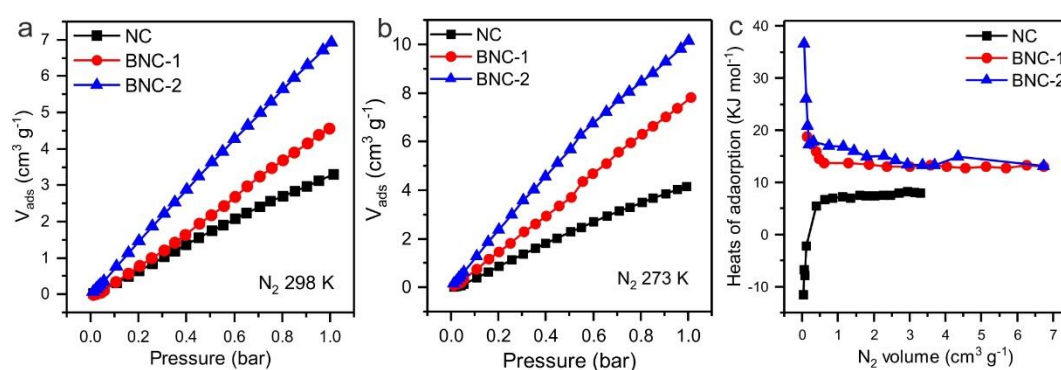


Figure 5.26. N₂ adsorption isotherms measured at (a) 298 K and (b) 273 K for NC, BNC-1 and BNC-2 materials. (c) Heat of N₂ adsorption for NC, BNC-1 and BNC-2 materials.

In summary, a novel N and B co-doped carbon catalyst with porous structure has been synthesized from simple precursors. The introduction of N and B heteroatoms leads to the construction of N-B motives and Frustrated Lewis pairs in a microporous architecture which is also rich in point defects. The latter can improve the strength of adsorption of reactants (N₂ and HMF) and thus their activation. As a result, BNC-2 exhibits a desirable electrochemical NRR and HMF oxidation performance. Gas adsorption experiments support the unusually strong binding and activation of N₂ and might serve as a simple descriptor to relate structure and catalytic activity. This work provides novel and deep insights into the rational design and the origin of activity in metal-free electrocatalysts and enable a physically viable discussion of the active motives. It also has a deep instruction for the construction of active sites as well as the search for their further catalytic applications.

6. Conclusions and perspectives

The central motivation of the thesis was to provide possible solutions and concepts to improve the performance (e.g. activity and selectivity) of electrochemical N_2 reduction reaction (NRR). Given that porous carbon-based materials usually exhibit a broad range of structural properties, they could be promising NRR catalysts. Therefore, the advanced design of novel porous carbon-based materials and the investigation of their application in electrocatalytic NRR including the particular reaction mechanism are the most crucial points to be addressed. In this regard, three main topics were investigated. All of them are related to the functionalization of porous carbon for electrochemical NRR with heteroatoms and metal-based materials in order to tailor their active reaction sites.

In chapter 3, a novel C-Ti_xO_y/C nanocomposite has been described that has been obtained via simple pyrolysis of MIL-125(Ti), and applied in electrochemical NRR. The density of covalent (O-)Ti-C bonds originating from carbon atoms and OVs (which can both be active sites for NRR) can be regulated by the synthesis temperature. Meanwhile, a novel mode for N_2 activation is achieved by doping carbon atoms from nearby porous carbon into the anion lattice of Ti_xO_y. By comparing the NRR performance of M-Ts and by carrying out DFT calculations, it is found that the existence of (O-)Ti-C bonds in C-doped Ti_xO_y can largely improve the ability to activate and reduce N_2 as compared to unoccupied OVs in TiO₂. In addition, such porous carbon-based materials can enhance electron conductivity and N_2 mass transfer as well. The strategy of rationally doping heteroatoms into the anion lattice of transition metal oxides to create active centers may open many new opportunities beyond the use of noble metal-based catalysts also for other reactions that require the activation of small molecules as well.

Heteroatom and metal co-functionalized porous carbon-based materials have also been described in chapter 4, where a novel catalyst construction composed of Au single atoms decorated on the surface of NDPCs was reported. The introduction of Au single atoms leads to active reaction sites, which are stabilized by the N species present in NDPCs. Thus, the interaction within as-prepared AuSAs-NDPCs catalysts enabled promising performance for electrochemical NRR. In detail, this highly open porous structure provides high SSA and favourable access to the active sites and enhances mass transport as well. For the reaction mechanism, Au single sites and N or C species can act as Frustrated Lewis pairs to enhance the electron donation and back-donation process to activate N_2 molecules. Under a potential of -0.2 V vs. RHE, a high FE of 12.3% and a NH_3 production rate of $2.32 \mu g h^{-1} cm^{-2}$ are achieved with the desirable stability. This work provides new opportunities for catalyst design in order to achieve efficient N_2 fixation at ambient conditions by utilizing recycled electric energy.

6. Conclusions and perspectives

The last topic described in chapter 5 mainly focused on the synthesis of dual heteroatom-doped porous carbon from simple precursors. The introduction of N and B heteroatoms leads to the construction of N-B motives and Frustrated Lewis pairs in a microporous architecture which is also rich in point defects. This can improve the strength of adsorption of different reactants (N_2 and HMF) and thus their activation. As a result, BNC-2 exhibits a desirable electrochemical NRR and HMF oxidation performance. Gas adsorption experiments have been used as a simple tool to elucidate the relationship between the structure and catalytic activity. This work provides novel and deep insights into the rational design and the origin of activity in metal-free electrocatalysts and enables a physically viable discussion of the active motives, as well as the search for their further applications.

Throughout this thesis, the ubiquitous problems of low selectivity and activity of electrochemical NRR are tackled by designing porous carbon-based catalysts with high efficiency and exploring their catalytic mechanisms. NRR with these catalysts provides a step towards practical value as promising alternative for the Haber-Bosch process. The structure-performance relationships and mechanisms of activation of the relatively inert N_2 molecules are revealed by either experimental results or DFT calculations. These fundamental understandings pave way for a future optimal design and targeted promotion of NRR catalysts with porous carbon-based structure, as well as study of new N_2 activation modes. Some other concepts are also inspired by the proved experiments. One example is that in addition to enhancement of the catalysts themselves, a major step forward in the efficiency of NRR will lie in finding ways to increase the local concentration of N_2 in close proximity to the catalysts. For example, ionic liquid with high N_2 solubility can be used as advanced electrolyte with higher NH_3 production rate, and HER can also be effectively inhibited due to low proton concentration. Porous carbon materials with hierarchical pore structure are potential candidates to both provide more N_2 adsorption sites and enhance mass transfer. In addition, composites of porous carbon with versatile structures and properties can also be applied to overcome the high energy barrier for N_2 reduction. For example, the catalytic properties of the reported Au single site catalysts and the dual-doped carbon materials could be further modified by engineering them into composites with pristine porous carbon materials. Notably, NH_3 can sometimes have stronger interaction with the active sites than N_2 , and result in a decreasing NH_3 production with reaction time. Thus, it will be also desirable to find some solutions to solve this problem with intelligent reactor engineering, such as designing flow cell system.

7. Appendix

7.1. Abbreviations

<i>Abbreviation</i>	<i>Full name</i>
AuSAs-NDPCs	Au single sites supported on N-doped carbons
AuNPs-NDPCs	Au nanoparticles supported on N-doped carbons
AuNPs-STCs	Au nanoparticles supported on salt-templated carbons
BNC	B and N co-doped carbon
BET	Brunauer-Emmett-Teller
CV	Cyclic voltammetry
C_{dl}	Double-layer capacity
CO ₂ RR	CO ₂ reduction reaction
C-Ti _x O _y /C	Carbon-doped and oxygen deficient titanium oxide/carbon
CNTs	Carbon nanotubes
DFF	2,5-diformylfuran
DFT	Density functional theory
DMF	Dimethylformamide
ECSA	Electrochemical active surface area
EELS	Electron energy loss spectrum
EPR	Electron paramagnetic resonance
EDX	Energy-dispersive X-ray spectroscopy
FE	Faradaic efficiency
FT-IR	Fourier transform infrared
FDCA	2,5-furandicarboxylic acid
FFCA	5-formyl-2-furancarboxylic acid
FLP	Frustrated Lewis pairs
¹ H NMR	¹ H nuclear magnetic resonance
HPLC	High performance liquid chromatography
HAT	Hexaazatriphenylene-hexacarbonitrile
HRTEM	High resolution transmission electron microscopy
HAADF-STEM	High-angle annular dark-field scanning transmission electron microscopy
HER	Hydrogen evolution reaction

7. Appendix

HMF	5-hydroxymethylfurfural
HMFOA	5-hydroxymethyl-2-furancarboxylic acid
H ₂ BDC	Terephthalic acid
ICP-MS	Inductively coupled plasma analysis coupled with mass spectrometry
IUPAC	International Union of Pure and Applied Chemistry
IEA	International Energy Agency
LSV	Linear sweep voltammetry
MOFs	Metal organic frameworks
MvK	Mars-van Krevelen
MeOH	Methanol
NRR	N ₂ reduction reaction
NHE	Normal hydrogen electrode
NDPCs	N-doped porous carbons
NC	N-doped carbon
OVs	Oxygen vacancies
ORR	Oxygen reduction reaction
OER	Oxygen evolution reaction
PSD	Pore size distribution
PCET	Proton-coupled electron transfer
PBE	Perdew-Burke-Ernzerhof
QSDF	Quenched solid density functional theory
Q _{st}	Heat of adsorption
RHE	Reversible hydrogen electrode
STCs	Salt-templated carbons
SSA	Specific surface area
SEM	Scanning electron microscopy
SCE	Saturated calomel electrode
SSAs	Specific surface areas
TPES	Total primary energy supply
TPV	Total pore volume
TEOS	Tetraethyl orthosilicate
TGA	Thermogravimetric analysis

TEM	Transmission electron microscopy
XRD	X-ray powder diffraction
XPS	X-ray photoelectron spectroscopy

7.2. Applied methods

7.2.1. Thermogravimetric analysis (TGA)

TGA is based on the measurement of mass change for one sample as a function of temperature and time. The temperature is generally increased with a constant rate. A variety of atmospheres including air, vacuum, inert gas, oxidizing/reducing gases and many others can be used for the thermal reaction. It allows to monitor different thermodynamic events such as thermal decomposition, oxidation/reduction events, as well as the adsorption and desorption of gases.

7.2.2. Electron paramagnetic resonance (EPR)

EPR is usually used to investigate the presence of unpaired electrons within materials. EPR signals can be obtained based on the following theory: As every electron has a magnetic moment of $m_s = \pm\frac{1}{2}$ and spin quantum number of $s = \frac{1}{2}$. Under an external magnetic field (B_0), the magnetic moment can be either $+\frac{1}{2}$ or $-\frac{1}{2}$, assigning to align itself parallel or antiparallel, respectively. According to the Zeeman effect, every alignment has its specific energy (E) (Equation 7.1):

$$E = m_s g_e \mu_B B_0 \quad (7.1)$$

Besides, the energy difference between those two types of alignments can be calculated (Equation 7.2):

$$\Delta E = E_{-\frac{1}{2}} - E_{+\frac{1}{2}} = g_e \mu_B B_0 \quad (7.2)$$

where g_e is the so-called g-factor of an electron ($g_e = 2.0023$ for a free electron),²³³ and μ_B is the Bohr magneton.

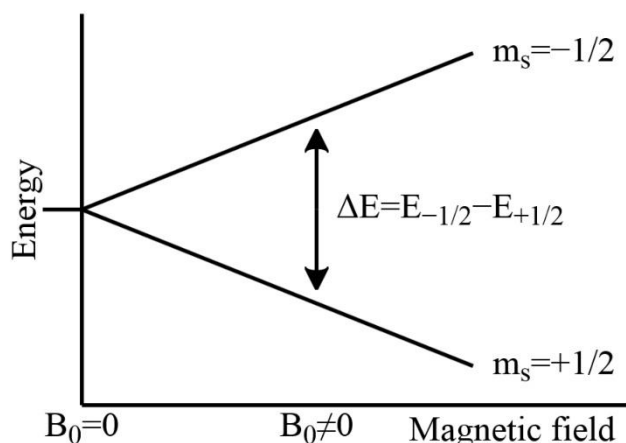


Figure 7.1. The energy difference of unpaired electrons between the parallel and antiparallel alignments.²³⁴

Therefore, it can be concluded that ΔE of unpaired free electrons is proportional to B_0 . As unpaired electrons can move between two energy levels by absorbing or emitting a photon with the energy of $h\nu$, leading to the fundamental equation of EPR spectroscopy (Equation 7.3):

$$h\nu = g_e\mu_B B_0 \quad (7.3)$$

In order to generate EPR signals, the value of ν is normally fixed by exposing paramagnetic centers to constant microwaves, and the intensity of B_0 is increased until the energy gap matches the energy of given microwave, thereby unpaired electrons can move between two spin states. According to the Maxwell-Boltzmann distribution, the number of electrons in the lower state dominates, and there is a net energy adsorption, which can be detected and then transformed into a spectrum.

7.2.3. Nuclear magnetic resonance (NMR) spectroscopy

NMR spectroscopy is based on a comparable theory like EPR, but uses the resonance of the nucleus. As the magnetic moment of an electron is larger than the corresponding quantity for any nucleus, there is much lower electromagnetic frequency needed for the spin resonance of nucleus, although the higher frequency results in higher sensitivity.²³⁵ In detail, a magnetic field is applied to the sample, followed by the excitation with radio waves to produce an NMR signal. It is widely used in determining the structure of compounds according to their different local chemical environment (e.g. chemical shift and J-coupling). Notably, it is also an isotope-sensitive method, which can be employed to track reaction processes and understand reaction mechanisms.²³⁶ By using internal or external standard methods, the quantification of different compounds can be achieved.

7.2.4. X-ray Diffraction (XRD)

XRD is based on the interaction between the X-ray and electrons in the specimen, and gives information about the structure of crystalline materials. Firstly, X-ray beams are generated by hitting inner electrons in the atoms with the help of high-energy electrons, resulting in the radiation of continuous X-rays and specific X-rays. The latter are monochromatic and can be used for XRD measurements. Therefore, when monochromatic X-rays interact with the sample, there are two types of interactions between them, including elastic and inelastic interactions, where the latter can lead to coherent scattering. Due to the light interference, the strongest radiation can be achieved when the wavelength of radiation (λ) is in the same range with the distance of the diffraction lattice, and it is called diffraction radiation (Figure 7.2). Considering that crystalline materials have many diffraction lattices, diffraction radiation only occurs when the optical path difference (Δ) is an integral multiple of the wavelength based on the Bragg's Law (Equation 7.4),

$$\Delta = n\lambda = 2d\sin\theta \quad (7.4)$$

where d is the interlayer spacing of the atomic lattices, θ is specific diffraction angles. As λ is fixed, d can be calculated by measuring θ or the reverse. Therefore, the recorded diffractogram reveals the characteristic diffraction pattern of the investigated sample.

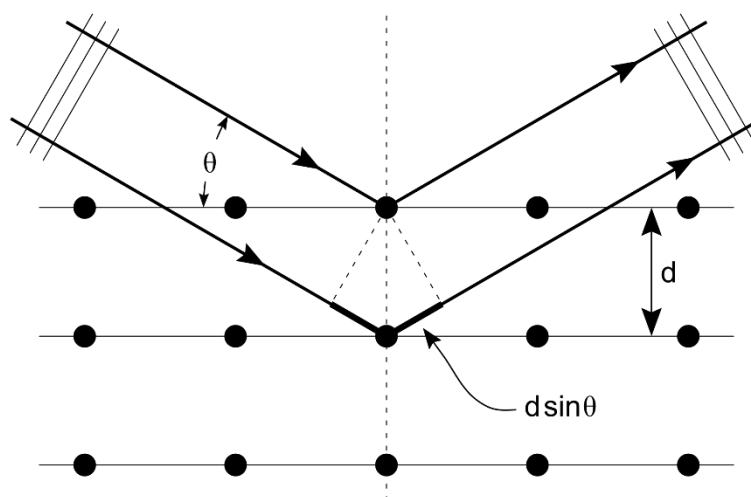


Figure 7.2. Constructive interference between the X-ray and sample.²³⁷

7.2.5. Infrared (IR) spectroscopy/Raman spectroscopy

As another structure-determining technique, Infrared spectroscopy or Raman spectroscopy can be used to observe the vibrational, rotational, and other low-frequency modes in molecules and crystals, corresponding to characteristic chemical bonding motives. Infrared spectroscopy is based on the interaction between infrared light and molecules. The infrared adsorption only

occurs when the frequency of the adsorbed radiation matches the vibrational frequency of a given bond. Raman spectroscopy is based on the analysis of Raman scattering (inelastic scattering). The specimen is illuminated with a laser beam, due to the interaction between the laser light and molecular vibrations, the energy of photons can decrease (Stokes shift) or increase (Anti-Stokes shift), corresponding to various vibration modes in the system. Notably, Raman spectroscopy and Infrared spectroscopy are complementary with each other. Raman active molecules must undergo polarization during the vibration, while IR adsorption is based on the change of molecular dipole moment. Notably, molecules with a strong dipole moment are typically hard to polarize.

7.2.6. Transitional electron microscopy (TEM) / Scanning electron microscopy (SEM)

TEM and SEM are based on the interactions between electrons and samples. After the interaction, different types of electrons are formed (Figure 7.3), e.g., transmission electrons, scattered electrons, auger electrons, secondary electrons and others, which contain specific information about the sample.²³⁸ Generally, electrons are generated by an electron gun, accelerated by an electromagnetic field, and then vertically directed as well as focused on the specimen by different lense systems. Finally, the image is recorded, magnified and focused onto an image recording device.

In TEM, electrons collide with the sample atoms and change the direction to produce solid angle scattering. The scattering angles are related with the density, composition, and thickness of the sample, and thus different angles correspond to the bright or dark areas in the TEM images. For example, non-scattered (transmitted) electrons or slightly scattered electrons and largely scattered electrons are detected for the bright field mode and dark field mode of TEM, respectively. According to the corrected de Broglie equation (Equation 7.5), the wavelength of electrons is related to their kinetic energy, and thus high acceleration voltage allows for high resolution TEM (HRTEM).

$$\lambda_e = \frac{h}{\sqrt{2m_0E \left(1 + \frac{E}{2m_0c^2}\right)}} \quad (7.5)$$

where h is the Planck's constant, m_0 is the mass of an electron, and E is the energy of the accelerated electrons.

Scanning TEM (STEM) is performed by scanning the sample with an aggregated electron beam and detecting the beam of transmitted electrons or elastically scattered electrons. It is mostly used in high angle annular dark field (HADDF-STEM) mode to characterize the atomic structure. In addition, for the inelastic scattering, the electron energy loss spectroscopy (EELS)

can reflect the characteristic properties of the sample, such as compositions, chemical bonds and electronic structures.

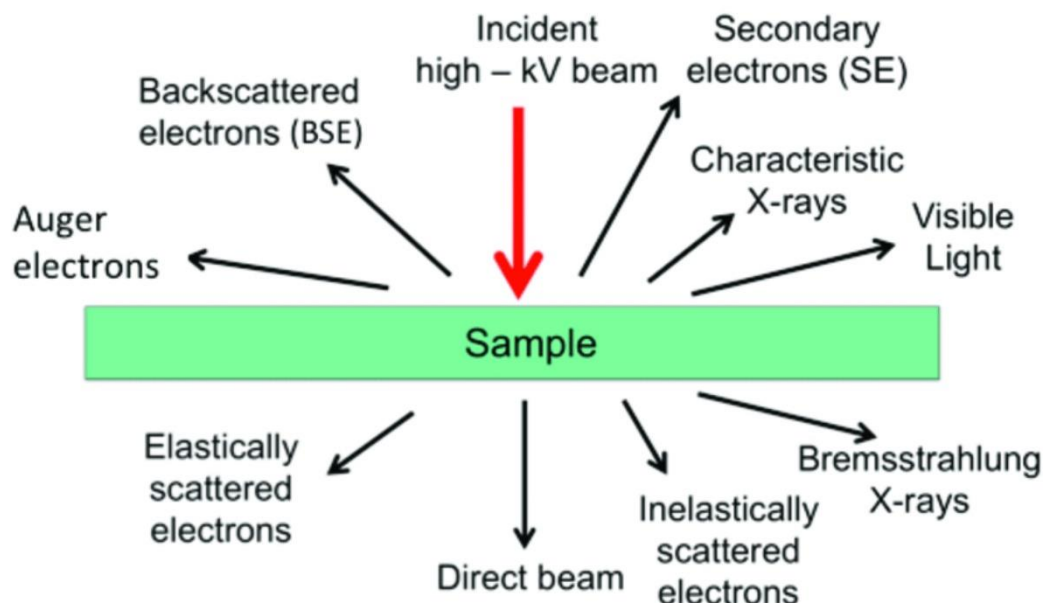


Figure 7.3. Possible interactions between a sample and high energy electrons.

SEM is based on the scanning of the sample surface by focused beam of electrons and detection of different electrons, containing information about surface topography and composition. For example, secondary electrons with low energy, generated by the interaction of electron beam and valence electron of sample surface, are used to characterize the morphology. As the local curvatures (e.g., edges, corners, or plates) can facilitate the release of secondary electrons, the intensity contrast in the SEM image contains information about the surface topology. Backscattered electrons with high energy are used to detect contrasts between areas with different chemical compositions. When an electron in the inner shell of an atom is excited to form an electron hole, this hole can be occupied by an electron from the outer shell. During this process, X-rays are released due to the energy difference between the inner and outer shell. Notably, the energy and intensity of these X-rays are specific for each element and their corresponding content, and thus identification and quantification can be achieved, respectively, named energy-dispersive X-ray spectroscopy (EDX). EDX-mapping can be performed to study the element distribution on the sample surface, because it is a surface-sensitive technique.

7.2.7. X-ray photoelectron spectroscopy (XPS)

XPS is also a surface-sensitive technique, which can be used to measure the element compositions and their contents, and more importantly, it can provide information about the chemical and electronic state of different elements. XPS is based on the interaction between X-rays and the sample surface, as the kinetic energy ($E_{kinetic}$) and number of the emitted electrons

that escape from the top 0 to 10 nm of the sample can be measured. As a result, the electron binding energy (E_{binding}) can be calculated according to the Equation 7.6 based on the work of Ernest Rutherford:

$$E_{\text{binding}} = E_{\text{photon}} - (E_{\text{kinetic}} + \phi) \quad (7.6)$$

where E_{photon} is the energy of X-ray photon and ϕ is the work function related to the instrument and specimen. The value of E_{binding} is specific for with fixed beam of X-ray to achieve identification for different elements. Notably, elemental quantification can only be achieved for the relative surface composition.

In addition, due to the different chemical environment of elements, their E_{binding} can have corresponding shift, indicating the chemical state as well as the type and amount of formed chemical bonds.

7.2.8. High performance liquid chromatography (HPLC)

HPLC is a very useful tool in the analytical area to separate, identify, and quantify different components in a solution. It is based on a continuous exchange process of solute between the stationary phase and the mobile phase. Thus, different partition coefficients of components result in their separation. Through internal and external standard method, in combination with suitable detectors, identification and quantification of specific components can be achieved.

7.2.9. N₂ physisorption

Physisorption, namely physical adsorption, is based on van-der Waals interactions (without the formation of covalent chemical bonds) between the adsorbates (molecules adsorbed on a surface) and the adsorbents (solid materials). Gas physisorption is one of the most useful tools to study the textural structure (e.g., porosity, pore geometry and surface polarity) of porous materials, including N₂ physisorption at 77 K, Ar physisorption at 87 K and CO₂ physisorption at 273 K. Among them, N₂ at 77 K is the most widely used strategy, due to its convenience, non-destructivity, and precise analysis over a wide range of pore size from smallest micropores to large mesopores.

During the N₂ physisorption measurement, an isotherm with adsorption part and desorption part is recorded and plotted by the amount of adsorbates as a function of the relative pressure (p/p_0 , p is the absolute pressure and p_0 is the saturation pressure of the adsorbates at a specific temperature). In the detailed procedures, N₂ is firstly dosed in small portions into the closed thermostatted tube cell with the sample to be tested on the bottom, and the volume of adsorbed and then desorbed N₂ at different p/p_0 (from ~0 to ~1.0) is detected and recorded as various points to form the adsorption and desorption branch of isotherm, respectively. Especially, the

shape of N₂ physisorption isotherm at 77 K can represent the interactions between N₂ molecules and adsorbents, thus indicating the pore structure (e.g. size and shape).²³⁹

Therefore, it can be generally classified into eight types of isotherms according to their different shapes (Figure 7.4). Type I(a) and (b) are the typical isotherms of microporous materials with small external surface areas, and the difference between them is attributed to the size of micropores. A steep N₂ uptake at lower p/p_0 in I(a) is due to the filling of narrow micropores (with width < 0.7 nm), whereas the filling of wide micropores or even narrow mesopores (with width of 0.7-2.5 nm) results in the isotherm of I(b). Type II represents the isotherm of nonporous or macroporous materials, which is ascribed to the unrestricted monolayer to multilayer adsorption on the surface. Point B corresponds to the completion of the monolayer coverage. Compared with type II isotherms, type III also represents nonporous or macroporous materials but with weak interactions between the adsorbents and adsorbates. In addition, there is no distinctive B point in type III isotherms due to the absence of monolayer formation, and the adsorbed molecules are clustered on the most favorable sites. Isotherms of type IV(a) and IV(b) with a hysteresis and a typical saturation plateau are typical for mesoporous materials, and the adsorption behavior is determined by the adsorbate-adsorbent interactions and also interactions between the adsorptive molecules in the condensed state. The adsorption at lower p/p_0 occurs on the mesopore walls with a similar shape of corresponding part in type II isotherm. When the pressure increases to a certain value (less than saturation pressure p_0 of the bulk liquid), gas adsorbates condense to a liquid-like phase in the mesopores.²⁴⁰ The difference between the type IV(a) and IV(b) is due to the mesopore size. In the case of type IV(a), capillary condensation occurs with the formation of hysteresis loop as the pore exceeds a certain critical size (e.g., > 4 nm for N₂ adsorption in the cylindrical pores at 77 K). If the mesopores are smaller, a reversible type IV(b) isotherm can be observed. A type V isotherm exhibits similar shape with type III at low p/p_0 range due to the weak interactions between the adsorbents and adsorbates, and can be observed in the water adsorption on hydrophobic microporous or mesoporous materials.²⁴⁰ A type VI isotherm represents layer-by-layer adsorption on a nonporous material.

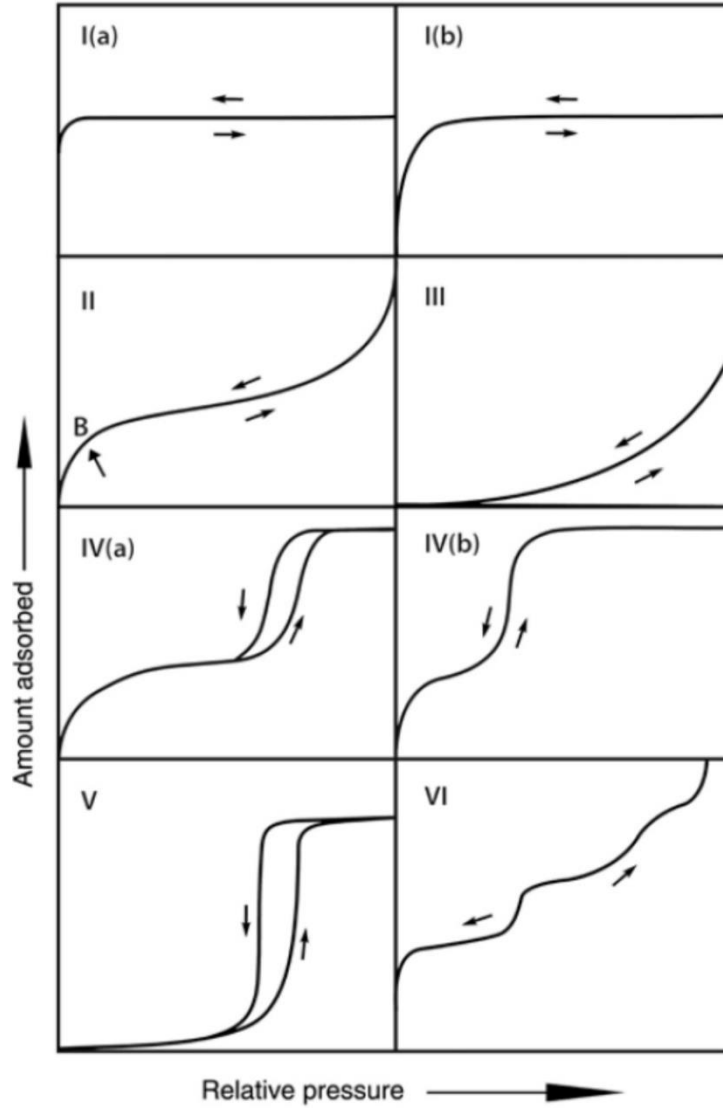


Figure 7.4. Classification of physisorption isotherms according to IUPAC.³¹

The recorded isotherms can also be used to calculate the SSA of materials according to different models, e.g., Langmuir method, DFT-based method and Brunauer-Emmett-Teller (BET) method.^{239, 241} The BET model is widely applied, as it considers both the monolayer and multilayer adsorption on the pore structure with different adsorption enthalpy for the corresponding layer. The BET equation in the linear form is as following (Equation 7.7):

$$\frac{p/p_0}{V_{ads}(1-p/p_0)} = \frac{1}{C \cdot V_{mono}} + \frac{1}{C \cdot V_{mono}} \frac{p}{p_0} \quad (7.7)$$

where V_{ads} is the total adsorbed volume, V_{mono} is volume of monolayer adsorption, C is adsorption constant, and $\frac{p}{p_0}$ is the relative pressure. If $\frac{p/p_0}{V_{ads}(1-p/p_0)}$ is plotted against $\frac{p}{p_0}$, V_{mono} can be obtained from the intercept of y-axis or the slope.

SSA can be further evaluated from the V_{mono} value according to Equation 7.8:

$$SSA = \frac{N_A \cdot V_{mono} \cdot \sigma_{N_2}}{V_{mol} \cdot m_{ads}} \quad (7.9)$$

where $\bar{\sigma}_{N_2}$ is the surface area needed for one N_2 molecule in dense package (0.162 nm^2). N_A , V_{mol} and m_{ads} are the Avogadro constant ($6.022 \cdot 10^{23} \text{ mol}^{-1}$), the ideal gas volume ($0.0224 \text{ m}^3 \text{ mol}^{-1}$), and the adsorbent mass, respectively.

However, there are still some limitations for BET method. For example, in the case of micro-mesoporous materials, an overestimation of the V_{mono} usually occurs, as it is difficult to distinguish the monolayer and multilayer adsorption in the low relative pressure, where the plot shows linear relation. Therefore, DFT-based methods are also developed, which can achieve a more realistic explanation and modelling of the adsorption mechanism, and allow a more reliable calculation of the SSA and pore size distribution over the complete range of micro- and mesopores. The quenched solid density functional theory (QSDFT) even considers surface roughness and defects on the heterogeneous surface which is of particular importance for carbon materials.²⁴²

7.3. Experimental Section

7.3.1. Chemicals

Table 7.1. List of used chemicals.

<i>Chemical</i>	<i>Chemical formula</i>	<i>Purity</i>	<i>Supplier</i>
Acetonitrile	CH_3CN	99.8%	Sigma Aldrich
Acetic acid	CH_3COOH	$\geq 99\%$	Sigma Aldrich
Ammonia	$\text{NH}_3 \cdot \text{H}_2\text{O}$	$\geq 28\%$	Sigma Aldrich
Ammonium chloride	NH_4Cl	$\geq 99\%$	Sigma Aldrich
Ammonium- ^{15}N chloride	$^{15}\text{NH}_4\text{Cl}$	98%	Sigma Aldrich
Boric acid	H_3BO_3	$\geq 99\%$	Alfa Aesar
Carbon paper	C	ultrapure	Shanghai Hesun Electric Co., Ltd
Deuterium oxide	D_2O	99.9%	Sigma Aldrich
Diaminomaleonitril	$\text{C}_4\text{H}_4\text{N}_4$	99.8%	Sigma Aldrich
2,5-diformylfuran	$\text{C}_6\text{H}_4\text{O}_3$	97%	Sigma Aldrich
Dimethylformamide	$\text{C}_3\text{H}_7\text{NO}$	99.8%	Sigma Aldrich
Ethanol	$\text{CH}_3\text{CH}_2\text{OH}$	$\geq 99.8\%$	Sigma Aldrich
5-formyl-2-furancarboxylic acid	$\text{C}_6\text{H}_4\text{O}_4$	$\geq 98\%$	Tokyo Chemical Industry

7. Appendix

2,5-furandicarboxylic acid	$C_6H_4O_5$	97%	Sigma Aldrich
Gold (III) chloride trihydrate	$HAuCl_4 \cdot 3H_2O$	$\geq 99.9\%$	Sigma Aldrich
Hexaketocyclohexane octahydrate	$C_6O_6 \cdot 8H_2O$	97%	Sigma Aldrich
5-hydroxymethylfurfural	$C_6H_6O_3$	99%	Sigma Aldrich
5-hydroxymethyl-2-furancarboxylic acid	$C_6H_6O_4$	97%	Cayman Chemical Company
Hydrogen peroxide	H_2O_2	30%	Sigma Aldrich
Hydrofluoric acid	HF	$\geq 48\%$	Sigma Aldrich
Hydrochloric acid	HCl	37%	Sigma Aldrich
Lithium perchlorate	$LiClO_4$	$\geq 99.99\%$	Sigma Aldrich
L-cysteine	$C_3H_7NO_2S$	97%	Sigma Aldrich
Melamine	$C_3H_6N_6$	99%	Sigma Aldrich
Nitric acid	HNO_3	65%	Sigma Aldrich
Nessler reagent	HgI_4K_2	Nessler reagent	Sigma Aldrich
Para-(dimethylamino) benzaldehyde	$C_9H_{11}NO$	99%	Sigma Aldrich
Potassium sodium tartrate	$KNaC_4H_6O_6$	99%	Sigma Aldrich
Sodium hydroxide	NaOH	$\geq 99.5\%$	Merck
Sulfuric acid	H_2SO_4	98%	Merck
Salicylic acid	$C_7H_6O_3$	$\geq 99.5\%$	Sigma Aldrich
Sodium citrate	$Na_3C_6H_5O_7$	$\geq 99\%$	Sigma Aldrich
Sodium hypochlorite	NaClO	6%-14% active chlorine	Merck
Sodium nitroferricyanide	$C_5FeN_6Na_2O$	99%	Sigma Aldrich
Sucrose	$C_{12}H_{22}O_{11}$	$\geq 99.5\%$	Sigma Aldrich
Tetraethyl orthosilicate	$Si(OC_2H_5)_4$	$\geq 99\%$	Sigma Aldrich
Terephthalic acid	$C_8H_6O_4$	98%	Sigma Aldrich
Tetra-n-butyl titanate	$C_{16}H_{40}O_4Ti$	97%	Sigma Aldrich
Titanium dioxide	TiO_2	99%	Sigma Aldrich
Zinc chloride	$ZnCl_2$	$\geq 98\%$	Alfa Aesar

7.3.2. Materials synthesis of enhanced electrocatalytic N₂ reduction via partial anion substitution in titanium oxide-carbon composites

Synthesis of MIL-125(Ti): MIL-125(Ti) was synthesized by a modified method reported in literature.¹⁶⁴ 0.5 g of Terephthalic acid (H₂BDC) and 0.26 mL of tetra-n-butyl titanate Ti(OC₄H₉)₄ were added into a mixed solution with dimethylformamide (DMF) (9 mL) and dry MeOH (1 mL). The mixture was stirred for 1 h at room temperature, followed by transferring into a 50 mL Teflon-lined autoclave and heating at 150 °C for 20 h. The white-colored products were collected, rinsed several times with acetone and dried under vacuum at 60 °C overnight for further use.

Synthesis of M-Ts: M-Ts were prepared by simple pyrolysis. In a typical procedure, 0.25 g MIL-125(Ti) was transferred to a tubular furnace and heated at different temperatures for 2 h with a heating rate of 4 °C min⁻¹ under Ar atmosphere.

Synthesis of M-Ts-N₂: M-Ts-N₂ was prepared by following the procedures of M-Ts, while only changing the protection gas from Ar to N₂.

Synthesis of C-treated TiO₂ and non-C-treated TiO₂: 0.5 g of H₂BDC and 0.1 g commercial TiO₂ were mixed ground uniformly in a mortar, followed by transferring into a tubular furnace and heating at 1000 °C for 2 h with a heating rate of 4 °C min⁻¹ under Ar atmosphere. As a comparison, commercial TiO₂ was also treated under the same experimental conditions without the use of H₂BDC to obtain non-C-treated TiO₂.

7.3.3 Materials synthesis of single-site gold catalysts on hierarchical N-doped porous noble carbon for enhanced electrochemical reduction of nitrogen

Synthesis of SiO₂ nanospheres: According to modified Stöber method reported in the literature,²⁴³ Tetraethyl orthosilicate (TEOS) (6 mL) was rapidly injected into a mixture of ethanol (74 mL) and deionized water (10 mL), followed by the addition of ammonia aqueous solution (28%, 3.15 mL). After stirring at room temperature for 1 h, obtained colloidal suspension was washed with water and ethanol several times for further use.

Synthesis of STCs: STCs were prepared following the method described in the literature by using ZnCl₂ as the salt template.²⁴⁴ In a typical procedure, sucrose (5 g), ZnCl₂ (5 g) and concentrated sulfuric acid (0.55 g) were mixed in ultrapure water (30 mL). The mixture was then dried at 100 °C for 6 h under air, followed by heating to 160 °C and keeping for 6 h. As-obtained product was finally transferred to a tubular furnace for carbonization at 900 °C for 2 h to get STCs with a heating rate of 1 °C min⁻¹ under N₂ atmosphere.

Synthesis of HAT: HAT was synthesized according to previous reports.²⁴⁵ In detail, hexaketocyclohexane octahydrate (4 g) and diaminomaleonitrile (10.88 g) were refluxed in

acetic acid (AcOH, 150 mL) for 2 h to form a black suspension, followed by filtering off immediately and washing with hot AcOH (3×25 mL). As-obtained black solid was dispersed in HNO₃ aqueous solution (30%, 60 mL), and then heated at 100 °C for 3 h. The suspension with dark brown color was mixed with ice water (200 mL) to cool down overnight, followed by filtering again. The final purification was achieved by refluxing in acetonitrile (400 mL) for 2 h. The filtrate was evaporated under vacuum to yield an orange solid.

Synthesis of NDPCs: HAT was employed as the precursor for the synthesis of STCs. In a typical process, 100 mg of HAT and 500 mg of SiO₂ nanospheres were dispersed in a mixture of water (15 mL) and acetonitrile (15 mL) by ultrasound and stirred at room temperature for 6 h. After washing with water for several times and drying under vacuum, the light-yellow solid was carbonized at 900 °C under N₂ flow with a heating rate of 4 °C min⁻¹ for 1 h. NDPCs were finally obtained by using aqueous hydrofluoric acid (5 wt.%) to remove the SiO₂ template.

Synthesis of AuSAs-NDPCs, AuNPs-NDPCs and AuNPs-STCs: Typically, NDPCs were dispersed in water (15 mL) with stirring. Then, different amount of HAuCl₄ aqueous solution (0.02 M) was slowly added into the above mixture. AuSAs-NDPCs were obtained by adding 0.10 mL HAuCl₄ aqueous solution, while 0.370 mL dosage resulted in the formation of AuNPs-NDPCs. After stirring at room temperature for 7 h, the product was collected by centrifugation, washing with water and drying under vacuum at 60 °C overnight, followed by reducing by Ar/H₂ (with H₂ content of 5 %) atmosphere. Synthesis of AuNPs-STCs was carried out by only replacing the NDPCs with STCs.

7.3.4 Materials synthesis of electrochemical fixation of nitrogen and its coupling with biomass valorization with a strongly adsorbing and defect optimized boron-carbon-nitrogen Catalyst

Synthesis of BNC and NC: In a typical synthesis, different ratios of melamine to L-cysteine to boric acid were mixed by ball milling (for 5 minutes), and as-obtained uniform precursors were used to synthesize N, B co-doped carbon (BNC-1 and BNC-2) and N-doped carbon (NC). The obtained precursors were then transferred to a tubular furnace to undergo pyrolysis at 600 °C for 2 h and then 1000 °C for another 2 h under a flow of N₂ gas. The final products were collected after the furnace was cooled down to room temperature.

7.3.5 Materials characterization

X-ray powder diffraction (XRD) patterns were collected on a Bruker D8 advance X-ray diffractometer with Cu K α radiation. Scanning electron microscopy (SEM) images were recorded on a JSM-7500F instrument (JEOL). Energy-dispersive X-ray (EDX) investigations

were conducted on a Link ISIS-300 system equipped with a Si (Li) detector. Transmission electron microscopy (TEM) and high-resolution TEM (HRTEM) was conducted on a JEOL ARM 200F instrument operating at 200 kV. The samples were dispersed in ethanol, and then coated on a carbon-coated copper TEM grid and finally dried at room temperature before the test. X-ray photoelectron spectroscopy (XPS) measurements were conducted on a Thermo Scientific K-Alpha⁺ X-ray photoelectron spectrometer. All samples were analyzed using a microfocused, monochromated Al-K α X-ray source (1486.68 eV; 400 μ m spot size). Fourier transform infrared (FT-IR) spectra were measured on a Thermo Scientific Nicolet iS5 FT-IR spectrometer. Raman spectra were recorded on a Witec (focus innovations) Raman Microscope, carried out with an objective (Nikon, 10x/0.25, ∞ - WD 6.1) and an excitation wavelength of 532 nm and a laser power of 3.5 mW. EPR measurements at room temperature (296 K) were conducted on a Magnettech Minscope MS300 X-band EPR spectrometer. Samples were prepared in 50 μ l-ringcaps micropipettes with an inner diameter of 1 mm. N₂ physisorption isotherms measurements were firstly carried out at 77 K on a Quadrasorb apparatus from Quantachrome Instruments. The specific surface area (SSA) was calculated using the Brunauer-Emmett-Teller (BET) equation applied to nitrogen adsorption data in the relative pressure range $P/P_0 < 0.2$ in the linear region with the best correlation. Total pore volume was calculated from the amount of N₂ adsorbed at the relative pressure of 0.995. The N₂ pore size distribution was obtained by QSDFT model with slit/cylindrical pore shape using nitrogen adsorption data at 77 K (adsorption branch kernel). N₂ and CO₂ adsorption measurements were also carried out up to 1 bar at 273 K (ice-water bath) and 298 K (room temperature) on a Quantachrome Quadrasorb SI apparatus. The heat of adsorption of N₂ and CO₂ was calculated by Quantachrome ASiQwin software. Prior to all gas adsorption measurements, the samples were outgassed at 150 °C for 15 h under vacuum. The content of Au was analyzed by inductively coupled plasma mass spectrometry (ICP-MS). Elemental analysis was accomplished by a Vario Micro device. UV-Vis spectroscopic measurements were conducted with a Cary 50 UV-Vis spectrometer. High performance liquid chromatography (HPLC) analysis was conducted at an HPLC instrument from Agilent Technologies 1200 series equipped with a 1200 Diode-array-detector with Thermo Scientific Hypersil GOLD Column-Length 250 mm, 4.6 mm ID, 5 μ m, C18 column. A Shimadzu GC-2014 gas chromatograph equipped with both TCD and FID detectors was used to detect the gas products. Thermogravimetric analysis (TGA) was conducted on a Netzsch TG 209 F₁ device under constant artificial air flow. The sample was put into a platinum pan at a heating rate of 10 °C min⁻¹ to 1000 °C.

7.3.6 DFT calculations

Computation details (in cooperation with Dr. Yun Zhao and Dr. Haijun Jiao): Spin-polarized periodic DFT calculations were performed by using Vienna ab initio Simulation Package (VASP).²⁴⁶⁻²⁴⁷ The generalized gradient approximation was used with the Perdew-Burke-Ernzerhof (PBE) of exchange-correlation functional.²⁴⁸⁻²⁴⁹ The PBE functional with Grimme's D3 correction is used to include van der Waals dispersion interaction.²⁵⁰ The valence electronic states were expanded in plane wave basis sets with an energy cutoff of 450 eV and geometry optimizations were performed until the maximum force on each relaxed atom was less than 0.02 eV/Å. Due to the strong correlation effect among the partially filled Ti 3d states, the Hubbard parameter, U ,²⁵¹ was used for the Ti 3d electrons to take the on-site Coulomb interaction into account. According to previous work, the value of $U-J$ of 4.2 eV was applied.²⁵²⁻²⁵³

The Gibbs free energy change (ΔG) of the elementary step was calculated with the equation: $\Delta G = \Delta E_{\text{DFT}} + \Delta E_{\text{zpe}} - T\Delta S_{\text{vib}}$, where ΔE_{DFT} is change of DFT total energy, ΔE_{zpe} and $T\Delta S_{\text{vib}}$ is change of zero point energies and the entropy. ΔE_{zpe} and $T\Delta S_{\text{vib}}$ are calculated by vibrational frequencies of the surface intermediates within DFT calculation ($T = 298.15$ K), for the gaseous molecules, the entropy contributions ($T\Delta S$) were obtained from the experimental values at 298.15 K.

Since XRD analysis proved that the NRR catalysts mainly contain the Rutile phase, a Rutile TiO_2 model was calculated. The calculated lattice parameters of the unit cell are $a = 4.69$ Å and $c = 3.04$ Å, in excellent agreement with the experimental values ($a = 4.587$ Å and $c = 2.956$ Å).²⁵⁴ In our calculations, the most stable $\text{TiO}_2(110)$ surface was used,²⁵⁵⁻²⁵⁶ which was modeled with a $p(3 \times 1)$ periodic slab with twelve layers (Figure S30), and the vacuum between slabs is 15 Å, correspondingly, a $4 \times 5 \times 1$ k-point mesh was used.²⁵⁷ During the structural optimization, the lowest three layers were fixed in the bulk positions and the upper nine layers and the adsorbates were allowed to relax (Figure 3.39). The stoichiometric Rutile $\text{TiO}_2(110)$ surface exhibits five- and six-fold coordinated Ti atoms (Ti_{5c} and Ti_{6c}) as well as two- and three-fold coordinated oxygen atoms (O_{2c} and O_{3c}) (Figure 3.39).

Since only partial surface oxygen atoms of TiO_2 were substituted by carbon atoms to form $\text{C-Ti}_x\text{O}_y$ at very high temperature, both C-doped and surface oxygen vacancy models have been constructed for the calculation. In the C-doped model, one surface oxygen atom was replaced by one carbon atom (Figure 3.40a). Since both O_{2c} and O_{3c} are available on the surface, the formation energy was computed on the basis of the formal reaction of $\text{TiO}_2 + 2\text{C}(\text{graphene}) = \text{TiO}_{2-x}\text{C} + \text{CO}(\text{g})$. The calculation shows that the O_{3c} substitution is more favoured

thermodynamically than O_{2c} substitution by 0.18 eV (+7.64 vs. +7.82eV). To understand the specific role of C doping, the reaction on the surface with an oxygen vacancy was also computed by deleting one O_{2c} (Figure 3.40c), and the removal of one O_{2c} is thermodynamically more favourable than that of one O_{3c} by 0.98 eV (3.25 vs. 4.23 eV). As a consequence, both more stable models were used to compute N_2 activation and NH_3 formation. Since hydrogen is available under the reaction condition, all surface O_{2c} atoms were saturated by adsorbing H atoms (Figure 3.40b). Accordingly, this hydrogenation addition is strongly exothermic by 2.88 eV for the C-doped model and by 0.58 eV for the surface oxygen vacancy model.

7.3.7. Electrochemical tests

Electrode preparation: Typically, the working electrode, which was prepared by depositing an ethanol dispersion of catalysts ink onto a carbon paper electrode ($1 \times 1 \text{ cm}^2$) with 0.60 mg cm^{-2} catalyst loading, and a saturated calomel reference electrode (SCE) were placed in cathodic compartment, while platinum foil ($1 \times 1 \text{ cm}^2$) was used as a counter electrode in the anodic compartment. All the electrochemical properties were investigated on a Gamry potentiostat. All the potentials in this work were calculated to RHE, $E(\text{RHE}) = E(\text{SCE}) + 0.24 + 0.059 * \text{pH}$.

Electrochemical NRR measurements: Different electrolyte aqueous solution was prepared with ultrapure water from Millipore system. Electrolysis was performed in a H-type cell separated by Nafion membrane. Prior to the test, the Nafion membrane was pretreated by heating in 5% H_2O_2 aqueous solution at $85 \text{ }^\circ\text{C}$ for 1 h and ultrapure water for another 1 h. Cyclic voltammetry (CV) and linear sweep voltammetry (LSV) tests were conducted in N_2 - and Ar-saturated electrolyte solutions with a scan rate of 5 mV s^{-1} . During the test, the feeding of gas was stopped. 10 cycles of CV sweeps were conducted before the collection of LSV curves. All the gases used have a purity of 99.999 %. Control experiments were also carried out to exclude the presence of nitrogen oxides in N_2 gas. Besides, all LSV curves were steady-state ones after several cycles and directly used without additional iR correction. Before all the potentiostatic tests, which were carried out at different potentials under continuous stirring, pure Ar or N_2 was purged into the cathodic compartment for at least 30 min with a flow rate of 10 mL min^{-1} and kept feeding during the whole test.

Electrochemical active surface area (ECSA): It was determined by capacitive current density which was measured with double-layer (C_{dl}) charging from the scan-rate dependence of cyclic voltammetry (CV) (the potential range was chosen according to the reaction system).

Estimation of activation energy: NRR was also conducted at different temperatures ($0 \text{ }^\circ\text{C}$, $20 \text{ }^\circ\text{C}$, $40 \text{ }^\circ\text{C}$ and $60 \text{ }^\circ\text{C}$) to investigate the influence of temperature on the reaction rate. Thus, activation energy can be calculated according to Arrhenius equation as follows (Equation 7.10),

7. Appendix

where A is Arrhenius constant, Ea is activation energy, T is reaction temperature, R is gas constant and v is corresponding reaction rate:

$$v = Ae^{-\frac{Ea}{RT}} \quad (7.10)$$

Determination of NH₃ by indophenol blue method: In detail, 2 mL of the electrolyte solution after electrochemical testing was mixed with 2 mL of a 1 M NaOH solution (contains 5 wt.% sodium citrate and 5 wt.% salicylic acid). Then, 1 mL of 0.05 M NaClO solution was also added into the mixture, followed by the addition of 1 wt.% C₅FeN₆Na₂O (sodium nitroferricyanide). As-obtained solution was measured by UV-Vis spectroscopy after staying at room temperature for 1 h, and the adsorption peak of indophenol blue appeared at around 655 nm. In order to accurately quantify NH₃, a calibration curve of concentration-absorbance was plotted by preparing a series of ammonium chloride standard solutions. The linear relation was repeated for three times.

Determination of NH₃ by Nessler's method: 10 mL of electrolyte solution was mixed with 1 mL of 0.2 M KNaC₄H₆O₆ and 1 mL of Nessler reagent and then the absorbance at 420 nm was measured by UV-Vis spectroscopy. A calibration curve with known concentration of NH₄⁺ was also plotted for further calculation. The absorbance of the blank sample without adding standard NH₃ solution is subtracted from all tested samples for background correction.

Determination of N₂H₄: N₂H₄ was detected by the Watt and Chrisp method with a color reagent containing 5.99 g of para-(dimethylamino) benzaldehyde, 30 mL of HCl (concentrated) and 300 mL of ethanol.²⁷ In detail, 5 mL electrolyte was mixed with 5 mL as-prepared color reagent and stirred for 20 minutes at room temperature.

Calculations of FE and production rate of NH₃: The FE of NH₃ was calculated according to Equation 7.11:

$$FE = \frac{3 * F * c * V}{Q} \quad (7.11)$$

NH₃ production rate was obtained according to Equation 7.12:

$$NH_3 \text{ production rate} = \frac{c * V * 17}{t * m} \quad (7.12)$$

Calculations of FE and of H₂ production rate: The FE of H₂ was calculated by testing the amount of H₂ generated in the cathodic part using GC-2014. The specific Equation 7.13 is as following:

$$FE = \frac{2 * F * n}{Q} \quad (7.13)$$

H₂ production rate was obtained according to Equation 7.14:

$$H_2 \text{ production rate} = \frac{n * 2}{t * m} \quad (7.14)$$

where F is Faraday constant; c is the calculated concentration of NH_3 ; V is total volume of electrolyte in cathodic compartment; Q is the total charge passed through the electrochemical system; t is the total time of chronoamperometry test; n is the actually produced H_2 (mol); and m is the catalysts loading.

^{15}N labeling experiment: ^1H NMR spectra of ^{15}N isotope labeling experiment were tested for the post-electrolysis 0.1 M LiClO_4 electrolytes with $^{15}\text{N}_2$, $^{14}\text{N}_2$ as the feeding gas. $^{15}\text{NH}_4^+$ and $^{14}\text{NH}_4^+$ standard samples were also tested for comparison.

HMF electrooxidation: LSV curves were recorded in 0.1 M NaOH electrolyte solution with and without the adding of HMF at a scan rate of 5 mV s^{-1} , as HMF remains almost stable at the pH of 13.²⁵⁸ The oxidation product in the anodic part was analyzed by HPLC to calculate the HMF conversion and yields of FDCA. In detail, the HPLC equipment has a column of $4.6 \text{ mm} \times 250 \text{ mm}$ Shim-pack GWS $5 \mu\text{m}$ C18 and an ultraviolet-visible detector set at 265 nm. A mixture of methanol and 5 mM ammonium formate aqueous solution was used as eluent solvent, and gradient elution was used to achieve the separation of different products by changing the volume percentage of methanol from 30% to 25% during 0 to 10 min with a flow rate of 1.2 mL/min. By plotting the calibration curves of HMF and FDCA, the final HMF conversion and FDCA yields were calculated according to Equations 7.15 and 7.16, respectively:

$$\text{HMF conversion} = \frac{\text{mol of HMF consumed}}{\text{mol of initial HMF}} \quad (7.15)$$

$$\text{FDCA yield} = \frac{\text{mol of FDCA formed}}{\text{mol of initial HMF}} \quad (7.16)$$

8. References

1. Chu, S.; Majumdar, A., Opportunities and challenges for a sustainable energy future. *Nature* **2012**, *488*, 294-303.
2. Lee, R., The outlook for population growth. *Science* **2011**, *333*, 569-73.
3. Yu, M.; Cheng, X.; Zeng, Y.; Wang, Z.; Tong, Y.; Lu, X.; Yang, S., Dual-Doped Molybdenum Trioxide Nanowires: A bifunctional anode for fiber-shaped asymmetric supercapacitors and microbial fuel cells. *Angew. Chem. Int. Ed.* **2016**, *55*, 6762-6.
4. Conti, J.; Holtberg, P.; Diefenderfer, J.; LaRose, A.; Turnure, J. T.; Westfall, L. International energy outlook 2016 with projections to 2040. **2016**.
5. Rajeshwar, K.; McConnell, R.; Licht, S., Solar hydrogen generation. Toward a Renewable Energy Future. **2008**.
6. Kozarcenin, S.; Liu, H. L.; Andresen, G. B., 21st century climate change impacts on key Properties of a large-scale renewable-based electricity system. *Joule* **2019**, *3*, 992-1005.
7. Qin, Q.; Heil, T.; Antonietti, M.; Oschatz, M., Single-site gold catalysts on hierarchical N-Doped porous noble carbon for enhanced electrochemical reduction of nitrogen. *Small Methods* **2018**, *2*, 1800202.
8. Shafiee, S.; Topal, E., When will fossil fuel reserves be diminished? *Energy policy* **2009**, *37*, 181-189.
9. Dincer, I.; Acar, C., Review and evaluation of hydrogen production methods for better sustainability. *Int. J. Hydrogen Energy* **2015**, *40*, 11094-11111.
10. Lu, Q.; Jiao, F., Electrochemical CO₂ reduction: Electrocatalyst, reaction mechanism, and process engineering. *Nano Energy* **2016**, *29*, 439-456.
11. Megahed, S.; Scrosati, B., Lithium-ion rechargeable batteries. *J. Power Sources* **1994**, *51*, 79-104.
12. Arico, A. S.; Bruce, P.; Scrosati, B.; Tarascon, J.-M.; Van Schalkwijk, W. In *Materials for sustainable energy: A collection of peer-reviewed research and review articles from nature publishing group*, World Scientific: 2011; pp 148-159.
13. Trogadas, P.; Fuller, T. F.; Strasser, P., Carbon as catalyst and support for electrochemical energy conversion. *Carbon* **2014**, *75*, 5-42.
14. Hu, L.; Khaniya, A.; Wang, J.; Chen, G.; Kaden, W. E.; Feng, X. F., Ambient electrochemical ammonia synthesis with high selectivity on Fe/Fe oxide catalyst. *ACS Catal.* **2018**, *8*, 9312-9319.
15. Murakami, T.; Nishikiori, T.; Nohira, T.; Ito, Y., Electrolytic synthesis of ammonia in molten salts under atmospheric pressure. *J. Am. Chem. Soc.* **2003**, *125*, 334-5.

8. References

16. Erisman, J. W.; Sutton, M. A.; Galloway, J.; Klimont, Z.; Winiwarter, W., How a century of ammonia synthesis changed the world. *Nat. Geosci.* **2008**, *1*, 636-639.
17. Cui, X. Y.; Tang, C.; Zhang, Q., A review of electrocatalytic reduction of dinitrogen to ammonia under ambient conditions. *Adv. Energy Mater.* **2018**, *8*, 1800369.
18. Durst, J.; Siebel, A.; Simon, C.; Hasche, F.; Herranz, J.; Gasteiger, H. A., New insights into the electrochemical hydrogen oxidation and evolution reaction mechanism. *Energy Environ. Sci.* **2014**, *7*, 2255-2260.
19. Matsumoto, Y.; Sato, E., Electrocatalytic properties of transition-metal oxides for oxygen evolution reaction. *Mater. Chem. Phys.* **1986**, *14*, 397-426.
20. Shipman, M. A.; Symes, M. D., Recent progress towards the electrosynthesis of ammonia from sustainable resources. *Catal. Today* **2017**, *286*, 57-68.
21. Liu, H.; Wei, L.; Liu, F.; Pei, Z.; Shi, J.; Wang, Z.-j.; He, D.; Chen, Y., Homogeneous, heterogeneous, and biological catalysts for electrochemical N₂ reduction toward NH₃ under ambient conditions. *ACS Catal.* **2019**, *9*, 5245-5267.
22. Demming, A., King of the elements? *Nanotechnol.* **2010**, *21*, 300201.
23. Greenwood, N. N.; Earnshaw, A., *Chemistry of the Elements*. Elsevier: 2012.
24. Titirici, M. M.; White, R. J.; Brun, N.; Budarin, V. L.; Su, D. S.; del Monte, F.; Clark, J. H.; MacLachlan, M. J., Sustainable carbon materials. *Chem. Soc. Rev.* **2015**, *44*, 250-90.
25. Allotropes of carbon, https://en.wikipedia.org/wiki/Allotropes_of_carbon.
26. Zhai, Y.; Dou, Y.; Zhao, D.; Fulvio, P. F.; Mayes, R. T.; Dai, S., Carbon materials for chemical capacitive energy storage. *Adv. Mater.* **2011**, *23*, 4828-50.
27. Yao, F.; Pham, D. T.; Lee, Y. H., Carbon-Based Materials for Lithium- Ion Batteries, Electrochemical Capacitors, and Their Hybrid Devices. *ChemSusChem* **2015**, *8*, 2284-2311.
28. Liu, J.; Wickramaratne, N. P.; Qiao, S. Z.; Jaroniec, M., Molecular-based design and emerging applications of nanoporous carbon spheres. *Nat. Mater.* **2015**, *14*, 763-74.
29. Kang, J.; Duan, X. G.; Wang, C.; Sun, H. Q.; Tan, X. Y.; Tade, M. O.; Wang, S. B., Nitrogen-doped bamboo-like carbon nanotubes with Ni encapsulation for persulfate activation to remove emerging contaminants with excellent catalytic stability. *Chem. Eng. J.* **2018**, *332*, 398-408.
30. Jariwala, D.; Sangwan, V. K.; Lauhon, L. J.; Marks, T. J.; Hersam, M. C., Carbon nanomaterials for electronics, optoelectronics, photovoltaics, and sensing. *Chem. Soc. Rev.* **2013**, *42*, 2824-60.
31. Thommes, M.; Kaneko, K.; Neimark, A. V.; Olivier, J. P.; Rodriguez-Reinoso, F.; Rouquerol, J.; Sing, K. S. W., Physisorption of gases, with special reference to the evaluation

8. References

- of surface area and pore size distribution (IUPAC Technical Report). *Pure Appl. Chem.* **2015**, *87*, 1051-1069.
32. Molina-Sabio, M.; Rodriguez-Reinoso, F., Role of chemical activation in the development of carbon porosity. *Colloid. Surf. A-Physicochem. Eng. Aspects* **2004**, *241*, 15-25.
33. Sevilla, M.; Mokaya, R., Energy storage applications of activated carbons: supercapacitors and hydrogen storage. *Energy Environ. Sci.* **2014**, *7*, 1250-1280.
34. Otowa, T.; Tanibata, R.; Itoh, M., Production and adsorption characteristics of MAXSORB: High-surface-area active carbon. *Gas Sep. Purif.* **1993**, *7*, 241-245.
35. Sakintuna, B.; Yurum, Y., Templated porous carbons: A review article. *Ind. Eng. Chem. Res.* **2005**, *44*, 2893-2902.
36. Xia, Y.; Yang, Z.; Mokaya, R., Templated nanoscale porous carbons. *Nanoscale* **2010**, *2*, 639-59.
37. Gu, D.; Schuth, F., Synthesis of non-siliceous mesoporous oxides. *Chem. Soc. Rev.* **2014**, *43*, 313-44.
38. Libbrecht, W.; Verberckmoes, A.; Thybaut, J. W.; Van der Voort, P.; De Clercq, J., Soft templated mesoporous carbons: Tuning the porosity for the adsorption of large organic pollutants. *Carbon* **2017**, *116*, 528-546.
39. Kyotani, T., Synthesis of various types of nano carbons using the template technique. *Bull. Chem. Soc. Jpn.* **2006**, *79*, 1322-1337.
40. Nishihara, H.; Yang, Q. H.; Hou, P. X.; Unno, M.; Yamauchi, S.; Saito, R.; Paredes, J. I.; Martinez-Alonso, A.; Tascon, J. M. D.; Sato, Y.; Terauchi, M.; Kyotani, T., A possible bucky bowl-like structure of zeolite templated carbon. *Carbon* **2009**, *47*, 1220-1230.
41. Liu, B.; Shioyama, H.; Akita, T.; Xu, Q., Metal-organic framework as a template for porous carbon synthesis. *J. Am. Chem. Soc.* **2008**, *130*, 5390-1.
42. Jun, S.; Joo, S. H.; Ryoo, R.; Kruk, M.; Jaroniec, M.; Liu, Z.; Ohsuna, T.; Terasaki, O., Synthesis of new, nanoporous carbon with hexagonally ordered mesostructure. *J. Am. Chem. Soc.* **2000**, *122*, 10712-10713.
43. Strubel, P.; Thieme, S.; Biemelt, T.; Helmer, A.; Oschatz, M.; Brückner, J.; Althues, H.; Kaskel, S., ZnO hard templating for synthesis of hierarchical porous carbons with tailored porosity and high performance in lithium-sulfur battery. *Adv. Funct. Mater.* **2015**, *25*, 287-297.
44. Liu, X.; Fechler, N.; Antonietti, M., Salt melt synthesis of ceramics, semiconductors and carbon nanostructures. *Chem. Soc. Rev.* **2013**, *42*, 8237-65.
45. Liu, X.; Giordano, C.; Antonietti, M., A facile molten-salt route to graphene synthesis. *Small* **2014**, *10*, 193-200.

8. References

46. Fechler, N.; Fellingner, T. P.; Antonietti, M., "Salt templating": a simple and sustainable pathway toward highly porous functional carbons from ionic liquids. *Adv. Mater.* **2013**, *25*, 75-79.
47. Chaikittisilp, W.; Ariga, K.; Yamauchi, Y., A new family of carbon materials: synthesis of MOF-derived nanoporous carbons and their promising applications. *J. Mater. Chem. A* **2013**, *1*, 14-19.
48. Yang, S. J.; Kim, T.; Im, J. H.; Kim, Y. S.; Lee, K.; Jung, H.; Park, C. R., MOF-derived hierarchically porous carbon with exceptional porosity and hydrogen storage capacity. *Chem. Mater.* **2012**, *24*, 464-470.
49. Yang, Y.; Le, T.; Kang, F. Y.; Inagaki, M., Polymer blend techniques for designing carbon materials. *Carbon* **2017**, *111*, 546-568.
50. Shen, K.; Chen, X. D.; Chen, J. Y.; Li, Y. W., Development of MOF-derived carbon-based nanomaterials for efficient catalysis. *ACS Catal.* **2016**, *6*, 5887-5903.
51. Dutta, S.; Bhaumik, A.; Wu, K. C. W., Hierarchically porous carbon derived from polymers and biomass: effect of interconnected pores on energy applications. *Energy Environ. Sci.* **2014**, *7*, 3574-3592.
52. Paraknowitsch, J. P.; Thomas, A., Doping carbons beyond nitrogen: an overview of advanced heteroatom doped carbons with boron, sulphur and phosphorus for energy applications. *Energy Environ. Sci.* **2013**, *6*, 2839-2855.
53. Zhou, Y. K.; Neyerlin, K.; Olson, T. S.; Pylypenko, S.; Bult, J.; Dinh, H. N.; Gennett, T.; Shao, Z. P.; O'Hayre, R., Enhancement of Pt and Pt-alloy fuel cell catalyst activity and durability via nitrogen-modified carbon supports. *Energy Environ. Sci.* **2010**, *3*, 1437-1446.
54. Li, X. H.; Antonietti, M., Metal nanoparticles at mesoporous N-doped carbons and carbon nitrides: functional Mott-Schottky heterojunctions for catalysis. *Chem. Soc. Rev.* **2013**, *42*, 6593-604.
55. Antonietti, M.; Oschatz, M., The concept of "noble, heteroatom-doped carbons," their directed synthesis by electronic band control of carbonization, and applications in catalysis and energy materials. *Adv. Mater.* **2018**, *30*, e1706836.
56. Fellingner, T. P.; Thomas, A.; Yuan, J.; Antonietti, M., 25th anniversary article: "Cooking carbon with salt": carbon materials and carbonaceous frameworks from ionic liquids and poly(ionic liquid)s. *Adv. Mater.* **2013**, *25*, 5838-54.
57. Wang, X.; Maeda, K.; Thomas, A.; Takanabe, K.; Xin, G.; Carlsson, J. M.; Domen, K.; Antonietti, M., A metal-free polymeric photocatalyst for hydrogen production from water under visible light. *Nat. Mater.* **2008**, *8*, 76.

8. References

58. Shui, J.; Wang, M.; Du, F.; Dai, L., N-doped carbon nanomaterials are durable catalysts for oxygen reduction reaction in acidic fuel cells. *Sci. Adv.* **2015**, *1*, e1400129.
59. Sheng, Z. H.; Gao, H. L.; Bao, W. J.; Wang, F. B.; Xia, X. H., Synthesis of boron doped graphene for oxygen reduction reaction in fuel cells. *J. Mater. Chem.* **2012**, *22*, 390-395.
60. Pang, Q.; Tang, J.; Huang, H.; Liang, X.; Hart, C.; Tam, K. C.; Nazar, L. F., A nitrogen and sulfur dual-doped carbon derived from polyrhodanine@cellulose for advanced lithium-sulfur batteries. *Adv. Mater.* **2015**, *27*, 6021-8.
61. Nasini, U. B.; Bairi, V. G.; Ramasahayam, S. K.; Bourdo, S. E.; Viswanathan, T.; Shaikh, A. U., Phosphorous and nitrogen dual heteroatom doped mesoporous carbon synthesized via microwave method for supercapacitor application. *J. Power Sources* **2014**, *250*, 257-265.
62. Liu, G.; Li, X.; Ganesan, P.; Popov, B. N., Development of non-precious metal oxygen-reduction catalysts for PEM fuel cells based on N-doped ordered porous carbon. *Appl. Catal. B-Environ.* **2009**, *93*, 156-165.
63. Oschatz, M.; Hofmann, J. P.; van Deelen, T. W.; Lamme, W. S.; Krans, N. A.; Hensen, E. J. M.; de Jong, K. P., Effects of the functionalization of the ordered mesoporous carbon support surface on iron catalysts for the Fischer-Tropsch synthesis of lower olefins. *ChemCatChem* **2017**, *9*, 620-628.
64. Lama, S. M. G.; Weber, J. L.; Heil, T.; Hofmann, J. P.; Yan, R.; de Jong, K. P.; Oschatz, M., Tandem promotion of iron catalysts by sodium-sulfur and nitrogen-doped carbon layers on carbon nanotube supports for the Fischer-Tropsch to olefins synthesis. *Appl. Catal. A-Gen.* **2018**, *568*, 213-220.
65. Han, Y.; Wang, Y.-G.; Chen, W.; Xu, R.; Zheng, L.; Zhang, J.; Luo, J.; Shen, R.-A.; Zhu, Y.; Cheong, W.-C.; Chen, C.; Peng, Q.; Wang, D.; Li, Y., Hollow N-Doped carbon spheres with isolated cobalt single atomic sites: superior electrocatalysts for oxygen reduction. *J. Am. Chem. Soc.* **2017**, *139*, 17269-17272.
66. Chen, Y.; Ji, S.; Wang, Y.; Dong, J.; Chen, W.; Li, Z.; Shen, R.; Zheng, L.; Zhuang, Z.; Wang, D.; Li, Y., Isolated single iron atoms anchored on N-Doped porous carbon as an efficient electrocatalyst for the oxygen reduction reaction. *Angew. Chem. Int. Ed.* **2017**, *56*, 6937-6941.
67. Jiang, H.-L.; Yang, Q.; Yang, C.-C.; Lin, C.-H., Metal-Organic-Framework-derived hollow N-Doped porous carbon with ultrahigh concentrations of single Zn atoms for efficient carbon dioxide conversion. *Angew. Chem. Int. Ed.* **2019**, *58*, 3511-3515.
68. Grimme, S.; Kruse, H.; Goerigk, L.; Erker, G., The mechanism of dihydrogen activation by frustrated Lewis pairs revisited. *Angew. Chem. Int. Ed.* **2010**, *49*, 1402-5.

8. References

69. Momming, C. M.; Otten, E.; Kehr, G.; Frohlich, R.; Grimme, S.; Stephan, D. W.; Erker, G., Reversible metal-free carbon dioxide binding by frustrated Lewis pairs. *Angew. Chem. Int. Ed.* **2009**, *48*, 6643-6.
70. Stephan, D. W., "Frustrated Lewis pairs": A concept for new reactivity and catalysis. *Org. Biomol. Chem.* **2008**, *6*, 1535-9.
71. Bernhard, A., The nitrogen cycle: Processes. *Players, and Human* **2010**.
72. Liu, J.; Kelley, M. S.; Wu, W.; Banerjee, A.; Douvalis, A. P.; Wu, J.; Zhang, Y.; Schatz, G. C.; Kanatzidis, M. G., Nitrogenase-mimic iron-containing chalcogels for photochemical reduction of dinitrogen to ammonia. *Proc. Natl. Acad. Sci.* **2016**, *113*, 5530-5.
73. Licht, S.; Cui, B.; Wang, B.; Li, F. F.; Lau, J.; Liu, S., Ammonia synthesis by N₂ and steam electrolysis in molten hydroxide suspensions of nanoscale Fe₂O₃. *Science* **2014**, *345*, 637-40.
74. Milton, R. D.; Abdellaoui, S.; Khadka, N.; Dean, D. R.; Leech, D.; Seefeldt, L. C.; Minter, S. D., Nitrogenase bioelectrocatalysis: heterogeneous ammonia and hydrogen production by MoFe protein. *Energy Environ. Sci.* **2016**, *9*, 2550-2554.
75. Yandulov, D. V.; Schrock, R. R., Catalytic reduction of dinitrogen to ammonia at a single molybdenum center. *Science* **2003**, *301*, 76-8.
76. Patil, B. S.; Wang, Q.; Hessel, V.; Lang, J., Plasma N₂-fixation: 1900-2014. *Catal. Today* **2015**, *256*, 49-66.
77. Kitano, M.; Inoue, Y.; Yamazaki, Y.; Hayashi, F.; Kanbara, S.; Matsuishi, S.; Yokoyama, T.; Kim, S. W.; Hara, M.; Hosono, H., Ammonia synthesis using a stable electrone as an electron donor and reversible hydrogen store. *Nat. Chem.* **2012**, *4*, 934-40.
78. Honkala, K.; Hellman, A.; Remediakis, I. N.; Logadottir, A.; Carlsson, A.; Dahl, S.; Christensen, C. H.; Norskov, J. K., Ammonia synthesis from first-principles calculations. *Science* **2005**, *307*, 555-8.
79. Modak, J. M., Haber process for ammonia synthesis. *Reson.* **2002**, *7*, 69-77.
80. Boudart, M., Ammonia synthesis: the bellwether reaction in heterogeneous catalysis. *Top. Catal.* **1994**, *1*, 405-414.
81. Galloway, J. N.; Cowling, E. B., Reactive nitrogen and the world: 200 years of change. *AMBIO: J. Human Environ.* **2002**, *31*, 64-71.
82. Paull, J., A century of synthetic fertilizer: 1909-2009. *J. Bio-Dynam. Tasmania* **2009**, *94*, 16-21.

8. References

83. Nørskov, J.; Chen, J.; Miranda, R.; Fitzsimmons, T.; Stack, R. Sustainable Ammonia Synthesis-Exploring the scientific challenges associated with discovering alternative, sustainable processes for ammonia production; US DOE Office of Science: **2016**.
84. Vojvodic, A.; Medford, A. J.; Studt, F.; Abild-Pedersen, F.; Khan, T. S.; Bligaard, T.; Nørskov, J., Exploring the limits: a low-pressure, low-temperature Haber-Bosch process. *Chem. Phys. Lett.* **2014**, *598*, 108-112.
85. Burgess, B. K.; Lowe, D. J., Mechanism of molybdenum nitrogenase. *Chem. Rev.* **1996**, *96*, 2983-3012.
86. Eady, R. R., Structure-function relationships of alternative nitrogenases. *Chem. Rev.* **1996**, *96*, 3013-3030.
87. Jodin, H., Du rôle physiologique de l'azote. *Compt. Rend. Acad. Sci.* **1862**, *55*, 612.
88. Bulen, W. A.; Burns, R. C.; LeComte, J. R., Nitrogen fixation: cell-free system with extracts of *Azotobacter*. *Biochem. Biophys. Res. Commun.* **1964**, *17*, 265-71.
89. Carnahan, J. E.; Mortenson, L. E.; Mower, H. F.; Castle, J. E., Nitrogen fixation in cell-free extracts of *Clostridium pasteurianum*. *Biochimica. et Biophysica. Acta* **1960**, *44*, 520-535.
90. Peters, J. W.; Szilagyi, R. K., Exploring new frontiers of nitrogenase structure and mechanism. *Curr. Opin. Chem. Biol.* **2006**, *10*, 101-8.
91. Hoffman, B. M.; Lukoyanov, D.; Yang, Z. Y.; Dean, D. R.; Seefeldt, L. C., Mechanism of nitrogen fixation by nitrogenase: the next stage. *Chem. Rev.* **2014**, *114*, 4041-62.
92. Hu, Y.; Lee, C. C.; Ribbe, M. W., Extending the carbon chain: hydrocarbon formation catalyzed by vanadium/molybdenum nitrogenases. *Science* **2011**, *333*, 753-5.
93. Milton, R. D.; Cai, R.; Abdellaoui, S.; Leech, D.; De Lacey, A. L.; Pita, M.; Minteer, S. D., Bioelectrochemical Haber-Bosch Process: An Ammonia-Producing H₂/N₂ Fuel Cell. *Angew. Chem. Int. Ed.* **2017**, *56*, 2680-2683.
94. Brown, K. A.; Harris, D. F.; Wilker, M. B.; Rasmussen, A.; Khadka, N.; Hamby, H.; Keable, S.; Dukovic, G.; Peters, J. W.; Seefeldt, L. C.; King, P. W., Light-driven dinitrogen reduction catalyzed by a CdS:nitrogenase MoFe protein biohybrid. *Science* **2016**, *352*, 448-50.
95. Anderson, J. S.; Rittle, J.; Peters, J. C., Catalytic conversion of nitrogen to ammonia by an iron model complex. *Nature* **2013**, *501*, 84-7.
96. Arashiba, K.; Miyake, Y.; Nishibayashi, Y., A molybdenum complex bearing PNP-type pincer ligands leads to the catalytic reduction of dinitrogen into ammonia. *Nat. Chem.* **2010**, *3*, 120.
97. Macleod, K. C.; Holland, P. L., Recent developments in the homogeneous reduction of dinitrogen by molybdenum and iron. *Nat. Chem.* **2013**, *5*, 559-65.

8. References

98. Fenwick, A. Q.; Gregoire, J. M.; Luca, O. R., Electrocatalytic reduction of nitrogen and carbon dioxide to chemical fuels: Challenges and opportunities for a solar fuel device. *J. Photochem. Photobiol. B* **2015**, *152*, 47-57.
99. Nishibayashi, Y.; Saito, M.; Uemura, S.; Takekuma, S.; Takekuma, H.; Yoshida, Z., Buckminsterfullerenes: a non-metal system for nitrogen fixation. *Nature* **2004**, *428*, 279-80.
100. Banerjee, A.; Yuhas, B. D.; Margulies, E. A.; Zhang, Y.; Shim, Y.; Wasielewski, M. R.; Kanatzidis, M. G., Photochemical nitrogen conversion to ammonia in ambient conditions with FeMoS-chalcogenides. *J. Am. Chem. Soc.* **2015**, *137*, 2030-4.
101. Schrauzer, G. N.; Guth, T. D., Photolysis of water and photoreduction of nitrogen on titanium-dioxide. *J. Am. Chem. Soc.* **1977**, *99*, 7189-7193.
102. Thacker, C. M.; Folkins, H. O.; Miller, E. L., Free energies of formation of gaseous hydrocarbons and related substances. *Ind. Eng. Chem.* **1941**, *33*, 584-590.
103. Oshikiri, T.; Ueno, K.; Misawa, H., Plasmon-induced ammonia synthesis through nitrogen photofixation with visible light irradiation. *Angew. Chem. Int. Ed.* **2014**, *53*, 9802-9805.
104. Rusina, O.; Eremenko, A.; Frank, G.; Strunk, H. P.; Kisch, H., Nitrogen photofixation at nanostructured iron titanate films. *Angew. Chem. Int. Ed.* **2001**, *40*, 3993-3995.
105. Cao, Y. H.; Hu, S. Z.; Li, F. Y.; Fan, Z. P.; Bai, J.; Lu, G.; Wang, Q., Photofixation of atmospheric nitrogen to ammonia with a novel ternary metal sulfide catalyst under visible light. *RSC Adv.* **2016**, *6*, 49862-49867.
106. Li, H.; Shang, J.; Ai, Z.; Zhang, L., Efficient Visible Light Nitrogen fixation with BiOBr nanosheets of oxygen vacancies on the exposed {001} facets. *J. Am. Chem. Soc.* **2015**, *137*, 6393-9.
107. Bhattacharyya, K.; Datta, A., Visible light driven efficient metal free single atom catalyst supported on nanoporous carbon nitride for nitrogen fixation. *Phys. Chem. Chem. Phys.* **2019**, *21*, 12346-12352.
108. Yang, J.; Guo, Y.; Jiang, R.; Qin, F.; Zhang, H.; Lu, W.; Wang, J.; Yu, J. C., High-efficiency "Working-in-Tandem" nitrogen photofixation achieved by assembling plasmonic gold nanocrystals on ultrathin titania nanosheets. *J. Am. Chem. Soc.* **2018**, *140*, 8497-8508.
109. Hu, C.; Chen, X.; Jin, J.; Han, Y.; Chen, S.; Ju, H.; Cai, J.; Qiu, Y.; Gao, C.; Wang, C.; Qi, Z.; Long, R.; Song, L.; Liu, Z.; Xiong, Y., Surface plasmon enabling nitrogen fixation in pure water through a dissociative mechanism under mild conditions. *J. Am. Chem. Soc.* **2019**, *141*, 7807-7814.

8. References

110. Hirakawa, H.; Hashimoto, M.; Shiraishi, Y.; Hirai, T., Photocatalytic conversion of nitrogen to ammonia with water on surface oxygen vacancies of titanium dioxide. *J. Am. Chem. Soc.* **2017**, *139*, 10929-10936.
111. Ling, C.; Niu, X.; Li, Q.; Du, A.; Wang, J., Metal-free single atom catalyst for N₂ fixation driven by visible light. *J. Am. Chem. Soc.* **2018**, *140*, 14161-14168.
112. Colmenares, J. C.; Luque, R.; Campelo, J. M.; Colmenares, F.; Karpinski, Z.; Romero, A. A., Nanostructured photocatalysts and their applications in the photocatalytic transformation of lignocellulosic biomass: An overview. *Mater.* **2009**, *2*, 2228-2258.
113. Dong, H.; Zeng, G.; Tang, L.; Fan, C.; Zhang, C.; He, X.; He, Y., An overview on limitations of TiO₂-based particles for photocatalytic degradation of organic pollutants and the corresponding countermeasures. *Water. Res.* **2015**, *79*, 128-46.
114. Davy, H., I. The Bakerian Lecture, on some chemical agencies of electricity. *Philos. Trans. R. Soc. London* **1807**, *97*, 1-56.
115. Fichter, F.; Suter, R., Zur frage der kathodischen reduktion des elementaren stickstoffs. *Helv. Chim. Acta* **1922**, *5*, 246-255.
116. Deng, J.; Iniguez, J. A.; Liu, C., Electrocatalytic nitrogen reduction at low temperature. *Joule* **2018**, *2*, 846-856.
117. Foster, S. L.; Bakovic, S. I. P.; Duda, R. D.; Maheshwari, S.; Milton, R. D.; Minteer, S. D.; Janik, M. J.; Renner, J. N.; Greenlee, L. F., Catalysts for nitrogen reduction to ammonia. *Nat. Catal.* **2018**, *1*, 490-500.
118. Kyriakou, V.; Garagounis, I.; Vasileiou, E.; Vourros, A.; Stoukides, M., Progress in the electrochemical synthesis of ammonia. *Catal. Today* **2017**, *286*, 2-13.
119. Cui, X.; Tang, C.; Zhang, Q., A review of electrocatalytic reduction of dinitrogen to ammonia under ambient conditions. *Adv. Energy Mater.* **2018**, *8*, 1800369.
120. Martin, A. J.; Shinagawa, T.; Perez-Ramirez, J., Electrocatalytic reduction of nitrogen: from Haber-Bosch to ammonia artificial leaf. *Chem* **2019**, *5*, 263-283.
121. Liu, Y.; Su, Y.; Quan, X.; Fan, X.; Chen, S.; Yu, H.; Zhao, H.; Zhang, Y.; Zhao, J., Facile ammonia synthesis from electrocatalytic N₂ reduction under ambient conditions on N-doped porous carbon. *ACS Catal.* **2018**, *8*, 1186-1191.
122. Legare, M. A.; Belanger-Chabot, G.; Dewhurst, R. D.; Welz, E.; Krummenacher, I.; Engels, B.; Braunschweig, H., Nitrogen fixation and reduction at boron. *Science* **2018**, *359*, 896-900.
123. Wang, S. Y.; Ichihara, F.; Pang, H.; Chen, H.; Ye, J. H., Nitrogen fixation reaction derived from nanostructured catalytic materials. *Adv. Funct. Mater.* **2018**, *28*, 1803309.

8. References

124. Yu, X.; Han, P.; Wei, Z.; Huang, L.; Gu, Z.; Peng, S.; Ma, J.; Zheng, G., Boron-doped graphene for electrocatalytic N₂ reduction. *Joule* **2018**, *2*, 1610-1622.
125. Lv, C.; Yan, C.; Chen, G.; Ding, Y.; Sun, J.; Zhou, Y.; Yu, G., An amorphous noble-metal-free electrocatalyst that enables nitrogen fixation under ambient conditions. *Angew. Chem. Int. Ed.* **2018**, *57*, 6073-6076.
126. Wang, Y.; Shi, M. M.; Bao, D.; Meng, F. L.; Zhang, Q.; Zhou, Y. T.; Liu, K. H.; Zhang, Y.; Wang, J. Z.; Chen, Z. W.; Liu, D. P.; Jiang, Z.; Luo, M.; Gu, L.; Zhang, Q. H.; Cao, X. Z.; Yao, Y.; Shao, M. H.; Zhang, Y.; Zhang, X. B.; Chen, J. G.; Yan, J. M.; Jiang, Q., Generating defect-rich bismuth for enhancing the rate of nitrogen electroreduction to ammonia. *Angew. Chem. Int. Ed.* **2019**, *58*, 9464-9469.
127. Lazouski, N.; Schiffer, Z. J.; Williams, K.; Manthiram, K., Understanding continuous lithium-mediated electrochemical nitrogen reduction. *Joule* **2019**, *3*, 1127-1139.
128. Sakamoto, R.; Takada, K.; Pal, T.; Maeda, H.; Kambe, T.; Nishihara, H., Coordination nanosheets (CONASHs): strategies, structures and functions. *Chem. Commun.* **2017**, *53*, 5781-5801.
129. Tsuneto, A.; Kudo, A.; Sakata, T., Lithium-mediated electrochemical reduction of high-pressure N₂ to NH₃. *J. Electroanal. Chem.* **1994**, *367*, 183-188.
130. Peng, P.; Chen, P.; Addy, M.; Cheng, Y.; Anderson, E.; Zhou, N.; Schiappacasse, C.; Zhang, Y.; Chen, D.; Hatzenbeller, R.; Liu, Y.; Ruan, R., Atmospheric plasma-assisted ammonia synthesis enhanced via synergistic catalytic absorption. *ACS Sustain. Chem. Eng.* **2018**, *7*, 100-104.
131. Hawtof, R.; Ghosh, S.; Guarr, E.; Xu, C.; Mohan Sankaran, R.; Renner, J. N., Catalyst-free, highly selective synthesis of ammonia from nitrogen and water by a plasma electrolytic system. *Sci. Adv.* **2019**, *5*, eaat5778.
132. Iwamoto, M.; Akiyama, M.; Aihara, K.; Deguchi, T., Ammonia Synthesis on Wool-Like Au, Pt, Pd, Ag, or Cu electrode catalysts in nonthermal atmospheric-pressure plasma of N₂ and H₂. *ACS Catal.* **2017**, *7*, 6924-6929.
133. Mehta, P.; Barboun, P.; Herrera, F. A.; Kim, J.; Rumbach, P.; Go, D. B.; Hicks, J. C.; Schneider, W. F., Overcoming ammonia synthesis scaling relations with plasma-enabled catalysis. *Nat. Catal.* **2018**, *1*, 269-275.
134. Guo, C.; Ran, J.; Vasileff, A.; Qiao, S.-Z., Rational design of electrocatalysts and photo(electro)catalysts for nitrogen reduction to ammonia (NH₃) under ambient conditions. *Energy Environ. Sci.* **2018**, *11*, 45-56.

8. References

135. Abghoui, Y.; Garden, A. L.; Howalt, J. G.; Vegge, T.; Skúlason, E., Electroreduction of N₂ to ammonia at ambient conditions on mononitrides of Zr, Nb, Cr, and V: A DFT guide for experiments. *ACS Catal.* **2015**, *6*, 635-646.
136. Abghoui, Y.; Skúlason, E., Electrochemical synthesis of ammonia via Mars-van Krevelen mechanism on the (111) facets of group III-VII transition metal mononitrides. *Catal. Today* **2017**, *286*, 78-84.
137. Zeinalipour-Yazdi, C. D.; Hargreaves, J. S.; Catlow, C. R. A., Nitrogen activation in a Mars-van Krevelen mechanism for ammonia synthesis on Co₃Mo₃N. *J. Phys. Chem. C* **2015**, *119*, 28368-28376.
138. Yang, X.; Nash, J.; Anibal, J.; Dunwel, M.; Kattel, S.; Stavitski, E.; Attenkofer, K.; Chen, J. G. G.; Yan, Y. S.; Xu, B. J., Mechanistic insights into electrochemical nitrogen reduction reaction on vanadium nitride nanoparticles. *J. Am. Chem. Soc.* **2018**, *140*, 13387-13391.
139. McEnaney, J. M.; Singh, A. R.; Schwalbe, J. A.; Kibsgaard, J.; Lin, J. C.; Cargnello, M.; Jaramillo, T. F.; Nørskov, J. K., Ammonia synthesis from N₂ and H₂O using a lithium cycling electrification strategy at atmospheric pressure. *Energy Environ. Sci.* **2017**, *10*, 1621-1630.
140. Costentin, C.; Robert, M.; Saveant, J. M., Concerted proton-electron transfers: electrochemical and related approaches. *Acc. Chem. Res.* **2010**, *43*, 1019-29.
141. Weinberg, D. R.; Gagliardi, C. J.; Hull, J. F.; Murphy, C. F.; Kent, C. A.; Westlake, B. C.; Paul, A.; Ess, D. H.; McCafferty, D. G.; Meyer, T. J., Proton-coupled electron transfer. *Chem. Rev.* **2012**, *112*, 4016-93.
142. Zhou, F. L.; Azofra, L. M.; Ali, M.; Kar, M.; Simonov, A. N.; McDonnell-Worth, C.; Sun, C. H.; Zhang, X. Y.; MacFarlane, D. R., Electro-synthesis of ammonia from nitrogen at ambient temperature and pressure in ionic liquids. *Energy Environ. Sci.* **2017**, *10*, 2516-2520.
143. Strelets, V. V.; Gavrilov, A. B.; Pospisil, L., The Role of ligands in the electrochemical-behavior and catalytic activity of molybdenum-containing catalyst for dinitrogen fixation under mild conditions. *J. Electroanal. Chem.* **1987**, *217*, 425-433.
144. Wang, S.; Ichihara, F.; Pang, H.; Chen, H.; Ye, J., Nitrogen fixation reaction derived from nanostructured catalytic materials. *Adv. Funct. Mater.* **2018**, *28*, 1803309.
145. Montoya, J. H.; Tsai, C.; Vojvodic, A.; Nørskov, J. K., The challenge of electrochemical ammonia synthesis: A new perspective on the role of nitrogen scaling relations. *ChemSusChem* **2015**, *8*, 2180-2186.

8. References

146. Yao, Y.; Zhu, S.; Wang, H.; Li, H.; Shao, M., A spectroscopic study on the nitrogen electrochemical reduction reaction on gold and platinum surfaces. *J. Am. Chem. Soc.* **2018**, *140*, 1496-1501.
147. Hao, Y.-C.; Guo, Y.; Chen, L.-W.; Shu, M.; Wang, X.-Y.; Bu, T.-A.; Gao, W.-Y.; Zhang, N.; Su, X.; Feng, X.; Zhou, J.-W.; Wang, B.; Hu, C.-W.; Yin, A.-X.; Si, R.; Zhang, Y.-W.; Yan, C.-H., Promoting nitrogen electroreduction to ammonia with bismuth nanocrystals and potassium cations in water. *Nat. Catal.* **2019**, *2*, 448-456.
148. Jiao, Y.; Zheng, Y.; Jaroniec, M.; Qiao, S. Z., Origin of the electrocatalytic oxygen reduction activity of graphene-based catalysts: a roadmap to achieve the best performance. *J. Am. Chem. Soc.* **2014**, *136*, 4394-403.
149. Zhao, Z.; Li, M.; Zhang, L.; Dai, L.; Xia, Z., Design principles for heteroatom-doped carbon nanomaterials as highly efficient catalysts for fuel cells and metal-air batteries. *Adv. Mater.* **2015**, *27*, 6834-40.
150. Antonietti, M.; Lopez-Salas, N.; Primo, A., Adjusting the structure and electronic properties of carbons for metal-free carbocatalysis of organic transformations. *Adv. Mater.* **2019**, *31*, e1805719.
151. Zhao, Y.; Nakamura, R.; Kamiya, K.; Nakanishi, S.; Hashimoto, K., Nitrogen-doped carbon nanomaterials as non-metal electrocatalysts for water oxidation. *Nat. Commun.* **2013**, *4*, 2390.
152. Petrosius, S. C.; Drago, R. S.; Young, V.; Grunewald, G. C., Low-temperature decomposition of some halogenated hydrocarbons using metal-oxide porous carbon catalysts. *J. Am. Chem. Soc.* **1993**, *115*, 6131-6137.
153. Ma, T. Y.; Dai, S.; Jaroniec, M.; Qiao, S. Z., Metal-organic framework derived hybrid Co₃O₄-carbon porous nanowire arrays as reversible oxygen evolution electrodes. *J. Am. Chem. Soc.* **2014**, *136*, 13925-31.
154. Yang, S. J.; Nam, S.; Kim, T.; Im, J. H.; Jung, H.; Kang, J. H.; Wi, S.; Park, B.; Park, C. R., Preparation and exceptional lithium anodic performance of porous carbon-coated ZnO quantum dots derived from a metal-organic framework. *J. Am. Chem. Soc.* **2013**, *135*, 7394-7.
155. Browne, M. P.; Sofer, Z.; Pumera, M., Layered and two dimensional metal oxides for electrochemical energy conversion. *Energy Environ. Sci.* **2019**, *12*, 41-58.
156. Browne, M. P.; Nolan, H.; Duesberg, G. S.; Colavita, P. E.; Lyons, M. E. G., Low-overpotential high-Activity mixed manganese and ruthenium oxide electrocatalysts for oxygen evolution reaction in alkaline media. *ACS Catal.* **2016**, *6*, 2408-2415.

8. References

157. Luo, Y.; Chen, G.-F.; Ding, L.; Chen, X.; Ding, L.-X.; Wang, H., Efficient electrocatalytic N₂ fixation with MXene under ambient conditions. *Joule* **2019**, *3*, 279-289.
158. Guo, C. X.; Ran, J. R.; Vasileff, A.; Qiao, S. Z., Rational design of electrocatalysts and photo(electro) catalysts for nitrogen reduction to ammonia (NH₃) under ambient conditions. *Energy Environ. Sci.* **2018**, *11*, 45-56.
159. Cheng, H.; Ding, L. X.; Chen, G. F.; Zhang, L.; Xue, J.; Wang, H., Molybdenum carbide Nanodots enable efficient electrocatalytic nitrogen fixation under ambient conditions. *Adv. Mater.* **2018**, *30*, e1803694.
160. Yang, L.; Wu, T.; Zhang, R.; Zhou, H.; Xia, L.; Shi, X.; Zheng, H.; Zhang, Y.; Sun, X., Insights into defective TiO₂ in electrocatalytic N₂ reduction: combining theoretical and experimental studies. *Nanoscale* **2019**, *11*, 1555-1562.
161. Wang, Y.; Jia, K.; Pan, Q.; Xu, Y.; Liu, Q.; Cui, G.; Guo, X.; Sun, X., Boron-doped TiO₂ for efficient electrocatalytic N₂ fixation to NH₃ at ambient conditions. *ACS Sustain. Chem. Eng.* **2018**, *7*, 117-122.
162. Shen, K.; Chen, X. D.; Chen, J. Y.; Li, Y. W., Development of MOF-derived carbon-based nanomaterials for efficient catalysis. *ACS Catal.* **2016**, *6*, 5887-5903.
163. Jiang, H. L.; Liu, B.; Lan, Y. Q.; Kuratani, K.; Akita, T.; Shioyama, H.; Zong, F.; Xu, Q., From metal-organic framework to nanoporous carbon: toward a very high surface area and hydrogen uptake. *J. Am. Chem. Soc.* **2011**, *133*, 11854-7.
164. Kim, S. N.; Kim, J.; Kim, H. Y.; Cho, H. Y.; Ahn, W. S., Adsorption/catalytic properties of MIL-125 and NH₂-MIL-125. *Catal. Today* **2013**, *204*, 85-93.
165. Wang, W. K.; Chen, J. J.; Zhang, X.; Huang, Y. X.; Li, W. W.; Yu, H. Q., Self-induced synthesis of phase-junction TiO₂ with a tailored rutile to anatase ratio below phase transition temperature. *Sci. Rep.* **2016**, *6*, 20491.
166. Huang, C. H.; Gu, D.; Zhao, D. Y.; Doong, R. A., Direct synthesis of controllable microstructures of thermally stable and ordered mesoporous crystalline titanium oxides and carbide/carbon composites. *Chem. Mater.* **2010**, *22*, 1760-1767.
167. Lohse, B. H.; Calka, A.; Wexler, D., Raman spectroscopy sheds new light on TiC formation during the controlled milling of titanium and carbon. *J. Alloys Compd.* **2007**, *434*, 405-409.
168. Mohapatra, S.; Mishra, D. K.; Singh, S. K., Microscopic and spectroscopic analyses of TiC powder synthesized by thermal plasma technique. *Powder Technol.* **2013**, *237*, 41-45.

8. References

169. Portehault, D.; Maneeratana, V.; Candolfi, C.; Oeschler, N.; Veremchuk, I.; Grin, Y.; Sanchez, C.; Antonietti, M., Facile general route toward tunable Magneli nanostructures and their use as thermoelectric metal oxide/carbon nanocomposites. *ACS Nano* **2011**, *5*, 9052-61.
170. Schnadt, J.; O'Shea, J. N.; Patthey, L.; Schiessling, J.; Krempasky, J.; Shi, M.; Martensson, N.; Bruhwiler, P. A., Structural study of adsorption of isonicotinic acid and related molecules on rutile TiO₂(110) II: XPS. *Surf. Sci.* **2003**, *544*, 74-86.
171. Krishnamoorthy, K.; Pazhamalai, P.; Sahoo, S.; Kim, S. J., Titanium carbide sheet based high performance wire type solid state supercapacitors. *J. Mater. Chem. A* **2017**, *5*, 5726-5736.
172. Dong, F.; Guo, S.; Wang, H.; Li, X. F.; Wu, Z. B., Enhancement of the visible light photocatalytic activity of C-Doped TiO₂ nanomaterials prepared by a green synthetic approach. *J. Phys. Chem. C* **2011**, *115*, 13285-13292.
173. Huang, Y.; Ho, W.; Lee, S.; Zhang, L.; Li, G.; Yu, J. C., Effect of carbon doping on the mesoporous structure of nanocrystalline titanium dioxide and its solar-light-driven photocatalytic degradation of NO_x. *Langmuir* **2008**, *24*, 3510-6.
174. Reyes-Garcia, E. A.; Sun, Y.; Reyes-Gil, K. R.; Raftery, D., Solid-state NMR and EPR analysis of carbon-doped titanium dioxide photocatalysts TiO_{2-x}C_x. *Solid State Nucl. Magn. Reson.* **2009**, *35*, 74-81.
175. Oshikiri, T.; Ueno, K.; Misawa, H., Selective dinitrogen conversion to ammonia using water and visible light through plasmon-induced charge separation. *Angew. Chem. Int. Ed.* **2016**, *55*, 3942-6.
176. Bao, D.; Zhang, Q.; Meng, F. L.; Zhong, H. X.; Shi, M. M.; Zhang, Y.; Yan, J. M.; Jiang, Q.; Zhang, X. B., Electrochemical reduction of N₂ under ambient conditions for artificial N₂ fixation and renewable energy storage using N₂/NH₃ cycle. *Adv. Mater.* **2017**, *29*, 1604799.
177. Shi, M. M.; Bao, D.; Wulan, B. R.; Li, Y. H.; Zhang, Y. F.; Yan, J. M.; Jiang, Q., Au sub-Nanoclusters on TiO₂ toward highly efficient and selective electrocatalyst for N₂ conversion to NH₃ at ambient conditions. *Adv. Mater.* **2017**, *29*, 1606550.
178. Koleli, F.; Ropke, T., Electrochemical hydrogenation of dinitrogen to ammonia on a polyaniline electrode. *Appl. Catal. B-Environ.* **2006**, *62*, 306-310.
179. Chen, G. F.; Cao, X.; Wu, S.; Zeng, X.; Ding, L. X.; Zhu, M.; Wang, H., Ammonia electrosynthesis with high selectivity under ambient conditions via a Li⁺ incorporation strategy. *J. Am. Chem. Soc.* **2017**, *139*, 9771-9774.
180. Lv, C.; Qian, Y.; Yan, C.; Ding, Y.; Liu, Y.; Chen, G.; Yu, G., Defect engineering metal-free polymeric carbon nitride electrocatalyst for effective nitrogen fixation under ambient conditions. *Angew. Chem. Int. Ed.* **2018**, *57*, 10246-10250.

8. References

181. Qiao, B.; Wang, A.; Yang, X.; Allard, L. F.; Jiang, Z.; Cui, Y.; Liu, J.; Li, J.; Zhang, T., Single-atom catalysis of CO oxidation using Pt₁/FeO_x. *Nat. Chem.* **2011**, *3*, 634.
182. Zhou, Y. J.; Sun, Y.; Wang, H. B.; Zhu, C.; Gao, J.; Wu, D.; Huang, H.; Liu, Y.; Kang, Z. H., A nitrogen and boron co-doped metal-free carbon electrocatalyst for an efficient oxygen reduction reaction. *Inorg. Chem. Front.* **2018**, *5*, 2985-2991.
183. Shi, Y.; Zhao, C.; Wei, H.; Guo, J.; Liang, S.; Wang, A.; Zhang, T.; Liu, J.; Ma, T., Single-atom catalysis in mesoporous photovoltaics: the principle of utility maximization. *Adv. Mater.* **2014**, *26*, 8147-53.
184. Marcinkowski, M. D.; Liu, J. L.; Murphy, C. J.; Liriano, M. L.; Wasio, N. A.; Lucci, F. R.; Flytzani-Stephanopoulos, M.; Sykes, E. C. H., Selective formic acid dehydrogenation on Pt-Cu single-atom alloys. *ACS Catal.* **2017**, *7*, 413-420.
185. Li, Y.; Wang, Z.; Xia, T.; Ju, H.; Zhang, K.; Long, R.; Xu, Q.; Wang, C.; Song, L.; Zhu, J.; Jiang, J.; Xiong, Y., Implementing metal-to-ligand charge transfer in organic semiconductor for improved visible-near-infrared photocatalysis. *Adv. Mater.* **2016**, *28*, 6959-65.
186. Qie, L.; Chen, W. M.; Wang, Z. H.; Shao, Q. G.; Li, X.; Yuan, L. X.; Hu, X. L.; Zhang, W. X.; Huang, Y. H., Nitrogen-doped porous carbon nanofiber webs as anodes for lithium ion batteries with a superhigh capacity and rate capability. *Adv. Mater.* **2012**, *24*, 2047-2050.
187. Walczak, R.; Kurpil, B.; Savateev, A.; Heil, T.; Schmidt, J.; Qin, Q.; Antonietti, M.; Oschatz, M., Template- and metal-free synthesis of nitrogen-rich nanoporous "noble" carbon materials by direct pyrolysis of a preorganized hexaazatriphenylene precursor. *Angew. Chem. Int. Ed.* **2018**, *57*, 10765-10770.
188. Vile, G.; Albani, D.; Nachtegaal, M.; Chen, Z.; Dontsova, D.; Antonietti, M.; Lopez, N.; Perez-Ramirez, J., A stable single-site palladium catalyst for hydrogenations. *Angew. Chem. Int. Ed.* **2015**, *54*, 11265-9.
189. Martin, D. J.; Qiu, K.; Shevlin, S. A.; Handoko, A. D.; Chen, X.; Guo, Z.; Tang, J., Highly efficient photocatalytic H₂ evolution from water using visible light and structure-controlled graphitic carbon nitride. *Angew. Chem. Int. Ed.* **2014**, *53*, 9240-5.
190. Kamiya, K.; Kamai, R.; Hashimoto, K.; Nakanishi, S., Platinum-modified covalent triazine frameworks hybridized with carbon nanoparticles as methanol-tolerant oxygen reduction electrocatalysts. *Nat. Commun.* **2014**, *5*, 5040.
191. Oshikiri, T.; Ueno, K.; Misawa, H., Selective dinitrogen conversion to ammonia using water and visible light through plasmon-induced charge separation. *Angew. Chem. Int. Ed.* **2016**, *55*, 3942-3946.

8. References

192. Kordali, V.; Kyriacou, G.; Lambrou, C., Electrochemical synthesis of ammonia at atmospheric pressure and low temperature in a solid polymer electrolyte cell. *Chem. Commun.* **2000**, 1673-1674.
193. Hwang, D.-Y.; Mebel, A. M., Reaction mechanism of N₂/H₂ conversion to NH₃: A theoretical study. *J. Phy. Chem. A* **2003**, *107*, 2865-2874.
194. Qu, K. G.; Zheng, Y.; Dai, S.; Qiao, S. Z., Graphene oxide-polydopamine derived N, S-codoped carbon nanosheets as superior bifunctional electrocatalysts for oxygen reduction and evolution. *Nano Energy* **2016**, *19*, 373-381.
195. Antonietti, M.; Oschatz, M., The concept of "noble, heteroatom-doped carbons," their directed synthesis by electronic band control of carbonization, and applications in catalysis and energy materials. *Adv. Mater.* **2018**, *30*, e1706836.
196. Zhang, J.; Zhao, Z.; Xia, Z.; Dai, L., A metal-free bifunctional electrocatalyst for oxygen reduction and oxygen evolution reactions. *Nat. Nanotechnol.* **2015**, *10*, 444-52.
197. Lu, Z. Y.; Wang, J.; Huang, S. F.; Hou, Y. L.; Li, Y. G.; Zhao, Y. P.; Mu, S. C.; Zhang, J. J.; Zhao, Y. F., N,B-codoped defect-rich graphitic carbon nanocages as high performance multifunctional electrocatalysts. *Nano Energy* **2017**, *42*, 334-340.
198. Zhao, C. J.; Zhang, S. B.; Han, M. M.; Zhang, X.; Liu, Y. Y.; Li, W. Y.; Chen, C.; Wang, G. Z.; Zhang, H. M.; Zhao, H. J., Ambient electrosynthesis of ammonia on a biomass-derived nitrogen-doped porous carbon electrocatalyst: Contribution of pyridinic nitrogen. *ACS Energy Lett.* **2019**, *4*, 377-383.
199. Ghausi, M. A.; Xie, J.; Li, Q.; Wang, X.; Yang, R.; Wu, M.; Wang, Y.; Dai, L., CO₂ overall splitting by a bifunctional metal-free electrocatalyst. *Angew. Chem. Int. Ed.* **2018**, *57*, 13135-13139.
200. Liu, S.; Yang, H. B.; Huang, X.; Liu, L. H.; Cai, W. Z.; Gao, J. J.; Li, X. N.; Zhang, T.; Huang, Y. Q.; Liu, B., Identifying active sites of nitrogen-doped carbon materials for the CO₂ reduction reaction. *Adv. Funct. Mater.* **2018**, *28*, 1800499.
201. Zhang, J.; Dai, L., Nitrogen, Phosphorus, and fluorine tri-doped graphene as a multifunctional catalyst for self-Powered electrochemical water splitting. *Angew. Chem. Int. Ed.* **2016**, *55*, 13296-13300.
202. Zhang, J.; Sun, Y. M.; Zhu, J. W.; Kou, Z. K.; Hu, P.; Liu, L.; Li, S. Z.; Mu, S. C.; Huang, Y. H., Defect and pyridinic nitrogen engineering of carbon-based metal-free nanomaterial toward oxygen reduction. *Nano Energy* **2018**, *52*, 307-314.

8. References

203. Chen, C.; Yan, D.; Wang, Y.; Zhou, Y.; Zou, Y.; Li, Y.; Wang, S., BN pairs enriched defective carbon nanosheets for ammonia synthesis with high efficiency. *Small* **2019**, *15*, e1805029.
204. Yazyev, O. V.; Helm, L., Defect-induced magnetism in graphene. *Phys. Rev. B* **2007**, *75*, 125408.
205. Zhou, J.; Wang, Q.; Sun, Q.; Chen, X. S.; Kawazoe, Y.; Jena, P., Ferromagnetism in semihydrogenated graphene sheet. *Nano Lett.* **2009**, *9*, 3867-70.
206. Cervenka, J.; Katsnelson, M. I.; Flipse, C. F. J., Room-temperature ferromagnetism in graphite driven by two-dimensional networks of point defects. *Nat. Phys.* **2009**, *5*, 840-844.
207. Nichols, J. A.; Saito, H.; Deck, C.; Bandaru, P. R., Artificial introduction of defects into vertically aligned multiwalled carbon nanotube ensembles: Application to electrochemical sensors. *J. Appl. Phys.* **2007**, *102*, 064306.
208. Bepete, G.; Voiry, D.; Chhowalla, M.; Chiguvare, Z.; Coville, N. J., Incorporation of small BN domains in graphene during CVD using methane, boric acid and nitrogen gas. *Nanoscale* **2013**, *5*, 6552-7.
209. Shinde, P. P.; Kumar, V., Direct band gap opening in graphene by BN doping: Ab initio calculations. *Phys. Rev. B* **2011**, *84*, 125401.
210. Xu, B.; Lu, Y. H.; Feng, Y. P.; Lin, J. Y., Density functional theory study of BN-doped graphene superlattice: Role of geometrical shape and size. *J. Appl. Phys.* **2010**, *108*, 073711.
211. Antonietti, M.; Savateev, A., Splitting water by electrochemistry and artificial photosynthesis: Excellent science but a nightmare of translation? *Chem. Rec.* **2018**, *18*, 969-972.
212. Besson, M.; Gallezot, P.; Pinel, C., Conversion of biomass into chemicals over metal catalysts. *Chem. Rev.* **2014**, *114*, 1827-70.
213. Huber, G. W.; Iborra, S.; Corma, A., Synthesis of transportation fuels from biomass: chemistry, catalysts, and engineering. *Chem. Rev.* **2006**, *106*, 4044-98.
214. Chatterjee, C.; Pong, F.; Sen, A., Chemical conversion pathways for carbohydrates. *Green Chem.* **2015**, *17*, 40-71.
215. Binder, J. B.; Raines, R. T., Simple chemical transformation of lignocellulosic biomass into furans for fuels and chemicals. *J. Am. Chem. Soc.* **2009**, *131*, 1979-85.
216. Tong, X. L.; Ma, Y.; Li, Y. D., Biomass into chemicals: Conversion of sugars to furan derivatives by catalytic processes. *Appl. Catal. A-Gen.* **2010**, *385*, 1-13.

8. References

217. van Putten, R. J.; van der Waal, J. C.; de Jong, E.; Rasrendra, C. B.; Heeres, H. J.; de Vries, J. G., Hydroxymethylfurfural, a versatile platform chemical made from renewable resources. *Chem. Rev.* **2013**, *113*, 1499-597.
218. Gandini, A.; Silvestre, A. J. D.; Neto, C. P.; Sousa, A. F.; Gomes, M., The furan counterpart of poly(ethylene terephthalate): An alternative material based on renewable resources. *J. Polym. Sci. Pol. Chem.* **2009**, *47*, 295-298.
219. Casanova, O.; Iborra, S.; Corma, A., Biomass into chemicals: aerobic oxidation of 5-hydroxymethyl-2-furfural into 2,5-furandicarboxylic acid with gold nanoparticle catalysts. *ChemSusChem* **2009**, *2*, 1138-44.
220. Davis, S. E.; Houk, L. R.; Tamargo, E. C.; Datye, A. K.; Davis, R. J., Oxidation of 5-hydroxymethylfurfural over supported Pt, Pd and Au catalysts. *Catal. Today* **2011**, *160*, 55-60.
221. Jiang, N.; You, B.; Boonstra, R.; Terrero Rodriguez, I. M.; Sun, Y., Integrating electrocatalytic 5-hydroxymethylfurfural oxidation and hydrogen production via Co-P-derived electrocatalysts. *ACS Energy Lett.* **2016**, *1*, 386-390.
222. Yang, H. B.; Miao, J.; Hung, S. F.; Chen, J.; Tao, H. B.; Wang, X.; Zhang, L.; Chen, R.; Gao, J.; Chen, H. M.; Dai, L.; Liu, B., Identification of catalytic sites for oxygen reduction and oxygen evolution in N-doped graphene materials: Development of highly efficient metal-free bifunctional electrocatalyst. *Sci. Adv.* **2016**, *2*, e1501122.
223. Ci, L.; Song, L.; Jin, C.; Jariwala, D.; Wu, D.; Li, Y.; Srivastava, A.; Wang, Z. F.; Storr, K.; Balicas, L.; Liu, F.; Ajayan, P. M., Atomic layers of hybridized boron nitride and graphene domains. *Nat. Mater.* **2010**, *9*, 430-5.
224. Zhao, Y.; Yang, L.; Chen, S.; Wang, X.; Ma, Y.; Wu, Q.; Jiang, Y.; Qian, W.; Hu, Z., Can boron and nitrogen co-doping improve oxygen reduction reaction activity of carbon nanotubes? *J. Am. Chem. Soc.* **2013**, *135*, 1201-4.
225. Yang, L.; Jiang, S.; Zhao, Y.; Zhu, L.; Chen, S.; Wang, X.; Wu, Q.; Ma, J.; Ma, Y.; Hu, Z., Boron-doped carbon nanotubes as metal-free electrocatalysts for the oxygen reduction reaction. *Angew. Chem. Int. Ed.* **2011**, *50*, 7132-5.
226. Wang, S.; Zhang, L.; Xia, Z.; Roy, A.; Chang, D. W.; Baek, J. B.; Dai, L., BCN graphene as efficient metal-free electrocatalyst for the oxygen reduction reaction. *Angew. Chem. Int. Ed.* **2012**, *51*, 4209-12.
227. Tabbal, M.; Christidis, T.; Isber, S.; Mérel, P.; El Khakani, M. A.; Chaker, M.; Amassian, A.; Martinu, L., Correlation between the sp²-phase nanostructure and the physical properties of unhydrogenated carbon nitride. *J. Appl. Phys.* **2005**, *98*, 044310.

8. References

228. Zhang, J.; Zhang, G.; Chen, X.; Lin, S.; Mohlmann, L.; Dolega, G.; Lipner, G.; Antonietti, M.; Blechert, S.; Wang, X., Co-monomer control of carbon nitride semiconductors to optimize hydrogen evolution with visible light. *Angew. Chem. Int. Ed.* **2012**, *51*, 3183-7.
229. Barklie, R. C., Characterisation of defects in amorphous carbon by electron paramagnetic resonance. *Diamond Relat. Mater.* **2001**, *10*, 174-181.
230. Vuyyuru, K. R.; Strasser, P., Oxidation of biomass derived 5-hydroxymethylfurfural using heterogeneous and electrochemical catalysis. *Catal. Today* **2012**, *195*, 144-154.
231. Chadderton, D. J.; Xin, L.; Qi, J.; Qiu, Y.; Krishna, P.; More, K. L.; Li, W. Z., Electrocatalytic oxidation of 5-hydroxymethylfurfural to 2,5-furandicarboxylic acid on supported Au and Pd bimetallic nanoparticles. *Green Chem.* **2014**, *16*, 3778-3786.
232. Dijkman, W. P.; Groothuis, D. E.; Fraaije, M. W., Enzyme-catalyzed oxidation of 5-hydroxymethylfurfural to furan-2,5-dicarboxylic acid. *Angew. Chem. Int. Ed.* **2014**, *53*, 6515-8.
233. Gabrielse, G.; Hanneke, D.; Kinoshita, T.; Nio, M.; Odom, B., Erratum: New Determination of the Fine Structure Constant from the Electron gValue and QED. *Phys. Rev. Lett.* **2006**, *97*, 030802.
234. Electron paramagnetic resonance, https://en.wikipedia.org/wiki/Electron_paramagnetic_resonance.
235. Keeler, J., *Understanding NMR spectroscopy*. John Wiley & Sons: 2011.
236. Shah, N.; Sattar, A.; Benanti, M.; Hollander, S.; Cheuck, L., Magnetic resonance spectroscopy as an imaging tool for cancer: a review of the literature. *J. Am. Osteopath. Assoc.* **2006**, *106*, 23-27.
237. X-ray crystallography, https://en.wikipedia.org/wiki/X-ray_crystallography.
238. Ameruddin, A. Growth and characterisation of gold-seeded indium gallium arsenide nanowires for optoelectronic applications. 2015.
239. Cychosz, K. A.; Guillet-Nicolas, R.; Garcia-Martinez, J.; Thommes, M., Recent advances in the textural characterization of hierarchically structured nanoporous materials. *Chem. Soc. Rev.* **2017**, *46*, 389-414.
240. Thommes, M.; Cychosz, K. A., Physical adsorption characterization of nanoporous materials: progress and challenges. *Adsorpt. J. Int. Adsorpt. Soc.* **2014**, *20*, 233-250.
241. Ambroz, F.; Macdonald, T. J.; Martis, V.; Parkin, I. P., Evaluation of the BET theory for the characterization of meso and microporous MOFs. *Small Methods* **2018**, *2*, 1800173.

8. References

242. Thommes, M.; Cychosz, K. In recent advances in the textural characterization of hierarchically structured nanoporous materials, Meeting Abstracts, *Electrochem. Soc.*: **2018**; pp 2374-2374.
243. Fang, X.; Chen, C.; Liu, Z.; Liu, P.; Zheng, N., A cationic surfactant assisted selective etching strategy to hollow mesoporous silica spheres. *Nanoscale* **2011**, *3*, 1632-1639.
244. Suryanto, B. H. R.; Du, H. L.; Wang, D. B.; Chen, J.; Simonov, A. N.; MacFarlane, D. R., Challenges and prospects in the catalysis of electroreduction of nitrogen to ammonia. *Nat. Catal.* **2019**, *2*, 290-296.
245. Rademacher, J. T.; Kanakarajan, K.; Czarnik, A. W., Improved synthesis of 1,4,5,8,9,12-hexaazatriphenylenehexacarboxylic acid. *Synthesis-Stuttgart* **1993**, *1*, 378-380.
246. Kresse, G.; Furthmüller, J., Efficiency of ab-initio total energy calculations for metals and semiconductors using a plane-wave basis set. *Comput. Mater. Sci.* **1996**, *6*, 15-50.
247. Kresse, G.; Furthmüller, J., Efficient iterative schemes for ab initio total-energy calculations using a plane-wave basis set. *Phys. Rev. B* **1996**, *54*, 11169-11186.
248. Kresse, G.; Joubert, D., From ultrasoft pseudopotentials to the projector augmented-wave method. *Phys. Rev. B* **1999**, *59*, 1758-1775.
249. Perdew, J. P.; Burke, K.; Ernzerhof, M., Generalized gradient approximation made simple. *Phys. Rev. Lett.* **1996**, *77*, 3865-3868.
250. Grimme, S.; Antony, J.; Ehrlich, S.; Krieg, H., A consistent and accurate ab initio parametrization of density functional dispersion correction (DFT-D) for the 94 elements H-Pu. *J. Chem. Phys.* **2010**, *132*, 154104.
251. Dudarev, S. L.; Botton, G. A.; Savrasov, S. Y.; Humphreys, C. J.; Sutton, A. P., Electron-energy-loss spectra and the structural stability of nickel oxide: An LSDA+U study. *Phys. Rev. B* **1998**, *57*, 1505-1509.
252. Mattsson, A.; Hu, S.; Hermansson, K.; Österlund, L., Adsorption of formic acid on rutile TiO₂(110) revisited: An infrared reflection-absorption spectroscopy and density functional theory study. *J. Chem. Phys.* **2014**, *140*, 034705.
253. Chrétien, S.; Metiu, H., Electronic structure of partially reduced rutile TiO₂(110) surface: where are the unpaired electrons located? *J. Phys. Chem. C* **2011**, *115*, 4696-4705.
254. Burdett, J. K.; Hughbanks, T.; Miller, G. J.; Richardson, J. W.; Smith, J. V., Structural-electronic relationships in inorganic solids: powder neutron diffraction studies of the rutile and anatase polymorphs of titanium dioxide at 15 and 295 K. *J. Am. Chem. Soc.* **1987**, *109*, 3639-3646.
255. Diebold, U., The surface science of titanium dioxide. *Surf. Sci. Rep.* **2003**, *48*, 53-229.

8. References

256. Ramamoorthy, M.; Vanderbilt, D.; King-Smith, R. D., First-principles calculations of the energetics of stoichiometric TiO₂ surfaces. *Phys. Rev. B* **1994**, *49*, 16721-16727.
257. Monkhorst, H. J.; Pack, J. D., Special points for Brillouin-zone integrations. *Phys. Rev. B* **1976**, *13*, 5188-5192.
258. Nam, D. H.; Taitt, B. J.; Choi, K. S., Copper-based catalytic anodes to produce 2,5-furandicarboxylic acid, a biomass-derived alternative to terephthalic Acid. *ACS Catal.* **2018**, *8*, 1197-1206.

9. List of publications

9.1 Peer-reviewed journal publications

1. **Qin Q.**,* Heil T., Schmidt J., Schmallegger M., Gescheidt-Demner G., Antonietti M. and Oschatz M.,* Electrochemical fixation of nitrogen and its coupling with biomass valorization with a strongly adsorbing and defect optimized boron-carbon-nitrogen catalyst. *ACS Catal.* **2019**, under review.
2. **Qin, Q.**, Zhao Y., Schmallegger M., Heil, T., Schmidt J., Walczak R., Gescheidt-Demner G., Jiao H. and Oschatz, M.,* Enhanced electrocatalytic N₂ reduction via partial anion substitution in titanium oxide-carbon composites. *Angew. Chem. Int. Ed.* **2019**, 58, 2-8.
3. **Qin, Q.**, Heil, T., Antonietti, M. and Oschatz, M.,* Single-site gold catalysts on hierarchical N-doped porous noble carbon for enhanced electrochemical reduction of nitrogen. *Small Methods* **2018**, 2, 1800202.
4. Walczak, R.; Kurpil, B.; Savateev, A.; Heil, T.; Schmidt, J.; **Qin, Q.**; Antonietti, M.; Oschatz, M.* Template- and metal-free synthesis of nitrogen-rich nanoporous “noble” carbon materials by direct pyrolysis of a preorganized hexaazatriphenylene precursor. *Angew. Chem. Int. Ed.* **2018**, 130, 10926.

9. List of publications

9.2 Conference contributions

9.2.1 Oral presentation as the presenting author

2019.08.18-08.23 EuropaCat 2019, Aachen, Germany
Title: Rational design of novel electrocatalysts for N₂ fixation with enhanced performance
Qin Q., Oschatz M., and Antonietti M.

9.2.2 Poster presentation as the presenting author

2018.09.24-09.26 Electrochemistry 2018, Ulm, Germany
Title: Au single atoms on N-rich carbon structures for enhanced N₂ electrochemical reduction
Qin Q., Oschatz M., and Antonietti M.

10. Declaration

Die vorliegende Dissertation entstand im Zeitraum zwischen September 2017 und September 2019 am Max-Planck-Institut für Kolloid und Grenzflächenforschung unter Betreuung von Prof. Dr. Dr. h.c. Markus Antonietti.

Hiermit erkläre ich, dass die vorliegende Arbeit selbstständig angefertigt wurde und keine anderen als die angegebenen Hilfsmittel und Quellen verwendet wurden.

The present work was carried out during the period from September 2017 to September 2019 at the Max Planck Institute of Colloids and Interfaces under supervision of Prof. Dr. Dr. h.c. Markus Antonietti.

I declare that I have written this work on my own and used no other than the named aids and references.

Qing Qin

Potsdam, September 2019